SEL-76-009

The Response of the Ionosphere to the Injection of Chemically Reactive Vapors

by

Paul Alan Bernhardt

May 1976

Technical Report No. 17

AUG 1976
RECEIVED
NASA STI FACILITY
INPUT BRANCH

RADIOSCIENCE LABORATORY

STANFORD ELECTRONICS LABORATORIES

STANFORD UNIVERSITY · STANFORD, CALIFORNIA

THE RESPONSE OF THE IONOSPHERE TO THE
INJECTION OF CHEMICALLY REACTIVE VAPORS

by

Paul Alan Bernhardt

May 1976

Technical Report No. 17

Radioscience Laboratory
Stanford Electronics Laboratories
Stanford University   Stanford, California

ABSTRACT

An opening in the ionosphere may be created by the release of
reactive chemicals that promote ion-electron recombination. The
following sequence of events is initiated by a gas realease. As
the gas expands, it is rapidly cooled. If the temperature of the
vapor falls below the saturated vapor temperature, some of the
gas condenses. During the day, the condensate is re-vaporized by
sunlight, but at night the condensed molecules remain as clusters
that do not effectively interact chemically with the ionospheric
plasma.

When the vapor becomes sufficiently tenuous, it is reheated by
collisions with the ambient atmosphere and its flow is then governed
by diffusive expansion. As the injected gas becomes well mixed
with the plasma, a "hole" is created by chemical processes. In the
case of diatomic hydrogen release, depression of the electron concen-
trations is governed by the charge exchange reaction between oxygen
ions and the hydrogen, a reaction that produces positive hydroxyl
ions. This latter ion rapidly reacts with the electron gas to produce
excited oxygen and hydrogen atoms. Enhanced airglow emissions will
result from the transition of the excited atoms to lower energy
states.

Owing to the ion depletion, the remaining electrons are no longer
effectively cooled by Coulomb collisions and the electron temperature
in the depleted region rises sharply causing a thermal expansion of
the plasma and a further reduction in the local plasma concentration.
Replenishment of the plasma in the depleted region takes place in

part by plasma flow from the protonosphere. Such a flow produces a tube of reduced plasma that extends into the magnetosphere and, for cases of extreme depletion, may extend into the conjugate ionosphere.

Flights of space vehicles, such as the Space Shuttle, into the ionosphere may permit the controlled depletion of the F2-layer by the injection of selected gases. Estimation of the optimum modification experiment is based on calculations of temporal and spatial characteristics of the ionospheric hole for various types and amounts of injected gas. Criteria for judging candidate gases include the amount of ionospheric plasma depleted per unit mass of released gas, the chemical reaction rates, and the resistance to photodissociation during the day and to condensation during the night. Based on these criteria, H_2 is recommended for gas release experiments. Water vapor and carbon dioxide are acceptable for daytime releases, but lose efficiency at night due to condensation.

The amount of gas released partially determines the size and duration of the depletion. The release of 100 kg of diatomic hydrogen into the ionosphere produces an F-layer depletion lasting over 2 hours.

Measurements of the temporal variation in the spatial structure of the ionospheric hole may provide information about the dynamic processes that maintain the ionosphere. These processes include chemical dissociation, diffusion, and photoionization.

Artificially produced ionospheric holes may significantly affect radiowave propagation. During the early period of chemical

modification, the hole may act as a lens that focuses or bends VHF or HF radio waves. In the later period, a few percent plasma density depression may extend over the entire geomagnetic field line. Such field-aligned irregularities may guide HF and VLF radio waves for interhemispheric propagation.

Acknowledgement

I want to thank all persons involved in the final preparation of this manuscript, in particular Michal Plume for her excellent typing.

CONTENTS

CONTENTS (Cont.)

ILLUSTRATIONS

ILLUSTRATIONS (Cont.)

ILLUSTRATIONS (Cont.)

TABLES

Chapter I

INTRODUCTION

This research examines the ionospheric depletion produced by gases that react chemically in the F2-layer. The gases that promote O^+ ion and electron recombination in the ionosphere are common in rocket exhausts. It is therefore not unexpected that the first observations of chemical depression of the F2-layer plasma were made while a rocket was firing at ionospheric altitudes. However, since expanding gases produce local depletion by simply displacing the ambient atmosphere, it was not always known that the ionospheric depletion by rocket exhaust was predominantly due to chemical effects.

On February 17, 1959 around 1100 EST, Vanguard II penetrated the F-region. At the time of the passage of the missile, ionosphere sounders located at Cape Canaveral and Grand Bahama Island recorded unusually disturbed ionograms. These ionograms were interpreted as resulting from a hole created in the F-region by the missile's exhaust gases. This hole lasted for half an hour or more. It was theorized that the expansion of the hot exhaust gases had "punched" a hole in the ionospheric layer [Booker, 1961; Barnes, 1961].

A similar effect was observed by Faraday rotation measurements obtained from the Scout rocket (NASA ST-7/P-21) launched from Wallops Island, Virginia at 1238 EST on October 19, 1961. During the third stage burning period, when the rocket was at an altitude of 200 km,

1

Faraday rotation of signals emitted from the rocket indicated an apparent reduction in ionospheric electron densities in the wake of the rocket [Jackson et al., 1962]. Again it was speculated that the deficiency of electrons in the wake of the rocket was due perhaps to a displacement of the ambient electrons by the exhaust gases.

The theory that the rocket produced a depletion of the F-layer solely through the displacement of the ionospheric plasma by the rocket exhaust gases was inadequate to explain the observed effects. The size and duration of the opening in the ionosphere indicated another process was responsible for the formation of this opening. It is now clear that chemical reaction between the rocket exhaust gases and the F-region ions was the main mechanism for production of the ionospheric hole.

Chemicals were released into the E and F-regions by the Air Force during Project Firefly 1962 [Rosenberg, 1964]. Of the many controlled releases during this project, only one dealt with a chemical which might accelerate the ion and electron loss process. This was the injection of 5.44 kg CO_2 at an altitude of 234 km. With this gas, the loss of electrons in the F-region is promoted by the following chemical process:

$$CO_2 + O^+ \rightarrow O_2^+ + CO$$

$$O_2^+ + e \rightarrow O + O$$
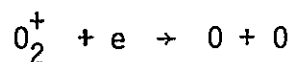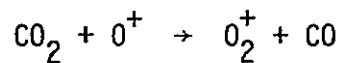
No measurable distrubance of the ionosphere could be attributed to the CO_2 realease because it coincided with the passage of a large meteor that perturbed the ionospheric record and that masked the effects of the CO_2. In this author's opinion, failure of the CO_2 release may also be attributed to the condensation of a significant portion of the CO_2, after the release.

Except for the one CO_2 release, chemical experiments in the ionosphere, during and after Project Firefly, were designed to explore processes other than acceleration of dissociative recombination. Discussion of ionospheric modification by the release of electron attaching materials such as sulfur hexafluoride [Rosenberg, 1964] or by the release of easily ionized material such as barium or strontium [Haser, 1967] is beyond the scope of the report.

It was not until the late 1960's that the reaction rates between the ionospheric ion constituents and possible neutral perturbing agents were measured accurately in the laboratory. An excellent summary of ion-molecule reaction rates is given by Ferguson [1973].

The interest in chemical depletion of the ionosphere was re-kindled in 1975 with the launch of the Skylab orbiting spacecraft by a Saturn V rocket. It was reported by Mendillo et al. [1975a,b] that a large and rapid decrease was produced in the ionospheric total electron content within 1000 km of the Saturn V burn. The large hole was attributed to chemical reactions initiated by the H_2 and H_2O in the rocket exhaust.

The development of the Space Shuttle and large payload rockets makes controlled releases of large quantities of reactive gases

3

practical. Thus, with increased knowledge of the F-region chemistry, and increased payload capabilities of space vehicles, the use of gas releases for scientific exploration of the ionosphere is more feasible than it was a decade ago.

There are three general applications for experiments involving release of gases that promote ionospheric depletion. First, communications may be disrupted or improved by modification of the F-layer. Second, the ionosphere may be used as a laboratory for the measurement of the perturbations resulting from the gas release. Observations· of the hole created in the ionosphere can provide important information about the chemical and diffusive processes that govern the F-region dynamics. Third, the depletion of the ionosphere can allow the penetration of radio signals that normally are reflected by the F-layer. These signals include cosmic radio waves of interest to radio astronomers and ducted VLF radio waves of interest to magnetospheric physicists.

The organization of this report is illustrated by the flow diagram of Figure 1. Following this Introduction, four chapters deal with the theory necessary for a complete understanding of the response of the ionosphere to chemical releases. Chapter II is a discussion of chemicals that may be used to reduce the F-layer O^+ and electron concentrations. Chapter III is a theoretical treatment of the released gas dynamics from the time of injection to the time of thermalization with the background atmosphere. Chapter IV presents the theory of diffusion necessary for modeling the flow of the released gas after thermalization has occurred. Also, the diffusive

4
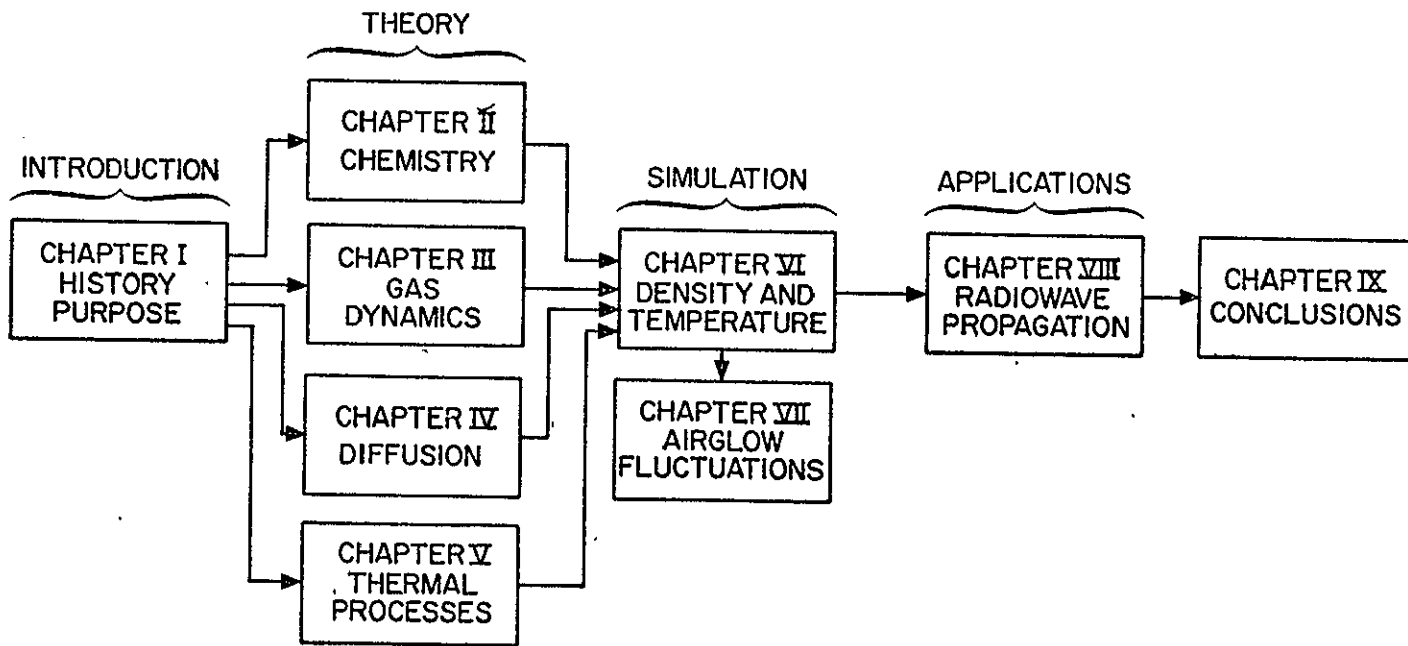
Fig. 1. Structure of Report.

flow of the perturbed ionosphere is described in this chapter.
Chapter V presents the energy balance equations used in modeling the
disturbed thermal processes resulting from the release of reactive
gases.

The theory presented in Chapters II through V becomes the basis
of a numerical model used to simulate the disturbances produced in
the plasmasphere. In Chapter VI, the fluctuations in density and
temperature caused by hydrogen releases into the F-layer are modeled.
Chapter VII is a description of the extraordinary airglow emissions
accompanying the depletion. Chapter VIII illustrates several uses
of the depleted plasmasphere for guiding or focusing radio waves.
Conclusions and recommendations for further research are presented
in Chapter IX.

This research has contributed to scientific knowledge by
borrowing from the diverse scientific disciplines of chemistry, gas-
dynamics, aeronomy, and electromagnetic theory to provide a detailed
description of the ionospheric depletion experiment. Some specific
contributions in the area of theoretical analysis of the controlled
modification process are:

1) Comparitive analysis of candidate chemicals for depletion
of the F2-layer. Gases such as H_2O, H_2, CO_2 and NO_2 cause signifi-
cant depletion of the ionosphere because of their high reaction rates
with O^+ ions.

2) Theoretical study of condensation of expanding gas clouds.
Condensation may limit the usefulness of released gases. After the
gas is injected into the ionosphere, it expands and cools. Gases,

such as H_2O, CO_2, and NO_2, with high saturated vapor temperatures will partially condense during the early period of expansion. At night, the condensed droplets will not re-evaporate. The injected chemical in droplet form loses effectiveness as an ionospheric modifier.

3) Treatment of the transition between free molecular expansion and diffusive expansion of a released gas cloud. The injected gas cloud thermalizes by collisions with the background atmosphere. Thermalization occurs within 10 seconds of the time of initial gas release.

4) Development of a numerical model of the thermosphere for simulation of perturbations in density, temperature, and airglow produced by the release of reactive gases. Several phenomena accompanying the ionospheric depletion include changes in the electron temperatures and enhancement in the airglow emissions. During the day, the temperature of the electron gas may rise by 1000 K. The temperature of the ions drops slightly in the perturbed regions. An expanding airglow ring is formed around the point of gas release. The intensity of the ring may be five times the unperturbed airglow intensity.

The ionospheric depletion experiment permits:

1) Measurement of chemical and diffusion coefficients in the ionospheric "laboratory". Coefficients not available from ground-based laboratory measurements may be obtained.

2) High resolution observation of extragalactic radio sources by using the ionospheric hole as a lens. A refracting radiotelescope using the ionospheric lens may have a factor of ten better resolving power than existing radiotelescopes.

3) Ducting of HF and VLF radio signals in the protonosphere above the depleted ionosphere. The depletion of the ionosphere produces ducts in the overlying protonosphere. Radio waves guided by this duct may be used for interhemispherical communication or for controlled wave-particle interaction experiments.

4) Measurement of ionospheric electric fields and neutral winds by observing the perturbed airglow emissions. The expanding airglow ring is a new type of chemical tracer that may be used at any time of day.

Chapter II

CHEMICAL PROCESSES IN THE IONOSPHERE

A knowledge of ionospheric chemistry is necessary to predict the F-region plasma depletion caused by the release of certain gases. Fortunately, the F-region chemistry is well understood, thus permitting accurate modeling of artificially induced depletions.

This chapter reviews the dominant chemical mechanisms in the region of interest and discusses in detail the plasma depletion caused by chemically increasing the ion-electron recombination rate.

A. F-Region Photochemistry

The plasma that constitutes the ionosphere is created by ionization of gases in the neutral atmosphere by the sun. Photoionization by shortwave solar extreme ultraviolet (EUV), i.e., radiation with wavelengths less than 1027 A, is the main mechanism for maintaining the daytime ionosphere. The photoionization of the neutral atmospheric constituents (i.e., mono and diatomic oxygen and diatomic nitrogen) proceeds according to these reactions

$$O + h\nu \rightarrow O^+ + e^-$$
$$O_2 + h\nu \rightarrow O_2^+ + e^- \quad\quad (1)$$
$$N_2 + h\nu \rightarrow N_2^+ + e^-$$
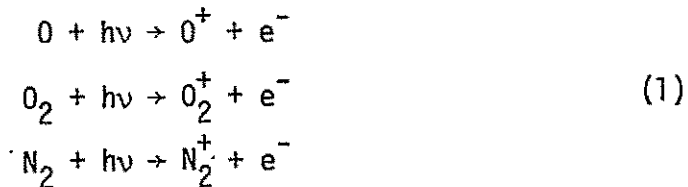
The rates at which these reactions occur depend on the frequency (ν) and intensity of the solar extreme ultraviolet radiation, on the ionization cross sections and on the local gas concentration.

Variations in soft x-ray and EUV fluxes produce corresponding variations in the F-region ionization level. The effects of the changes in solar radiation produced by solar flares and eclipses have been discussed by Garriott et al. [1967], Evans [1965], and others.

Ionization by energetic charged particles is known as corpuscular ionization. The energetic particles, guided by geomagnetic field lines, produce ionization by collisions with neutral particles. Corpuscular ionization may be important when there is little or no photoionization (i.e., in the night F-layer or in the polar winter F-layer). Electron impact ionization is an example of this ionization mechanism.

$$O + e^{-*} \rightarrow O^{+} + 2e^{-} - 13.618 \quad eV$$

$$O_2 + e^{-*} \rightarrow O_2^{+} + 2e^{-} - 12.07 \quad eV \qquad (2)$$

$$N_2 + e^{-*} \rightarrow N_2^{+} + 2e^{-} - 15.58 \quad eV$$
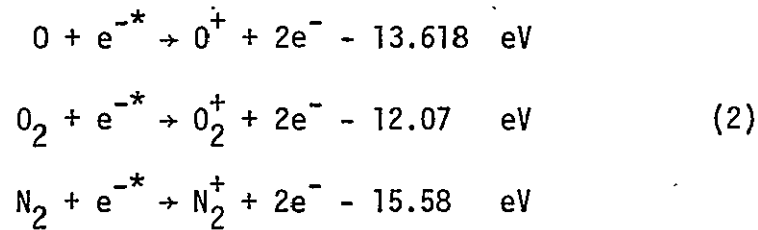
where e^{-*} represents an energetic electron.

The rates of these reactions depend on the concentration and ionization cross section of the neutral gas, the latter being strongly dependent on the energy of the impacting electron. Natural sources of energetic electrons are photoelectrons produced in the photoionization process (1), high energy electrons produced during magnetic storms, and energetic electrons precipitating from the magnetosphere into the high latitude ionosphere.

Fluxes of plasma into and out of the protonosphere may have a significant effect on the ionosphere. The protonosphere is composed of ionized hydrogen atoms (i.e. protons). The neutral atmosphere in the protonosphere is composed of the light elements H and He. H^+ ions that diffuse to lower altitudes where monoatomic oxygen is abundant may undergo the charge exchange reaction

$$H^+ + 0 \rightarrow 0^+ + H \quad \text{rate} = 2.2 \times 10^{-11} \, T_i^{1/2} \, [0] \, \text{sec}^{-1}$$

$$\text{[Banks and Kockarts, 1973]} \quad (3)$$
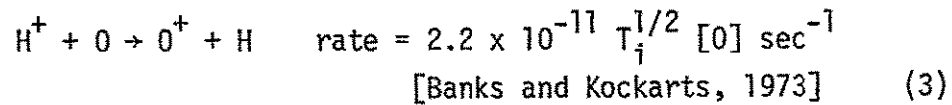
to produce atomic oxygen ions. The rate of this reaction is proportional to the square root of the H^+ ion temperature, T_i, and proportional to the atomic oxygen concentration [0]. Plasma flow from the ionosphere to the protonosphere, subject to the charge exchange reaction

$$0^+ + H \rightarrow H^+ + 0 \quad \text{rate} = 2.5 \times 10^{-11} \, T_n^{1/2} \, [H] \quad (4)$$

$$\text{[Banks and Kockarts, 1973]}$$
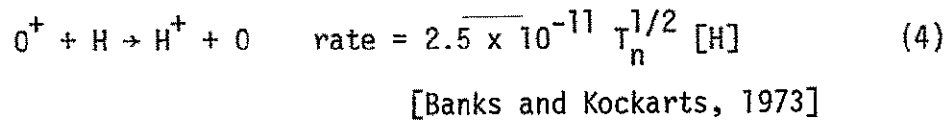
Here, T_n is the neutral temperature.

The direction of the plasma flow depends on the time of day. At night the flow is downward with H^+ being converted to 0^+ by the reaction in (3). The nighttime ionosphere is supported by this mechanism. During the daytime, an overabundance of 0^+ is produced in the F-region. The 0^+ that diffuses upward is converted into H^+ according to (4) and fills the protonospheric reservoir.

Fluctuations in the protonospheric content are communicated to the ionosphere by flux variations. Natural events, such as magnetic storms may deplete the protonospheric reservoir. A depleted protonosphere will tend to produce a reduction in downward fluxes during the night and an increase in upward fluxes during the day. In either case, a reduced F-region ionosphere may result.

Recombination of ions with electrons occurs either through radiative recombination

$$X^+ + e^- \rightarrow X + h \tag{5}$$

or through dissociative recombination

$$XY^+ + e^- \rightarrow X + Y \tag{6}$$

Radiative recombination (5) involves the collision of an ion (X^+) with an electron (e^-). In the collision process a neutral atom is formed and energy is released as a photon. The radiative recombination rate is about 10^{-12} cm^3 sec^{-1}. The 0^+-electron recombination reaction is $0^+ + e^- \rightarrow 0 + h\nu$.

Dissociative recombination (6) occurs when an electron collides with polyatomic ion which splits into two neutral particles. Because of the large recombination rate for this process $(\sim 10^{-7}$ cm^3 $sec^{-1})$, it is the principle mechanism for ion-electron recombination in most of the ionosphere. The dissociative recombination reactions for 0_2^+ and N_2^+ are

$$0_2^+ + e^- \rightarrow 0 + 0 \quad \alpha(0_2^+) = 2.2 \times 10^{-7} \ (300/T_e)^{.8} \ cm^3 \ sec^{-1}$$

$$\tag{7}$$

$$N_2^+ + e^- \rightarrow N + N \quad \alpha(N_2^+) = 3 \times 10^{-7} \ (300/T_e)^{.3} \ cm^3 \ sec^{-1}$$

The recombination rate decreases with electron temperature (T_e) because the electron-ion collision frequency varies as $T_e^{-3/2}$.

The loss of 0^+ in the ionosphere occurs principally through charge-exchange reactions with the neutral polyatomic constituents of the atmosphere. These ion-neutral reactions are

$$0^+ + 0_2 \rightarrow 0_2^+ + 0 + 1.55 \ eV \quad \gamma(0_2) = 2.0 \times 10^{-11} (\tfrac{300}{T})^{1/2} \ cm^3 \ sec^{-1}$$

$$\tag{8}$$

$$0^+ + N_2 \rightarrow NO^+ + N + 1.1 \ eV+ \quad \gamma(N_2) = 1.2 \times 10^{-12} (\tfrac{300}{T})^{1/2} \ cm^3 \ sec^{-1}$$

where T is the neutral temperature.

The charge exchange rates, $\gamma(0_2)$ and $\gamma(N_2)$, are higher than the radiative recombination rates for 0^+ but are significantly lower than the dissociative recombination rates of (7). The ion charge exchange products given by (8), NO^+ and 0_2^+, are mainly lost through dissociative recombination

$$NO^+ + e^- \rightarrow N + 0 \ , \quad \alpha(NO^+) = 4.1 \times 10^{-7} \ cm^3 \ sec^{-1}$$

$$\tag{9}$$

$$0_2^+ + e^- \rightarrow 0 + 0 \quad \alpha(0_2^+) = 2.2 \times 10^{-7} \ cm^3 \ sec^{-1}$$

14

TABLE 1. Perturbing gas reactions in the ionosphere.
(See Appendix A)

	Weakly Reactive	Moderately Reactive		Strongly Reactive			
	N_2	O_2	N_2O	CO_2	NO_2	H_2	H_2O
Ion-molecule Reaction with O^+ (rate: cm³/sec)	$O^+ + N_2 \to NO^+ + N + 1.11$ eV. 1.3[-12]	$O^+ + O_2 \to O_2^+ + O + 1.55$ eV. 2.[-11]	$O^+ + N_2O \to N_2O^+ + O + .72$ eV. $\to NO^+ + NO + 5.9$ eV. 2.2[-10]	$O^+ + CO_2 \to O_2^+ + CO + 1.18$ eV. 1.2[-9]	$O^+ + NO_2 \to NO_2^+ + O + 3.84$ eV. 1.6[-9]	$O^+ + H_2 \to OH^+ + H + .37$ eV. 2.[-9]	$O^+ + H_2O \to H_2O^+ + O + 1.01$ eV. 2.3[-9]
Ion-molecule Reaction with N^+ (rate: cm³/sec)		$N^+ + O_2 \to O_2^+ + N + 2.48$ eV. $\to NO^+ + N + 6.88$ eV. 7.[-12]		$N^+ + CO_2 \to CO_2^+ + N + .78$ eV. 1.3[-9]	$N^+ + NO \to NO^+ + N + 5.3$ eV. 8.[-10]	$N^+ + H_2 \to NH^+ + H + .66$ eV. 7.[-10]	$N^+ + H_2O \to H_2O^+ + N + 1.94$ eV. 2.6[-9]
Other Ion-molecule Reactions (rate: cm³/sec)				$CO_2^+ + O \to O_2^+ + CO + 1.33$ eV. $\to O^+ + CO_2 + .15$ eV. 2.6[-10]	$O_2^+ + NO_2 \to NO_2^+ + O_2 + 2.29$ eV. 6.6[-10]	$OH^+ + H_2 \to H + H_2O^+ + 1.82$ eV. $OH^+ + O_2 \to OH + O_2^+ + 1.12$ eV. 2.[-10]	$H_2O^+ + H_2O \to H_3O^+ + OH + .43$ eV. 1.7[-9]
Primary Electron-ion Recombination Reactions (rate cm³/sec)	$NO^+ + e^- \to N + O + 2.75$ eV. 4.1[-7]	$O_2^+ + e^- \to O + O + 6.95$ eV. 2.[-7]	$NO^+ + e^- \to N + O + 2.75$ eV. 4.1[-7]	$O_2^+ + e^- \to O + O + 6.95$ eV. 2.[-7]	$NO_2^+ + e^- \to NO + O + 4.81$ eV. 4.[-7]	$OH^+ + e^- \to O + H + 8.77$ eV. 1.[-7]	$H_2O^+ + e^- \to OH + H + 7.46$ eV. 3.[-7]
Other Electron-ion Recombination Reactions (rate: cm³/sec)		$NO^+ + e^- \to N + O + 2.75$ eV. 4.1[-7]	$N_2O^+ + e^- \to NO + N + 7.93$ eV. 4.[-7]	$CO_2^+ + e^- \to CO + O + 8.28$ eV. 3.8[-7]	$NO^+ + e^- \to N + O + 2.75$ eV. 4.1[-7]	$NH^+ + e^- \to N + H + 9.41$ eV. 1.[-7]	$H_3O^+ + e^- \to H_2O + H + 7.04$ eV. 1.[-6]
Photo-dissociation Reactions (rate: sec⁻¹)	$N_2 + h\nu \to N + N$ 5.[-12]	$O_2 + h\nu \to O + O$ 4.[-6]	$N_2O + h\nu \to NO + N$ $\to N_2 + O$ 2.[-6]	$CO_2 + h\nu \to CO + O$ 1.9[-7]	$NO_2 + h\nu \to NO + O$ 8.1[-3]	$H_2 + h\nu \to H + H$ ≈ 0	$H_2O + h\nu \to OH + H$ 1.[-5]

NOTATION: [-x] represents 10^{-x}

Variations in temperature and composition of the neutral atmosphere produce changes in the ion composition. The neutral atmosphere density increases as altitude decreases. At some altitude below the F2 layer, the O_2 and N_2 densities become sufficiently high so that the charge exchange with O^+, Eq. (8), produces polyatomic ion densities that are greater than the O^+ densities. This region is called the F1 layer.

By considering the dependence of ion loss on temperature and composition several means of artificial modification of the ionosphere may be suggested. Heating of the F-region will promote increased ion densities due to the reduced recombination rate but will also tend to lower ion densities due to thermal expansion. The loss of O^+ through charge exchange can be promoted by the introduction of relatively small quantities of foreign gases with high affinities with O^+. This latter type of chemical modification is discussed in the next section.

B. Chemical Perturbation of the Ionosphere

In Section A, it is stated that the chemical loss is controlled by charge exchange with N_2 and O_2. As shown in Table 1, numerous gases react faster with O^+ than do O_2 or N_2. Consider the ion molecule reaction with diatomic hydrogen

$$H_2 + O^+ \rightarrow OH^+ + H \qquad \gamma(H_2) = 2 \times 10^{-9} \text{ cm}^3 \text{ sec}^{-1} \qquad (10)$$

15
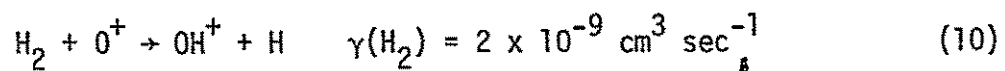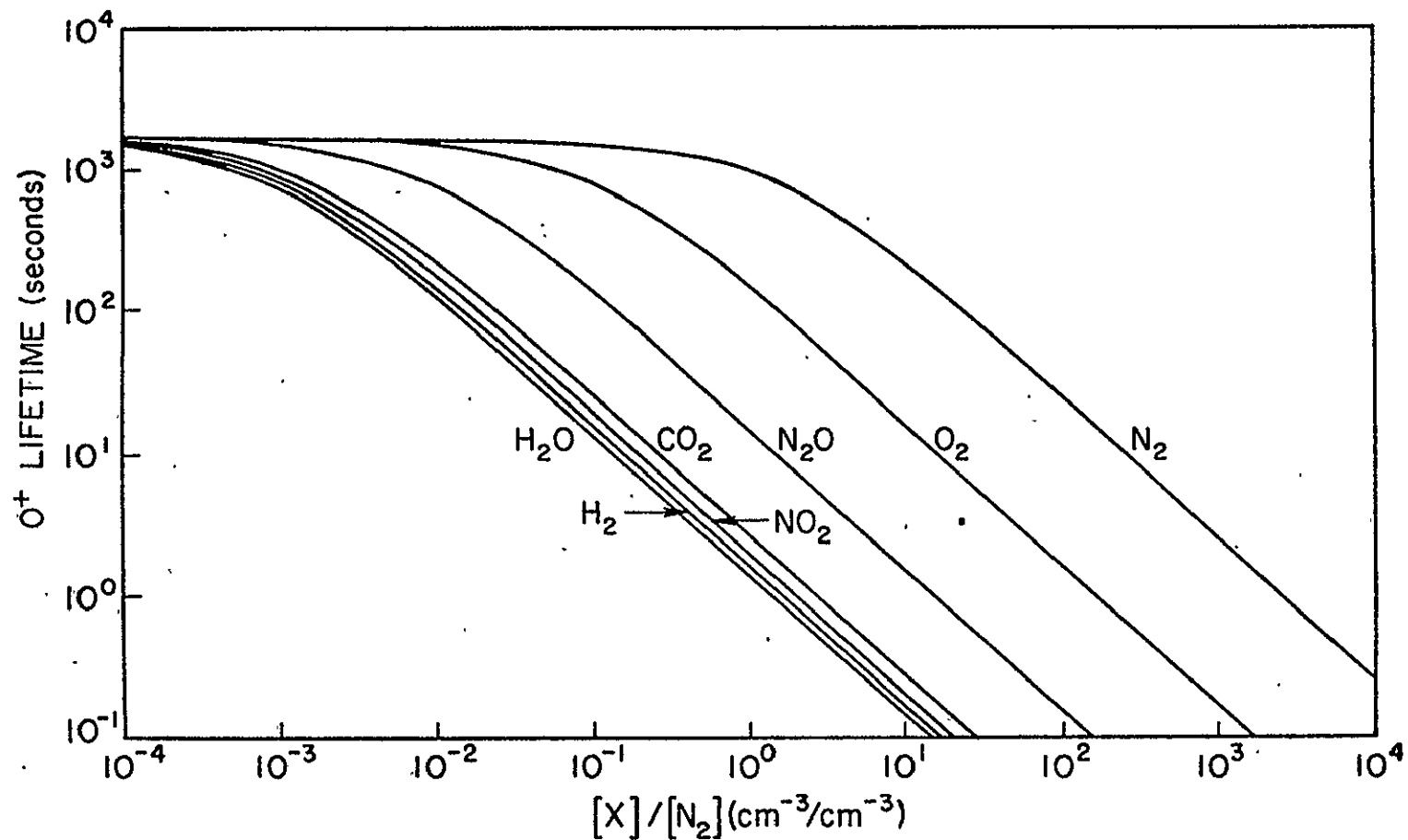
Fig. 1. Change in O^+ lifetime with the introduction of chemically reactive gases into the ionosphere. Ambient N_2 concentration is 3×10^8 cm^{-3}. O_2 concentration is 10^7 cm^{-3}. Undisturbed O^+ concentration is 2×10^5 cm^{-3}.

Because H_2 is three orders of magnitude more reactive than N_2, the release of a small amount of diatomic hydrogen will rapidly reduce the local O^+ population.

Significant decrease in average lifetime of an O^+ ion occurs when

$$\frac{[X]}{[N_2]} > \frac{K_{N_2}}{K_X}$$

where   [X] = concentration of released gas,

$[N_2]$ = concentration of N_2,

K_{N_2} = (O^+, N_2) reaction rate, and

K_X = $(O^+,$ released gas) reaction rate.

For the example of the release of H_2, the inequality becomes

$$\frac{[H_2]}{[N_2]} > \frac{1}{1540}$$

The curves in Figure 1 show the reduction in O^+ lifetime for different values of the ratio of released gas to nitrogen conentrations. It appears that substantial reduction in the ionospheric O^+ concentrations can be caused by the release of modest amounts of certain gases.

In the unperturbed F2-layer, the electron loss coefficient is essentially the O^+ recombination coefficient. This is because the ion-molecule charge exchange reactions with N_2 and O_2 (8) are

slow compared with the dissociative recombination of the resulting molecular ions NO^+ and O_2^+ (9).

This is not necessarily true in the perturbed ionosphere. The reaction rates between O^+ and certain gases are comparable to polyatomic ion dissociative recombination reaction rates. As an example, consider the dissociative recombination of the OH^+ produced by (10).

$$OH^+ + e^- \rightarrow O + H \qquad \alpha(OH^+) \quad 1 \times 10^7 \text{ cm}^3 \text{ sec}^{-1} \qquad (11)$$
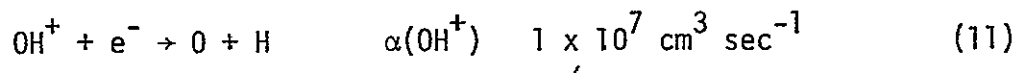
If H_2 is released into the ionosphere, rapid depletion of O^+ occurs and large quantities of OH^+ are produced. This OH^+ then reacts with the electron gas to produce neutral atoms. There is a significant time delay between the O^+ depletion and the electron depletion when gases with high charge exchange reaction rates are injected into the F2 region ionosphere.

Examination of Table 1 indicates that the perturbed ionosphere chemical processes are complicated by ion molecule reactions with the foreign polyatomic ions. Again consider OH^+, the product of the O^+-H_2 charge exchange reaction. OH^+ may react with the injected gas, H_2,

$$OH^+ + H_2 \rightarrow H_3O^+ + H + 1.82 \text{ eV} \qquad \gamma(OH^+,H_2) = 1.4 \times 10^{-7} \text{ cm}^3 \text{ sec}^{-1}$$

$$(12)$$
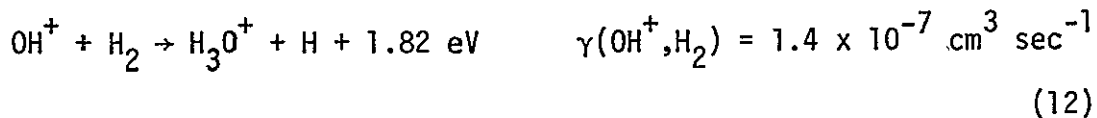
or react with the atmospheric O_2

$$OH^+ + O_2 \rightarrow O_2^+ + OH + 1.2 \text{ eV} \qquad \gamma(OH^+, O_2) = 2 \times 10^{-10} \text{ cm}^3 \text{ sec}^{-1}$$

$$(13)$$
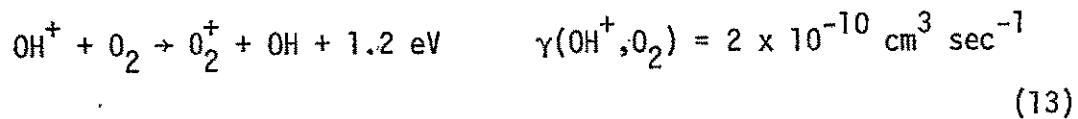
The polyatomic ions produced in these reactions have dissociative recombination reaction rates which are comparable to the recombination rates of their parent ion, OH^+. The production of secondary polyatomic ions can be neglected in the modeling of chemical ionospheric perturbation because of the rapid dissociation of these ions.

During the daytime, photodissociation of the injected gases must be considered. If the gas is photodissociated into non-reactive components it is not useful as an ionospheric modifier. Consider NO_2 which has the highest photodissociation coefficient in Table 1. . A comparison of its charge exchange time constant, $\tau_{CE} = 1/([O^+]$ $1.2 \times 10^{-9})$, with its solar photodissociation time constant, $\tau_{PD} = 1/(8.1 \times 10^{-3})$, shows that it is not an effective gas if $\tau_{PD} < \tau_{CE}$ or if $[O^+] < 6.8 \times 10^6 \text{ cm}^{-3}$. This inequality usually is true throughout the F-region ionosphere. NO_2 must be discounted as an efficient daytime perturbation gas.

Gases, such as H_2, with negligible solar photodissociation properties are useful as daytime injectants.

An important consideration concerning chemical modification is the depletion efficiency per unit mass of the released gases. Diatomic injectants, such as H_2, remove only one O^+-electron pair. Triatomic injectants may remove two O^+-electron pairs per released molecule. Water vapor is an example of this type of gas.

H_2O is dissociated into monoatomic hydrogen and the hydroxyl radical upon reaction with the O^+-electron pair.

$$H_2O + O^+ + e^- \rightarrow H_2O^+ + e^- + O \rightarrow OH + H + O \qquad (14)$$
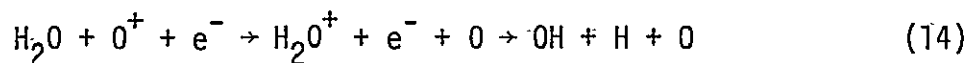
A second O^+-electron pair is removed by reaction with OH.

$$OH + O^+ + e^- \rightarrow \left\{ \begin{array}{c} O_2^+ + H \\ \text{or} \\ OH^+ + O \end{array} \right\} + e^- \rightarrow O + O + H \qquad (15)$$
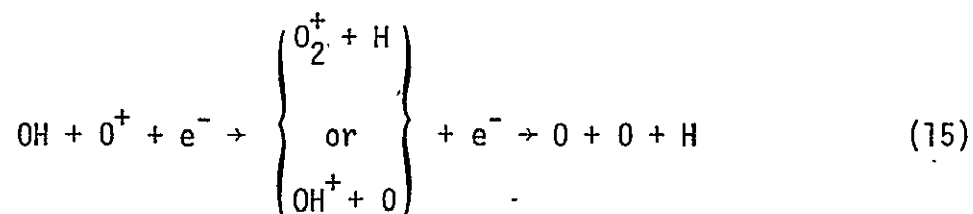
The rate of this reaction has not been measured.

Nitrogen dioxide is an inefficient tri-atomic modified because it chemically removes only one O^+-electron pair. Charge exchange and dissociative recombination reactions involving O^+, electrons, and NO_2 proceed rapidly.

$$NO_2 + O^+ \rightarrow NO_2^+ + O \qquad \gamma(NO_2) = 1.6 \times 10^{-9} \; cm^3 \; sec^{-1}$$

$$NO_2^+ + e^- \rightarrow NO + O \qquad \alpha(NO_2^+) = 4 \times 10^{-7} \; cm^3 \; sec^{-1}$$
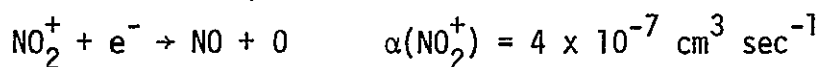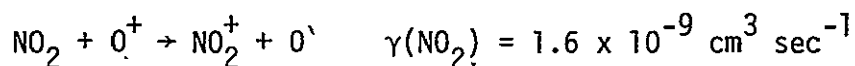
However, charge exchange with the produced nitric oxide is negligible.

$$NO + O^+ \rightarrow \left\{ \begin{array}{c} NO^+ + O \\ \\ N + O_2^+ \end{array} \right. \qquad \gamma(NO) < 10^{-12} \; cm^3 \; sec^{-1}$$
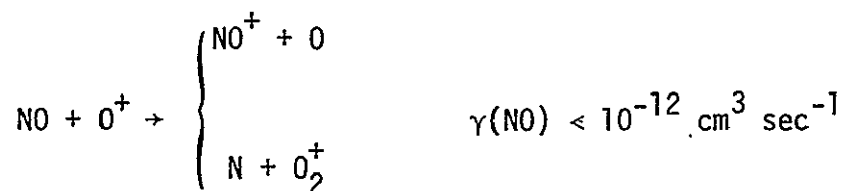
The ratio of the gas molecular weight to the number of O^+ electron pairs annihilated by several gases is shown in the following table.

Injected Substance	N_2	O_2	N_2O	CO_2	NO_2	H_2	H_2O
Mol. Wt./$(O^+ - e^-)$ pair	28	32	44	44	46	2	9

The highest depletion efficiency per unit mass is obtained by the use of diatomic hydrogen and water vapor.

C. Summary

The feasibility of artificial modification of the ionosphere has been examined with respect to the F-region chemical mechanisms. Depletion of the ion population may result from increased chemical loss processes. The release of reactive gases is an efficient method of increasing the ion-electron recombination in the ionosphere. When the ion-molecule reaction rates, photodissociation rates and mass depletion efficiency are considered for various gases, H_2 and H_2O are found to be the most useful gases for temporary depletion of the ionosphere.

21

Chapter III

THE SUDDEN RELEASE OF A GAS INTO A TENUOUS ATMOSPHERE

Chemical modification of the ionosphere can be promoted by the release of a dense cloud into the ambient atmosphere. The cloud expands rapidly, driven by its thermal energy which is converted into kinetic energy, causing a rapid drop in temperature and, possibly, gas condensation. When the gas cloud expands to an extremely rarified state, condensation ceases because of the lack of collisions between the free molecules and the condensation centers. At this stage, any particles that have condensed will begin to re-evaporate.

After being cooled by expansion, the gas is re-heated by collisions with the ambient atmosphere. During thermalization with the atmosphere, the gas cloud temperature approaches the atmospheric temperature and expansion is dominated by collisional, diffusive processes.

This chapter is a discussion of the rapid expansion of the released cloud between the time of release and the time of diffusively controlled expansion. Chapter IV is an analysis of the later epoch of isothermal, diffusive expansion.

Gas releases from vehicles passing through the ionosphere can be classified into two types. The first type is the spherical flow produced by an instantaneous release of gas at a given location. Examples of this type of source model are releases involving spherical detonations of an explosive gas mixture or pulsed gas jet releases. The second type of release is the continuous release of gas over a period of time, such as is produced by a rocket exhaust plume. The

The analysis of both types of releases is similar. Only the spherical release will be considered in detail.

The notation is consistant throughout this chapter. Number density, velocity, and temperature at time t_i are denoted as n_i, $\vec{u}_i$, and T_i respectively. The subscript i is constant for all variables at a fixed time.

A. Spherical Expansions

The problem of spherical gas expansion has been studied for a number of years. Point source shape preserving (similarity) solutions for expansion into a vacuum have been derived by Mirels and Mullen [1963], Greifinger and Cole [1965], and Hubbard [1967]. These solutions are based on the assumption of continuum, inviscid flow. If the mean free path inside the gas cloud is larger than the cloud diameter (i.e. Knudson number greater than 1), collisionless solutions apply. Gas cloud expansions into a vacuum are considered from the free molecular point of view by Mirels and Mullen [1963], and Narasimha [1962]. For models of spherical expansions involving a wide range of Knudson numbers, representing continuum to collisionless regimes, kinetic theory is employed. Solutions of the Boltzmann equation for expansions into a vacuum are produced by Edwards and Cheng [1966, 1967], Freeman [1967], Narasimha [1967], Grundy and Thomas [1969], Grundy [1969], Thomas [1971], Freeman and Thomas [1969], and Cooper and Bienkowski [1965]. A unification of the continuum and kinetic theory is presented by Grundy [1969].

24

Previous papers dealing with spherical expansions into an ambient atmosphere are similarly classified according to the method of solution. Continuum, inviscid analysis concerning expansions into a dense atmosphere are considered by Taylor [1946], Ness and Ambrosiani [1968], Cheng and Kirsch [1969], Hoffman and Bert [1974], and Baxter and Linson [1976]. Collisionless expansions are discussed by Bienkowski [1964]. Kinetic theory solutions for expansions into a rarified atmosphere are derived by Brode and Enstrom [1972], Brook and Hamel [1972], and Baum [1973, 1974]. A discussion of the expansion solutions appropriate for the gas release into ionospheric regions constitutes a large portion of this chapter.

The expansion and simultaneous cooling of a gas cloud is easily explained from a molecular point of view. Consider a collection of molecules confined in a spherical container with radius r_o. If these molecules are in translational equilibrium, they will have a Maxwellian velocity distribution. Assuming the gas temperature is T_o, the gas particle distribution in space and time is

$$f(\vec{x},\vec{v}) = n_o\left(\frac{m}{2\,kT_o}\right)^{3/2} \exp\left[\frac{-(\vec{v})^2 m}{2kT_o}\right] \qquad |\vec{x}| \leq r_o \qquad (1)$$

where $\vec{x}$ is the position vector, $\vec{v}$ the velocity vector, m the released gas molecular mass, n_o the number density inside the sphere, and k Boltzmann's constant. A velocity-position plot of this distribution is shown in Figure 1.
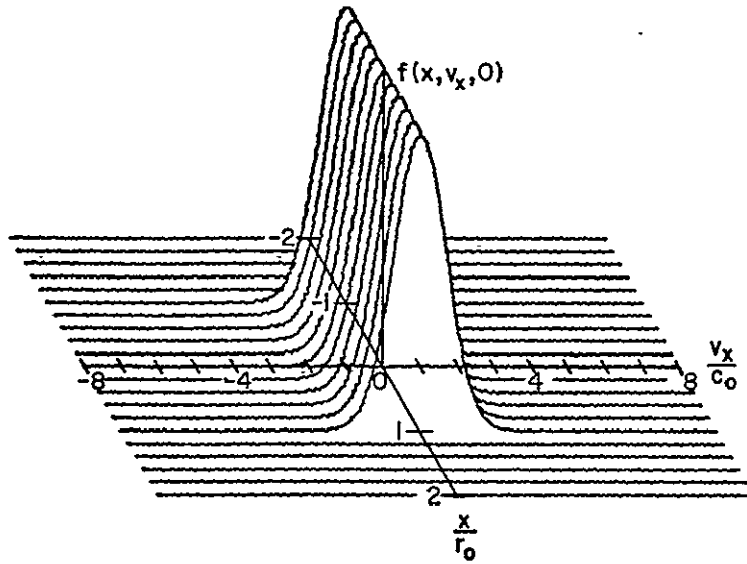
Fig. 1. Distribution function for a spherical
gas cloud. $c_0 = \sqrt{2kT_0/m}$

Macroscopic properties of the gas are found by calculating velocity

moments of the distribution. The density of the gas is related to the

"0th" moment of the distribution as follows:

$$n(x) = \int\int\int_{\infty}^{\infty} f(\vec{x},\vec{v})d^3 \vec{v} \qquad (2)$$

where $n(x)$ is the number density of the gas at position x. The

mean velocity and the temperature are calculated by the first and

second moments of the particle distribution.

$$\vec{u}(\vec{x}) = \frac{\int\!\!\int\!\!\int_{\infty}^{\infty} f(x,v)\,\vec{v}d^3\vec{v}}{n(x)} \qquad (3)$$

$$\frac{3kT_o}{m} = \frac{\int\!\!\int\!\!\int_{-\infty}^{\infty} f(\vec{x},\vec{v})v^2d^3v}{n(\vec{x})} - u^2(\vec{x}) \qquad (4)$$

Examination of Fig. 1 shows that 1) $n(\vec{x})$ is constant for $|\vec{x}| \leq r_o$ and equal to zero for $|\vec{x}| > r_o$, 2) $u(\vec{x}) = 0$ everywhere, and 3) T_o is constant inside the gas sphere.

If the walls of the spherical container are removed, the gas will expand. The change in the distribution function can be quickly calculated if one assumes no collisions. In collisionless expansions, the flow of the gas is determined by the inertia of each molecule. Those molecules with a positive velocity propagate in the positive direction at a constant speed. Similarly, the molecules with a negative velocity move in the negative direction and those with zero velocity remain stationary. Figure 2 shows the collisionless distribution function at a finite time, t, after the start of the expansion. The distribution remains constant along particle paths.
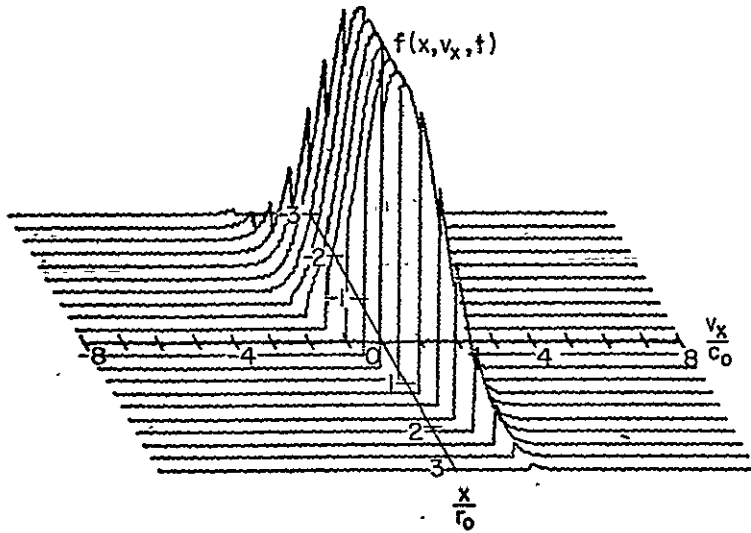
Fig. 2. Distribution function for a
spherical gas cloud undergoing
collisionless expansion.

Examination of the moments of the distribution in Figure 2 shows

a change in the radial structure of the density, velocity, and temper-

ature. At a fixed position, x_1, the range of velocities, Δv_x,

attained by the molecules is finite. The temperature is a measure of .

the "width" of the velocity distribution at each position. Since the

velocity distribution in Figure 2 is "narrower" than the one in

Figure 1, decrease in temperature is produced by the expansion.

After a long time, the distribution becomes a narrow strip (Fig. 3).
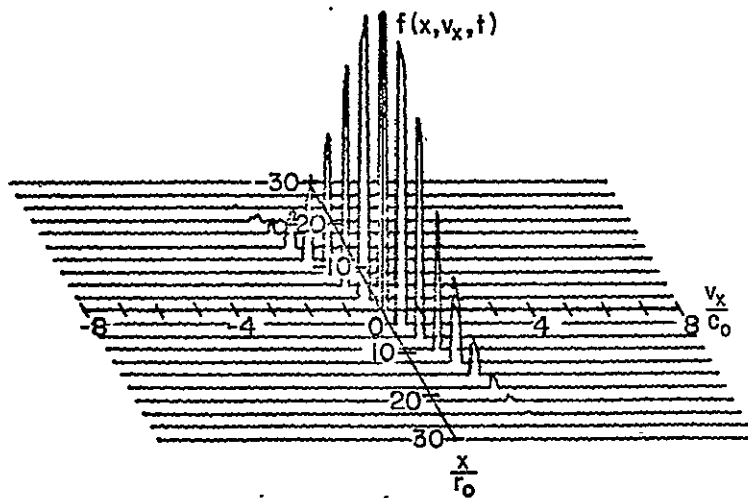
Fig. 3. Limiting form of the collision-
less velocity distribution.

Because the width of the velocity range, Δv_x, approaches zero, the density and the temperature are vanishing quantities. The velocity at each point in space asymptotically approaches $\vec{u} = \vec{x}/t$ where t is the time since beginning of the expansion.

The inclusion of collisions in the expansion model increases the width of the velocity distribution at a point in space. Thus, the temperature in collisional expansion remains higher than the temperature in collisionless expansions. These qualitative arguments about the flow of gas during a spherical expansion can be expressed in quantitative terms by the solution of the Boltzmann equation.

B. The Boltzmann Equation

The evolution of the particle distribution is found by solving the Boltzmann equation.

$$\frac{\partial f}{\partial t} + \vec{v} \cdot \nabla f = \left(\frac{\partial f}{\partial t}\right)_{coll} \qquad (5)$$

where f is the distribution function, $\vec{v}$, $\vec{x}$, and t the velocity space and time coordinates respectively, and $(\partial f/\partial t)_{coll}$ represents the change in the distribution function due to collisions. The collisionless solution to this equation is found by setting the collision term to zero. The Boltzmann equation for free molecular flow is

$$\frac{\partial f_m}{\partial t} + \vec{v} \cdot \nabla f_m = 0$$

29

The solution is a simple function of the initial distribution.

$$f_m(\vec{x},\vec{v},t) = f_m(\vec{x} - \vec{v}t,\vec{v},o) \qquad (6)$$

The subscript "m" refers to the free molecular solution. This result is a mathematical representation of the invariance of the distribution along particle paths as mentioned in the previous section.

Using the initial Maxwellian distribution in (1) and the collisionless solution to the Boltzmann equation in (6), the moment equations (2), (3), and (4) are evaluated. The mathematical details are given in Bienkowski (1964). The resulting solutions for density, velocity, and temperature are expressed as

$$\frac{n}{n_0} = \frac{1}{2}\left(\text{erf}\left(\frac{r+1}{\tau}\right) + \text{erf}\left(\frac{r-1}{\tau}\right) + \frac{\tau}{r\sqrt{\pi}}\left\{\exp\left[-\left(\frac{r+1}{\tau}\right)^2\right] - \left[\exp - \left(\frac{r-1}{\tau}\right)^2\right]\right\}\right) \qquad (7)$$

$$\frac{\bar{u}(r,t)}{c_0} = \frac{\dfrac{1}{2\pi^{1/2}}\left\{\exp\left[-\left(\frac{r+1}{\tau}\right)^2\right]\left(\frac{1}{r} + \frac{\tau^2}{2r^2}\right) + \exp\left[-\left(\frac{r-1}{\tau}\right)^2\right]\left(\frac{1}{r} - \frac{\tau^2}{2r^2}\right)\right\}}{n/n_0} \qquad (8)$$

$$\frac{T}{T_0} = \frac{\dfrac{n}{n_0} + \dfrac{1}{3\pi^{1/2}}\left\{\exp\left[-\left(\frac{r+1}{\tau}\right)^2\right]\left(1 + \frac{\tau^2+2}{2r}\right) + \exp\left[-\left(\frac{r-1}{\tau}\right)^2\left(1 - \frac{\tau^2+2}{2r}\right)\right]\right\}}{n/n_0}$$

$$- \frac{2}{3}\left(\frac{u}{c_0}\right)^2 \qquad (9)$$

where n_0 is the initial gas number density, c_0 the initial mean thermal speed $= \sqrt{2kT_0/m}$, T_0 the initial temperature. The radial and temporal parameters have been nondimensionalized as follows

$$r = \frac{|\vec{x}|}{r_0} \, , \quad \tau = \frac{tc_0}{r_0}$$

At the center of the spherical expansion, $r = 0$, these equations reduce to

$$n/n_0 = \text{erf}\, \frac{1}{\tau} \, - \, \frac{2}{\tau\pi^{1/2}} \, \exp\left[- \frac{1}{\tau^2} \right] \tag{10}$$

$$\bar{u}(o,\tau) = 0 \tag{11}$$

$$\frac{T(o,\tau)}{T_0} = \frac{n/n_0 - 4/(3\pi^{1/2}\tau^3)\, \exp\,(-1/\tau^2)}{n/n_0} \tag{12}$$

The inclusion of the collision term in the Boltzmann equation is necessary for realistic modeling of gas expansions. Bhatnagar, Gross, and Krook (1954) have proposed the following approximation to the collision term

$$\left(\frac{\partial f}{\partial t}\right)_c = \omega(nf_0 - f) \tag{13}$$

where n is the gas number density, ω is the gas collision frequency and f_0 is the Maxwellian distribution expressed in terms of the local mean velocity and the local temperature. The BGK model

31

represents the relaxation of a non-Maxwellian distribution to the Maxwellian distribution f_0. The gas relaxation time is $1/\omega$. Note that the three variables in the BGK model (ω, n, and f_0) are functions of n, $\bar{u}$, and T, which are functions of f, the required distribution function.

The Krook equation is the Boltzmann equation with the BGK collision model.

$$\frac{\partial t}{\partial t} + v \cdot \nabla f = \omega(nf_0 - f) \tag{14}$$

An expansion of f in terms of f_0 is valid for small departures from equilibrium. Using this method of expansion, the Chapman-Enskog solution of the Krook equation gives the Navier-Stokes equations of macroscopic gas dynamics [Vincenti and Kruger, 1965]. In the case of inviscid, continuum flow, the Navier-Stokes equations reduce to the equations of motion for unsteady flows.

Equation of Continuity

$$\frac{\partial n}{\partial t} + \nabla \cdot (n\vec{v}) = 0 \tag{15}$$

Equation of Motion

$$m\frac{Dv}{Dt} = -\frac{1}{n} \nabla p \tag{16}$$

First Law of Thermodynamics (Conservation of Energy)

$$m\frac{D}{Dt} \left(h + \frac{1}{2} \vec{v}^2\right) = \frac{1}{n} \frac{\partial p}{\partial t} \tag{17}$$

where $\frac{D}{Dt} = \frac{\partial}{\partial t} + v_x \frac{\partial}{\partial v_x} + v_y \frac{\partial}{\partial v_y} + v_z \frac{\partial}{\partial v_z}$, p is the gas pressure, h the enthalpy per unit mass and $\bar{v}^2$ the mean square velocity.

Under the assumptions of a perfect gas that is expanding isentropically (i.e., with no heat input into the gas) the pressure can be related to the density by solution of the first law of thermodynamics [Morse, 1967].

$$p = \text{const} \cdot n^\gamma \tag{18}$$

where γ is the ratio of the specific heats.

Making this substitution into the equations of motion yields the following equations, in spherical coordinate form

$$\frac{\partial n}{\partial t} + \frac{\partial nv}{\partial r} + 2\frac{nv}{r} = 0 \tag{19}$$

$$\frac{\partial v}{\partial t} + v\frac{\partial v}{\partial r} = \gamma \, \text{const} \, p^{(\gamma-2)} \frac{\partial p}{\partial r} \tag{20}$$

where v is the radial expansion velocity and r is the radial coordinate.

As pointed out by Stanynkovich [1960], the density gradient on the right side of (20) becomes negligible after long times. With this assumption, (20) is solved to give $v = r/t$ which was also the asymptotic velocity for free molecular flows. The substitution of the velocity expression into the continuity equation (19) leads to solutions of the form

$$nt^3 = A(r/t) \tag{21}$$

These long time solutions are called "self-similar" because v and nt^3 are functions only of r/t.

Using the perfect gas law, $p = nkT$, the time variations in temperature and density at $r = 0$ are calculated using (18) and (21)

$$\frac{T}{T_0} = \left(\frac{n}{n_0}\right)^{\gamma-1} \tag{22}$$

$$\frac{n}{n_0} = \left(\frac{t_0}{t}\right)^3 \tag{23}$$

where t_0 is the equivalent starting time of the self-similar expansion. Zeldovich and Raizer [1967] state that the characteristic time scale, t_0, is calculated from the long time velocity solution $t_0 = r_0/c_0$. If the time reference is shifted so that the gas expansion starts at $t = 0$, the temporal variation in temperature and density for the center of the continuum expansion are approximately given by

$$\frac{n}{n_0} = \left(\frac{r_0}{r_0 + tc_0}\right)^3 = \left(\frac{1}{1+\tau}\right)^3 \tag{24}$$

$$\frac{T}{T_0} = \left(\frac{r_0}{r_0 + tc_0}\right)^{3(\gamma-1)} = \left(\frac{1}{1+\tau}\right)^{3(\gamma-1)} \tag{25}$$
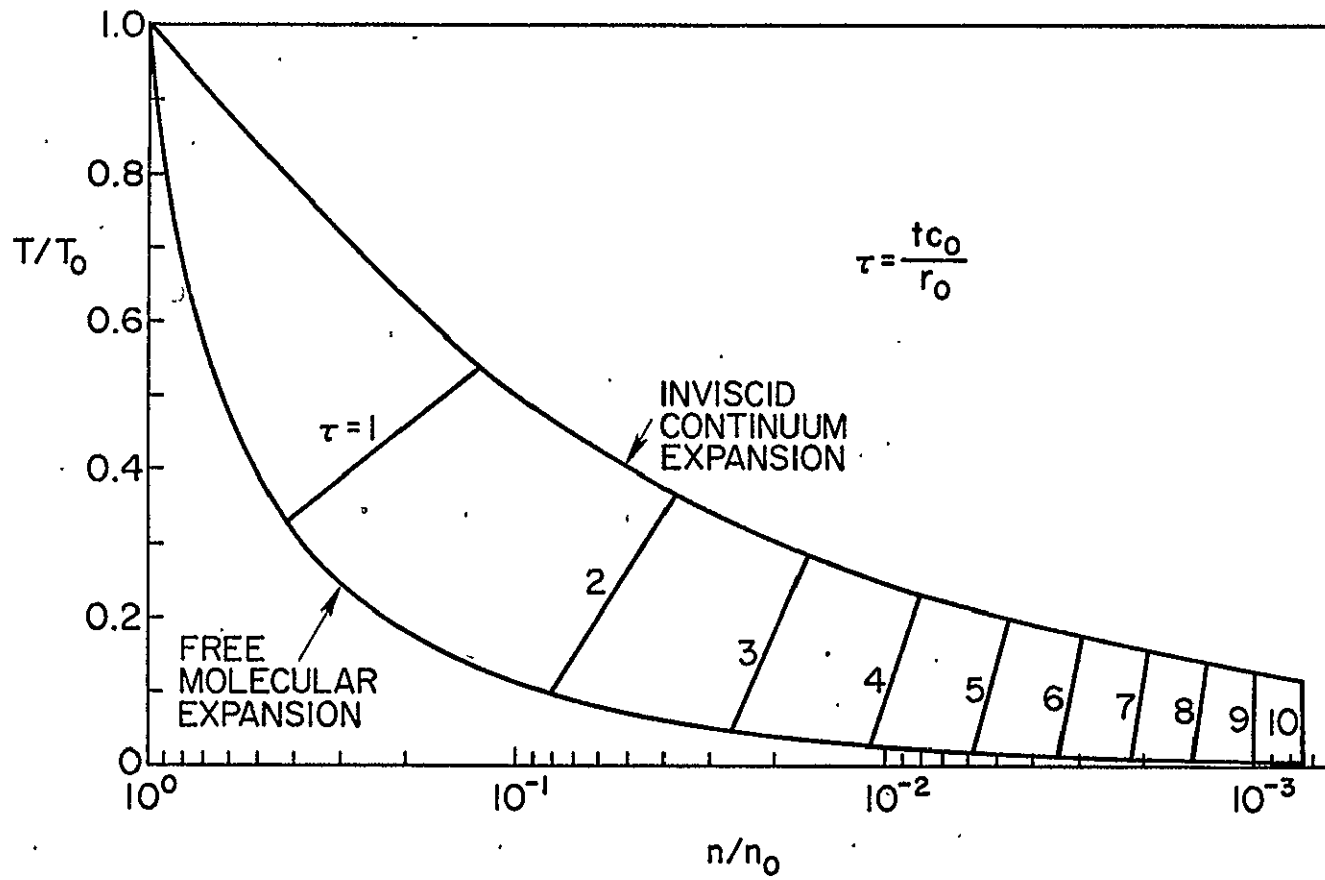
Fig. 4. Density and temperature variations in a spherical gas expansion.

where the nondimensionalized time unity, τ, has been used.

A comparison of the time variation of the density and of the temperature for free molecular flow (10) and (12), and for inviscid continuum flow, (24) and (25), is illustrated in Figure 4. The actual T - n path of the expanding gas cloud lies somewhere between these curves. Initially, the large central density of the gas is - in translational equilibrium due to collisions so that the T - n variation is close to the inviscid, continuum solution. As the central gas density decreases, collisions become rare and the free molecular solution is approached.

The analytic expressions derived in this section are representative of the temperature and density variations during the gas expansion. Because the gas density drops with increased radial distance from the center of the expanding cloud, the outer portions of the cloud may be in a state of free molecular flow while the inner core gas density obeys the ordinary laws of continuum gas dynamics. The outer, free molecular shell of the cloud is only subject to forces produced by collisions with the ambient atmosphere into which the gas is expanding.

When molecules in the dense inner core of the cloud collide with one another, they may adhere to each other. If the temperature of the cloud is low, these clusters are thermodynamically stable and the expanding cloud condenses into a fog. A discussion of condensation of expanding vapor clouds is found in the next section.

C. Condensation of Expanding Vapor Clouds

This section presents a discussion of the condensation resulting
from the rapid cooling of an expanding gas. Each step in the
condensation and subsequent re-evaporation process is described. An
analytic example appropriate for a spherical water vapor release with
an initial temperature of 2000 K and an initial density of $5 \times 10^{25}/m^3$
is presented. (The physical data for H_2O as well as for H_2 are
given in Appendix B).

As a gas cloud expands, the internal pressure and temperature
drop. At some point in the expansion, at time t_1, the gas pressure
curve may intersect the saturated vapor pressure curve for the solid-
liquid or liquid-vapor condensation system. The saturated vapor
pressure is defined as the vapor pressure of a condensation system in
equilibrium. The pressure of saturated vapor is governed by the
Clausius-Clapeyron equation

$$\frac{\partial p_v}{\partial T} = \frac{U}{T(v_g - v_\ell)} \quad \text{[Morse, 1969]} \tag{26}$$

where P_v is the saturated vapor pressure, T the gas temperature,
U the latent heat of vaporization, v_g the gas volume and v_ℓ
the liquid or solid volume. (All volumes are the reciprocal of the
local densities). Assuming 1) that the perfect gas law, $p_v v = RT$,
holds, 2) that the condensate density is much greater than the vapor
density, and 3) that the U is constant, (26) leads to the following
relation between saturated vapor volume, v_g, and temperature, T,

37

$$v_g = BTe^{U/RT} \qquad (27)$$

where B is a constant. The saturated vapor temperature-volume
(T-v) curve for H_2O based on measured data [Handbook of Chemistry
and Physics, 1959] closely matches the form of Eq. (27). The T-v
curves representing both solid-vapor and liquid-vapor systems for
H_2O are shown in Figure 5.

When the gas cloud expands beyond the state of saturation, it
becomes super-saturated and condensation rapidly forms around any
centers of inhomogeneity such as ions or dust particles. This is
called heterogeneous nucleation. If there are no impurities in the
expanding system to act as condensation centers, the gas expands in
a super-saturated state until self-nucleation begins. This process,
called homogeneous nucleation, involves embryos composed of clusters
of gas molecules. An excellent introductory discussion of homogeneous
nucleation is presented by McDonald [1962, 1963], reprinted in the
text by Abraham [1974]. For a comprehensive treatment of both hetero-
geneous and homogeneous nucleation see Zettlemoyer [1969].

Fundamental to the understanding of homogeneous nucleation is the
concept of critical cluster size. The saturated vapor pressure of a
nucleated cluster is dependent on the radius of the cluster. Clusters
will small radii of curvature have higher surface vapor pressure than
those with large radii of curvature. Consequently, a small cluster
in a solid-vapor system may evaporate while a large cluster in the
same environment may grow. The critical cluster size with respect
to a given situation is the transition size between evaporating and
growing clusters. The critical cluster radius is given by
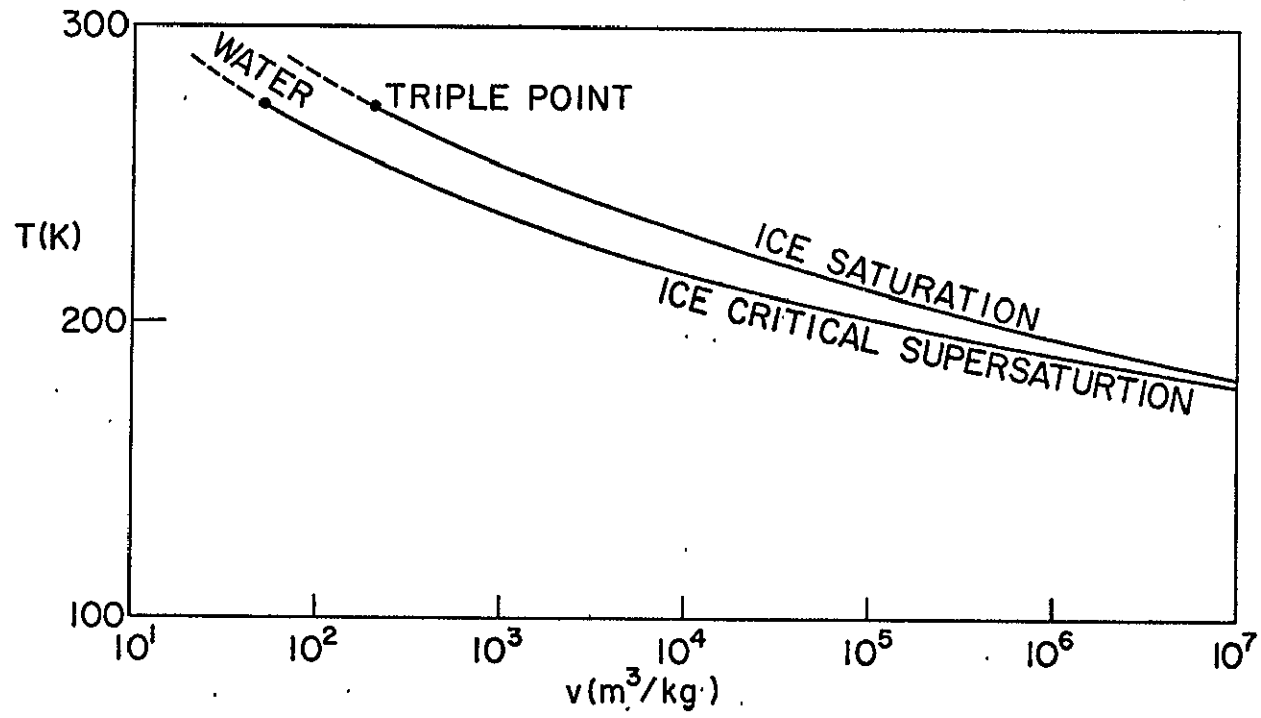
Fig. 5. Saturated vapor and critical supersaturation curves for H_2O.
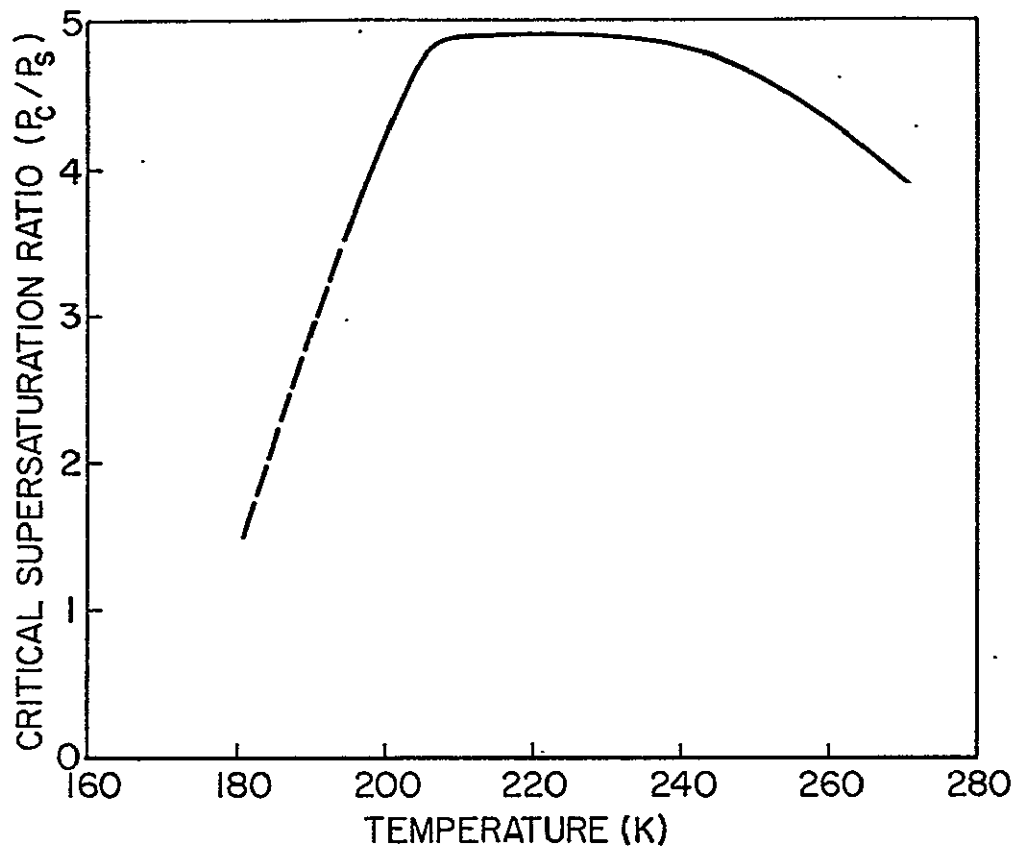
Fig. 6. Emperical critical supersaturation ratio curve.
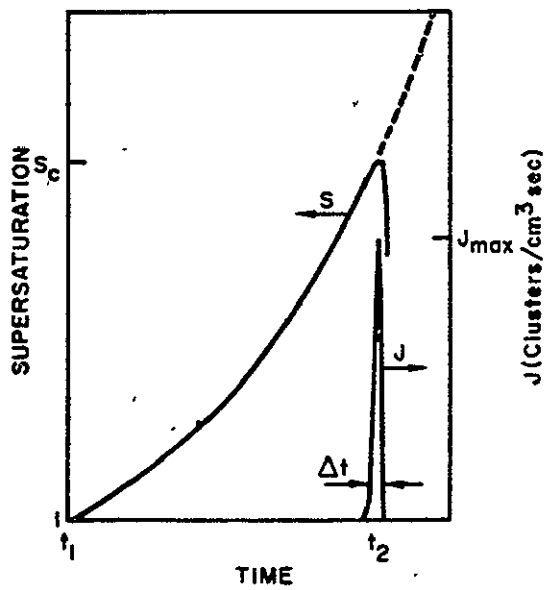
Fig. 7. The supersatu-
ration ratio and nucle-
ation rate as a function
of time.

$$r^* = \frac{2\sigma v_B}{kT \log_e(p/p_\infty)} \qquad (28)$$

where σ is the surface tension, v_B the volume per molecule in the cluster, T and p the vapor temperature and pressure, respectively, and p_∞ the flat surface vapor pressure.

Significant homogeneous nucleation occurs at critical super-saturation. The thermodynamic state (i.e., pressure, temperature, density) at the point of critical super-saturation is found by calculating the point at which the homogeneous nucleation rate becomes one embryo per cm^3 per second. The homogeneous nucleation rate of droplets from a super-saturated system was derived by Frenkel [1946]

$$J = \left(\frac{p}{kT}\right)^2 v\sqrt{\frac{2\sigma}{\pi m}} e^{-\frac{4\pi\sigma(r^*)^2}{3kT}} \qquad (29)$$

where σ is the surface tension, v the molecular volume in the liquid, N Avogadro's number, p the supersaturation pressure, and r^* the critical nucleus radius. The degree of super-saturation is defined as $S = p/p_0$. The point of critical super-saturation is insensitive to the definition of "significant" nucleation because of the exponential nature of (29) (i.e., setting $J = 1$ cm^{-3} sec^{-1} or 10^4 cm^{-3} sec^{-1} leads to approximately the same result for degree of critical super-saturation, $S_c = p_c/p_0$). In the case of water vapor, comparison of the theoretical variation of S_c with T with cloud chamber measurements shows good agreement only at temperatures above 260 K [Madonna et al., 1961]. Consequently, measured values for the

critical super-saturation pressure ratio for H_2O (Figure 6) are used in numerical examples. Knowing both the saturated vapor pressure and the critical super-saturation ratio as function of temperature, the critical T-v curve for H_2O is derived (Figure 5).

After critical super-saturation is achieved, condensation centers are formed and the gas rapidly nucleates until a state of equilibrium saturation is reached. The transition time from critical super-saturation to equilibrium saturation is on the order of a microsecond. The total number of condensation centers formed in this transition remains fixed as the gas continues to expand. This is schematically illustrated in Figure 7 adapted from Feder et al. [1966]. Simultaneously, plotted versus time, are saturation level, S, and the homogeneous nucleation rate J. As the degree of super-saturation increases with time, the nucleation rate remains low until critical supersaturation is reached. At this time, $t = t_2$, a spike in the nucleation rate is produced. This spike is quenched by the sudden lowering of the saturation level.

The number of condensation centers per unit volume is found by integration of the nucleation rate over time.

$$N = \int_0^{t_2} J(t)dt \simeq J_{max}\Delta t, \qquad (30)$$

where J_{max} is the maximum nucleation rate and Δt, the effective duration of the nucleation maximum. The cluster density for water vapor after critical super-saturation is reached, can vary between 10^{12} to 10^{18} clusters/cm^3 [Feder et al. 1966], depending on the

expansion rate, initial temperature and other thermodynamic factors. For the water vapor example of this section $N = 6.3 \times 10^{13}$.

Defining a growth factor, $g(t,t')$ as the number of molecules at time t in a cluster born from a nucleus which appears at time t', an expression for the amount of material condensed is written

$$x(t) = \int_0^t J(t')g(t,t')dt'/n \qquad (31)$$

where n is the fluid density and the degree of condensation, $x(t)$ is the ratio of the molecules in the condensed state to the total number of released molecules. The relation between the vapor density and the fluid density is $n_v = (1-x)n$. Because the nucleation embryos are almost instantaneously formed at the time of critical super-saturation, the nucleation rate is taken to be

$$J(t) = J_{max}\Delta t . \delta(t-t_2) = N\delta(t-t_2) \qquad (32)$$

where t_2 is the time of critical super-saturation, $\delta(\cdot)$ the impulse symbol and Δt the equivalent width of the nucleation spike. Equation (31) becomes

$$x(t) = N/n \; g(t,t_2) = \nu \; g(t,t_2) \qquad (33)$$

Assuming that the embryos expand with the free gas molecules, the ratio of cluster density to fluid density remains unchanged.

$$N/n = \nu = constant$$

43

Once the gas is in equilibrium saturation, it obeys the following adiabatic equation

$$[c_1(1-x) + c_2 x] \, dt + Rt(1-x) \, dv/v - [U - (c_2-c_1)T] \, dx = 0 \qquad (34)$$

where c_1 is the specific heat of the vapor at constant volume, c_2 the specific heat of the condensate, R the gas constant, U the heat of vaporization and v the specific volume of the vapor-solid fluid. The gas volume is related to the fluid volume by $v = v_g(1-x)$. Using this expression, the Claussius-Claperon relation (27) takes the form

$$v/(1-x) = BTe^{U/RT} \qquad (35)$$

Equations (34) and (35) are solved subject to the boundary conditions

$$v = v_1, \; T = T_1 \quad \text{when} \quad x = 0.$$

When the state of the gas returns to saturation after passing through critical super-saturation, it is assumed that the T-v curve returns to the saturation isentrope crossed before going to the super-saturated state. Thus, the boundary conditions, V and T are the volume and temperature when the gas becomes saturated but did not condense at time t_1.

The degree of condensation is most easily written as a function of fluid temperature.
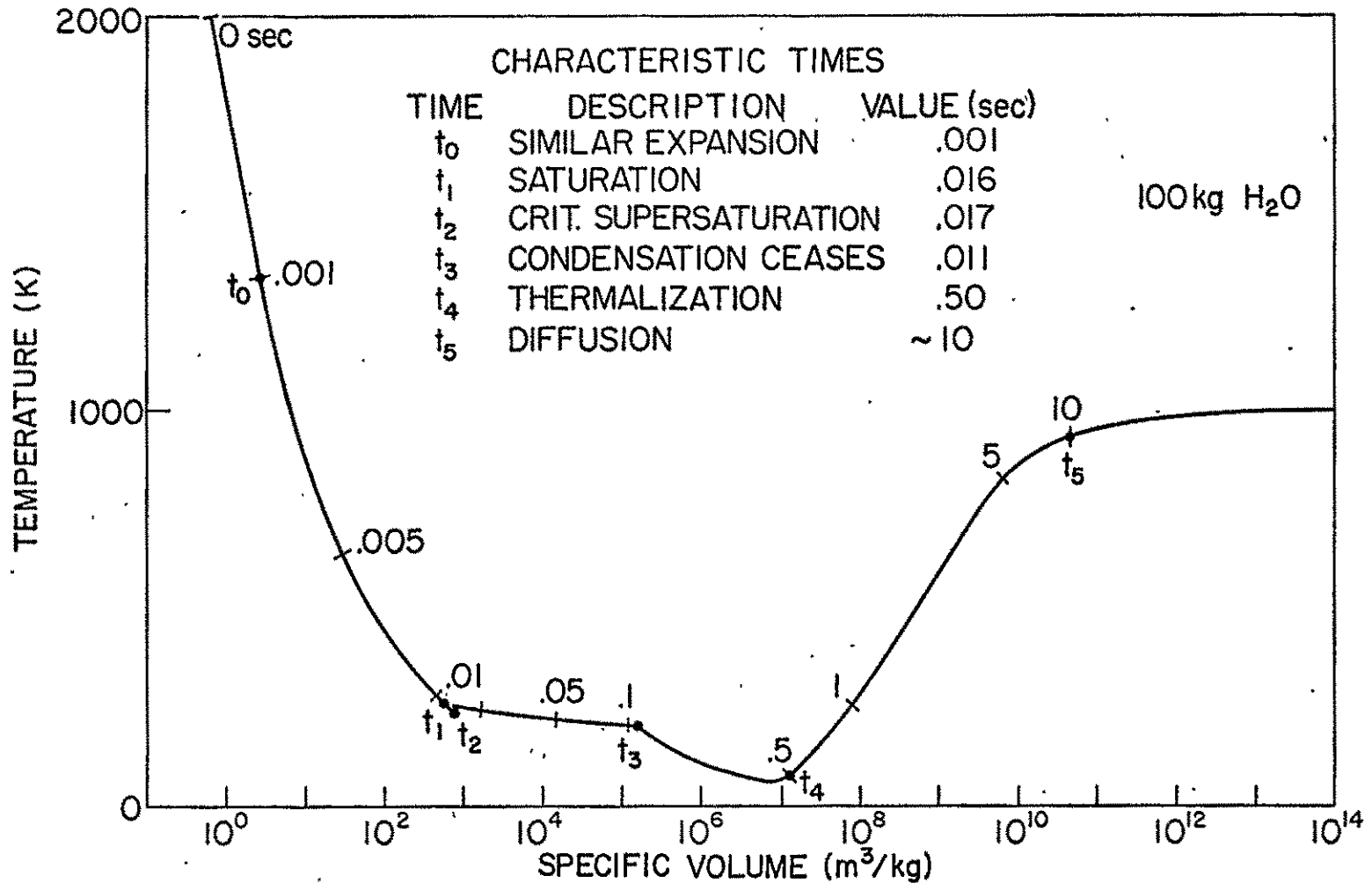
Fig. 8. Temporal variations in specific volume and temperature of an expanding H_2O vapor cloud with an initial pressure of one atm and an initial temperature of 2000K. Temperature and specific volume of the bacground atmosphere are 1000K and $3 \times 10^{+10}$ m³/kg, respectively.

$$x(T) = \frac{T}{(b_1 T - 1)^2} \left[(T_1 - T)\left(a_1 b_1 + \frac{1}{TT_1}\right) + (a_1 + b_1) \log_e(T/T_1) \right]$$

$$\tag{36}$$

where

$$a_1 = \frac{R + c_1}{U} \quad \text{and} \quad b_1 = \frac{c_2 - (c_1 + R)}{U}$$

Note that as temperature approaches zero, x approaches unity. (A derivation of this important expression appears in Appendix C.) The temperature is related to the volume by (35) and the volume is related to the expansion time through (24).

The expansion-condensation process is illustrated in Figure 8 for water vapor. At time $t = 0$ steam is released and the gas expands and cools adiabatically. After time t_1, the vapor becomes super-saturated. At the critical point, $t = t_2$, the latent heat of vaporization is released during the rapid condensation to ice crystals and T jumps to the saturation temperature. The vapor-ice system then expands and cools following the saturation isentrope.

The release of heat and the rise in vapor temperature during the condensation process is easily explained from a kinetic point of view. The free gas molecules that are attached to the nucleated clusters tend to have lower energy than the molecules that are reflected or ejected by the clusters. Thus, through nucleation, the lower energy gas molecules are sorted out and the temperature of the remaining vapor molecules is raised.

The gas expands along the saturated vapor isentrope given by (36) until the gas is far removed from thermodynamic equilibrium.

In equilibrium, the temperature of the fluid is close to the saturation temperature. As the fluid becomes rarified, the rate of adsorption of gas molecules onto the clusters falls below the evaporation rate of the clusters and a lower cluster temperature is needed to maintain the cluster size. Thus, when the temperature necessary to support a condensation center falls significantly below the saturated vapor temperature, condensation ceases. At this time, t_3, the maximum amount of injected material will have condensed.

The flux of molecules towards the surface of a nucleated cluster is given by

$$\phi = \frac{P - P_e}{\sqrt{2\pi \, mkT_s}} \quad \text{[Hirth and Pound, 1963]}$$

$$(37)$$

where ϕ is the flux due to adsorption and evaporation, P_e the equilibrium saturated vapor pressure, P the equivalent flux vapor pressure at surface temperature T_s given by $P = (T_s/T_v)^{1/2} P_v$, T_v the vapor temperature, P_v the vapor pressure, and m the molecular mass. This formula is used to determine the time of maximum nucleation and the evaporation rate of the cluster after nucleation ceases.

The equilibrium growth rate is calculated as follows: Under equilibrium conditions, T_s and P are very nearly equal to T_v and P_v, respectively. The equilibrium vapor pressure is derived from (27)

47

$$P_e = \frac{R}{B} e^{-U/RT_s} \qquad (38)$$

The effect of the curved cluster surface is neglected. The vapor pressure is given by the perfect gas law $P_v = n_v k T_v$. Near equilibrium the vapor pressure has the form of (38) (i.e., $P_v = R/B \exp[-U/RT_v]$). The flux of molecules into a cluster becomes

$$\phi = \frac{P_v\left(1 - \frac{P_e}{P_v}\right)}{\sqrt{2\pi \, mkT_v}} \simeq \frac{n_v k T_v \left\{1 - \exp\left[\frac{U}{R}\left(\frac{1}{T_v} - \frac{1}{T_s}\right)\right]\right\}}{\sqrt{2\pi \, mkT_v}} = \frac{n_v \bar{v}\left[1 - \left(\exp\frac{\theta U}{T_s R}\right)\right]}{\sqrt{4\pi}} \qquad (39)$$

where $\bar{v} = \sqrt{\dfrac{2kT_v}{m}}$ the mean thermal velocity, and, $\theta = \dfrac{T_s - T_v}{T_s}$ the super cooling factor. When θ is substantially greater than zero, the equilibrium condition is no longer valid and condensation ceases. The growth rate is the flux multiplied by the surface area of the cluster.

$$\frac{dg}{dt} = 4\pi r_c^2 \, \phi = \frac{4\pi r_m^2 \, g^{2/3}}{\sqrt{4\pi}} \left[1 - \exp\frac{\theta T_q}{T_s}\right] \qquad (40)$$

where r_c is the cluster radius $= r_m g^{1/3}$, g the number of molecules per cluster, r_m the molecule radius, and $T_q = U/R$. A similar expression is given by Zeldovich and Raizer [1967]...

Noting that $n_v = n_2(1-x) \, (t_2/t)^3$ and $g = x/\nu$, Eq. (40) is written as
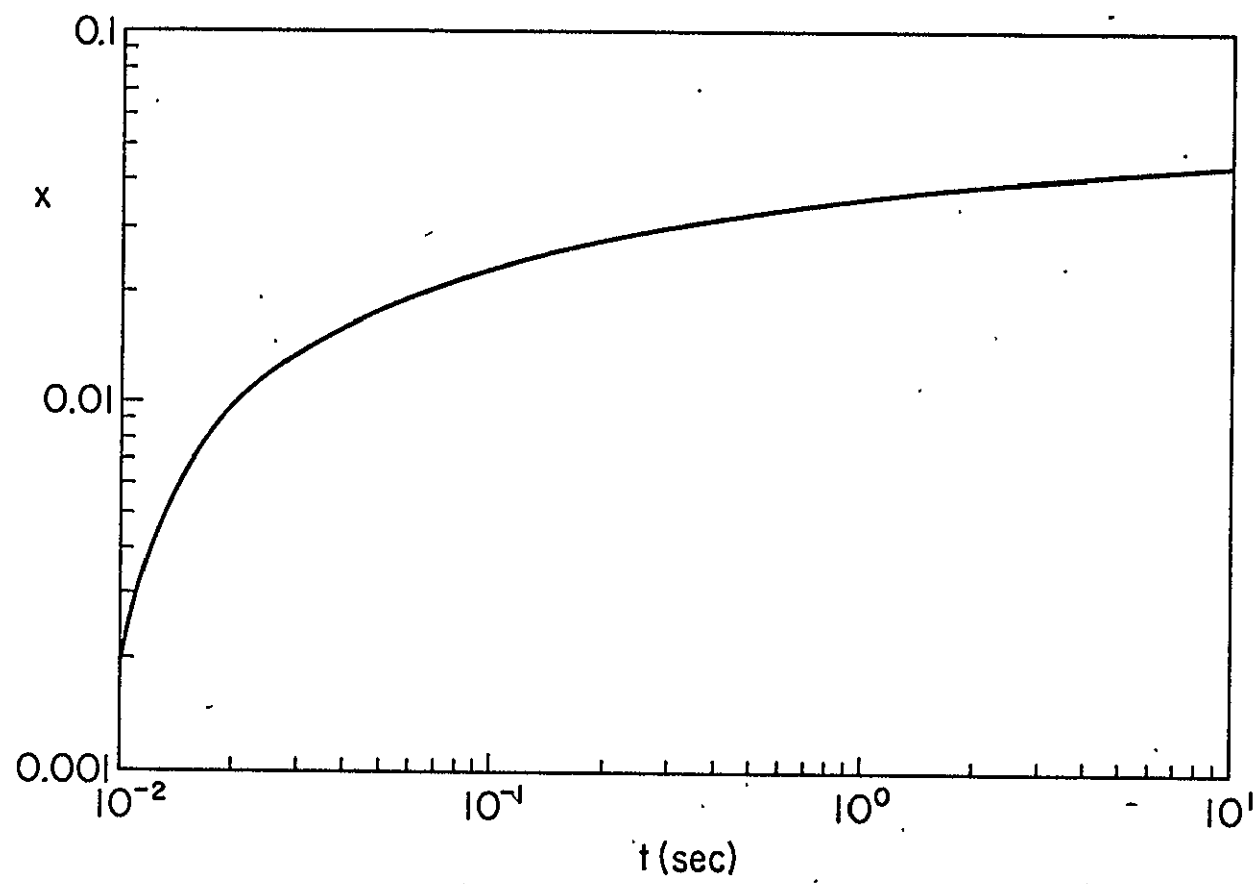
Fig. 9.   Temporal variation in the degree of condensation for H_2O.

$$\frac{dx}{dt} = \frac{\omega_m}{\sqrt{4\pi}} \, \nu^{1/3} \, x^{2/3}(1-x) \, (t_2/t)^3 \left(1-e^{-T_q\theta/T_s}\right) . \qquad (41)$$

where ω_m, the collision rate for free gas molecules at the time (t_2) of critical supersaturation $= 4\pi r_m^2 \bar{v} n_2$ and n_2 is the gas density at the same time. The cluster number, ν is found from the ratio of the cluster number density, N, to the fluid number density, n_2. In the water vapor example, $\nu = 1.4 \times 10^{-9}$ clusters/gas molecule.

The solution of (41) for θ results in

$$\theta = \frac{-T_s}{q} \log_e \left[1 - \frac{t^3 \, dx/dt}{x^{2/3}(1-x)A}\right] \qquad (42)$$

where $A = \dfrac{\omega_m \nu^{1/3} t_2^3}{\sqrt{4\pi}}$, θ is much less than unity except when

$$\frac{t^3 dx/dt}{x^{2/3}(1-x)A} \geq 1 \qquad (43)$$

This is the criterion for determining the time when condensation ceases. The values of x and dx/dt are derived from (25), (35), and (36). Figure 9 illustrates the temporal variations of x for the H_2O vapor release. Using the data from these figures and (43), it is found that condensation stops at $t_3 = .11$ sec. The temperature and degree of condensation at this time are $T_3 = 195$ K and $x_3 = .24$. The number of molecules per cluster is given by $g_3 = x_3/\nu = 1.71 \times 10^8$ indicating a cluster diameter of .2 microns.

Three forces affect the motion of the nucleated clusters. Gravity exerts a downward force, displacement of the atmosphere exerts an upward force according to Archimedes' principle, and aerodynamic drag exerts an additional upward force. The force equation is $\vec{F} = -\vec{g}m_c + \vec{g}m_a + \vec{D}_r$ where $\vec{g}$ is the acceleration of gravity, m_c the mass of the cluster $= 4\pi r_c^3 \rho_c/3$, m_a the mass of the displaced air $= 4\pi r_c^3 \rho_a/3$, r_c the cluster radius, ρ_c the cluster mass density, ρ_a the atmospheric density, and $\vec{D}_r$ the drag force. Since the cluster is much more dense than the atmosphere, $m_c \gg m_a$, the buoyancy force is negligible. Assuming a spherical particle, the pressure drag is $\vec{D}_r = 6\pi\mu r_c \vec{v}$ [Hoerner, 1965] where μ is the viscosity, and v the upward particle velocity with respect to the atmosphere. The acceleration of the cluster is $d\vec{v}/dt = -\vec{g} + \vec{D}_r/m_c = -\vec{g} - 9\mu\vec{v}/(2r_c^2\rho_c)$. The viscosity of the atmospheric constituents O, O_2 and N_2 is approximately given by $\mu = 4. \times 10^{-7} T^{.69}$ $kg\,m^{-1}(s^{-1})$ [Banks and Kockarts, 1973]. The equation of motion for the spherical particle becomes $d\vec{v}/dt = -\vec{g} - 1.8 \times 10^{-6} T^{.69} \vec{v}/(r_c^2\rho_c)$.

For the example of a .2 micron diameter ice cluster in a 1000 K F-region atmosphere, the equation of motion becomes $d\vec{v}/dt = -9 - 2 \times 10^7 \vec{v}$. The particle approaches steady state velocity with time constant $\tau = .5 \times 10^{-7}$ sec. The cluster velocity approaches a terminal velocity of $v = -4.5 \times 10^{-7}$ m/sec. Because of this low velocity, the falling motion of the nucleated clusters may be neglected.

After thermodynamic equilibrium is disturbed, the condensed particle clusters freely evaporate. The evaporation flux is given by (37) with the external vapor pressure term dropped

51

$$\phi = \frac{-P_e}{\sqrt{2\pi_m kT}} \qquad (44)$$

The cluster surface vapor pressure, including the effects of the spherical radius of curvature, is derived from (28)

$$P_e = P_\infty \exp\left[\frac{2\sigma V_B}{rkT}\right] \qquad (45)$$

The flat surface vapor pressure, P_∞, is given by (38) resulting in

$$P_e = \frac{R}{B} \exp\left[\left(\frac{2\sigma V_B}{rk} - \frac{U}{R}\right)\frac{1}{T}\right] \qquad (46)$$

The evaporation rate is the evaporation flux multiplied by the cluster surface area.

$$\frac{dg}{dt} = 4\phi\pi r_c^2 = -\frac{R}{B} \exp\left[\left(\frac{2\sigma V_B}{rk} - \frac{U}{R}\right)\frac{1}{T}\right] 4\pi r_m^2 g^{2/3} / \sqrt{2\pi mkT} \qquad (47)$$

The variation in cluster temperature is a function of cooling by evaporation and of heating by the sun's rays. Heat is removed from the clusters by evaporation because the high energy molecules escape leaving the cooler, low energy molecules attached to the cluster. The temperature change is given by the heat equation

$$\frac{dQ}{dt} = gm\ c_2\ \frac{dT}{dt} = gmU + Q_0 kV\epsilon \qquad (48)$$

52
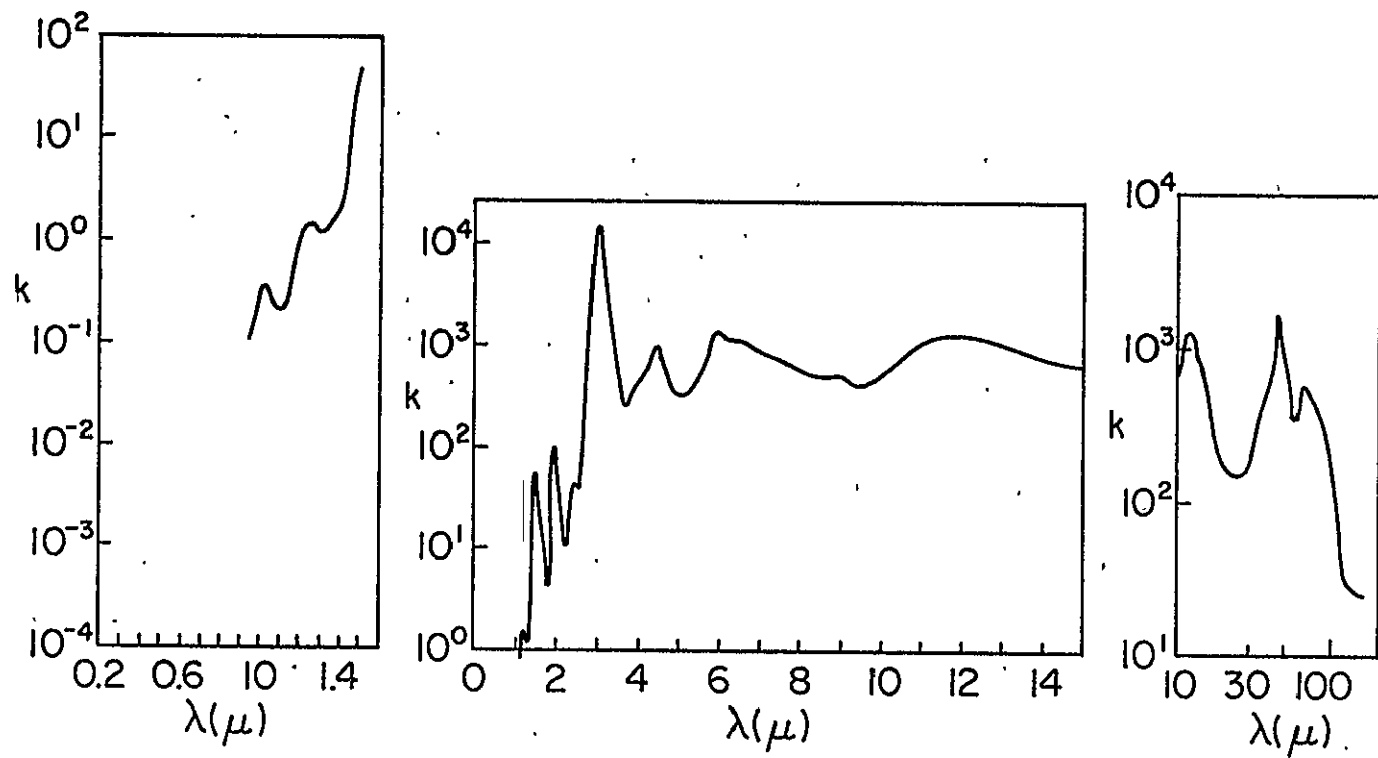
Fig. 10. Ice absorbtion coefficient (k) in cm^{-1} versus wavelength in microns.
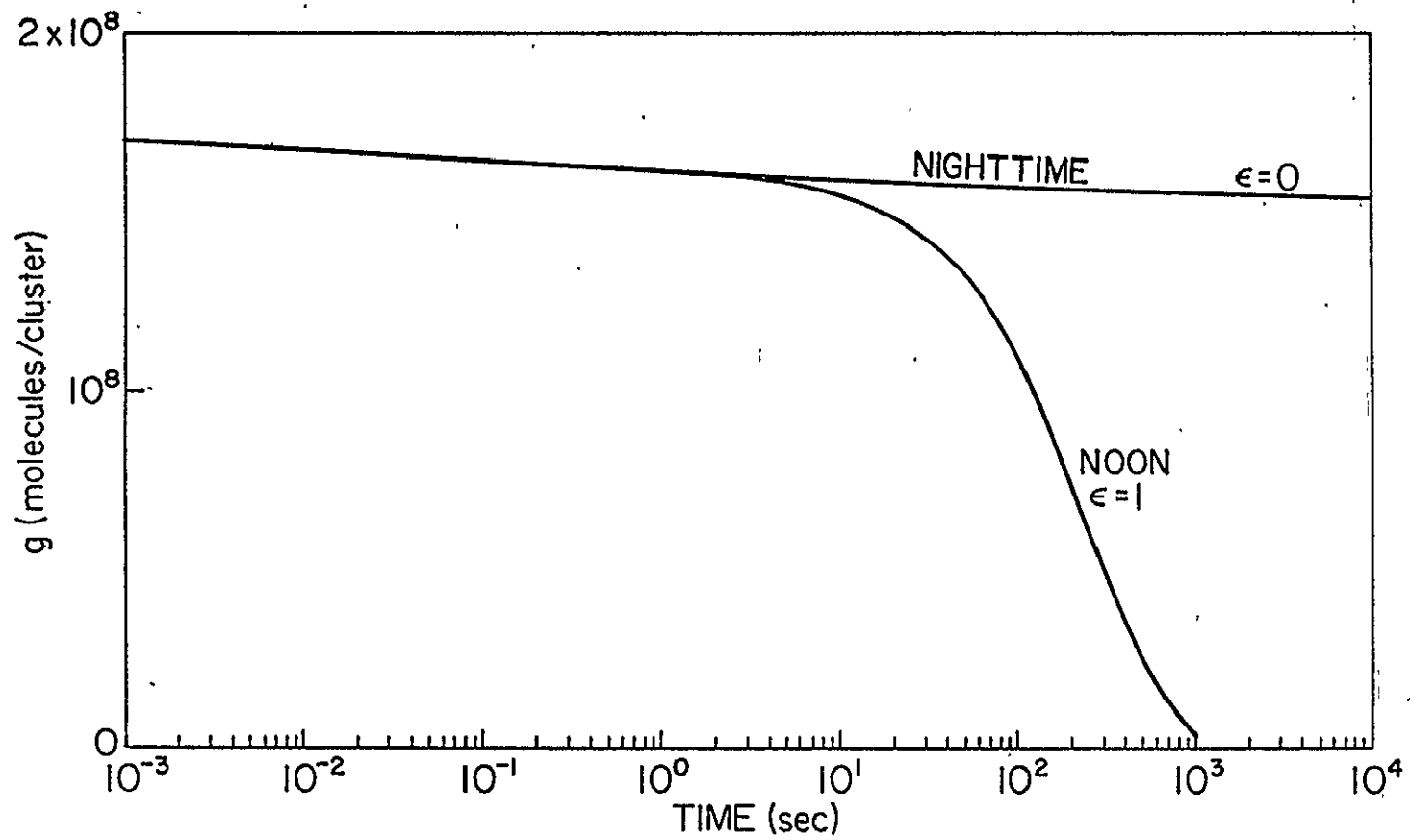
Fig. 11. The effect of solar radiation on the evaporation of ice clusters.

where Q is the heat energy of the cluster, c_2 the specific heat of the cluster, U the change in energy of the cluster associated with evaporation, Q_0 the solar constant = 1340 watts/m^2, $\bar{k}$ the average solar radiation absorption coefficient, V the cluster volume = $4/3\pi r_m^3 g$ and ε the solar heating factor depending on the sun's position ($\varepsilon = 0$ at night and $\varepsilon = 1$ at noontime). The average absorption coefficient is calculated as follows

$$\bar{k} = \frac{\int_0^\infty R(\lambda)k(\lambda)d\lambda}{\int_0^\infty R(\lambda)d\lambda} \tag{49}$$

where k is the wavelength dependent absorption coefficient and $R(\lambda)$ is the solar power radiated per unit wavelength. The spectrum of the absorption coefficient for H_2O is shown in Figure 10 as given by Irvine and Pollack [1968]. Averaging over the solar spectrum yields $\bar{k}_{H_2O} = 7770$ m^{-1}.

Substitution of (48) into (49) gives

$$\frac{dT}{dt} = -\frac{UR}{c_2 B}\exp\left[\frac{\left(\frac{2\sigma V_B}{vk} - \frac{U}{R}\right)\frac{1}{T}}{\sqrt{2\pi mkT}\ g^{1/3}}\right]4\pi r_m + \frac{Q_0\bar{k}\varepsilon}{\rho c_2} \tag{50}$$

where ρ is the mass density of the cluster. The cooling and evaporation of the nucleated clusters are found by solving the coupled first order nonlinear differential equations (48) and (50) subject to the initial conditions:

$$T = T_3, \quad g = x_3/\nu \quad \text{at time} \quad t_3 \tag{51}$$

The evaporation of nucleated ice clusters is illustrated in Figure 11. The difference between the nighttime and daytime cluster persistence is striking. After 1000 seconds, only 11% of the nighttime ice cluster has evaporated whereas, during the day, 98% of the same cluster has evaporated. From these calculations, it is concluded that nucleated gas molecules have negligible effect on the ionosphere during the night, but they will enter into recombination reactions during the daytime after some delay.

D. Transition Between Translational Equilibrium and Frozen Flow

After condensation equilibrium is disturbed and condensation ceases, the expanding gas temperature is no longer influenced by cluster cooling. The vapor is in translational equilibrium and expands according to the continuum isentropic expression

$$\frac{n}{n_3} = \left(\frac{t_3}{t}\right)^3 \qquad \frac{T}{T_3} = \left(\frac{t_3}{t}\right)^{3(\gamma-1)} \tag{52}$$

where n_3 and T_3 are the density and temperature of the gas at the time of deviation from saturated vapor equilibrium. The rapid cooling of H_2O vapor after this time is shown in Figure 8.

Under translational quasi-equilibrium conditions, the gas collision or relaxation time $\tau_R = 1/\omega$, is small in comparison with the time scale, τ_e, of the gas expansion. When $\tau_R \gg \tau_e$ the flow

56

becomes frozen in a nonequilibrium state. The transition time, t_4, between equilibrium and frozen, free molecular flow is calculated by equating the relaxation time with the characteristic expansion time.

The relaxation time is the ratio of the internal mean free path to the mean thermal velocity.

$$\tau_R = \frac{\lambda_c}{c} = \sqrt{\frac{m}{k}} \, \frac{1}{2\pi d^2} \, \frac{1}{n\sqrt{T}} \tag{53}$$

where $\lambda_c = \frac{1}{\sqrt{2}\pi d^2 n}$ is the mean free path inside the cloud, d is the molecular diameter, n the gas number density, k Boltzmann's constant, T the gas temperature, and m the molecular mass.

If the released gas does not go through a state of condensation, expressions for T and n from (22) and (23) are used in the expression for the relaxation time to yield

$$\tau_R = \frac{t_0}{v_0} \, \frac{\left(t/t_0\right)^{\frac{3}{2(\gamma+1)}}}{\sqrt{2}\pi d^2 n_3} \quad \text{where} \quad t_0 = \frac{v_0}{\sqrt{T_0}} \, \sqrt{\frac{m}{2k}} \tag{54}$$

If the gas does condense, the expansion after the terminal nucleation time, t_3, can be found by using (52) for temperature and density

$$\tau_R = \sqrt{\frac{m}{2kT_3}} \, \frac{\left(t/t_3\right)^{\frac{3}{2(\gamma+1)}}}{\sqrt{2}\pi d^2 n_3} \tag{55}$$

The characteristic expansion time is taken to be the expansion velocity time constant.

$$- \frac{1}{\tau_e} = \frac{dv}{vdt} \qquad (56)$$

Since $v = r/t$ in both continuum and collisionless expansions into a vacuum, $\tau_e = t$.

Equating τ_e and τ_R and solving for the transition time t_4 gives

$$t_4 = t_0 \ (\sqrt{2}\pi d^2 \ r_0 n_0)^{\frac{2}{3\gamma+1}} \quad \text{(without condensation)}$$

$$(57)$$

$$t_4 = t_3 \ (\sqrt{2}\pi d^2 t_3 \ \sqrt{2kT_3/m} \ n_3)^{\frac{2}{3\gamma+1}} \quad \text{(with condensation)}$$

$$(58)$$

Another, equally valid definition of the time separating the continuum flow from the collisionless flow is obtained by letting the Knudson number be unity.

$$K_n = \frac{\lambda_c}{d_c} = 1 \qquad (59)$$

where λ_c is the mean free path inside the cloud and d_c is the cloud diameter. The cloud diameter is taken to be an equivalent diameter of a sphere with the central cloud density

$$N_0 = n \ \frac{4}{3} \ \pi (\frac{d}{2})^3 = n_0 \ \frac{4}{3} \ \pi r_0^3 \qquad (60)$$

58

Equating d_c with λ_c and solving for n yields

$$n = \frac{1}{(2\sqrt{2}\pi d^2 r_0)^{3/2} \, n_0} \tag{61}$$

By using (23) $n = n_0\left(\frac{t_0}{t}\right)^3$, one gets

$$t = t_0(2\sqrt{2}\pi d^2 r_0 n_0)^{1/3} \tag{62}$$

Except for a factor of $2^{1/3}$, this is the same result as (57) with $\gamma = 5/3$. Thus, an estimate of the transition time between continuum and frozen flow for noncondensing gases is given by

$$t_4 = 2t_0(d^2 r_0 n_0)^{1/3} \tag{63}$$

For water vapor, this has the numerical value of $t_4 = .44$ second. The extimate transition time including condensation, (58), yields a value of $t_4 = .67$ seconds for the water vapor release. Since the transition time calculation is only approximate, values from (63) are sufficiently accurate in most cases.

E. Interaction with the Background Atmosphere

As the gas cloud expands, atmospheric particles will be imbedded in the outer shell of the cloud. The heating of the gas cloud by picking up atmospheric particles has been examined by Hoffman and Best [1974] and Baxter and Linson [1976]. This work only considers

the atmosphere-to-cloud energy transfer when the rarefied atmosphere is well mixed with the injected cloud. At this time, the gas molecules in the cloud are in a state of free molecular flow with themselves.

In this section, the gas expansion between the times of initial free molecular flow, t_4, and diffusive flow, t_5, is examined. The initial gas distribution at t_4 is modeled as a uniform sphere with density n_4 and temperature T_4. The radius of the sphere is defined so that the total number of particles is conserved (i.e., $N_0(1-x) = \frac{4}{3}\pi r_4^3 n_4$ where r_4 is the equivalent cloud radius at time t_4, N_0 is the number of molecules released, x is the maximum degree of condensation, and n_4 is the central number density). With this assumption, the free molecular flow expressions given by (7), (8), and (9) are used. The time and distance are normalized in the usual way: $\tau = tc_4/r_4$ and $r = |\vec{x}|/r_4$ where $c_4 = \sqrt{2kT_4/m}$. Since only the evolution of densities and temperatures near the center of the cloud will be considered, little error is made by using this model.

Assuming an unperturbed background atmosphere and negligible self scattering, the released gas distribution satisfies the following kinetic equation.

$$\frac{\partial f}{\partial t} + \vec{v} \cdot \nabla f = \omega_a(n\phi_a - f) + \delta(t) \, Q_0(\vec{x}) \, \phi_0(v) \qquad (64)$$

where $f(t,\vec{x})$ is the gas distribution function, $\omega_a = c_a/\lambda_a$, the ambient collision frequency, $\lambda_a = 1/(\sqrt{2}\pi d^2 n)$, the mean free path, d the gas molecules diameter, $c_a = \sqrt{2kT_a/m_a}$ the mean thermal speed, n

the released gas density, Q_0 the spherical source function,

$\phi_a = \exp\left\{-[(\vec{v} - \vec{u}_a)/c_a]^2\right\}/(\pi^{3/2}c_a^3)$, $\vec{u}_a$ the atmospheric velocity

relative to the gas release, and ϕ_0 the Maxwell source velocity

distribution of (1). This is the Krook equation with an atmospheric

collision term and a spherical source term. Equation (64) is solved

following the procedure used by Baum [1973].

The time and space derivatives are removed by operating with the

Laplace-Fourier transform as defined in (65) and (66).

$$\bar{g}(p,\vec{k}) = \int_{-\infty}^{\infty}d^3\vec{x} \int_{0}^{\infty}dt\; e^{-i\vec{k}\cdot\vec{x}-pt}\; g(t,\vec{x}) \tag{65}$$

$$g(t,\vec{x}) = \int_{-\infty}^{\infty}\frac{d^3\vec{k}}{(2\pi)^3} \int_{c}\frac{dp}{2\pi i}\; e^{pt+i\vec{k}\cdot\vec{x}}\; \bar{g}(p,\vec{k}) \tag{66}$$

The transformed Eq. (64) becomes

$$(p + i\vec{k}\cdot\vec{v} + \omega_a)\bar{f} = \omega_a\phi_a\bar{n} = \phi_0\bar{Q}_0(\vec{k}) \tag{67}$$

the overbar indicates transformed quantities. The solution for

is written as

$$\bar{f} = \frac{\omega_a\phi_a\bar{n} + \phi_0\bar{Q}_0(\vec{k})}{p+i\vec{k}\cdot\vec{v}+\omega_a} \tag{68}$$

Using $\bar{n} = \int\bar{f}\, d^3\vec{v}$, the transformed density function is found to be

$$\bar{n} = \bar{Q}_0(\vec{k}) \int\frac{\phi_0 d^3\vec{v}}{p+i\vec{k}\cdot\vec{v}+\omega_a} \left[1 - \omega_a \int\frac{\phi_a d^3\vec{v}}{p+i\vec{k}\cdot\vec{v}+\omega_a}\right]^{-1} \tag{69}$$

61

This density function is split into two parts

$$\bar{n} = \bar{n}_\alpha + \bar{n}_c$$

where

$$\bar{n}_\alpha = \bar{Q}_0(\vec{k}) \int \frac{\phi_0 d^3\vec{v}}{p+i\vec{k}\cdot\vec{v}+\omega_a} \qquad (70)$$

$$\bar{n}_c = \bar{n}_\alpha G(p,\vec{k}) \qquad (71)$$

and

$$G(p,\vec{k}) = \omega_a \quad \frac{\phi_0 d^3v}{p+i\vec{k}\cdot\vec{v}+\omega_a} \left[1 - \omega_a \int \frac{\phi_a d^3\vec{v}}{p+i\vec{k}\cdot\vec{v}+\omega_a} \right]^{-1}$$

$$(72)$$

The first term, n , is related to the collisionless solution to the Boltzmann equation. The collisionless Boltzmann equation with a source term is

$$\frac{\partial f_m}{\partial t} + \vec{v}\cdot\nabla f_m = \delta(t) \, Q_0(\vec{x}) \, \phi_0(\vec{v}) \qquad (73)$$

The Laplace-Fourier transform of this equation is manipulated to yield

$$\bar{f}_m = \frac{\phi_0 \bar{Q}_0(\vec{k})}{p+i\vec{k}\cdot\vec{v}} \qquad (74)$$

62

Integration over velocity space yields

$$r_m = \int f_m d^3\vec{v} = \bar{Q}_0(\vec{k}) \int \frac{\phi_0 d^3\vec{v}}{p + i\vec{k}\cdot\vec{v}} \tag{75}$$

Comparison with (70) shows that

$$\bar{n}_\alpha(p) = \bar{n}_m(p + \omega_a)$$

Finally we invoke the inverse Laplace-Fourier transform, Eq. (26), to get

$$n_\alpha = n_m \exp(-\omega_a t)$$

The first term in the density function is the free molecular flow solution multiplied by $\exp(-\omega_a t)$ which represents damping by the atmosphere. The free molecular solution for spherical expansion, n_m, has already been derived and is given in (7). Hence,

$$n_\alpha = \frac{n_4}{2}\left[\operatorname{erf}\left(\frac{r+1}{\tau}\right) - \operatorname{erf}\left(\frac{r-1}{\tau}\right) + \frac{\tau}{r\pi^{1/2}}\left\{\exp\left[-\left(\frac{r+1}{\tau}\right)^2\right] - \exp\left[-\left(\frac{r-1}{\tau}\right)^2\right]\right\}\right]e^{-\omega_a t} \tag{76}$$

The second term, n_c, in the density function represents the collision effects of the atmosphere. After many collisions, n vanishes and the scattered gas molecules, represented by n_c, constitute the expanding cloud. The multiplication of the two functions, $\bar{n}_\alpha$ and $G(p,k)$, in (71) transforms into convolution resulting in

63

$$n_c = n_\alpha(t,\vec{x}) * G(t,\vec{x}) = \int_0^t dt_1 \int d^3\vec{x}_1 \, n_\alpha(t_1\vec{x}_1) \, G(t-t_1, \vec{x}-\vec{x}_1)$$

(77)

where $G(t,\vec{x})$, the scattering Green's function is the inverse Laplace-Fourier transform of $\bar{G}(p,\vec{k})$.

The exact form of $G(t,\vec{x})$ is mathematically complex and the exact convolution in (77) is a formidable task. For large-times, Baum [1973] has derived the following asymptotic form for $G(t,\vec{x})$.

$$G(t^*,r^*) \simeq \frac{e^{-(r^*)^2/2t^*}}{(2\pi t^*)^{3/2}}$$

(78)

where $r^* = |\vec{x}^* - \vec{W}_a t^*|$, $\vec{x}^* = \frac{\vec{x}}{\lambda_a}$, $t^* = t\omega_a$, and $\vec{W}_a = \vec{u}_a/c_a$. (In the remaining part of this section, time, distance and velocity are nondimensionalized by $1/\omega_a$, λ_a, and c_a --the characteristic atmospheric quantities.) The use of this aymptotic Green's function simplifies the calculations and does not introduce appreciable qualitative error because n_2 is significant only after long times. The long-time expression for the free molecular term, n_m, is

$$n_m \simeq \frac{N_4}{\lambda_a^3} \frac{e^{(r^*)^2/(bt^*)^2}}{3/2(bt^*)^3}$$

(79)

where $b = c_4/c_a$ and $N_4 = N_0(1-x)$ is the number of gas molecules uncondensed. This is the free molecular density solution for an impulsive source release. The expression of the gas density of all finite, free molecular gas releases approaches (79) in the long-time limit.

Convolve $n_m \exp(-\omega_a t)$ with $G(t^*, r^*)$ to get

$$n_c = \frac{N_4}{\lambda_a^3} \int_0^{t^*} e^{-t'} \, G(T,R) dt' \tag{80}$$

where $R = |\vec{x}^* - \vec{W}_a(t^* - t')|$, $T = t^* - t + 1/2(bt')^2$, and $G(R,T)$ is given by (78)

The composite solution is found by adding the damped free molecular solution, Eq. (76), to the expression for the scattered gas density, Eq. (80)

$$n(t^*, x^*) = \frac{N_4}{\lambda_a^3} \left[\frac{3}{8\pi a^3} \left\{ \mathrm{erf}\left(\frac{a+r^*}{bt^*}\right) - \mathrm{erf}\left(\frac{a-r^*}{bt^*}\right) + \frac{bt^*}{\pi^{1/2} r^*} \right. \right.$$

$$\left. \left. \left(\exp\left[-\left(\frac{a+r^*}{bt^*}\right)^2\right] - \exp\left[-\left(\frac{a+r^*}{bt^*}\right)^2\right] \right) \right\} + \int_0^{t^*} e^{-t'} G(T,R) dt' \right] \tag{81}$$

where $a = r_3/\lambda_a$, $b = c_4/c_a$, $\vec{x}^* = \vec{x}/\lambda_a$, $t^* = t\omega_a$, $r^* = |x^*|$
$R = |\vec{x}^* - \vec{W}_a(t^* - t')|$, $T = t^* - t' + 1/2(bt')^2$, and $G(T,R) = \dfrac{e^{-R^2/2T}}{\pi^{3/2}(2T)^{3/2}}$.

The composite density solution consists of two modes, the collisionless mode and the scattered mode. This bimodal nature is evident if the gas is released at a supersonic velocity with respect to the atmosphere $(W_a > 1)$. The center of the collisionless mode continues in the inertial reference frame of the released gas. The center of the scattered mode will remain fixed with respect to the atmospheric point of release. Figure 12 illustrates the conversion from the collisionless mode to the scattered mode for a relative
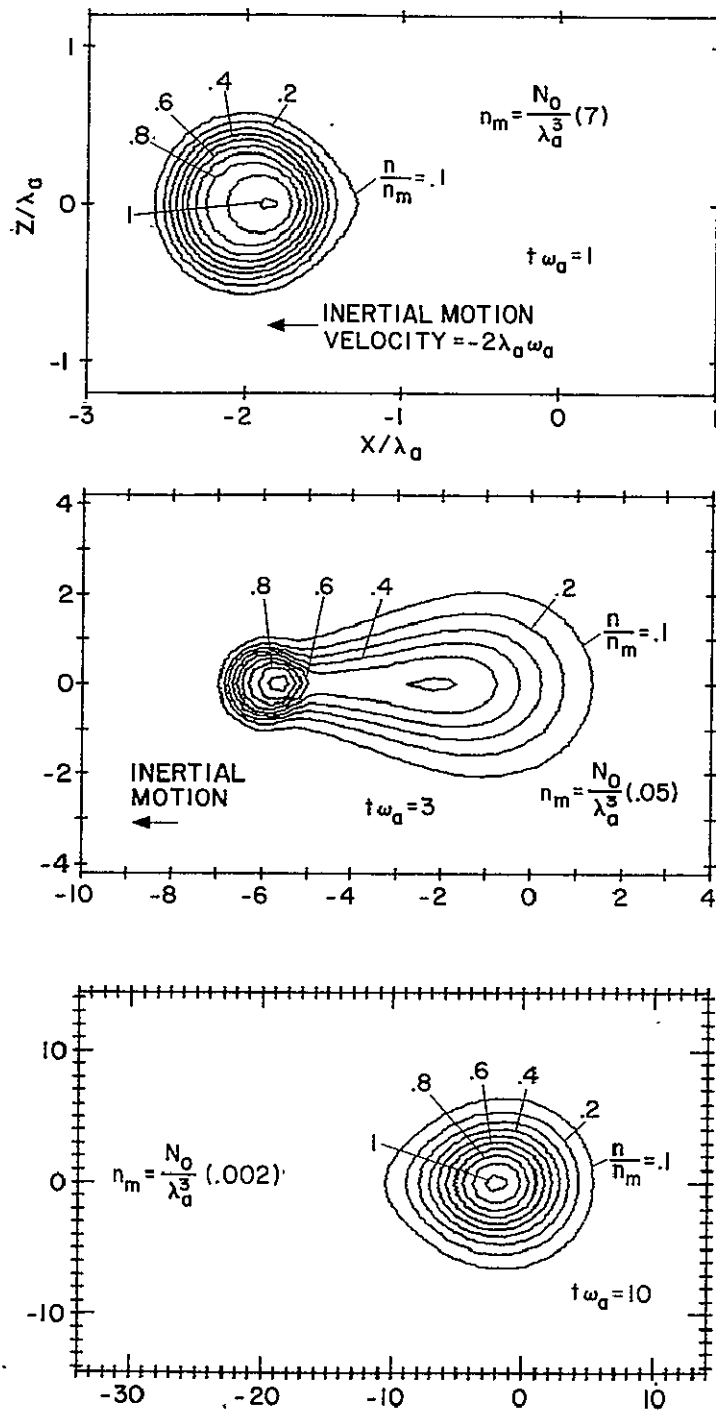
Fig. 12. Interaction of a moving gas ball with a stationary
atmosphere. An expanding hydrogen cloud containing
N_0 molecules is released at Mach 2 into an atmos-
phere with meanfree path λ_a and mean collision
frequency ω_a. Most of the injected gas becomes
thermalized with the atmosphere after 10 collision
times.

release velocity of Mach 2. To construct the isopycnic contours in this figure, the integral in (80) is evaluated by the Gaussian quadrature method. For times less than one mean collision time, the spherical gas cloud is only slightly perturbed by the atmosphere (Figure 12(a)). At about 3 collision times (Figure 12(b)), approximately half of the gas is in the free molecular state and the other half is moving with the atmosphere. The scattered gas molecules are hotter than the molecules that have not collided with the high temperature atmospheric gas. The high thermal velocities of the scattered mode result in a higher expansion rate for the scattered mode compared to the collisionless mode. This effect is represented by the widening of the density contours in going from the collisionless to the scattered regions. After many collision times, the injected gas flow approaches a spherically symmetric distribution about the point $\vec{x}^* = \vec{W}_a t^*$ where x^* is the position of the point of gas release in the inertial frame of reference (Figure 12(c)). Note the change of scale in Figure 12.

When the gas expansion is controlled by atmospheric collisions ($t^* \gg 1$), Eq. 80 becomes

$$n(t,\vec{x}) = \frac{N_4}{\lambda_a^3} \left(\frac{1}{2\pi t^*}\right)^{3/2} \exp\left\{\frac{-(\vec{x}^*-\vec{W}_a t)^2}{2t^*}\right\} \tag{82}$$

This expression can also be derived assuming diffusive expansion (Chapter IV).

The temperature of the released cloud is dependent on the loss of internal energy to radial expansive motion and energy transfer

from the ambient atmosphere through collisions. The temperature is found by calculating the second·velocity moment of the distribution function in (68) which is repeated here

$$\bar{f} = \frac{\omega_a \phi_a \bar{n} + \phi_0 \bar{Q}_0}{p + i\vec{k}\cdot\vec{v} + \omega_a}$$

Every variable in this expression is known. Density n, the inverse Laplace-Fourier transform of $\bar{n}$, is given by (81).

Considering the collisionless Boltzmann equation

$$\frac{\partial f_m}{\partial t} + v\cdot\nabla f_m = \delta(t)\ Q_0(\vec{x})\ \phi_0(v) \tag{83}$$

and the solution for $\bar{f}_m$ using the L-F transform

$$\bar{f}_m = \frac{\phi_0 \bar{Q}_0}{p + i\vec{k}\cdot\vec{v}} \tag{84}$$

Comparing this equation with (68) we see

$$\bar{f} = \bar{f}_c + \bar{f}_m\ (p + \omega_a) \tag{85}$$

where

$$\bar{f}_c = \frac{\omega_a \phi_a \bar{n}}{p + i\vec{k}\cdot\vec{v} + \omega_a}$$

68

Thus, the particle velocity distribution function is the sum of two distribution functions as follows

$$f = f_c + f_m e^{-\omega_a t} .$$

(86)

The free molecular distribution function, f_m, has been previously derived (6).

The collisional contribution to the distribution function, f_c, is found from the following convolution

$$f_c = n * (L\text{-}F)^{-1} \left[\frac{1}{p+i\vec{k}\cdot\vec{v}+\omega_a} \right]^{\omega_a \phi_a}$$

(87)

where $(L\text{-}F)^{-1}$ indicates the inverse Laplace-Fourier transform operation. It is easy to show that

$$(L\text{-}F)^{-1} \left[\frac{1}{p+i\vec{k}\cdot\vec{v}+\omega_a} \right] = H(t) \quad \delta(x-\vec{v}t) \, e^{-\omega_a t}$$

(88)

where $H(t) = 0 \quad t<0$
$\qquad\qquad\quad 1 \quad t>0$

The result of the convolution, expressed in nondimensionalized units, is

$$f_c = \frac{1}{\pi^{3/2}c_a^3} \, e^{-(\vec{v}*)^2} \int_0^{t*} n[\tau_1,\vec{x}*-\vec{v}*(t*-\tau_1)] \, e^{-(t*-\tau_1)} d\tau_1$$

(89)

where $\vec{v}* = \vec{v}/c_a$ and $n[\tau_1,\vec{x}*-\vec{v}*(t*-\tau_1)]$ is obtained from (80).

69

The temperature is found at the center of the cloud (x = 0)
under conditions of no relative atmospheric motion $(W_a = u_a = 0)$.
The temperature variation is composed of a damped free molecular
contribution and an atmospheric collision contribution.

$$T = \frac{m}{3k} \iiint\limits_{-\infty}^{\infty} f\vec{v}^2 d^3\vec{v} = \frac{m}{3k} e^{-\omega_a t} \iiint\limits_{-\infty}^{\infty} f_m \vec{v}^2 d^3\vec{v} + \frac{m}{3k} \iiint\limits_{-\infty}^{\infty} f_c \vec{v}^2 d^3\vec{v}$$

$$= T_m e^{-\omega_a t} + T_c \qquad\qquad (90)$$

T_m is given by (12). In nondimensionalized form

$$T_m = T_4 \left[erf \frac{1}{bt^*} - \frac{2}{\pi^{1/2} bt^*} \exp - \frac{1}{(bt^*)} - \frac{4}{3\pi^{1/2}(bt^*)^3} \exp -\left(\frac{1}{(bt^*)}\right) \right] \Big/ \frac{n}{n_4}$$

$$(91)$$

T_c is found by calculating the second moment of f_c as given by (89).

$$T_c = \frac{\frac{m}{3k} \iiint f_c \vec{v}^2 d^3\vec{v}}{n} = \frac{\frac{3}{2} T_a \iiint f_c \vec{v}*^2 d^3\vec{v}}{n} \qquad (92)$$

At x* = 0, the term inside the integral in (89) becomes

$$n[\tau_1, -v^*(t^*-\tau_1)] \exp[-(t^*-\tau_1)] = \frac{N_4}{\lambda_a^3} \left[\frac{\exp\{-[v^*(t^*-\tau_1)/(b\tau_1]^2 -\tau_1\}}{\pi^{3/2} (b\tau_1)^3} \right.$$

$$\left. + \int\limits_0^{\tau_1} d\tau_2 \frac{\exp\{-[r^*(t^*-\tau_1)]^2/T-\tau_2\}}{(\pi T)^{3/2}} \right]$$

$$(93)$$

70

where $T = 2(\tau_1 - \tau_2) + (b\tau_2)^2$ and the long time damped free molecular density (79) has been used. Substitution of (93) into (89) and integrating over velocity space results in

$$\frac{T_c}{T_a} = \frac{N_4}{n\lambda_a^3} \int_0^{t^*} d\tau_1 \frac{e^{-(t^*-\tau_1)}}{\pi^{3/2}} \left[\frac{e^{-\tau_1}(b\tau_1)^2}{[(b\tau_1)^2 + (b^*-\tau_1)]^{5/2}} + \int_0^{\tau_1} \frac{e^{-t}T}{[T+(t^*-\tau_1)^2]^{5/2}} \right] \tag{94}$$

The central density variation, $n(x^* = 0)$, takes the long-time form

$$n(o,t^*) = \frac{N_4}{\lambda_a^3} \left[\frac{e^{-t^*}}{\pi^{3/2}(bt^*)^3} + \int_0^{t^*} \frac{e^{-\tau_1} d\tau_1}{\pi^{3/2}[2(t^*-\tau_1)+(bt)^2]^{3/2}} \right] \tag{95}$$

Combining (94) and (95), we get an expression for the temperature increase produced by collisions with the ambient atmosphere.

$$T_c = \frac{T_a \int_0^{t^*} d\tau_1 e^{-(t^*-\tau_1)} \left[\frac{e^{-\tau_1}}{(A_1+(t^*-\tau_1))^{5/2}} + \int_0^{\tau_1} \frac{d_2 e^{-\tau_2} A_2}{[A_2+(t^*-\tau_1)]^{5/2}} \right]}{\frac{e^{-t^*}}{B_1^{3/2}} + \int_0^{t^*} d\tau_1 \frac{e^{-\tau_1}}{(B_2)^{3/2}}} \tag{96}$$

where

$$A_1 = (b\tau_1)^2 \qquad b_1 = (b\tau^*)^2$$

$$A_2 = 2(\tau_1 - \tau_2) + (b\tau_2)^2$$

$$B_2 = 2(\tau^* - \tau_1) + (b\tau_1)^2$$

The density and temperature expressions derived in this section are used to formulate the T-V variations of Figure 8 during the period when the released gas is thermalizing with the atmosphere.
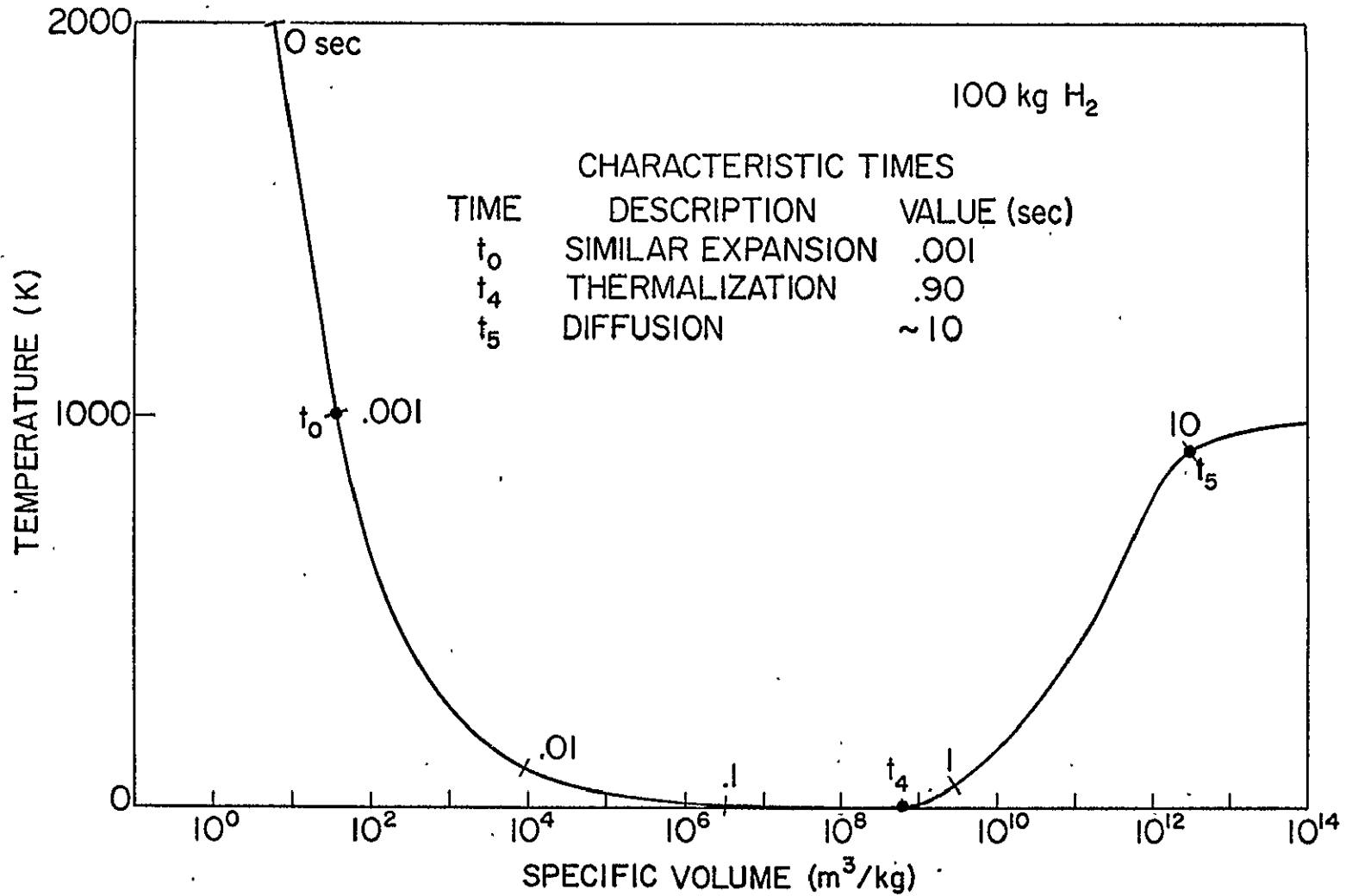
Fig. 13. Temporal variations in specific volume and temperature of an expanding H_2 cloud
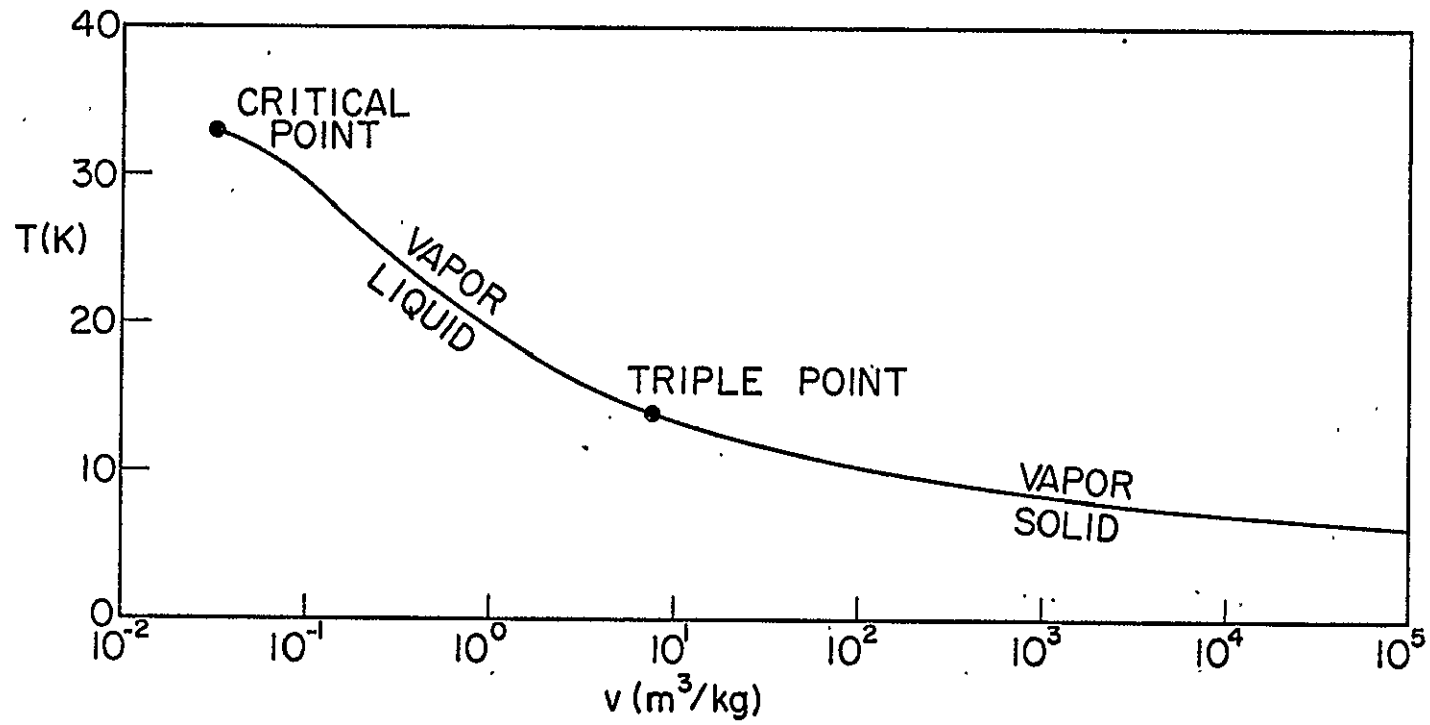
Fig. 14. H_2 saturated vapor curve.

F. Discussion

The expansion of molecular hydrogen differs from the expansion of water vapor for several reasons. Since the H_2 molecule is diatomic, its energy is partitioned into fewer degrees of freedom than the triatomic H_2O molecule. Thus, a greater portion of energy goes into the translational motion of the H_2 molecule as indicated by the higher specific heat ratio for H_2. Also for a given temperature, H_2 molecules have higher average velocities than the H_2O molecules because of the molecular weight difference. The larger values of specific heat ratio and mean thermal velocity for H_2 results in a higher expansion and cooling rate over H_2O. This is evident from a comparison of the time marks for the H_2 (Figure 13) and H_2O (Figure 8) expansions.

Condensation of H_2 is improbable because of the extremely low values of saturated vapor temperature (Figure 14). Since no latent heat of vaporization is released, the expanding H_2 gas temperature drops to a very low value before heating by atmospheric collisions occurs (Figure 13). Of the four most reactive gases (H_2, H_2O, CO_2 and NO_2), molecular hydrogen is the only one which does not condense appreciably after release.

Chapter IV

DIFFUSION IN A NON-UNIFORM, CHEMICALLY REACTIVE ATMOSPHERE

Diffusion is the statistical process by which particles intermingle as a result of their random motion. Diffusive motion of a gas is a function of the thermal velocity and the collision frequency of the gas molecules. The diffusive migration of gas molecules results from gradients of concentration or temperature.

A. Diffusion in a uniform Atmosphere

Diffusion in a uniform, one-dimensional medium can be modeled as a random walk. Consider a particle released at the origin of a one-dimensional coordinate axis at time zero (Figure 1). Imposed upon the

PARTICLE AT x=O WHEN t=O
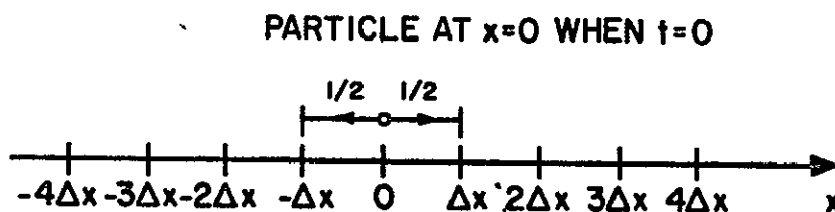
Fig. 1. One-dimensional random walk model of diffusion.

particle is probability one-half of decreasing its position by Δx in time Δt and probability one-half of increasing its position by Δx in time Δt. This is a model of a medium with mean free path Δx and mean collision time t. If $U(x,t)$ is the probability that the particle is at position x at time t, the following difference equation results from the law governing the motion of the particle:

$$U(x,t+ t) = 1/2 \ U(x- x,t) + 1/2 \ U(x+ x,t) \qquad (1)$$

The initial condition is $U(x=0, t=0) = 1$ and $U(x \neq 0, t=0) = 0$. The temporal change in probability at a fixed location is written with the aid of (1).

$$\frac{U(x,t+\Delta t) - U(x,t)}{\Delta t} = \frac{\Delta x^2}{2\Delta t} \frac{U(x+\Delta x,t) - 2U(x,t) + U(x-\Delta x,t)}{\Delta x^2} \qquad (2)$$

Taking the limit of $\Delta x \to 0$ and $\Delta t \to 0$ while keeping the quantity $\frac{\Delta x^2}{2\Delta t}$ constant gives

$$\frac{\partial U(x,t)}{\partial t} = D \frac{\partial^2 U(x,t)}{\partial x^2} \qquad (3)$$

where the following definitions of partial derivatives are used

$$\lim_{\Delta t \to 0} \frac{U(x,t+\Delta t) - U(x,t)}{\Delta t} = \frac{\partial U}{\partial t}$$

and

$$\lim_{\Delta x \to 0} \frac{U(x+\Delta x,t) - 2U(x,t) + U(x-\Delta x,t)}{\Delta x^2} = \frac{\partial^2 U}{\partial x^2}$$

If many particles are released, the single-particle probability function $U(x,t)$ is equivalent to the macroscopic multi-particle concentration. Thus, (3) is the simple diffusion equation for flow in a one-dimensional uniform medium. D, the diffusion coefficient with dimensions of length squared per time, is the square of the distance between collisions divided by twice the time between collisions. In the atmosphere, the distance between collisions is the mean free path λ_a, and the time between collisions is the reciprocal of the mean collision frequency ω_a. The atmospheric diffusion coefficient is written as

76

$$D = \frac{\Delta x^2}{2\Delta t} = \frac{\lambda_a^2 \omega_a}{2} \tag{4}$$

The mean free path is related to the collision frequency by

$$\lambda_a \omega_a = c_a = \sqrt{2kT_a/m_a} \tag{5}$$

where c_a is the mean thermal velocity, T_a the atmospheric temperature and m_a the molecular mass. The diffusion coefficient becomes

$$D = \frac{kT_a}{m_a \omega_a} \tag{6}$$

In three dimensions, the diffusion equation (3) is

$$\frac{\partial n}{\partial t} = D\left[\frac{\partial^2 n}{\partial x^2} + \frac{\partial^2 n}{\partial y^2} + \frac{\partial^2 n}{\partial z^2}\right] \tag{7}$$

where $n(x,y,z,t)$ is the partial number-density. The release of a large number of particles at a point implies an impulsive initial condition.

$$n(x,y,z,o) = N_0 \, \delta(x,y,z)$$

where N_0 is the total number of particles released. With this boundary condition, the solution to the 3-dimensional diffusion equation is

$$n(x,y,z,t) = \frac{N_0}{(4\pi Dt)^{3/2}} \, e^{-\frac{(x^2+y^2+z^2)}{4Dt}} \tag{8}$$

77

Substituting the mean free path and collision frequency factors for D (4) and using the nondimensionalized time and distance of the previous chapter (i.e., $t* = t\omega_a$ and $x* = x/\lambda_a$) results in

$$n(\vec{x}*,t*) = \frac{N_o}{\lambda_a^3(2\pi t*)^{3/2}} \exp[-\vec{x}*^2/(2t*)] \qquad (9)$$

This is identical to the asymptotic expression for a uniform sphere expanding into an ambient atmosphere after the released gas has thermalized with the atmosphere (Chapter III, Equation (82)).

B. General Diffusion Equation

The flow of the injected gas has been calculated neglecting the effects of gravity, of a non-uniform atmosphere and of chemical reactions. These effects are included by solving a general diffusion equation derived from the equations of continuity and momentum for the diffusing gas cloud.

The equation of continuity for a neutral gas is

$$\frac{dn}{dt} + \nabla \cdot [n\vec{v}] = p - L \qquad (10)$$

where n is the relased gas density, $\vec{v}$ the velocity of the gas, P the production or source term and L the loss term. The continuity equation is derived from the Boltzmann equation under the assumption of continuum flow.

The velocity of the gas is given by the momentum equation

$$\frac{d\vec{v}}{dt} = \vec{g} - k\frac{\nabla(nT)}{nT} + \omega_a(\vec{u}_a - \vec{v}) \tag{11}$$

where $\vec{g} = -g\hat{a}_z$ is the acceleration due to gravity, $\hat{a}_z$ the vertically upward unit vector, T the gas temperature, $\vec{U}_a$ the neutral drift velocity, and ω_a the collision frequency. For velocity fluctuations with time constants greater than a mean collision time, accelerations can be neglected, $dv/dt = 0$, and velocity is found to be

$$\vec{v} = -D\left[\frac{\nabla(nT)}{nT} + \frac{\hat{a}_z}{H_g} + \vec{u}_a\right] \tag{12}$$

where D is the diffusion coefficient, and $H_g = kT/mg$ is the gas scale height. The velocity of the gas is composed of two parts: the diffusion velocity produced by concentration and thermal gradients and the drift velocity due to the motion of the bacground atmosphere.

The general diffusion equation is found by substitution of (12) into (10)

$$\frac{\partial n}{\partial t} = \nabla \cdot \left[D\left(\frac{\nabla(nT)}{nT} + \frac{n\hat{a}_z}{H_g}\right) - n\vec{u}_a\right] + P - L \tag{13}$$

This reduces to the simple diffusion equation (7) if D and T are constant, and gravity, atmospheric motion, production and loss are neglected. Equation (13) will be solved analytically but first the properties of the diffusion gas cloud are discussed.

The expansion velocity of the diffusing cloud is one-half that of the cloud expanding into a vacuum. In a uniform stationary atmosphere, the expansion velocity given by (12) becomes

$$\vec{v} = -D \, \frac{\nabla n}{n} \tag{14}$$

Substitution of the spherical diffusive expansion solution, Eq. (8) yields

$$\vec{v} = \frac{\vec{r}}{2t} \tag{15}$$

to be compared with the vacuum-like expansion velocity $\vec{v} = \vec{r}/t$, derived in the previous chapter.

The motion of the center of mass of the gas cloud due to gravity and atmospheric density gradients is calculated as follows. The center of mass is defined as

$$\vec{a}(t) = \frac{1}{N_0} \int_{-\infty}^{\infty} \vec{x} \, n(x,t) \, d^3\vec{x} \tag{16}$$

where $\vec{a}(t)$ is the time varying position vector of the center of mass, N_0 is the total number of gas molecules, and $\vec{x}$ is the position vector to a point in space. The velocity of the center of mass is

$$\frac{d\vec{a}}{dt} = \frac{1}{N_0} \int_{-\infty}^{\infty} \vec{x} \, \frac{\partial n}{\partial t} \, d^3\vec{x} \tag{17}$$

Using (13)

$$\frac{d\vec{a}}{dt} = \frac{1}{N_0} \int_{-\infty}^{\infty} \vec{x} \, \nabla \cdot \left[D \, \frac{\nabla n}{n} + \frac{n\hat{a}_z}{H_g} \right] d^3\vec{x} \tag{18}$$

80

$$\frac{d\vec{a}}{dt} = -\frac{1}{N_0} \int_{-\infty}^{\infty} \left[\frac{D\nabla n}{n} + \frac{n\hat{a}_z}{H_g} \right] d^3\vec{x} \tag{19}$$

Assuming vertical atmospheric density gradients of the form $n_a = n_{ao}$ $\exp(-z/H_a)$ and thus exponential variation is collision frequency with altitude ($\omega_a = \omega_{ao} \exp(-z/H_a)$ where n_a is the atmospheric density, n_{ao} is the density at $z = 0$, $H_a = kT_a/mg$ is the atmospheric scale height and ω_{ao} is the atmospheric collision frequency at $z = 0$), the diffusion coefficient is inversely proportional to the collision frequency leading to

$$D = D_{ao} \exp[z/H_a] \tag{20}$$

With this substitution, the expression for the velocity of the center of the mass becomes

$$\frac{d\vec{a}}{dt} = \hat{a}_z \left(\frac{1}{H_a} - \frac{1}{H_g} \right) \int_{-\infty}^{\infty} D(z) \frac{n(\vec{x},t)}{N_0} d^3\vec{x} = \hat{a}_z \left(\frac{1}{H_a} - \frac{1}{H_g} \right) \bar{D}(t) \tag{21}$$

where $\bar{D}(t)$ is the average value of the diffusion coefficient inside the cloud. The buoyancy of the cloud depends on the relative scale heights of the atmosphere and the released gas. If the average atmospheric gas molecule is heavier than the released gas molecule, H_a will be less than H_g and the cloud will rise. Similarly, if the cloud is composed of a gas with a larger molecular weight than the background it will fall. Thus, the familiar bulk motion of gases in the atmosphere are inherent in the solution of the diffusion equation.

C. Solution of the General Diffusion Equation for Point Gas Releases

After the injected cloud has thermalized with the ambient atmosphere, its expansion is indistinguishable from that resulting from the solution of the diffusion equation assuming a point release. In the early stages of the diffusive expansion, gravity and the atmospheric density gradients have little effect on the expansion and the solution has the spherically symmetric form of (9). When the gas expands over many atmospheric scale heights, the effects of gravity and atmospheric density gradients become noticeable.

The diffusion equation for the injected gas is written as

$$\frac{\partial n}{\partial t} = D\left[\frac{\partial^2 n}{\partial x^2} + \frac{\partial^2 n}{\partial y^2}\right] + \frac{\partial}{\partial z}\left[D\left(\frac{\partial n}{\partial z} + \frac{n}{H_g}\right)\right] - \gamma[0^+]n \qquad (22)$$

where γ is the $(0^+$, injected gas) reaction rate, and $[0^+]$ the 0^+ density. A Cartesian coordinate system, centered at the point of gas release, with the z-axis pointing vertically upward is used. Assuming an exponential atmosphere yields $D(z) = D_0 \exp(z/H_a)$ where D_0 is the diffusion coefficient at the point of gas release $(z = 0)$, and H_a the atmospheric scale height. The last term in (22) represents the chemical depletion of the injected gas by reactions with the ionospheric 0^+. This term is negligible compared with the diffusion terms which dominate the gas behavior until the cloud is dissipated to an insignificant density level. The chemical loss term has appreciable effects only during the last stage of the gas expansion when the ionosphere is well on its way to recovery. Therefore, this small term is replaced with an approximation that greatly simplifies

the solution of (22). A constant $\alpha = \gamma[0^+]$ is substituted for $\gamma[0^+]$ where $<[0^+]>$ is the average 0^+ density in the unperturbed ionosphere.

After substitution for the diffusion coefficient and the chemical loss term, the diffusion equation becomes

$$\frac{\partial n}{\partial t} = \frac{D_0 e^{z/H_a}}{r} \frac{\partial}{\partial r}\left(r\frac{\partial n}{\partial r}\right) + \frac{\partial}{\partial z}\left[D_0 \ e^{z/H_a} \ \frac{\partial n}{\partial z} + \left(\frac{n}{H_g}\right)\right] - \alpha n \qquad (23)$$

Cyclindrical coordinates are used where $r^2 = x^2 + y^2$. The initial condition is $n(x,y,z,0) = N_0 \delta(x,y,z)$. The analytic solution of this equation without the chemical loss term is given by Yu and Klein [1964]. The solution is outlined as follows: Eq. (23) is Fourier transformed with respect to the variables x and y yielding

$$4\xi^2 \frac{\partial N_f}{\partial t} = \frac{D_0 \xi^2}{H_a^2} \frac{\partial^2 N_f}{\partial \xi^2} - \left(\frac{D_0}{H_a^2} + \frac{2D_0}{H_a H_g}\right)\xi \frac{\partial N_f}{\partial \xi} + 4D_0\left[\frac{1}{H_a H_g} - (2\pi)^2(f_x^2 + f_y^2) - \frac{\alpha \xi^2}{D_0}\right]N_f$$

$$(24)$$

where $\xi = \exp(-z/2 H_a)$, f_x and f_y are the transform variables corresponding to x and y, respectively, and N_f is the Fourier transform of n. This equation is Laplace transformed with respect to the variable t.

$$\xi^2 \frac{\partial^2 N_L}{\partial \xi^2} - \left(1 + \frac{2H_a}{H_g}\right)\frac{\xi \partial N_L}{\partial \xi} + 4\left[\frac{H_a}{H_g} - H_a^2(f_x^2 + f_y^2)(2\pi)^2 - \frac{H_a^2 \xi^2}{D_0}(p+\alpha)\right]N_L$$

$$= \frac{-2\xi^2 H_a N_0 \ \delta(\xi-1)}{D_0} \qquad (25)$$

83

where p is the transform variable corresponding to t, and $\bar{N}_L$ the Laplace transform of N_f. The homogeneous part of (25) is of the form

$$g^2 \frac{\partial^2 f}{\partial g^2} + ag \frac{\partial f}{\partial g} + (b+cg^2)\, f = 0$$

which has the Bessel function solution

$$f(g) = g^{\frac{1-a}{2}}\, Z_\nu(\sqrt{c}\,g) \qquad \text{[Kamke, 1959]}$$

where $\nu = 1/2 \sqrt{(1-a)^2 - 4b}$ and Z_ν is any linear combination of Bessel functions of the first kind $[J(\cdot)]$ and the second kind $[Y(\cdot)]$. The solution of (25) with the boundary conditions $N_L \to 0$ as $\xi \to 0$ or ∞ is

$$N_L(f_x,f_y,\xi,p) = \left(\frac{H_a N_0}{D_0}\right)\xi^{1+\frac{H_a}{H_g}}\, \pi i\left[J_\nu(2i\sqrt{p+\alpha}\,\xi)\, H_\nu^{(1)}(2i\sqrt{p+\alpha})\, \theta(1-\xi) \right.$$

$$\left. + J_\nu(2i\sqrt{p+\alpha}\, H_\nu^{(1)}(2i\sqrt{p+\alpha}\,\xi)\, \theta(\xi-1) \right]$$

(26)

where $\nu = \left[\left(\frac{H_a}{H_g} - 1\right)^2 + 4 H_a^2 (f_x^2 + f_y^2)\, (2\pi)^2\right]$, $H^{(1)}$ is the Hankel function of the first kind and $\theta(x)$ is zero for negative x and unity for positive x. The inverse Laplace transform of (26) is

$$N_f(f_x,f_y,\xi,p) = \frac{N_0 H_a}{tD_0}\, \xi^{1+a}\, \exp\left[\frac{-(\xi^2+1)H_a^2}{tD_0} - \alpha t\right] I_\nu\left(\frac{2\xi H_a}{tD_0}\right) \qquad (27)$$

84

where $a = H_a/H_g$ and $I(\cdot)$ is the modified Bessel function of the first kind. Applying the inverse Fourier transform one obtains

$$n(r,\xi,t) = \frac{N_o H_a}{t D_0} \, \xi^{1+a} \, \exp\left[-\left(\frac{\xi^2+1}{tD_0}\right) H_a^2 - \alpha t\right] 2\pi \int_0^\infty I_\nu\left(\frac{2\xi H_a^2}{tD_0}\right) J_0(2\pi r\rho)d\rho \tag{28}$$

where $\nu^2 = (a-1)^2 + (4\pi H_a \rho)^2$

The integral in (28) can be evaluated numerically, but during the time interval of interest, the Bessel function inside the integral can be closely approximated by $I_\nu(q) \simeq \dfrac{e^q}{\sqrt{2\,q}} e^{-\nu^2/eq}$. Justification for this approximation is based on examination of the following series for the modified Bessel function

$$I_\nu(q) = \frac{e^q}{\sqrt{2\pi q}} \int_{m=0}^\infty \frac{(8q)^{-m}}{m!} \prod_{k=1}^m \left[(2k-1)^2 - 4\nu^2\right] \tag{29}$$

Ignoring the product index,

$$I_\nu(q) \simeq \frac{e^q}{\sqrt{2\pi q}} \sum_{m=0}^\infty \frac{(-\nu^2/2q)^m}{m!} = \frac{e^q}{\sqrt{2\pi q}} e^{-\nu^2/2q} \tag{30}$$

as required. With this approximation, the expression for the released gas density becomes

$$n(x,y,z,t) = \frac{N_o}{(4\pi D_0 t)^{3/2}} \exp - \left[z\left(\frac{3}{4H_a} + \frac{1}{2H_g}\right) - \frac{H_a^2[1-\exp(-z/2H_a)]^2}{D_0 t}\right.$$

$$\left. - \alpha t - \frac{(x^2+y^2)e^{-\frac{z}{2H_a}}}{4D_0 t} - \left(\frac{1}{H_a} - \frac{1}{H_g}\right)^2 \frac{D_0 t \exp(z/2H_a)}{4}\right] \tag{31}$$

This expression gives values of n within a factor of two of those given by (28) for times less than half an hour under typical F2-region conditions. In the limit as time approaches zero, (31) reduces to

$$n(x,y,z,t) = \frac{N_0 \, e^{-\frac{(x^2+y^2+z^2)}{4D_0 t}}}{(4\pi D_0 t)^{3/2}}$$

which is the spherically symmetric expression for expansion into a uniform atmosphere.

The effects of gravity and the non-uniform atmosphere are seen in the time sequence of gas expansion in Figure 2. The time unit is defined as H_a^2/D_0 at the point of gas injection. The isopycnic contours containing the center of the cloud are plotted at .01, .1, and 1 unit times. The contours are nearly circular for cloud diameters less than one scale height. When the gas expands over many scale heights, the effects of atmospheric density variations becomes apparent. The increase of the diffusion coefficient with height produces rapid transport of gas molecules into high altitudes. The flow at low altitudes is impeded by the dense atmosphere and a hard bottom forms on the cloud. The location of the peak gas density falls with time because of the rapid diffusion out of the top of the cloud.

The atmospheric scale height and injected gas diffusion coefficient are determined from atmospheric and injected gas parameters. The F-region atmosphere contains, in order of abundance, monatomic oxygen, diatomic nitrogen, and diatomic oxygen. Because of the variations in the relative concentrations of these neutral species,
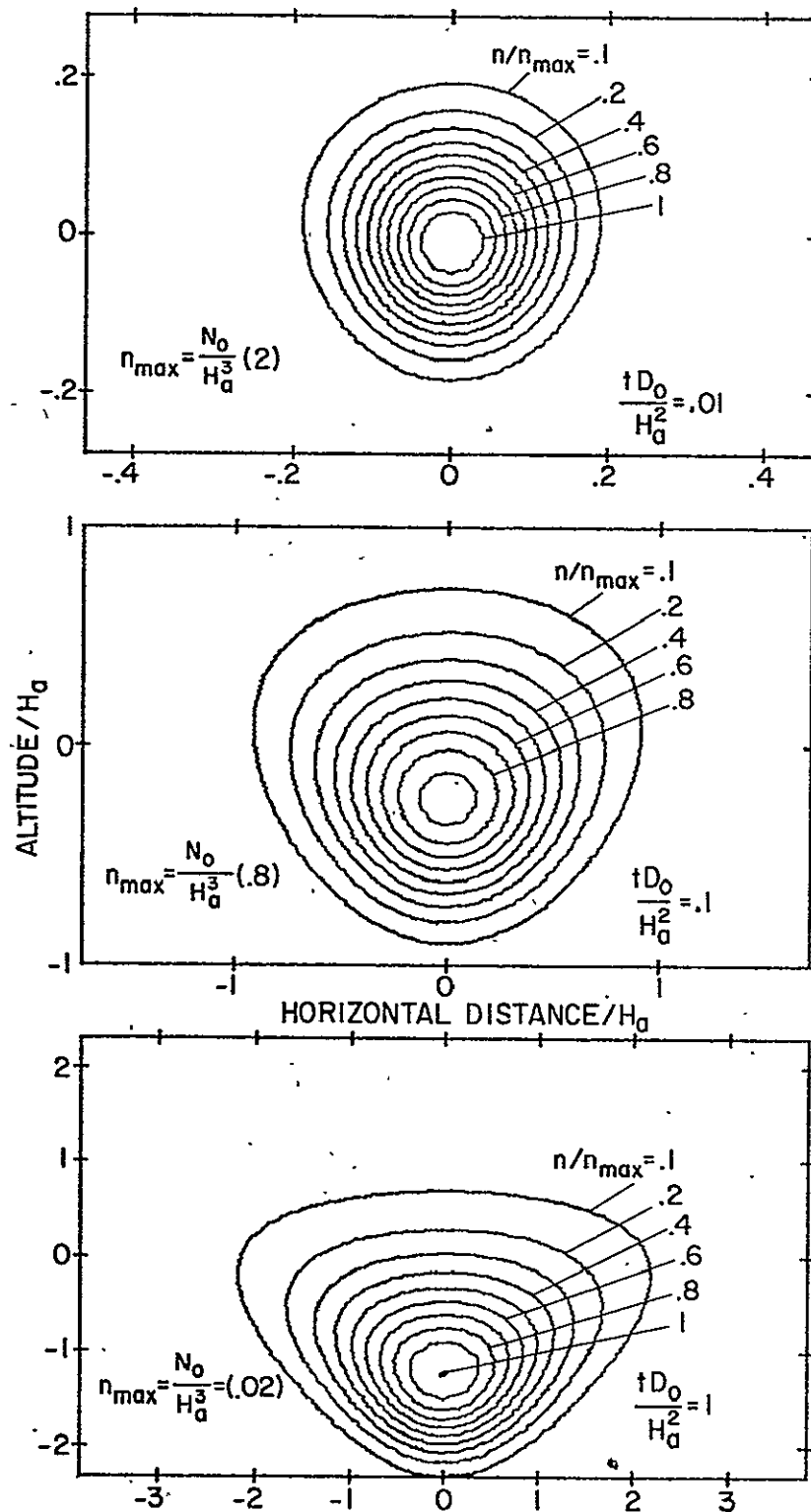
Fig. 2. Expansion of a gas cloud in a nonuniform atmosphere. The cloud becomes highly nonspherical after expanding over many scale heights. An expanding H_2 cloud containing N_0 molecules is released into an atmosphere with scale height H_a. The diffusion coefficient at the release point is D_0.

the scale height varies with altitude. In the injected gas expansion
model, the scale height at the point of injection is used. The
scale height is given by

$$H_a = .848(1 + h_o/R_e)^2 \ T/M$$ (32)

where h_o is the altitude to the point of injection, R_e the earth's
radius, T the neutral temperature, and M the average molecular
weight. At 300 km altitude, the scale height is approximately 50 km.

The diffusion coefficient at the gas release point is dependent
on the local temperature, and the composition of the injected and
background gases. A reasonable expression for binary gas mixture
diffusion coefficients is of the form

$$D_{12} = AT^s/n$$ (33)

where D_{12} is the mutual diffusion coefficient for the binary
mixture of gases 1 and 2, A a function only of the diffusing species,
T the neutral temperature, s a species dependent exonent, and n
the sum of the densities of the two diffusing gases. When the
injected gas is in a state of diffusion, its density is less than
the ambient atmospheric density. The density used in the diffusion
coefficient is taken to be that of the background gas.

The constants A and s, determined from experimental data (when
available) or from kinetic theory, are given in Table 1 for selected
reactive injectants.

TABLE 1

Diffusion Coefficients $D = AT^S/n$

| System | N_2 | | O_2 | | O | |
	A	s	A	s	A·	s
N_2	--	--	8.29[16]	.724	9.69[16]	.774
O_2	8.29[16]	.724	--	--	9.69[16]	.774
N_2O	2.34[17]	.5*	2.37[17]	.5*	5.87[17]	.5*
CO_2	6.58[16]	.752	5.77[16]	.749	5.87[17]	.5*
NO_2	2.31[17]	.5*	2.35[17]	.5*	8.84[17]	.5*
H_2	2.8 [17]	.740	3.06[17]	.732	2.97[18]	.5*
H_2O	2.04[17]	.632	2.02[17]	.632	8.46[17]	.5*

*Theoretical Values   Note: [x] means 10^x

The measured values of the diffusion constants are from Mason and Marrero (1970).

The theoretical values of the diffusion coefficient are based on the model of rigid, elastic spherical molecules. This model leads to the parameters

$$A = .75/(d_1+d_2)^2 \; \sqrt{2kN(m_1+m_2)/(\pi m_1 m_2)} \quad \text{and} \quad s = .5$$

[Chapman and Cowling, 1970].

where d_1 and d_2 are the molecular diameters of the binary diffusion system, m_1 and m_2 the mass of the molecules, and k Boltzmann's constant. The theoretical temperature dependence exponent $s = .5$ differs from the typical measured exponent $s = .7$ because of

the deviation from the assumed elastic-sphere molecular encounters. The diffusion coefficient for a gas in a multi-species mixture is given as

$$D_k = 1/\sum_j D_{jk}^{-1} \qquad (34)$$

where D_{jk} is the binary diffusion coefficient for the jth and k^{th} species. Typical values of diffusion coefficients for H_2 and H_2O in the 300 km atmosphere are $D(H_2) = 1.1 \times 10^{11}$ cm^2/sec and $D(H_2O)$ $= 3.4 \times 10^{10}$ cm^2/sec and $D(H_2O) = 3.4 \times 10^{10}$ cm^2/sec.

D. Solution of the Diffusion Equation for a General Gas Source Term

The solution of the linear diffusion equation (23) for any initial gas release may be expressed in terms of the solution for a point source. The linear diffusion equation with source term $\beta(x,y,z,t)$ is written as

$$\frac{\partial n}{\partial t} = D(z) \left[\left(\frac{\partial^2 n}{\partial x^2}\right) + \left(\frac{\partial^2 n}{\partial y^2}\right) \right] + \frac{\partial}{\partial z} \left[D(z) \left(\frac{\partial n}{\partial z} + \frac{n}{H_y}\right) \right] - \alpha n + \beta(x,y,z,t)$$

$$(35)$$

the source term for an instantaneous point release, $\beta(x,y,z,t) = \delta(x,y,z)\delta(t)$, represents the gas injection at point $(x,y,z) = (0,0,0)$ at time $t = 0$. The solution with this impulsive term is called the Green's function for (35). The solution for a general source term is written as

$$n = \int_0^t \iiint_{-\omega}^{\infty} \beta(\alpha,\beta,\lambda,\gamma) \ G(x-\alpha, \ y-\beta, \ z-\lambda, \ t-\gamma) \ d\alpha d\beta d\lambda d\gamma \qquad (36)$$

where $G(x,y,z,t)$ is the Green's function.

As an example, consider a moving source, such as a rocket, continuously releasing gas at a constant rate over m a period of time lasting t_μ seconds. Such a source may be modeled as an infinite sequence of uniform spherical gas releases. After the injected gas has thermalized with the atmosphere, each release has the form of the impulse response or Green's function solution to the diffusion equation. This model for the source term is expressed as

$$\beta(x,y,z,t) = \frac{N_0}{t_\mu} G(x-v_x t, \ y-v_y t, \ z-v_z t, \ t_0) \quad \text{for} \quad 0 \le t \le t_\mu \qquad (37)$$

where v_x, v_y, v_z are the x,y, and z components for the time dependent velocity of the source, t_μ the time duration of the source, N_0/t_μ the number of particles released per unit time and t_0 the time delay in the Green's function to account for thermalization with the atmosphere and the finite width of the emitting source. If t_0 is set to zero, the source function is a moving impulse.

$$\beta(x,y,z,t) = \frac{N_0}{t_\mu} \delta(v-v_x t, \ y-v_y t, \ z-v_z t) \quad \text{for} \quad 0 < t < t_\mu \qquad (38)$$

If the released gas distribution is identical to the Green's function response to an impulsive release some t_0 seconds before, the release will expand as if it was created by a point release at time t_0. Mathematically this is expressed in terms of the following theorem:

If $\beta(x,y,z,t) = G(x,y,z,t_0)\ \delta(t)$, then

$$n(x,y,z,t) = \int_0^t \iiint_{-\infty}^{\infty} G(\alpha,\beta,\lambda,t_0)\ \delta(\gamma)\ G(x-\alpha,\ y-\beta,\ z-\lambda,\ t-\gamma)\ d\alpha d\beta d\lambda d\gamma$$

$$= \iiint_{-\infty}^{\infty} G(\alpha,\beta,\lambda,t_0)\ G(x-\alpha,\ y-\beta,\ z-\lambda,\ t)\ d\alpha d\beta d\lambda d\gamma$$

$$= G(x,y,z,\ t+t_0)$$

This theorem is used in the derivation of the gas expansion for a moving source.

The moving source model, (37), is substituted into (36) yielding the expression

$$n(x,y,z,t) = \frac{N_0}{t_\mu} \int_0^{\min(t,t_\mu)} \iiint_{-\infty}^{\infty} G(\alpha-v_x\gamma,\ \beta-v_y\gamma,\ z-v_z\gamma,t_0)$$

$$\tag{40}$$

$$G(x-\alpha,\ y-\beta,\ z-\lambda,\ t-\gamma)\ d\alpha d\beta d\lambda d\gamma$$

where $\min(t,t_\mu)$ is the minimum value of time t and t_μ. By Eq. (39),

$$n(x,y,z,t) = \frac{N_0}{t_\mu} \int_0^{\min(t,t_\mu)} G(x-v_x\gamma,\ y-v_y\gamma,\ z-v_z\gamma,\ t_0+t-\gamma)\ d\gamma \tag{41}$$

The expression for the diffusive expansion of a point release in a non-uniform, reactive atmosphere, (31), may be used as Green's function but for simplification of the mathematics consider diffusion in a uniform atmosphere. Green's function for diffusion in a uniform non-reactive atmosphere is

92
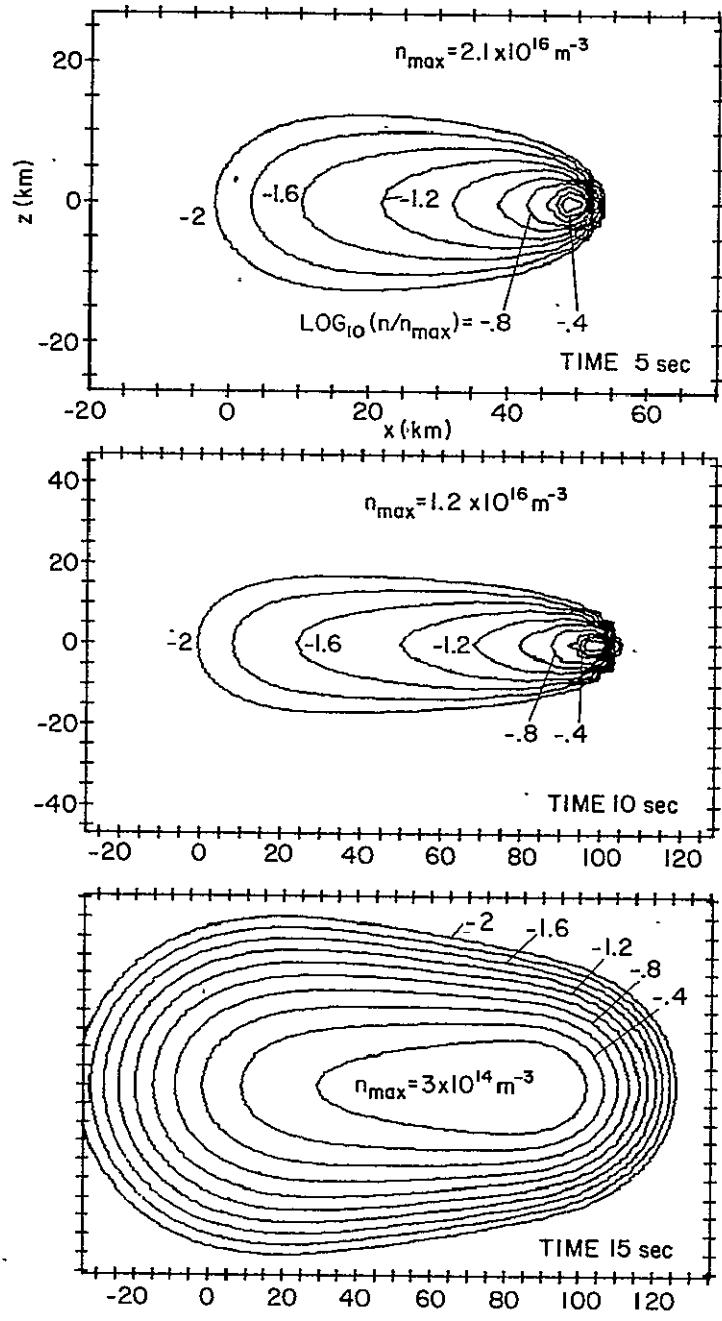
Fig. 3. Density contours for a source of gas moving at 10 km/sec continuously releasing gas at a rate of 10 kg/sec. Release starts at zero seconds and shuts off at ten seconds.

93

$$.G(x,y,z,t) = \exp[-(x^2+y^2+z^2)/(4Dt)]/(4\pi Dt)^{3/2} \qquad (42)$$

The solution for diffusive expansion of a moving source into a uniform atmosphere becomes

$$n(x,y,z,t) = \frac{N_o}{t_\mu} \int_0^{\min(t,t_\mu)} \exp[-(\vec{x}-\vec{v}\gamma)^2/4D(t_o-t-\gamma)]/]4\pi D(t_o+t-\gamma)]^{3/2} d\gamma$$

$$(43)$$

The diffusive expansion of a rocket plume in a uniform atmosphere is illustrated in Figure 3. The rocket travels horizontally, from left to right with a constant speed of 10^4 m/sec releasing H_2 at a rate of 10/kg/sec. The gas release lasts 10 seconds. The isopycnic contours along the rocket trajectory are shown at 5, 10 and 15 seconds after initial gas release. While the rocket is releasing gas, a high concentration resides near the rocket nozzle (Figure 3(a) and (b)). After the release is terminated, the concentration is more uniformly distributed along the trajectory (Figure 3(c)). In a uniform atmosphere, the exhaust gas distribution approaches a uniform sphere in the long-time limit.

E. Diffusion of Charged Particles

The flow of ions and electrons is affected by magnetic fields, electric fields, density gradients, and collisions. Charged particles are constrained to move along magnetic field lines if magnetic forces are stronger than collisional forces. In the F-region ionosphere, diffusive flow of plasma is so constrained.

94

The plasma velocity along geomagnetic field lines is

$$v = -D \left[\frac{\partial \, \ell n(n_p T_p)}{\partial s} + \frac{\sin I}{H_p} \right] + v_0 \qquad (44)$$

where n_p is the ion or electron density, T_p is the plasma temperature $= (T_e + T_i)/2$, H_p is the plasma scale height $= 2T_p k/(mg)$, I is the magnetic field dip angle, s is the distance along the magnetic field line, D is the effective ambipolar diffusion coefficient $= 2kT_p/(m\omega)$ and v_D is an externally·imposed drift velocity.

The continuity equation for ionization trapped on magnetic field lines is

$$\frac{\partial n_p}{\partial t} = - \frac{\partial (n_p v)}{\partial s} + P - L \qquad (45)$$

The field line path is related to the vertical axis coordinate by $s = z/\sin I$. The diffusion equation is found to be

$$\frac{\partial n_p}{\partial t} = \frac{\partial}{\partial z} \left[\sin^2 I \; D \; n_p \left(\frac{\partial \log_e (n_p T_p)}{\partial z} + \frac{1}{H_p} \right) - n_p \sin I \; v_D \right] + P - L$$

$$(46)$$

where L represents plasma loss due to recombination or charge exchange (Chapter II). It should be emphasized that the coordinate z is the vertical distance to a point on a given magnetic field line and the derivative with respect to z is taken along this line.

The interaction between the injected gas and the ionospheric plasma is represented by the coupled differential equations (22) and

(46). The injected gas density is depleted by expansion and chemical react on with the F-region O^+. If chemical depletion is small, (31) is used. Equation (46) can either represent depletion of O^+ by the injected gas or variation in the density of the minor ion produced by reactions with O^+ and the injected gas. Before these equations can be solved, a description of the ion, electron, and neutral temperatures must be obtained.

F. Discussion

H_2 has a higher diffusive expansion rate than H_2O because of the relative low mass and collisional cross section of the hydrogen molecule. The H_2 diffusion coefficient is 23 times the H_2O diffusion coefficient for expansion of either gas in the same atmosphere.

The comparatively rapid expansion of hydrogen may lead to difficulties in producing a desired reduction in the F-region ionization. Because the lighter molecules have higher expansion velocities, the concentration of light gases rapidly decreases and less localized chemical reaction occurs. Consequently more molecules must be released for a light, rapidly expanding gas than for a heavy, slowly expanding gas to produce the same depletion at a fixed point in space.

If a strong localized depletion of the ionosphere is desired, H_2O injection may be preferable to H_2 injection--provided the condensation effects discussed in Chapter III are tolerable.

Chapter V

THERMAL BEHAVIOR OF THE DEPLETED IONOSPHERE

The F-region thermal structure is characterized by the neutral, ion and electron temperatures. The relationship between these temperatures is determined by the heat source into and the collisional interaction between the neutral, ion and electron gas species. Each of these gases acts as a heat source or sink for the other gases.

A. Thermal Structure of·the Neutral Atmosphere

Because the neutral gas in the F-region is many orders of magnitude more dense than the plasma in this region, its thermal structure is independent of the ion or electron thermal structure. The main heat source for the neutral gas is solar ultraviolet radiation. The photoabsorption by neutrals may produce excited gas molecules which thermalize by collisions with other neutrals. The absorption of ultraviolet may photoionize ·instead of excite the neutrals as discussed in Chapter 1. Alternate sources of neutral heating are Joule heating by electric currents and tidal dissipation of energy.

Cooling of the neutral atmosphere is either by conductive or radiative processes. Heat flows by conduction from the high temperature rarified upper atmosphere to the cooler lower atmosphere. The local heat conductivity is approximately proportional to the temperature to the .7 power [Banks and Kockarts, 1973]. Emission of photons by excited neutral atoms results in radiative cooling of the atmosphere. Much of the radiation is emitted in the infrared spectrum. The

effectiveness of cooling by the release of optical energy is reduced by re-absorption of infrared by the atmosphere.

Because of the complexities and uncertainties of the physical processes determining the atmospheric temperature profile, an empirical model is used in this work.

$$T = T_\infty - [T_\infty - T(z_0)] \exp[-\alpha\phi] \qquad \text{[Antoniadis, 1976]} \qquad (1)$$

where T_∞ is the exospheric temperature, $T(z_0)$ is the temperature at a lower boundary at altitude z_0, α is a constant determining the shape of the curve and $\phi = (R+z_0)(z-z_0)/R+z)$ is the geopotential height given in terms of the Earth's radius R and altitude z. Solving the steady state diffusion equation with this temperature profile results in

$$n_i = n_i(z_0)\exp(\alpha\phi) \left[\frac{T(z_0)}{T_\infty[\exp(\alpha\phi) - 1] + T(z_0)} \right]^{1+\gamma_i}$$

where $\gamma_i = 1.43\, m_i/\alpha T_\infty$, n_i is the concentration and m_i is the molecular weight of the ith neutral constituent (i.e., N_2, O_2, or O). The neutral temperature and concentration profiles remain essentially unchanged throughout the period of ionospheric chemical modification.

B. Thermal Structure of the Electron Gas

The electron temperature in the depleted region is significantly perturbed as a result of the release of reactive gases. The electron

gas heat source and cooling processes are significantly affected in the region of reduced plasma density.

The heat balance equation for electrons is expressed as

$$\frac{3}{2} kn_e \frac{\partial T_e}{\partial s} + \frac{3}{2} n_e kv \frac{\partial T_e}{\partial s} + n_e kT_e \frac{\partial v}{\partial s} - \frac{\partial}{\partial s}\left(\lambda \frac{\partial T_e}{\partial s}\right) = \bar{Q} - \bar{L} \qquad (2)$$

where s is the coordinate parallel to the magnetic field line, n_e the electron concentration, T_e the electron temperature, λ the electron thermal conductivity, $\bar{Q}$ the heat energy input, and $\bar{L}$ the energy loss due to heat transfer to other species. One-dimensional heat flow along magnetic field lines may be assumed in regions where the ratio of collision frequency to gyro frequency is small. This condition is satisfied in the ionosphere above 150 km altitude. The energy transport terms due to convection $\left(\frac{3}{2} nkv \frac{\partial T_e}{\partial s}\right)$ and compression $\left(nkT_e \frac{\partial v}{\partial s}\right)$ are often neglected in modeling of the unperturbed ionosphere because they are usually small in comparison with the heat production and loss terms. However, these terms must be considered in modeling of the depleted ionosphere because of the large fluxes of plasma into the ionospheric hole.

The electron thermal conductivity is determined by particle collisions. In a fully ionized plasma, the conductivity is dependent on electron-ion collisions and is given by

$$\lambda = 7.7 \times 10^5 \, T_e^{5/2} \quad \text{ev cm}^{-1} \text{ sec}^{-1} \text{ K}^{-1} \qquad (3)$$

This expression provides an adequate description of the conductivity in the unperturbed ionosphere. In the weakly ionized plasma in the

depleted region, electron-neutral collisions become important and a more general expression must be considered.

$$\lambda = \frac{7.7 \times 10^5 \, T_e^{5/2}}{1 + 3.22 \times 10^4 \left(\frac{T_e^2}{n_e}\right) \sum_k n_k \bar{Q}_D} \tag{4}$$

where n_k and Q_D are the density and collision cross section of the kth neutral species. The electron thermal conductivity is substantially reduced in the ionospheric hole.

During the day, energy is transferred to the electron gas by collisions with photoelectrons. Photoelectrons are produced by photoionization of the neutral gas. Expressions for photoelectron heating are given by Swartz and Nisbet [1972]. The amount of heat energy transferred from photoelectrons to the electron gas is less in the depleted region than in the unperturbed ionosphere. This results from a larger fraction of the photelectron energy being transferred to the ions and neutrals. Other sources of energy input to the electron gas, such as Joule heating, are neglected in this work.

The main loss of heat by the electron gas is energy transfer to ions. The electron-ion loss rate is given by

$$L_{ei} = 7.7 \times 10^{-6} \frac{n_e n_i [T_e - T_i]}{A_i T_e^{3/2}} \quad eV \; cm^3 \; sec^{-1} \quad [Banks \; and \; Kockarts, \; 1973] \tag{5}$$

where A_i is the ion mass in atomic units and n_i the density of the ith ion species. The total loss rate to the ions is the sum of the loss rates to each individual ion species.

The ionospheric depletion produces a simultaneous reduction of the heat input and the ion cooling rate. The cooling rate drops faster than the heat input. The depression of both the ion and electron population has a larger effect on the electron to ion cooling than on the photoelectron heating. An overall increase in electron temperature results.

Direct energy transfer from the electron gas to the neutral gas is small in the unperturbed ionosphere. Collisions with neutrals become important in the ionosphere when the ion population is significantly reduced. Cooling may result from energy transfer to atomic oxygen as given by

$$L_{e0} = 7.2 \times 10^{-18} \, n_e n(0) \, T_e^{1/2} \, (T_e - T_n) \tag{6}$$

Thermal electron collisions with the neutral gas·may produce excited atoms which will release optical radiation (see Chapter 6). Monatomic oxygen also removes heat from the electron gas through fine structure transitions represented by the reactions

$$e + O(^3p_j) \rightarrow e + O(^3p_j') \tag{7}$$
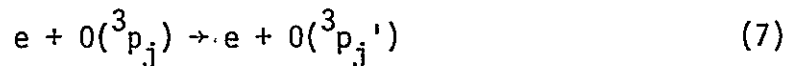
The fine structure loss is written as

101

$$L_{fs} = (5.92 - 4.68 \times 10^{-4} \, T_e) \, (9.06 + 6.57 \times 10^{-4} \, T_n)$$
$$\times 10^{-25} \, n_e n(o) \, (T_e - T_n)/T_n \text{ ergs cm}^{-3} \text{ sec}^{-1} \qquad (8)$$

[Herman and Chandra, 1969]

C. Thermal Structure of the Ion Gas

The ion temperature value is bounded by the electron and neutral temperature values. The electrons provide a heat source and the neutrals provide a heat sink for the ions. The ion heat source is identical to the electron loss given by (5). Other sources of heat input to the ion gas, such as electric fields and chemical reactions, can be neglected in the F-region ionosphere.

The cooling of the ions is dominated by collisions with neutrals--mainly atomic oxygen. The ion-neutral heat transfer is given by

$$L_{in} = 6 \times 10^{-14} \, n_i n_n \, (T_i - T_n)$$

Collisions between similar species of ions and atoms may result in cooling by resonance charge exchange. This reaction for O^+ and atomic oxygen is:

$$O^+ + O \rightarrow O + O^+ \qquad (9)$$

The charge exchange cooling rate for O^+ is given by

$$L_{ce} = n_i n_n \, 2.1 \times 10^{-14} \, (T_i + T_n)^{1/2} \, (T_i - T_n) \qquad (10)$$

The ion temperature is found by equating the heat source term to the heat loss term. This is justified because the convection, compression and conduction terms in the ion heat balance equation are negligible. Equating the source and sink terms gives

$$L_{ie} = L_{in} + L_{ce} \qquad (11)$$

Taking $(T_i + T_n)^{1/2}$ to be constant and numerically equal to 45, T_i is found to be

$$T_i = \frac{T_n + (\alpha n_e/n_n) \, T_e^{-1/2}}{1 + (\alpha n_e/n_n) \, T_e^{-3/2}} \qquad \text{where } \alpha = 6 \times 10^6 \qquad (12)$$

The ion collisional cooling rate decreases in the depleted region because of the reduction in ion density. However, the ion heating is reduced to a greater degree because of the reduction in both electron and ion populations. The overall effect is a slight reduction in ion temperature in the depleted region.

D. Summary

The release of reactive chemicals, such as hydrogen or water vapor, into the F-region ionosphere enhances recombination and thus may cause a significant depression in the local ion and electron densities accompanied by a rise in the electron temperature. This increase in electron temperature is a result of the reduction in ion cooling of the electron gas in the depleted region. During the day,

the energy input into the electron gas decreases slightly, but thermal electrons are not effectively cooled by ions in the region of reduced plasma density because the heat transfer from electrons to ions is dependent on the product of the ion and electron densities. The rise in electron temperature during the night is less dramatic because of the absence of photoelectron heating. Also, the electron thermal conductivity decreases with reduced electron densities partially insulating the region of high temperature electrons from its surroundings.

Chapter VI

SIMULATION OF THE MODIFICATION EXPERIMENT

The descriptions of the chemical, diffusive and thermal processes given in Chapters II, IV and V are combined to produce a model of the chemical ionospheric depletion. This model is used to simulate the temporal and spatial variations in plasma density and temperature resulting from the release of reactive gases. Only modification by the release of molecular hydrogen is discussed in this paper but perturbations produced by other gases may be simulated by changing the physical parameters in the perturbation part of the model.

A. Ionospheric Model

The ionospheric model incorporates the most recent F-region theory. This model has evolved over the last decade with contributions from several scientists. As more knowledge about ionospheric processes has been gained, the model has been updated. The present version of the ionospheric model is an extremely useful and sophisticated tool.

The geometry used in the model is illustrated in Figure 1. The x and y axes lie in the local surface plane of the earth. The z axis points vertically upward. The magnetic field line through the H_2 release point lies in the x-z plane and passes through the origin. The main plasma constituents along the field line are indicated in Figure 1.

The interaction of the various functional blocks in the model is shown in Figure 2. The blocks are categorized according to the processes they describe--neutral, plasma, and thermal processes--and according to the region of space they occupy--low (100-500 km) region, middle (500-3000) region, and high (> 3000 km) region. Two blocks are required to describe the extraordinary processes in the perturbed ionosphere.
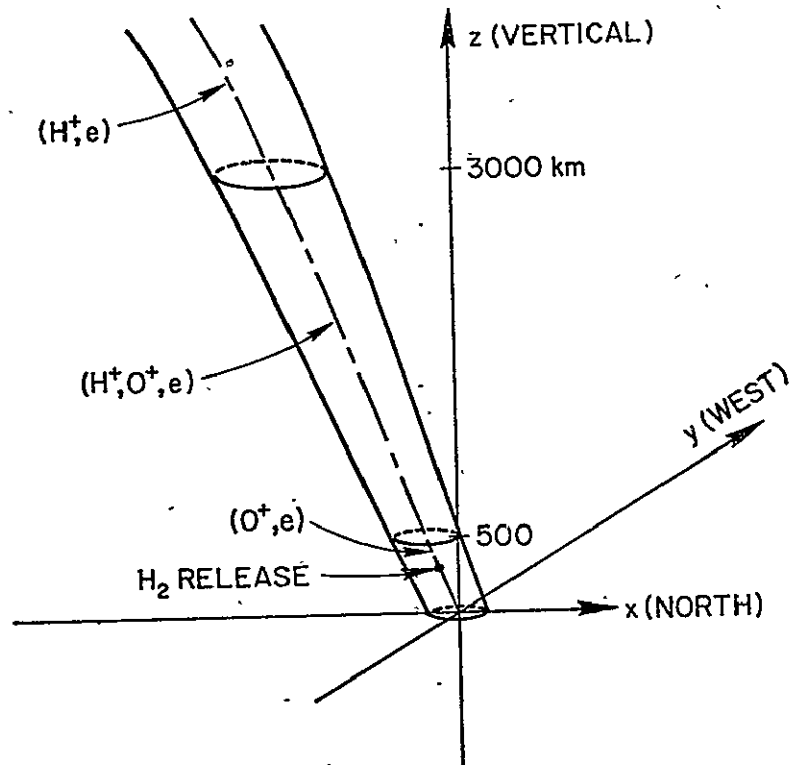
Fig. 1. Three dimensional coordinate system
used in the plasmaspheric model.

107
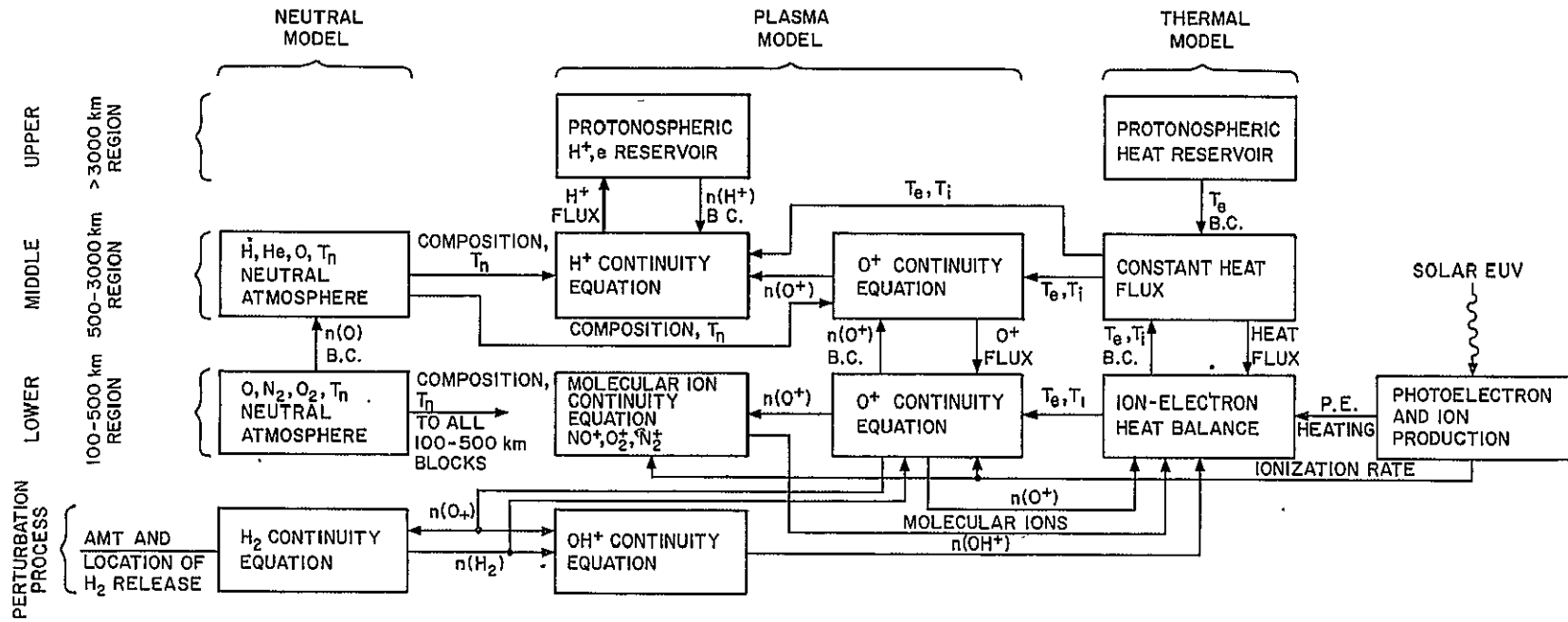
Fig. 2.   Block diagram of the model of the mid-latitude ionosphere and protonosphere used
in the simulation of the chemical modification experiment.

Starting from the high altitude region, the function of each block is discussed.

Following a procedure introduced by Park and Banks [1974, 1975], the region above 3000 km is treated as a reservoir of plasma and heat. The temperature of the protonosphere above 3000 km is assumed to remain constant. This is the upper boundary temperature. The plasma content above 3000 km varies as proton and electron fluxes flow in or out of this region. The upper boundary H^+ concentration is derived from this protonospheric content.

The plasma density between 500 and 3000 km is determined from the H^+, O^+ charge exchange reaction

$$O^+ + H \rightleftarrows O + H^+ \tag{1}$$

and from the upper H^+ boundary condition and the lower O^+ boundary condition. The electron temperature is calculated assuming constant heat flux from the upper and lower temperature boundary conditions. The model of the neutral atmosphere consists of monoatomic hydrogen, monoatomic oxygen and helium. Details of the model between 500 and 3000 km are given by Park and Banks [1974, 1975].

The 100 to 500 km region is an updated and expanded version of the model described by da Rosa [1966] and Waldman [1971]. The O^+ ion continuity equation is solved by using the 500 km flux from the middle region and chemical equilibrium at 100 km as boundary conditions. Daytime photoionization of the neutral atmosphere and charge exchange with the O^+ ion forms the basis of the molecular ion solution. During the day, photoelectrons produced by solar EUV act as the main electron gas heat source. At night, there is no photoelectron production and the electron temperature is maintained by conduction from the protono-

sphere heat reservoir. Thermal electron cooling is determined from electron to ion and electron to neutral heat transfer. The upper thermal boundary condition is heat flux. At 100 km it is assumed that the neutral and electron temperatures coincide. Plasma motion by an imposed neutral wind is included in all ion and neutral continuity equation solutions.

Two foreign constituents will be present in the modified F-region—1) the released gas and 2) the ions produced by reactions with this gas. For the molecular hydrogen release, the foreign constituents are H_2 and OH^+.

The H_2 continuity has been discussed in detail in Chapter III and in the paper by Bernhardt, Park and Banks [1975]. The interaction between the H_2 gas model and the unperturbed ionosphere model involves chemical conversion of the 0^+ ion into the OH^+ molecular ion. The low region neutral atmospheric density determines the diffusive expansion of the gas.

The solution of the OH^+ continuity equation is described in detail. This solution is typical of the procedure used in solving the other partial differential equations in the ionospheric model. The equation describing the motion of the OH^+ ion including diffusive and chemical processes is obtained from Equation (46) of Chapter IV.

$$\frac{\partial[OH^+]}{\partial t} = -\frac{\partial([OH^+]w)}{\partial z} + k_1[0^+][H_2] - k_2[OH^+]n_e \qquad (2)$$

where $n_e = [OH^+] + [0^+] + [NO^+] + [0_2^+] + [N_2^+]$, the electron density, w (the ion velocity) $= -D\left\{\frac{\partial n}{n\partial z} + \frac{1}{H_p} + \frac{\partial T_p}{T_p\partial z}\right\} + w_D$, w_D is the imposed drift, D the diffusion coefficient for OH^+ in the atmosphere, H_p the OH^+ scale height, T_p the plasma temperature $(T_e + T_i)$; k_1 and k_2 are the $(0^+,H_2)$ and (OH^+,e) reaction

rates respectively. The OH^+ diffusion coefficient is

$$D = D_{in}(1 + T_e/T_i)\sin^2 I \qquad (3)$$

where I is the magnetic dip angle and D_{in} is the ambipolar diffusion coefficient given by

$$D_{in}^{-1} (OH^+) = \frac{[O_2]}{\gamma_{O_2}T_i} + \frac{[N_2]}{\gamma_{N_2}T_i} + \frac{[O]}{\gamma_O T_i} \qquad (4)$$

The numerical values for γ_{O_2}, γ_{N_2}, and γ_O are:

$$\gamma_{O_2} = 7.62 \times 10^{15} \ cm^{-1} \ sec^{-1} \ K^{-1}$$

$$\gamma_{N_2} = 7.42 \times 10^{15} \ cm^{-1} \ sec^{-1} \ K^{-1}$$

$$\gamma_O = 1.25 \times 10^{16} \ cm^{-1} \ sec^{-1} \ K^{-1}$$

With the above substitutions, the OH^+ continuity equation is written in the form

$$\frac{\partial n}{\partial t} = D\frac{\partial^2 n}{\partial z^2} + A \frac{\partial n}{\partial z} + Bn + Cn^2 + P \qquad (5)$$

where n is the OH^+ concentration, and A, B, C, and P are time varying functions of the concentrations and temperatures at each point along a fixed field line. Finite differences are used to approximate the derivatives. The notation for values of the quantities in time and space will be a superscript k denoting the value at time $k\Delta t$ sec and a subscript m denoting position $z = m\Delta z + 100$ km.

Consider the Taylor expansion about time $t = (k + 1/2)\Delta t$ sec:

$$n_m^{k+1/2} \simeq n_m^k + \frac{\Delta t}{2} \left(\frac{\partial n}{\partial t}\right)_m^k \tag{6}$$

also

$$n_m^{k+1/2} \simeq n_m^{k+1} - \frac{\Delta t}{2} \left(\frac{\partial n}{\partial t}\right)_m^{k+1} \tag{7}$$

Equating these two expressions for $n_m^{k+1/2}$ gives

$$\frac{n_m^{k+1} - n_m^k}{\Delta t} = \frac{1}{2} \left[\left(\frac{\partial n}{\partial t}\right)_m^{k+1} + \left(\frac{\partial n}{\partial t}\right)_m^k \right] \tag{8}$$

The substitution of Equation (5) results in

$$\frac{[n_m^{k+1} - n_m^k]}{\Delta t} = \frac{1}{2} \left[D\frac{\partial^2 n}{\partial z^2} + A\frac{\partial n}{\partial z} + Bn + Cn^2 + P \right]_m^{k+1} + \frac{1}{2} \left[D\frac{\partial^2 n}{\partial z^2} + A\frac{\partial n}{\partial z} + Bn + Cn^2 + P \right]_m^k \tag{9}$$

The finite difference approximations to the partial spatial derivatives are

$$\left(\frac{\partial n}{\partial z}\right)_m^k \simeq \frac{n_{m+1}^k - n_{m-1}^k}{2\Delta z} \qquad \left(\frac{\partial^2 n}{\partial z^2}\right)_m^k \simeq \frac{n_{m+1}^k - 2n_m^k + n_{m-1}^k}{(\Delta z)^2} \tag{10}$$

These expressions are used to remove the derivatives from Equation (9) giving

$$\frac{n_m^{k+1} - n_m^k}{\Delta t} = \frac{1}{2} \left[D_m^{k+1} \frac{n_{m+1}^{k+1} - 2n_m^{k+1} + n_{m-1}^{k+1}}{(\Delta z)^2} + \frac{A_m^{k+1}}{2\Delta z} (n_{m+1}^{k+1} - n_{m-1}^{k+1}) \right.$$

$$+ B_m^{k+1} n_m^{k+1} + C_m^{k+1}(n_m^{k+1})^2 + P_m^{k+1} + D_m^k \frac{n_{m+1}^k - 2n_m^k + n_{m-1}^k}{(\Delta z)^2}$$

$$\left. + \frac{A_m^k}{2\Delta z} (n_{m+1}^k - n_{m-1}^k) + B_m^k n_m^k + C_m^k(n_m^k)^2 + P_m^k \right] \tag{11}$$

This formulation of the numerical solution of partial differential equations is due to Crank and Nicolson [1947].

Equation (11) is quadratic in the future density variable n_m^{k+1}. The equation is linearized by expanding the quadratic term in a Taylor series

$$(n_m^{k+1})^2 \simeq (n_m^k)^2 + \Delta t \frac{\partial (n_m^k)^2}{\partial t}$$

$$= (n_m^k)^2 + \Delta t \, 2 n_m^k \frac{\partial n_m^k}{\partial t} \simeq (n_m^k)^2 + 2\Delta t \, n_m^k \frac{(n_m^{k+1} - n_m^k)}{\Delta t}$$

$$= 2 n_m^k \, n_m^{k+1} - (n_m^k)^2 \tag{12}$$

With this substitution, Equation (11) is written in the form

$$n_{m-1}^{k+1} \, \alpha_m + n_m^{k+1} \, \beta_m + n_{m+1}^{k+1} \, \delta_m = \gamma_m \qquad \{1 \le m \le M - 1\} \tag{13}$$

where α_m, β_m, and δ_m are functions of D_m, A_m, B_m, C_m, P_m, Δt and Δz. γ_m is a function of n_m^k, n_{m-1}^k, n_{m+1}^k, D_m, A_m, B_m, C_m, P_m, Δt and Δz.

Equation (13) represents a system of linear equations which have unique solutions if two boundary conditions are specified. The boundary conditions for the OH^+ continuity equation are zero ion concentration at 100 and 500 km. (i.e, n_0^{k+1} and $n_M^{k+1} = 0$)

The system of linear equations has three unknown values at positions $(m-1)\Delta z$, $m\Delta z$, and $(m+1)\Delta z$. Such a system is called tridiagonal as is evident when the linear equations are expressed in matrix form

$$
\begin{bmatrix}
\beta_1 & \gamma_1 & 0 & 0 & & & 0 \\
\alpha_2 & \beta_2 & \gamma_2 & 0 & & & \\
0 & \alpha_3 & \beta_3 & \gamma_3 & & & \\
\cdot & & & \alpha_{M-2} & \beta_{M-2} & \gamma_{M-2} \\
0 & \cdot & \cdot & \cdot \ \cdot & \alpha_{M-1} & \beta_{M-1}
\end{bmatrix}
\begin{bmatrix}
n_1^{k+1} \\
n_2^{k+1} \\
\cdot \\
\cdot \\
\cdot \\
n_{M-1}^{k+1}
\end{bmatrix}
\begin{bmatrix}
\delta_1 \\
\delta_2 \\
\cdot \\
\cdot \\
\cdot \\
\delta_{M-1}
\end{bmatrix}
\qquad (14)
$$

The following efficient method is used for solving the tridiagonal system. Two sets of variables, s_m and q_m, are defined recursively

$$
s_1 = \frac{\delta_1}{\beta_1} \qquad q_1 = \frac{\gamma_1}{\beta_1}
$$

$$
s_m = \frac{\delta_m}{\beta_m - \alpha_m s_{m-1}} \qquad q_m = \frac{\gamma_m - \alpha_m q_{m-1}}{\beta_m - \alpha_m s_{m-1}} \qquad \{2 \le m \le M-2\} \qquad (15)
$$

$n_{m-1}, \ n_{m-2} \cdots n_2, n_1$ are then calculated from

$$
n_{M-1}^{k+1} = \frac{\gamma_M - \alpha_{M-1} \ q_{M-2}}{\beta_{M-1} - \alpha_{M-1} \ s_{m-1}}
$$

$$
n_m^{k+1} = q_m - s_m n_{m+1}^{k+1} \qquad \{M-2 \le m \le 1\} \qquad (16)
$$

Further detail on the solution of tridiagonal systems can be found in Todd [1962].

The ionospheric model initially creates an unperturbed plasma and temperature profile along a magnetic field line. The field line is separated into steady state and time varying regions. The region is considered to be in steady state where the recombination or the diffusion

time constants are greater than the time steps (Δt) used in the solution [Waldman, 1971]. This procedure insures numerical stability.

The hydrogen gas model is used to simulate the release of a spherical cloud of perturbing gas. The program time-steps are made small ($\Delta t \sim 1$ sec) and the initial transients in the chemical depletion are simulated. At later stages in the modification, the time steps are increased to one minute. The simulation continues until the hydrogen is exhausted and the ionosphere has recovered.

B. Results of the Simulation.

The density and temperature variations produced by the release of H_2 into the daytime and nighttime F-region are now examined in detail. The first part of this section describes the effects of the release of 100 kg of H_2 at an altitude of 300 km and at a geographic latitude of 40° N. The field line through the release point is at $L = 3$ with a dip angle of 70.5°. During the day, neutral winds are assumed to be zero. At night, a 100 m/sec meridional wind is used in the model. This nighttime equatorward wind both lifts the nighttime F-layer and moves the released gas cloud with respect to the magnetic field lines. The second part of this section examines the effects of varying the altitude and amount of H_2 injection.

Figure 3 shows the evolution of the night-time F-region profile along the field line through the hydrogen release point. The upward plasma flux at 500 km is indicated at the top of each profile. A deep hole is created within 1 minute after the H_2 injection, thus splitting the F-layer into two distinct layers. Increased loss of O^+ induces an increase in the downward plasma flow from the topside ionosphere which helps to maintain the uppermost of these two layers. The lower
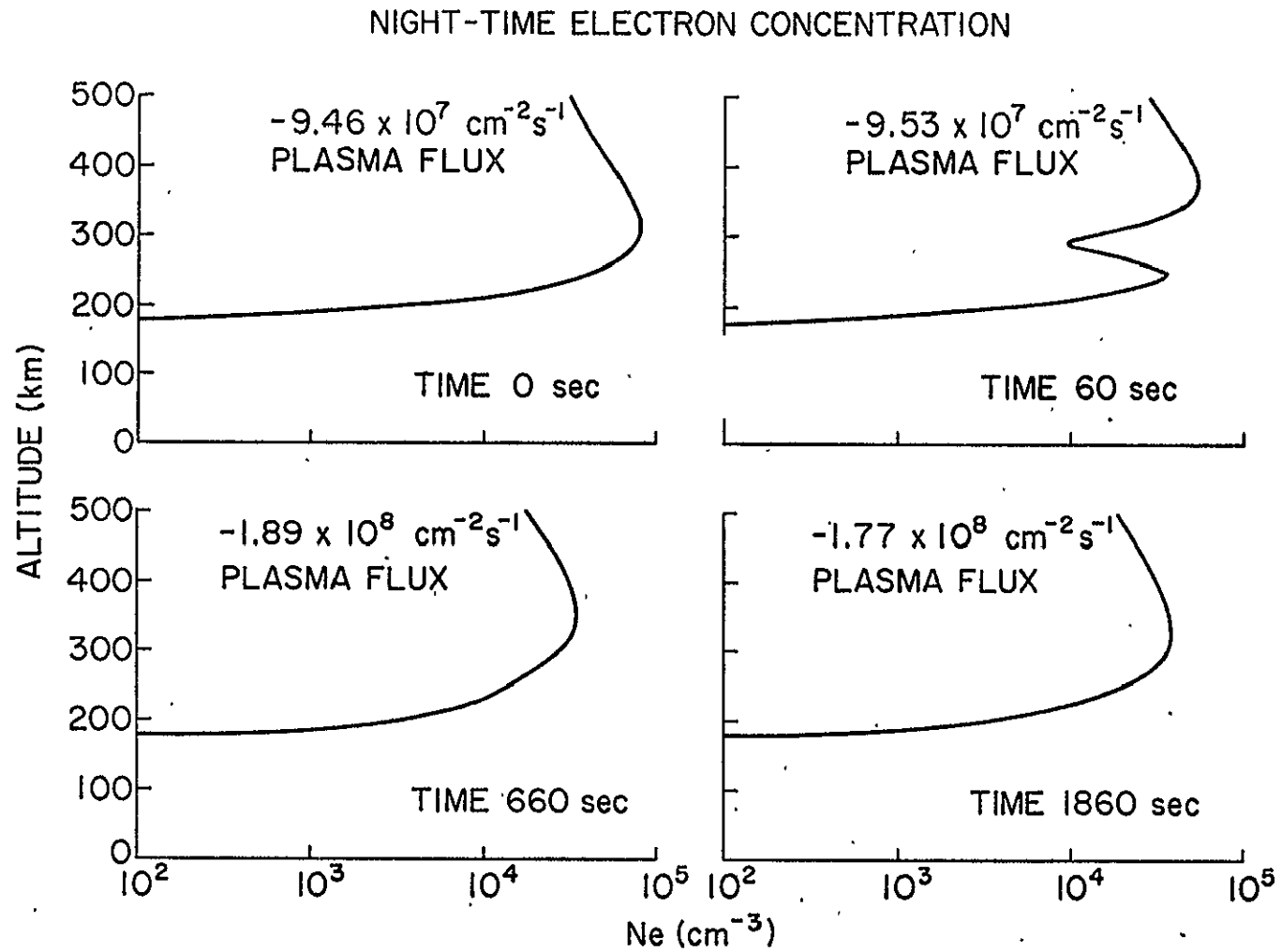
114

NIGHT-TIME ELECTRON CONCENTRATION

Fig. 3. Time sequence of nighttime F-region profiles illustrating the effects of hydrogen injection.

layer is cut off from the protonospheric flux by the diatomic hydrogen gas cloud blocking the magnetic flux tube. This lower layer, isolated from any plasma source, disappears after 660 seconds.

The temporal variation in the altitude and maximum density of the lower layer may be used in determining the mechanisms maintaining the night-time ionosphere. If protonospheric flux is the only maintenance mechanism, the lower peak density will decay exponentially through chemical recombination. If there is appreciable night-time production, i.e., by corpuscular ionization, the lower peak density levels off at a certain point after the initial period of exponential decay. Observations of such behavior with an incoherent scatter radar or an HF sounder should provide quantitative information on production and loss rates in the night-time ionosphere.

One half hour after gas release, the ionospheric profile has almost fully recovered, but the peak density is somewhat lower than the initial peak density for two reasons: (1) the recombination rate is still slightly higher because of residual H_2 molecules, and (2) the plasma-sphere which has been drained by increased downward flux, cannot provide the necessary plasma to maintain the original layer.

The formation of the persistant nighttime depletion is shown in Figure 4. Contours of constant electron concentration are plotted in the meriodonal plane. In the northern hemisphere, north is to the right of the plots. As the ionospheric hole forms, the effects of the magnetic inclination and the neutral wind become evident. Tilting of the isopycnic contours is produced by the depletion of plasma flowing along inclined magnetic flux tubes. In the later stages of depletion (times greater than 600 seconds), the F-layer to the left (south) of the release point is more depleted than the F-layer to the right (north) of the release

NIGHT-TIME ELECTRON CONCENTRATION
LOG_{10}(Number Density, cm^{-3})

TIME   0 SEC

NIGHT-TIME ELECTRON CONCENTRATION
LOG_{10}(Number Density, cm^{-3})

TIME   60 SEC

NIGHT-TIME ELECTRON CONCENTRATION
LOG_{10}(Number Density, cm^{-3})

TIME   180 SEC

NIGHT-TIME ELECTRON CONCENTRATION
LOG_{10}(Number Density, cm^{-3})

TIME   600 SEC

NIGHT-TIME ELECTRON CONCENTRATION
LOG_{10}(Number Density, cm^{-3})

TIME   2400 SEC

NIGHT-TIME ELECTRON CONCENTRATION
LOG_{10}(Number Density, cm^{-3})

TIME   4800 SEC

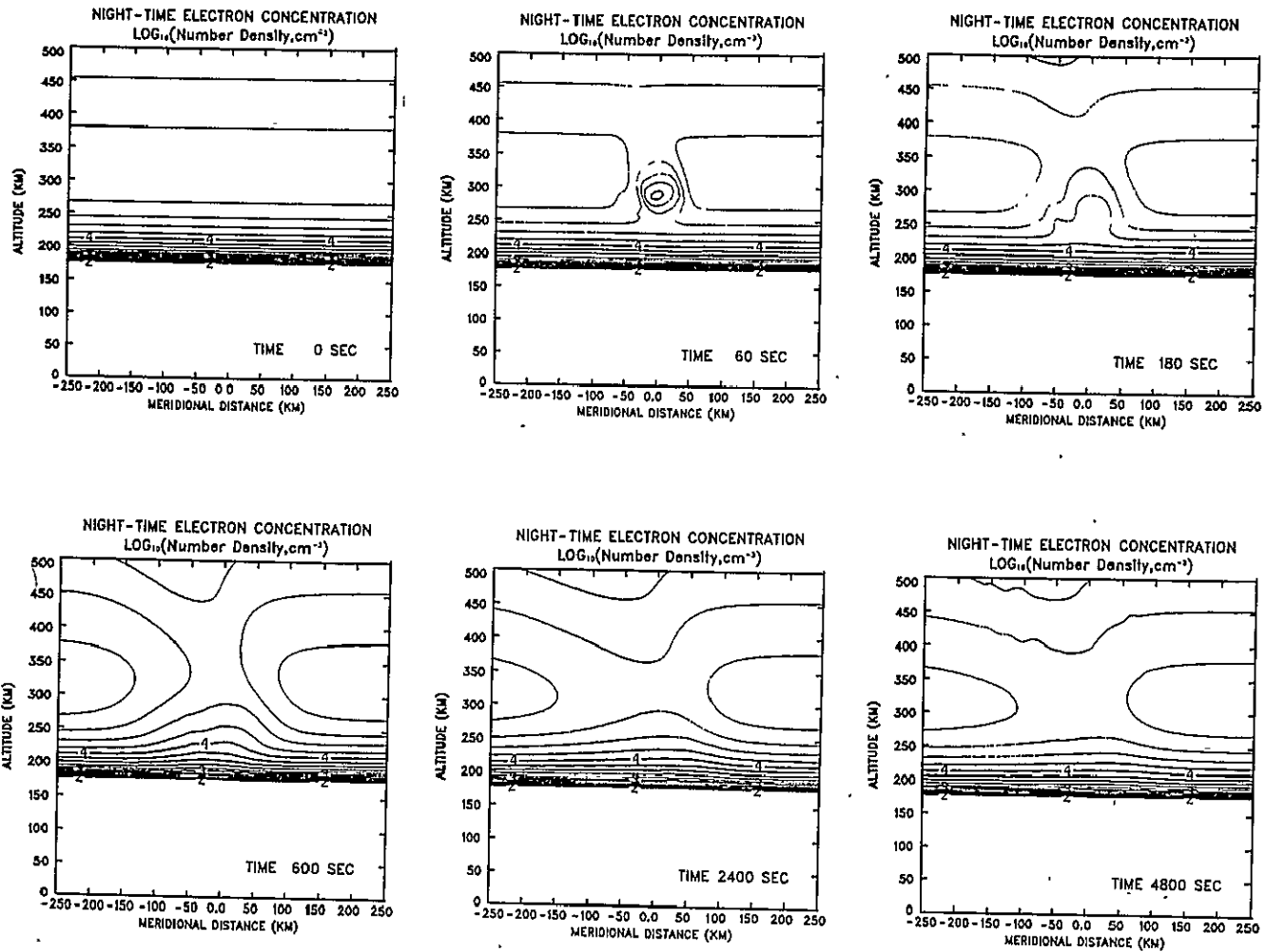ALTITUDE (KM)

MERIDIONAL DISTANCE (KM)

117

Fig. 4.   Meridional plane variations in the nighttime F-region electron concentration.

point. This is a consequence of the imposed N-S neutral wind of 100 m/s moving the H_2 gas cloud. After 4800 seconds the F-layer is recovering from the effects of the release of 100 kg H_2.

Figure 5 shows a sequence of electron profiles for the same conditions as Figure 3 except for the daytime ionosphere with an overhead sun. The unperturbed profile at 0 seconds shows a large F2 layer above an F1 layer. One minute after the release of H_2, the F2 peak is reduced by an order of magnitude while the F1 layer is unaffected. As at night, two layers are formed above and below the ionospheric hole. The daytime lower layer does not disappear as it did during the night because of the photoionization plasma source. The daytime increase in plasma temperature immediately after gas release produces a slight increase in the upward plasma flux. Eleven minutes after H_2 injection, the level of this flux has decreased below the unperturbed flux level because the F-region depletion has been communicated up the field line. After one half hour, the shape of the F-layer has recovered but the peak density has not.

The daytime meridional plane contours of electron concentration in Figure 6 show asymmetry and tilting resulting from the inclination of the geomagnetic field and nonuniformity of the neutral atmosphere. Because the H_2 cloud diffuses more rapidly upward into regions of lesser atmospheric density, its shape becomes nonspherical. The nonsphericity of the gas cloud coupled with the inclination of the magnetic flux tubes produces greater depletion to the north as compared with the depletion to the south of the release point. As with the nighttime depletion, the daytime F-region is still recovering from the H_2 release after 4800 seconds.

The difference between nighttime and daytime recovery is demonstrated by a comparison of Figures 4 and 6. The contours in the region
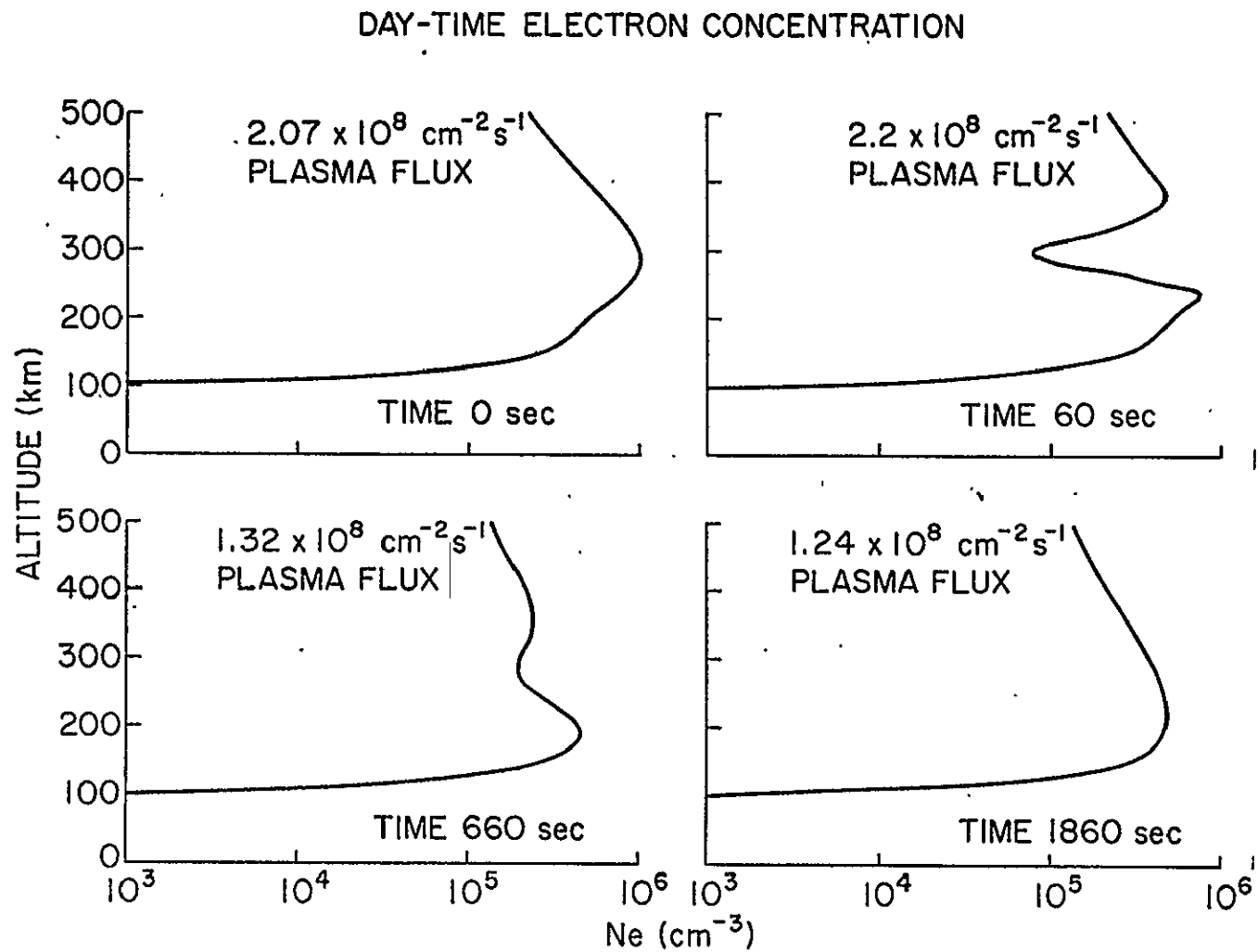
DAY-TIME ELECTRON CONCENTRATION

Fig. 5. Time sequence of daytime F-region profiles illustrating the effects of hydrogen injection.

DAY-TIME ELECTRON CONCENTRATION
LOG₁₀(Number Density,cm⁻³)

TIME   0 SEC

ALTITUDE (KM)

MERIDIONAL DISTANCE (KM)

DAY-TIME ELECTRON CONCENTRATION
LOG₁₀(Number Density,cm⁻³)

TIME   60 SEC

ALTITUDE (KM)

MERIDIONAL DISTANCE (KM)

DAY-TIME ELECTRON CONCENTRATION
LOG₁₀(Number Density,cm⁻³)

TIME 180 SEC

ALTITUDE (KM)

MERIDIONAL DISTANCE (KM)

DAY-TIME ELECTRON CONCENTRATION
LOG₁₀(Number Density,cm⁻³)

TIME 600 SEC

ALTITUDE (KM)

MERIDIONAL DISTANCE (KM)

DAY-TIME ELECTRON CONCENTRATION
LOG₁₀(Number Density,cm⁻³)

TIME 2400 SEC

ALTITUDE (KM)

MERIDIONAL DISTANCE (KM)

DAY-TIME ELECTRON CONCENTRATION
LOG₁₀(Number Density,cm⁻³)
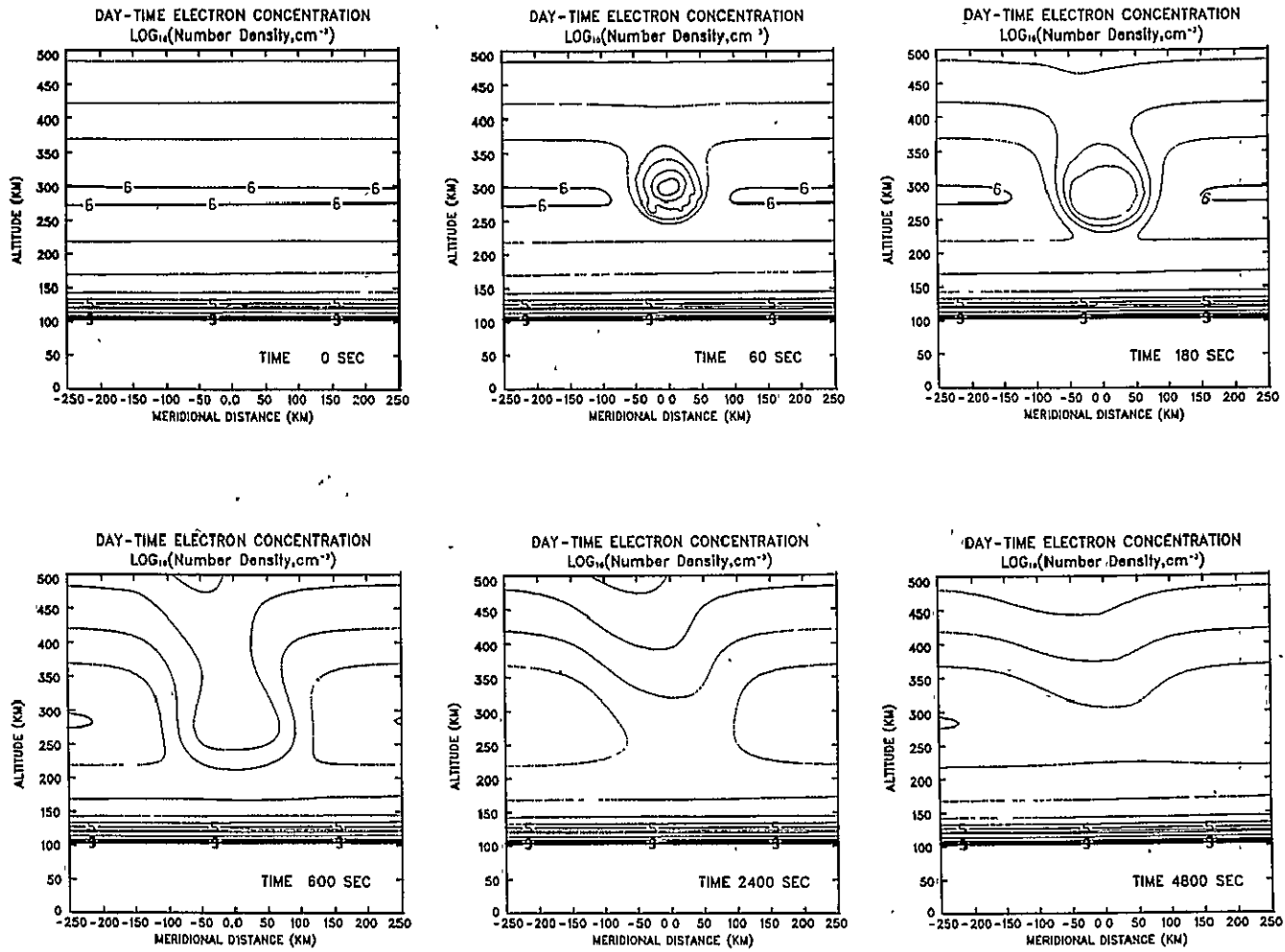
TIME 4800 SEC

ALTITUDE (KM)

MERIDIONAL DISTANCE (KM)

Fig. 6. Meridional plane variations in the daytime F-region electron conentration.

of the ionospheric hole open downward at night (time 180 sec) and upward during the day (time 600 sec). The nighttime plasma flux from above pushes the ionospheric hole down whereas the daytime photoionization source tends to replenish the depletion region from below.

Small changes occur in the nighttime electron temperature. (Figure 7). The slight increase in T_e is a consequence of lower electron to ion cooling resulting from the plasma density reduction. Magnetic inclination effects are apparent in the two dimension isothermal plots in Figure 8.

The rise in the electron temperature is more dramatic during the day than during the night. Examination of the daytime electron temperature profiles along the field line through the point of H_2 injection (Figure 9) illustrates the effect of the lowered ion cooling. The local electron temperature minimum at the altitude of the F-layer concentration peak (300 km) rapidly disappears as high temperature electrons produced by thermalized photoelectrons enter the depletion region. The rise in the electron temperature produces a decrease in the downward thermal heat flux from the overlying protonosphere. The maximum electron temperature occurs about 10 minutes after H_2 release. At this time the temperature at 300 km has increased by 1500 K.

The spatial extent of the thermospheric modification is shown in Figure 10. Before the gas release, time 0 seconds, a slight meridional variation in the daytime electron temperature results from the latitudinal variation in the solar zenithal angle. One minute after H_2 release, a 100 km wide region of temperature enhancement (Figure 10) coincides with a similarly sized reduction in electron concentration (Figure 6). After ten minutes, the width of the supra-normal temperature region has increased to 250 km. Later, the electron contours relax toward the
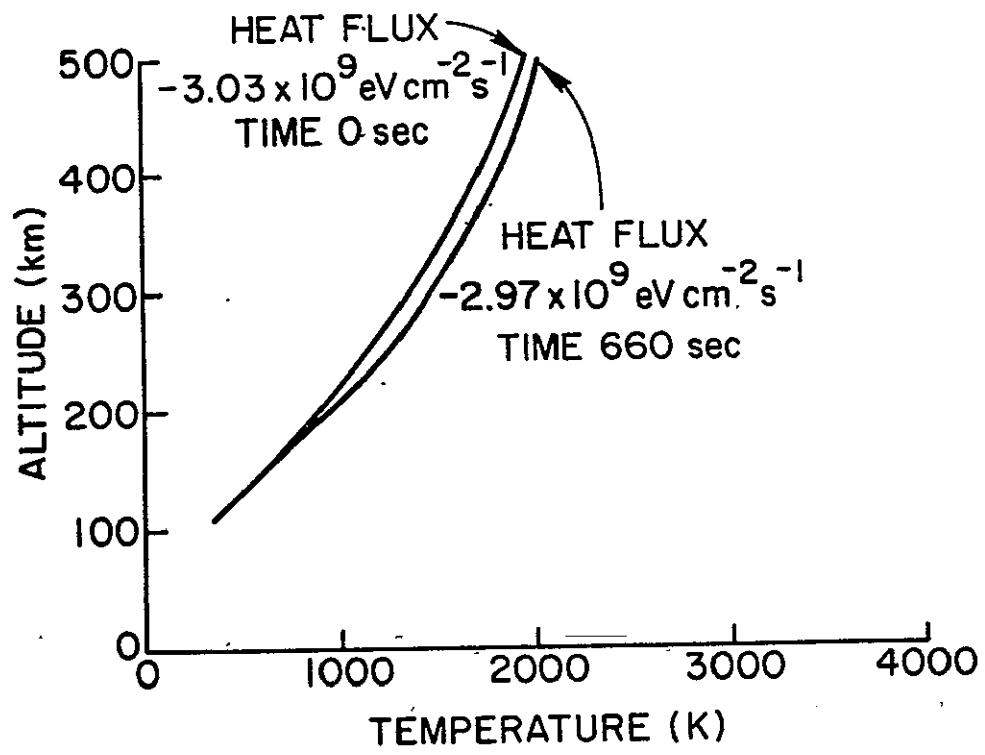
Fig. 7. The rise in nighttime electron temperature.

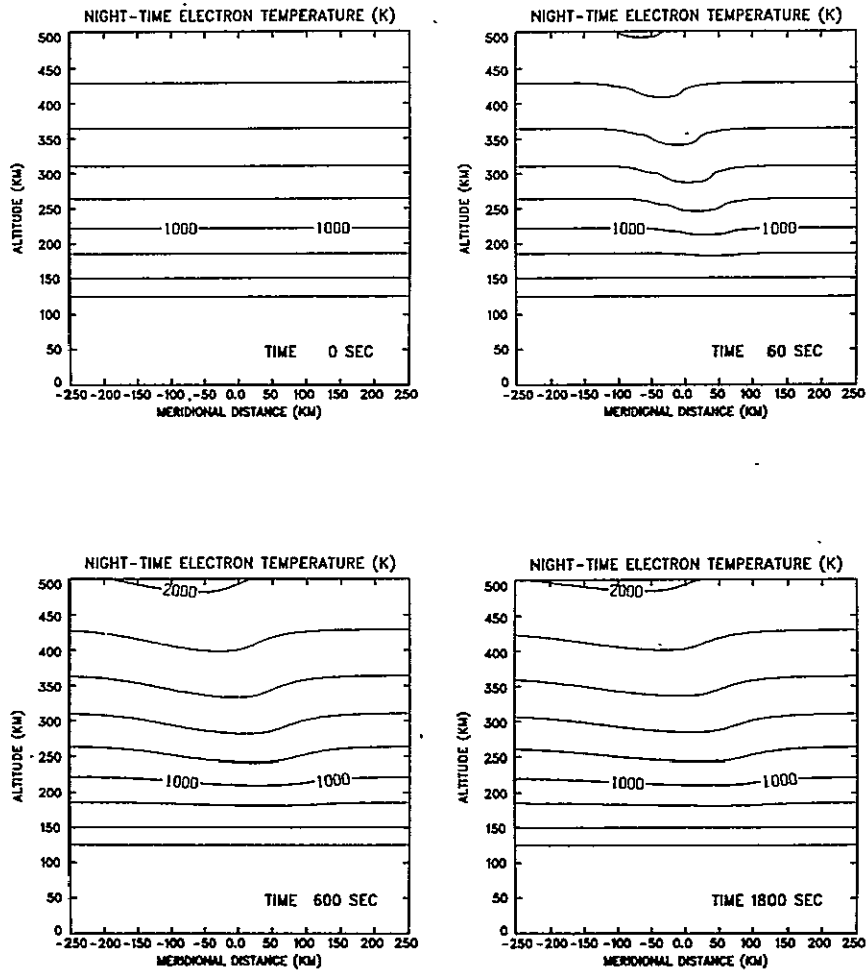Fig. 8.   Isothermal contour variations in the nighttime ionosphere.
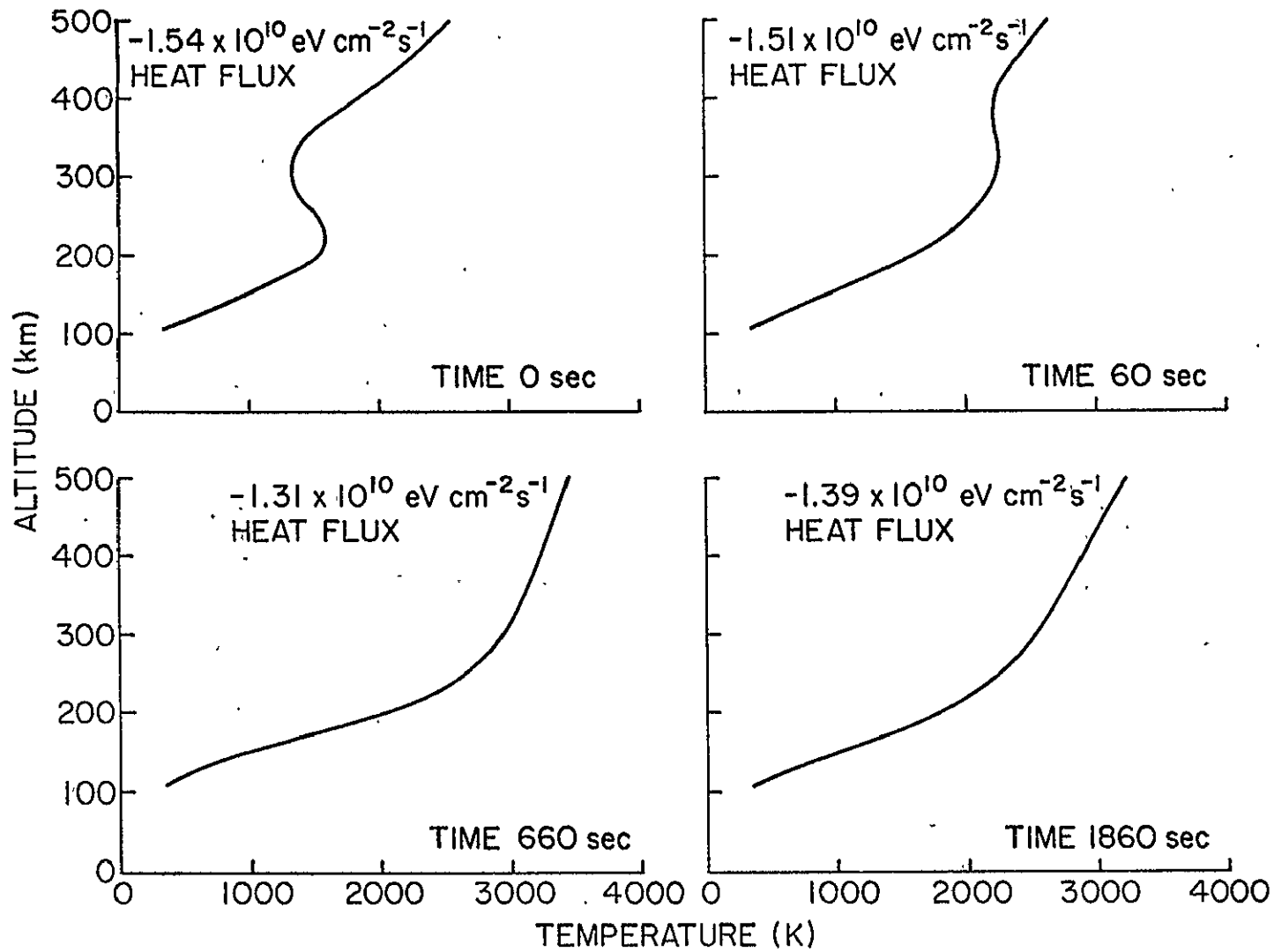
Fig. 9. Time sequence of daytime electron temperature profiles showing the large temperature increase.
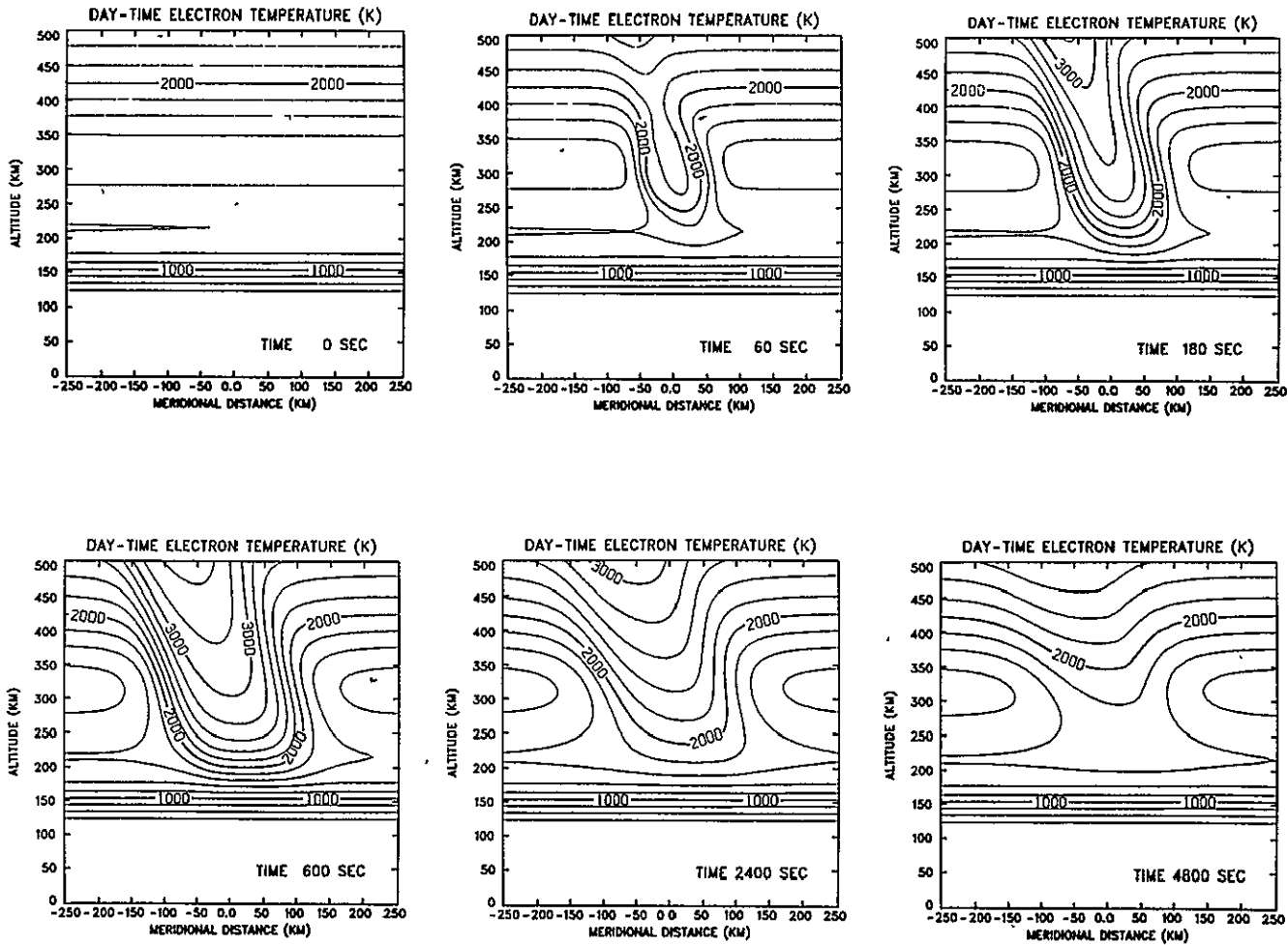
Fig. 10.   Isothermal contour variations in the daytime ionosphere.
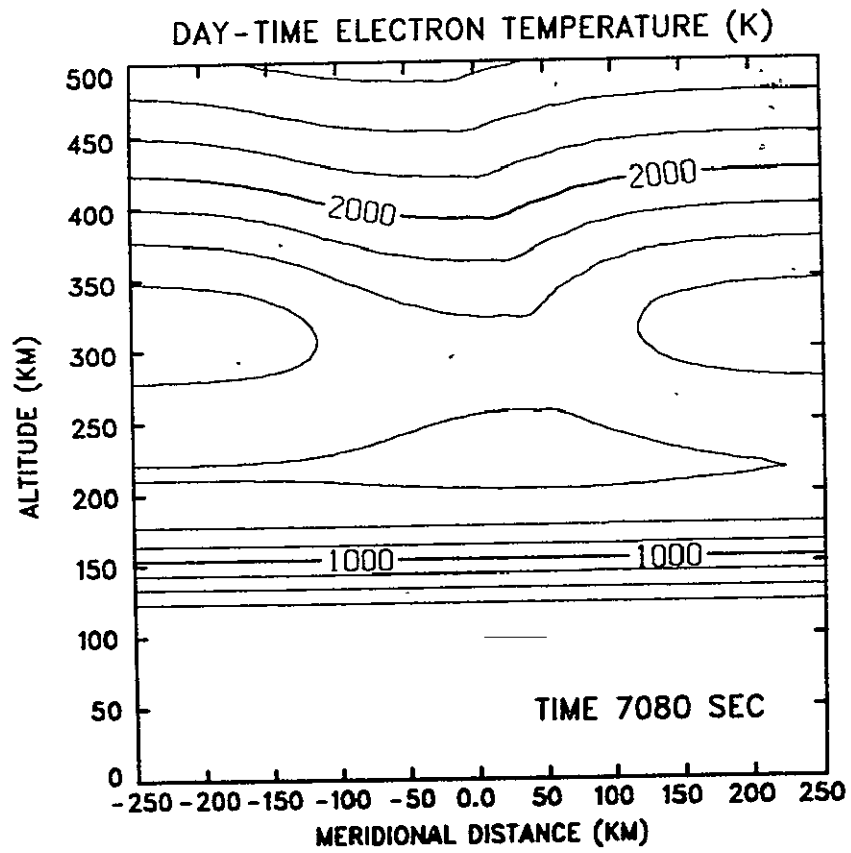
DAY-TIME ELECTRON TEMPERATURE (K)

TIME 7080 SEC

Fig. 11. Significant·perturbation of the daytime thermosphere lasting hours after the gas release.

126

unperturbed state but even after 2 hours, significant thermospheric perturbation exists (Figure 11).

Coincident with a rise in the electron temperature is a decrease in the ion temperature. The heat source for the ions are the electrons. In the depleted ionosphere, the electron-to-ion heat transfer is reduced. The nighttime unperturbed ion temperature profile is shown in Figure 12. After the reactive gas release, the ions are cooled by heat transfer to the neutral atmosphere (Figure 13). The magnitude of the ion cooling is similar during the day (Figure 14 and 15).

The ion temperature reduction has a significant effect on the topside ionospheric H^+ concentration. The reduction in the F-region O^+ concentration produces a reduction in the H^+ concentration under conditions of isothermal chemical equilibrium because reaction of O^+ and H is the main mechanism for H^+ production in the F-region. However, comparison of the H^+ profiles before and after nighttime H_2 injection reveals a decrease in H^+ only in a small region at the bottom of the H^+ layer (Figures 16 and 17). Throughout most of the layer, the H^+ concentration increases. This is due to changes in H^+ loss and diffusion rates produced by ion temperature variations. The (H^+,O) reaction rate is proportional to the square root of the ion temperature. Thus, the reduction in ion temperature tends to produce an increase in H^+. The H^+ diffusion coefficient is proportional to the ion temperature to the 5/2 power [Schunk and Walker, 1970] resulting in a reduction in the diffusive transport of H^+ through the depletion region. These two effects produce a bulge in the H^+ profile in regions where production of H^+ by O^+ is not important. After 2000 seconds, the protonosphere has been sufficiently drained so that the high altitude H^+ concentration is noticeably reduced but the lower altitude H^+ bulge persists (Figure 17).
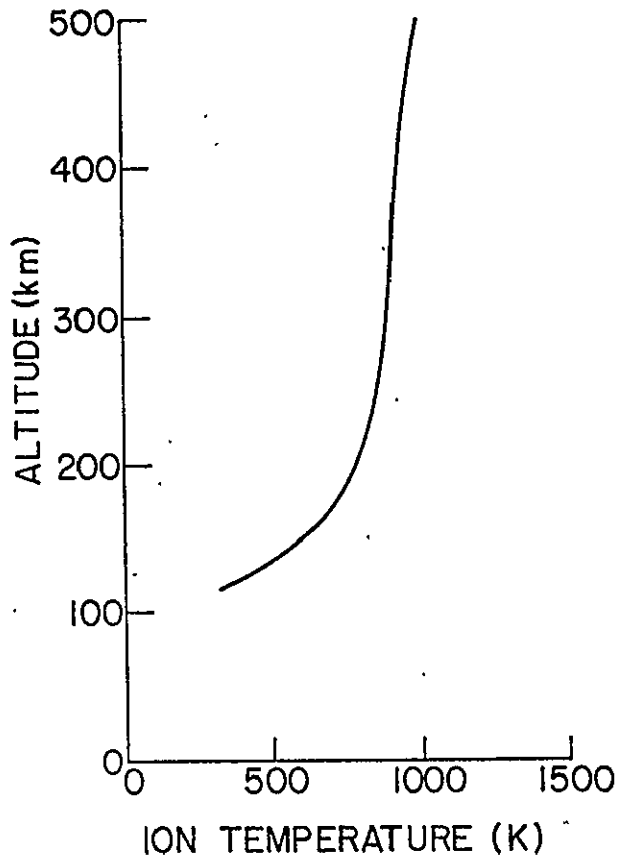
127

Fig. 12. Nighttime unperturbed temperature profile.
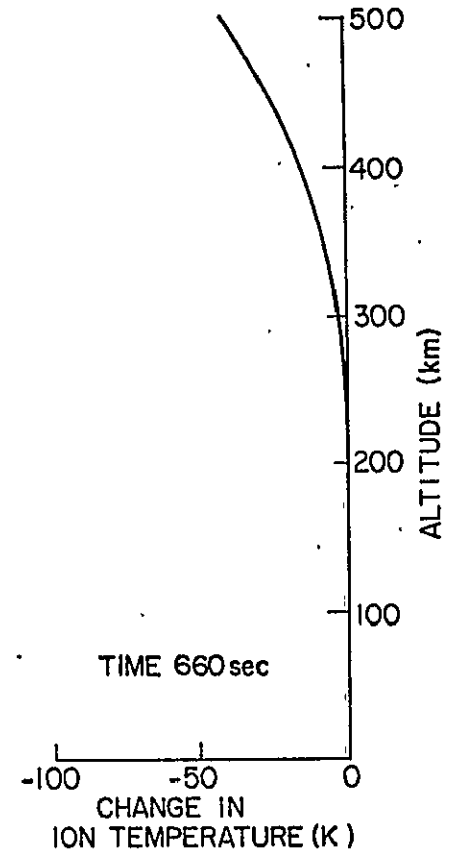

TIME 660 sec

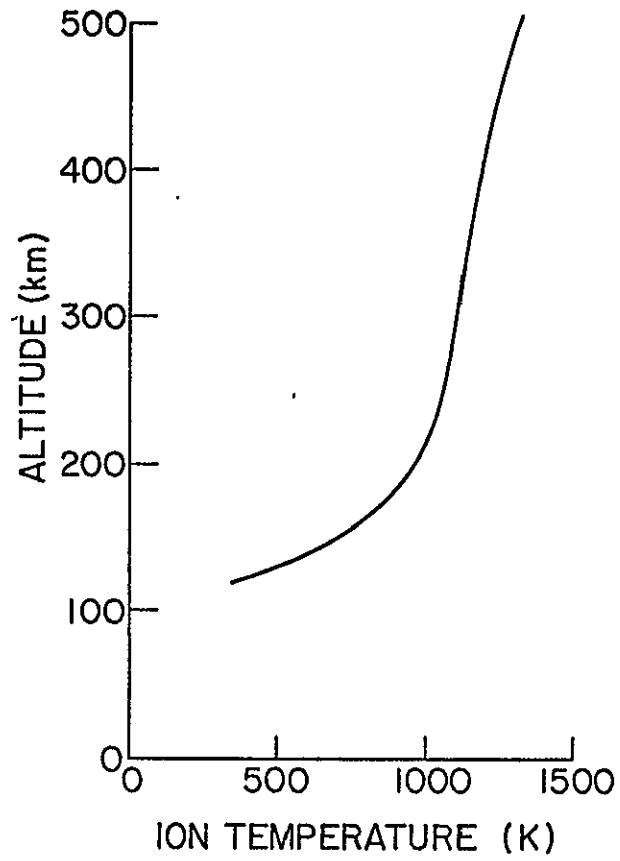Fig. 13. Nighttime ion cooling by chemical plasma depletion.

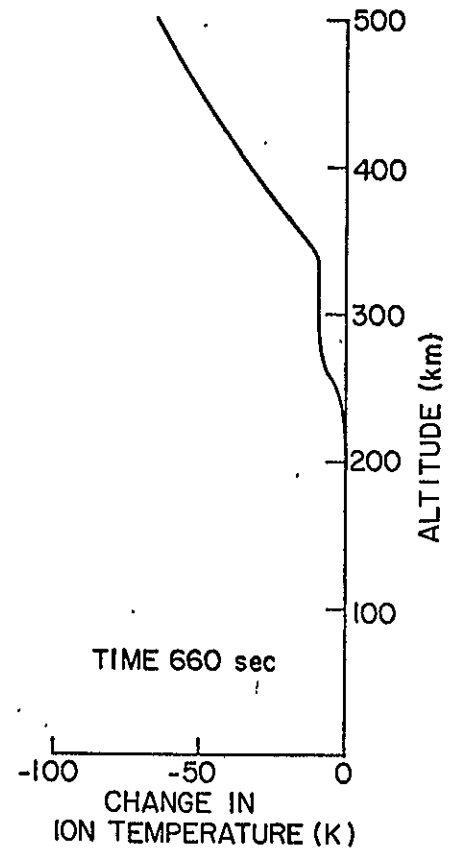Fig. 14. Daytime unperturbed tempera-
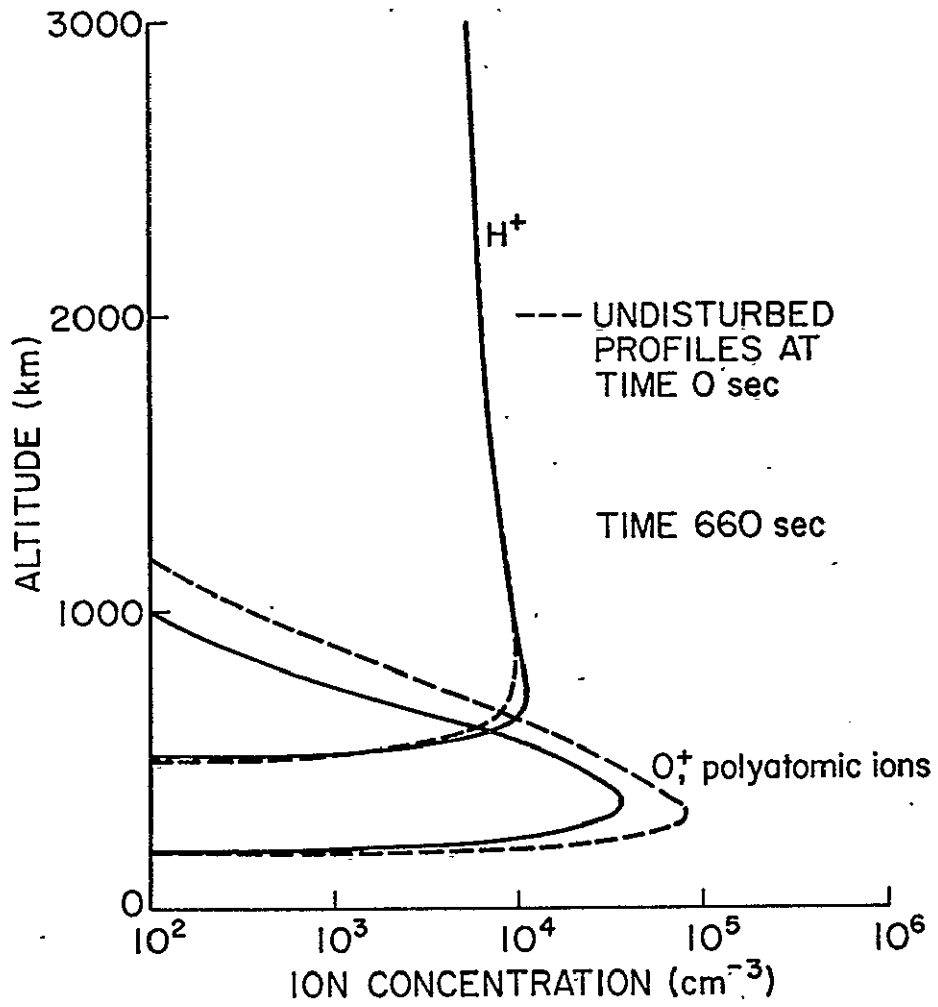ture profile.

Fig. 15. Daytime ion cooling.

Fig. 16. Nighttime H^+ and O^+ profiles along the field line through the point of H_2 realease.
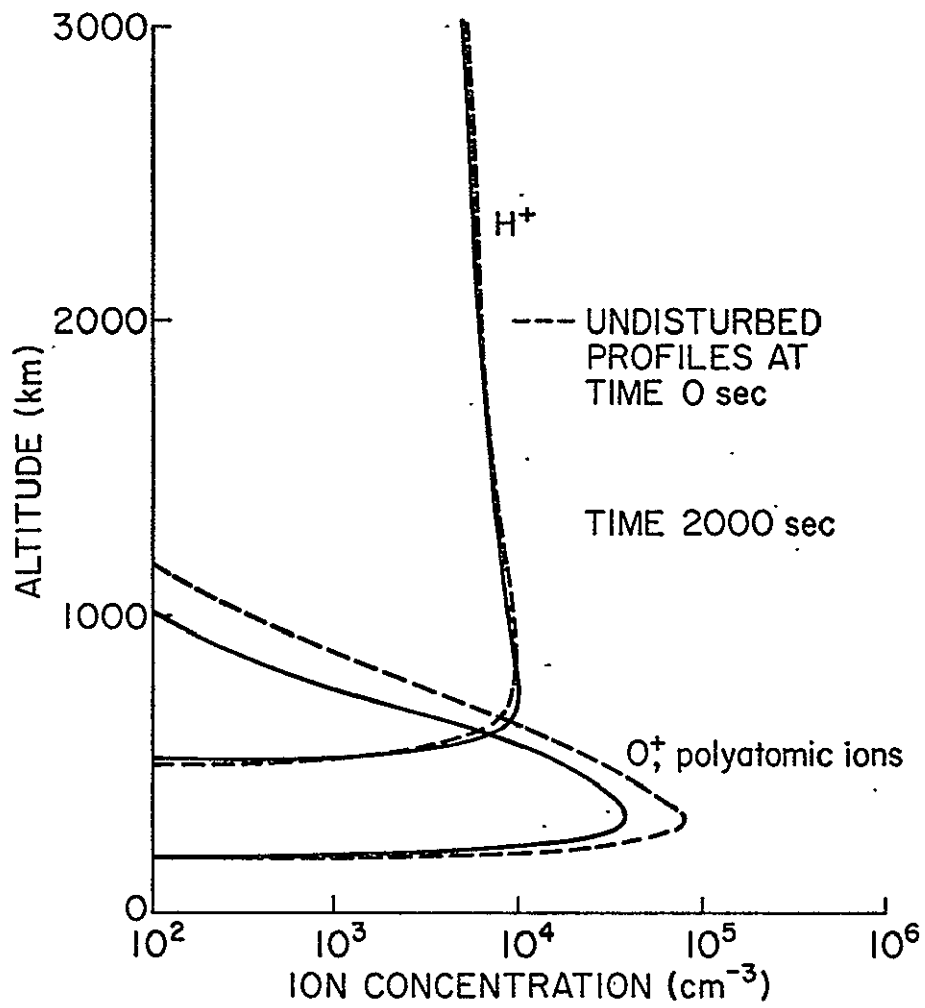
Fig. 17. Same as Figure 16 but at a later time.

The H^+ bulge occurs at higher altitudes in the daytime plasma-sphere. Since O^+ is a more important source of low altitude H^+ in the day than at night, the depression in the O^+ concentration produces a depression in the H^+ concentration up to an altitude of 1200 km (Figure 18). The daytime H^+ enhancement occurs at 1800 km where the O^+ and H^+ concentrations are comparable. 2000 seconds after the gas release, the upward daytime plasma flux has increased the protonospheric content, resulting in a larger bulge in the H^+ concentration at 1800 km (Figure 19). Note that the perturbed H^+ profiles in Figures 16 through 19 are referenced to the unperturbed H^+ profile just before H_2 injection. (The unperturbed concentrations during the times indicated in the figures would be slightly less during the night due to the continual drainage of the protonosphere and would be slightly more during the day due to the upward plasma flow into the protonosphere.) In summary, the release of H_2 into the F-region produces 1) a reduction of H^+ at low altitudes as a result of the O^+ depletion, and 2) an increase in H^+ at high altitudes due to the reduction in ion temperature.

The depletion of the F-layer produces a relative reduction in the protonospheric content above 3000 km. A temporal sequence in the formation of the nighttime protonospheric depleted tube or trough is shown in Figure 20. The protonospheric content reduction is plotted against the meridional cross-field distance at the base of the tube relative to the field line passing through the point of release. The asymmetry in the trough is due to the magnetic field inclination and to the motion of the neutral atmosphere. Since the nighttime neutral wind blows from north to sourth in the northern hemisphere, the tube
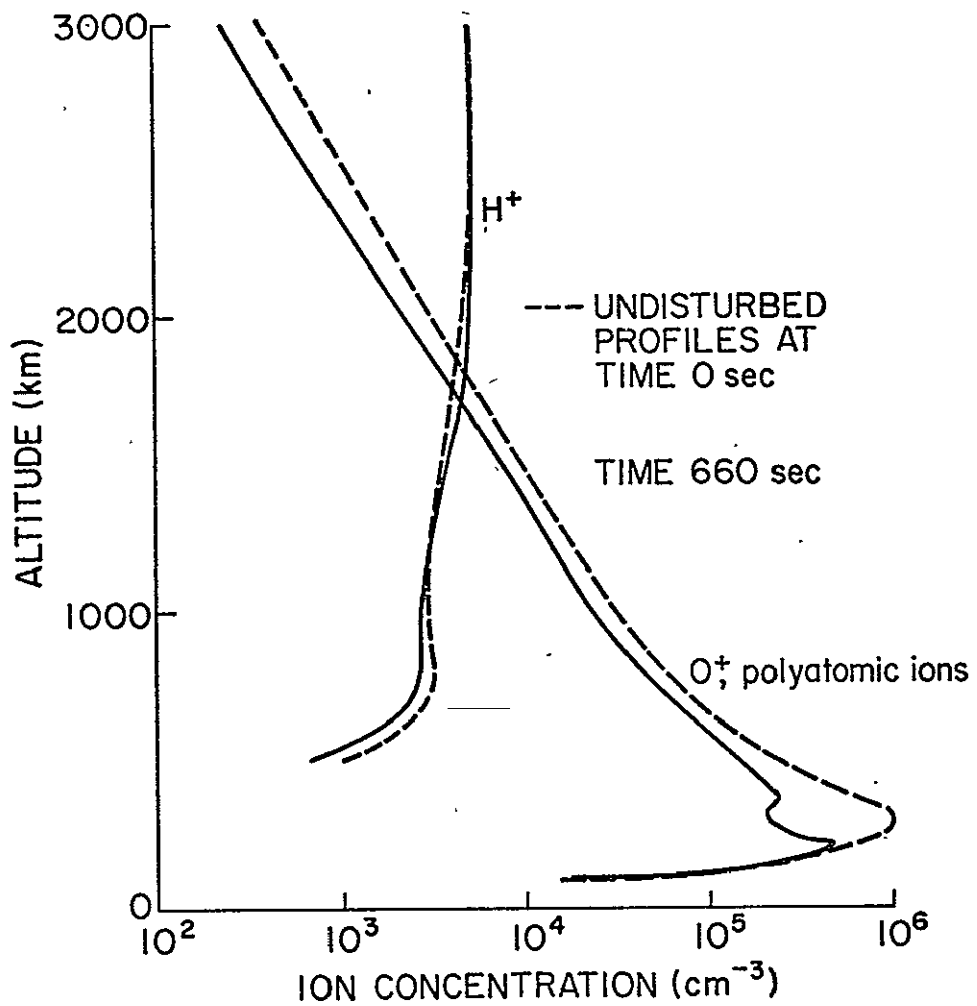
Fig. 18. Daytime H^+ and O^+ profiles along the field
line through the point of H_2 release.
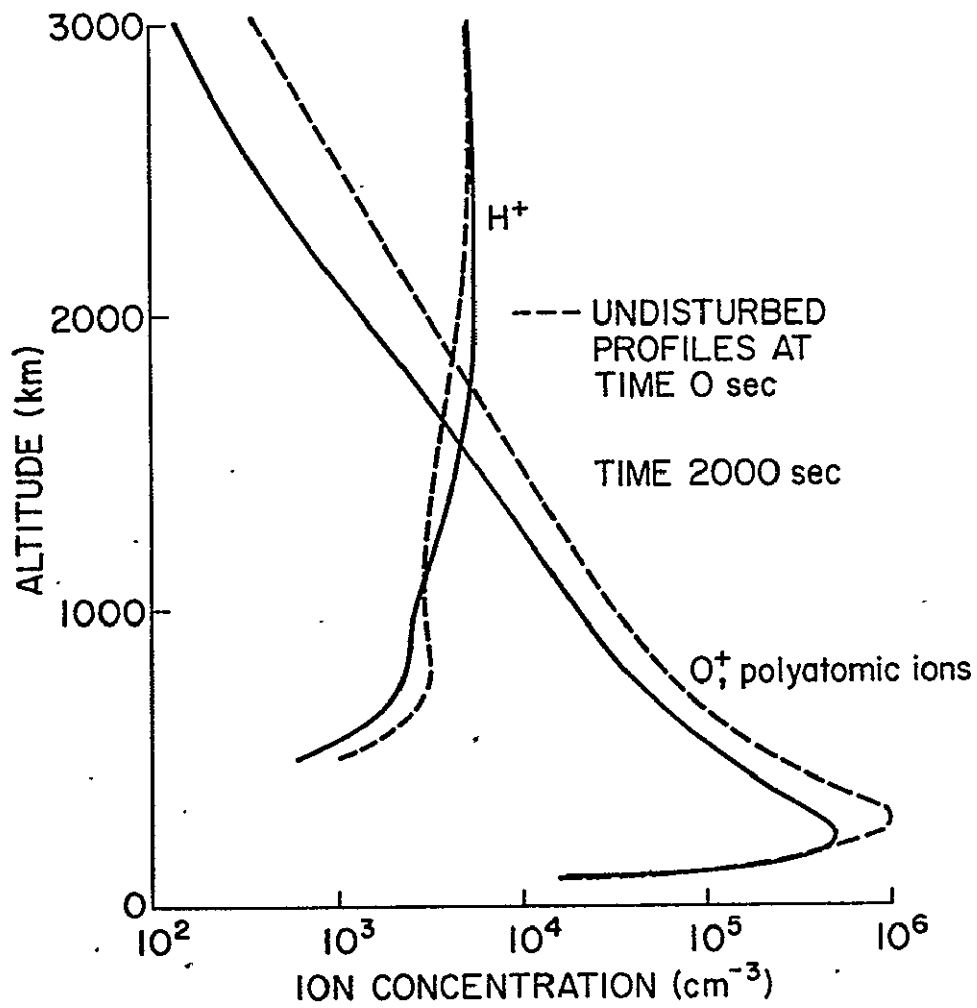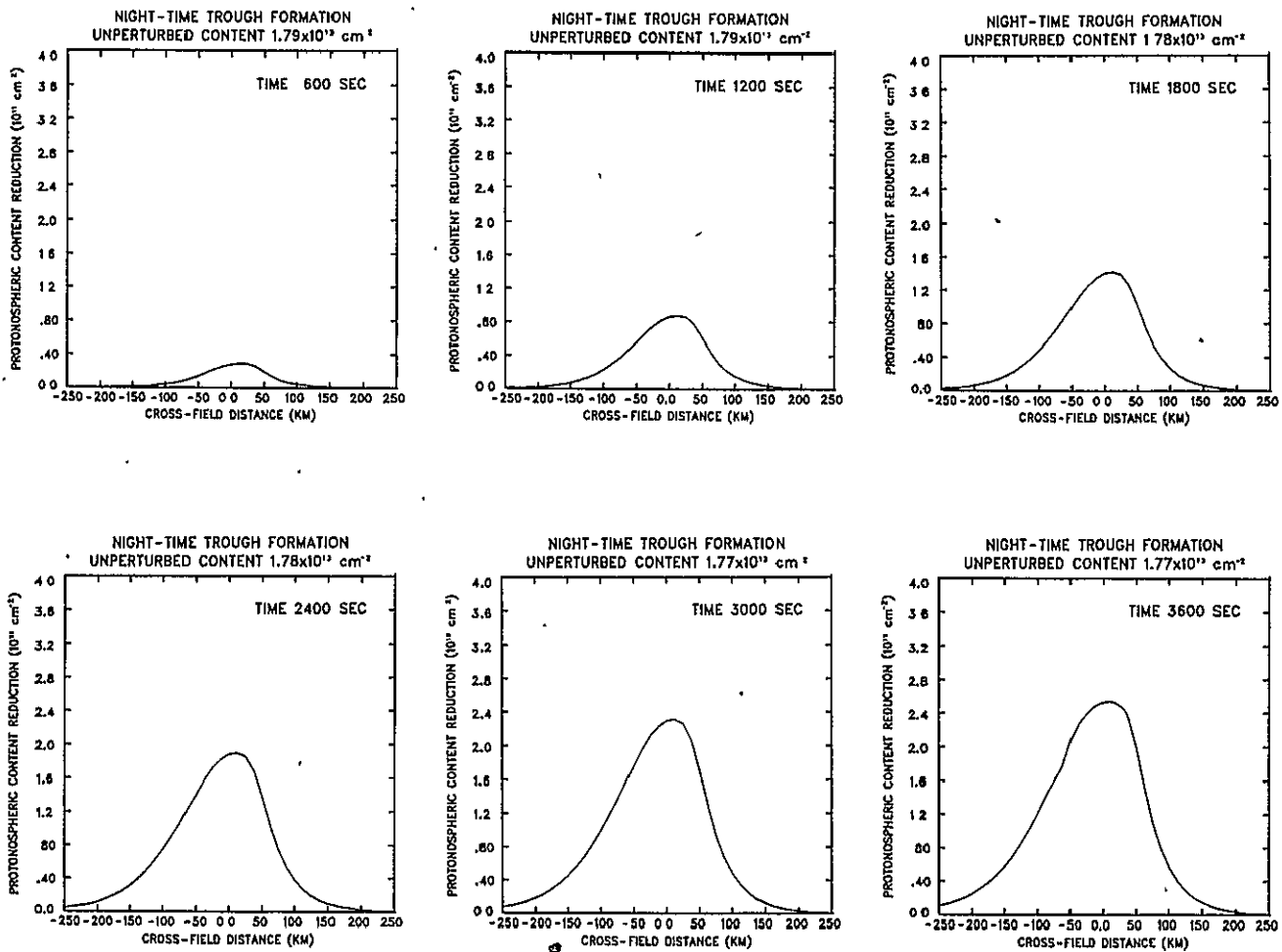
Fig. 19. Same as Figure 18 but at a later time.

Fig. 20. Nighttime depletion of the protonosphere. The reduction in protono-
spheric content from 3000 km to the equator is plotted against the
distance between adjacent field lines in the meridional plane on the
surface of the earth.
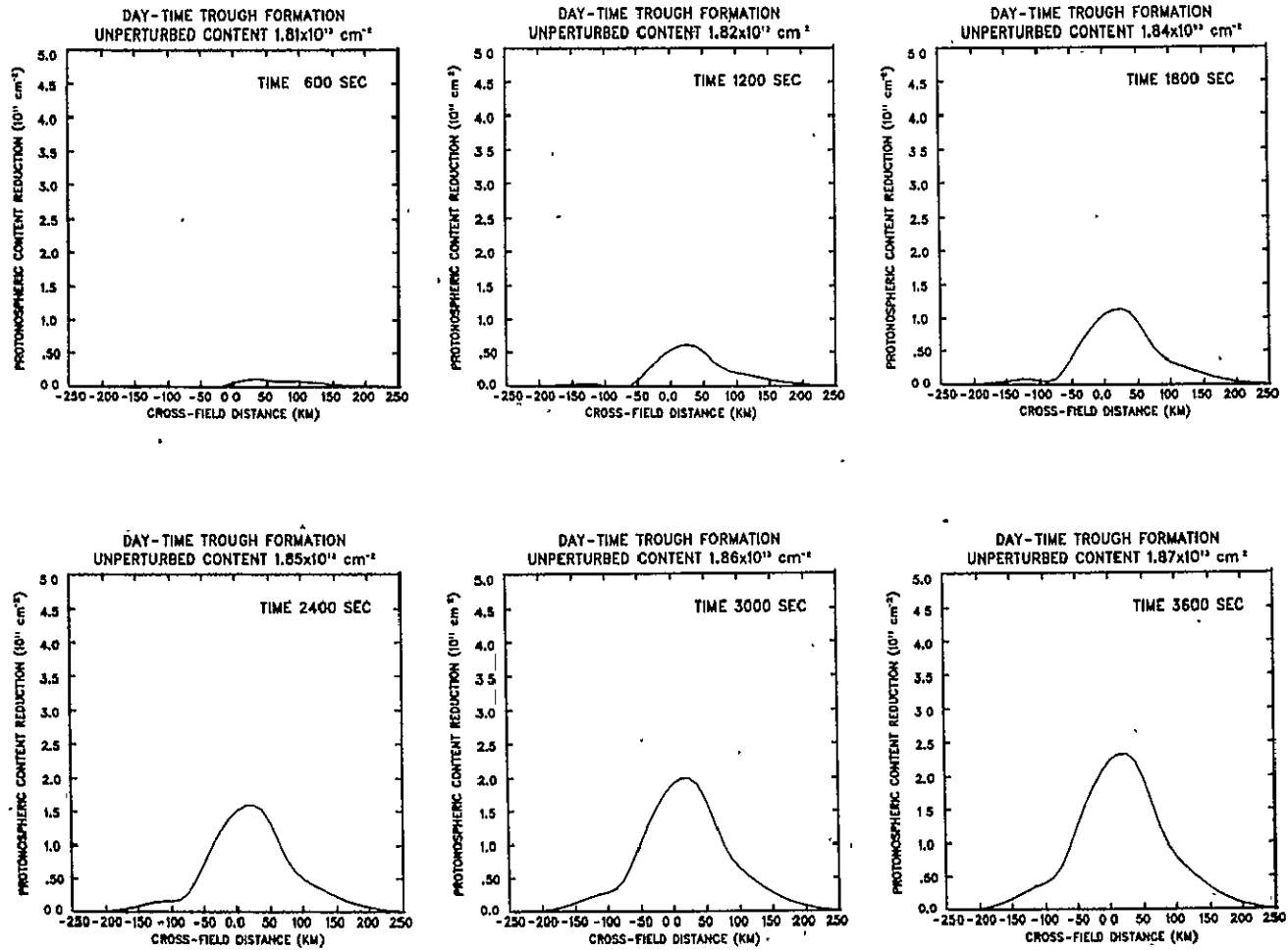
Fig. 21. Daytime depletion of the protonosphere.

is more depleted on its southern side. The central content reduction of the trough approaches a value of 4.2×10^{11} cm^{-2} (a 2.4% reduction in the unperturbed content) with a time constant of ~1 hour. The half width of the tube is 75 km at the surface of the earth. This corresponds to an equatorial tube half width of 390 km.

The daytime protonospheric trough formation is illustrated in Figure 21. The tube depletion is skewed toward the northern side because of the non-sphericity of the released gas cloud and the inclination of the field lines as mentioned earlier. The trough formation in the daytime protonosphere is less rapid than in the nighttime protonosphere because of the thermal plasma expansion produced by the rise in electron temperature. Since the daytime 0^+ concentration is larger tha the ni httime 0^+ concentration, more H_2 reacts in the daytime region near the release point. The diameter of the H_2 cloud, when a fixed amount of the injected gas has reacted with the ionosphere, is larger at night than during the day. Thus, the daytime trough is narrower and has a larger central content reduction than the nighttime trough. The central content reduction of the daytime trough illustrated in Figure 21 approaches a value of 8.8×10^{11} cm^{-2} (4.9% reduction) with a time constant of ~3 hours. The half width of the tube at the surface of the earth is 60 km corresponding to an equatorial half width of 300 km.

The protonospheric depletion may be controlled by varying the amount of gas released. Both the depletion level and the equatorial half width of the protonospheric trough increases with the release of larger quantities of H_2, but the increase is not linear. Figure 22 illustrates the tube content reduction and the tube radius as a function
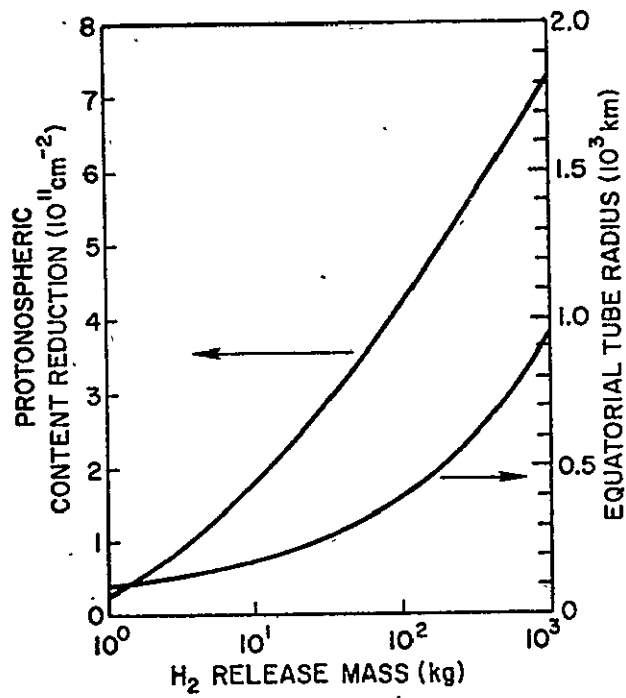
Fig. 22. Nighttime protonospheric depletion
produced by hydrogen released at
300 km altitude.
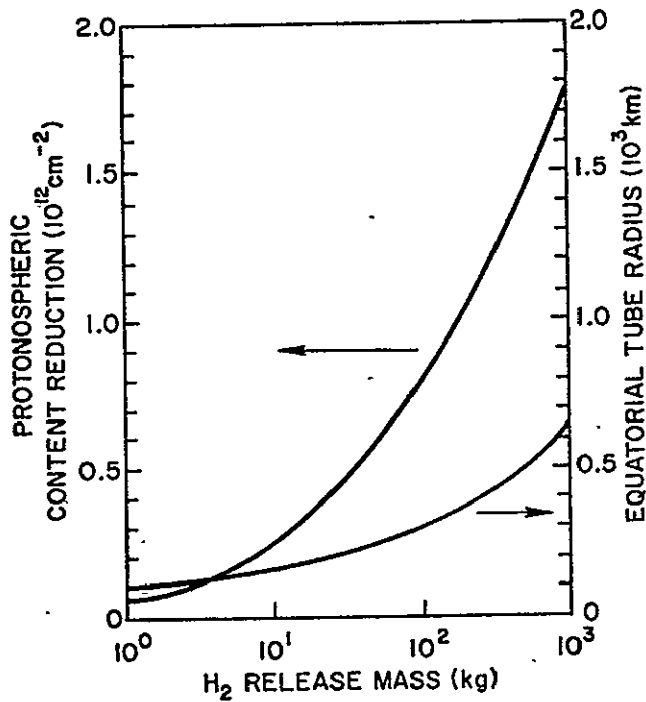
Fig. 23. Daytime protonospheric depletion
produced by hydrogen released at
300 km altitude.

of the amount of nydrogen released at an altitude of 300 km into the nighttime F-region. A tenfold increase in the amount of H_2 released approximately doubles the content reduct on and similarly doubles the tube radius. The variations in the size of the $L = 3$ daytime trough with the amount of H_2 injected at 300 km is shown in Figure 23. Figures 22 and 23 demonstrate that the daytime trough is narrower and more depleted than the nighttime trough.

If multiple releases of H_2 at a fixed point in the depleted magnetospheric tube are possible, any desired protonospheric tube depletion may be achieved. If after each H_2 injection, the F-layer recovers, the protonospheric content reduction will be the depletion produced by one release multiplied by the number of releases but the width of the depleted tube will be the width produced by one release alone. For example, consider the release of 500 kg into the daytime ionosphere. If all 500 kilograms are released at once, a 500 km tube with a depletion of 8% will be formed. However, if the gas is released as five 100 kg injections separated by 24 hours (to allow F-layer recovery), a 22% depletion tube with a half width of 300 km will be produced. In Chapter VIII, it will be demonstrated that a narrower and more depleted protonospheric trough traps a wider range of radio-waves. Thus, by multiple H_2 releases, radio wave guides through the protonosphere may be created. Unfortunately the random movement of the depleted flux tube by ionospheric electric fields makes multiple releases of reactive gases into the center of the tube highly unlikely.

The protonospheric depletion may also be affected by the position of the gas release. Figures 24 and 25 are graphs of the nighttime and daytime tube content reductions for releases of 100 kg H_2 at altitudes

Fig. 24. Nighttime protonospheric depletion produced
by 100 kg H_2 released between 100 and 500 km.
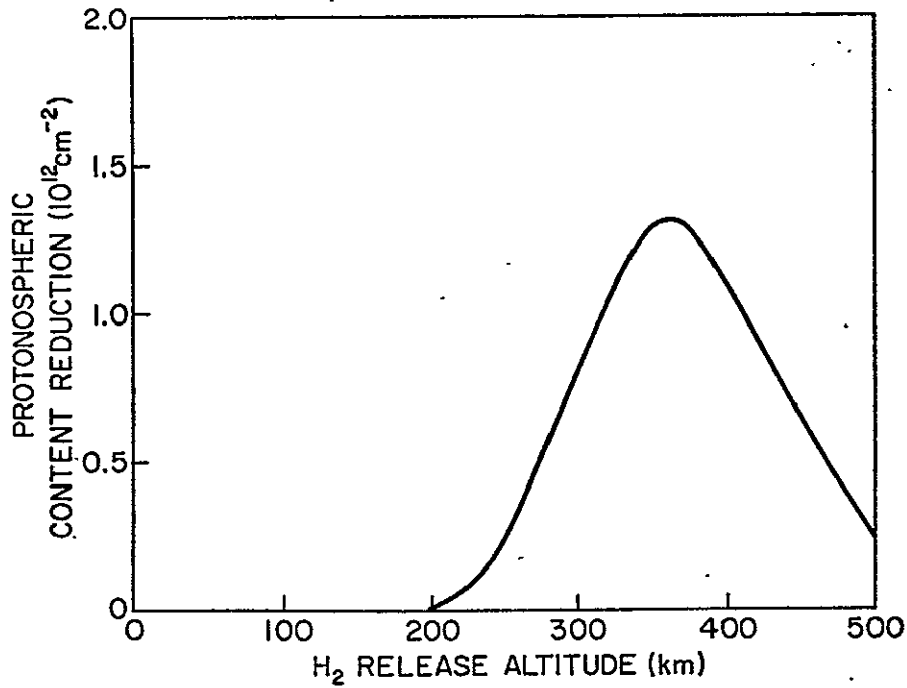
Fig. 25. Daytime protonospheric depletion produced by
100 kg H_2 released between 100 and 500 km.

140
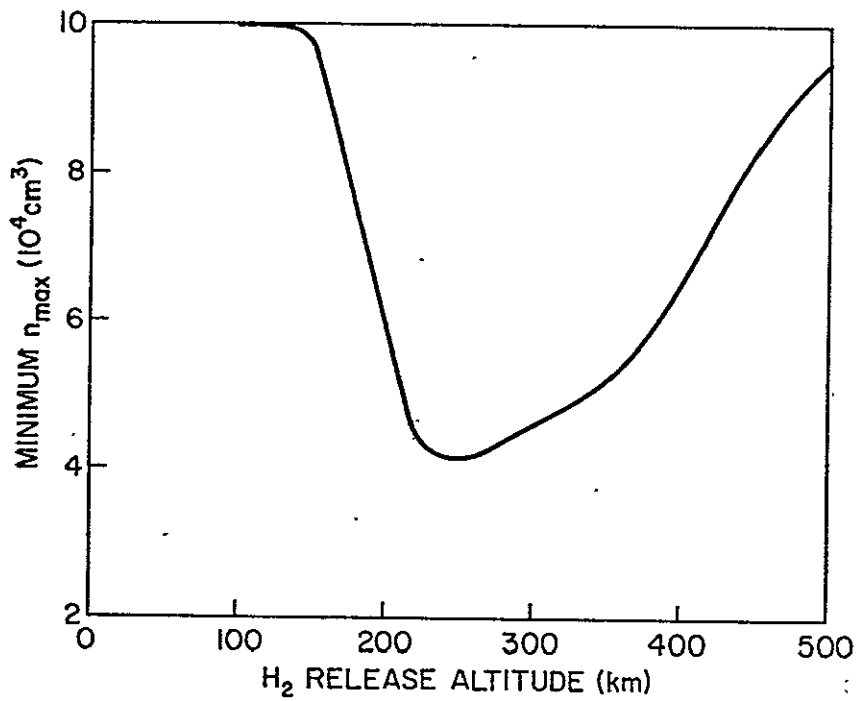
Fig. 26.   Minimum nighttime F-layer peak density pro-
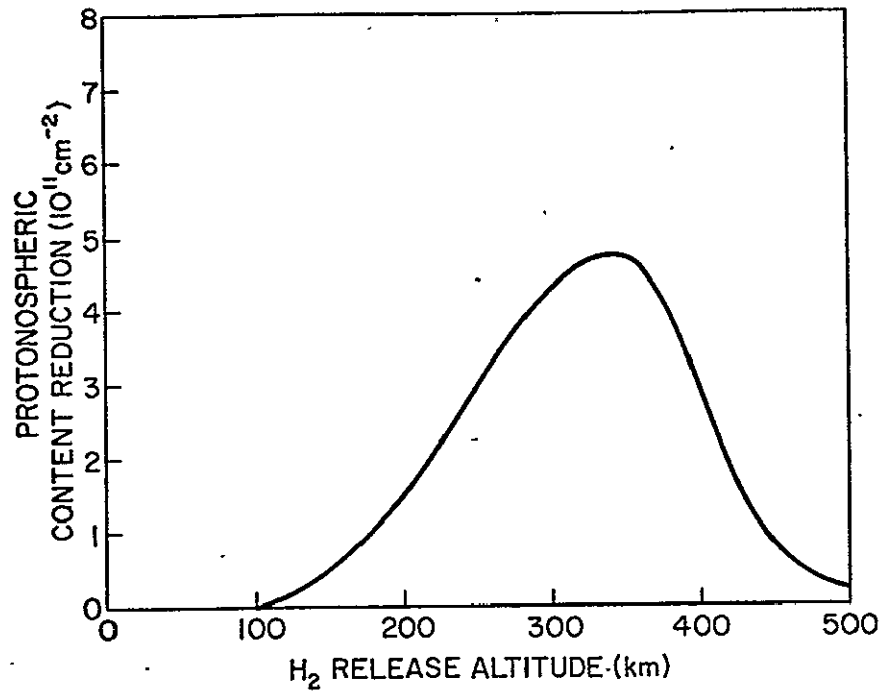duced by the injection of 100 kg H_2.
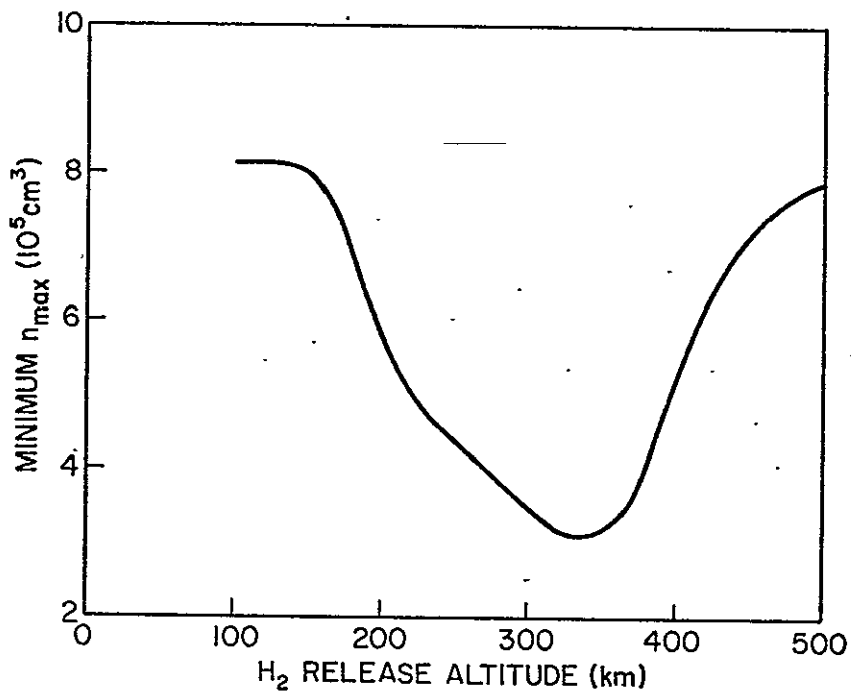
Fig. 27.   Minimum daytime F-layer peak density pro-
duced by the injection of 100 kg H_2.

141

ranging from 100 to 500 km along the $L = 3$ field line. Even though
the peak of the ionosphere is at 300 km, the maximum tube depletion
occurs for 330 km releases at night and for 240 km release during the
day.

The height of the release also has strong effect on the F-layer
peak density. Figures 26 (night) and 27 (day) show the minimum value
of the ionospheric peak density resulting from the release of 100 kg H_2
at varying altitudes. Again, the maximum effect does not occur for
releases right at the F-layer peak.

C. Summary - Stability of the Trough

The coupled plasmaspheric-thermospheric model has been used to
simulate the atmospheric perturbations produced by the release of
diatomic hydrogen into the F-region ionosphere. The gas injection
produces a reduction in the O^+ and electron concentrations, a slight
increase in the H^+ concentration in the $O^+ - H^+$ transition region
and a relative reduction in the H^+ and electron concentration in the
magnetosphere. The increase in the nighttime electron temperature is
small in comparision with the increase in the daytime electron tempera-
ture. The magnitudes of the slight reductions in ion temperatures
during both night and day are about the same.

Further investigation needs to be done concerning the stability
of the protonospheric trough. If strong plasma gradients are created
at the edge of the trough, electric fields may build up tending to
cause plasma transport across the magnetic field lines and produce a
kink in the trough. The problem of confining a neutral region inside
a plasma is the dual of the well studied problem of confining a plasma
inside a magnetic bottle for use in thermonuclear fusion. Thus, well
established theories on plasma stability may be applied to this problem.

142

Chapter VII

AIRGLOW EMISSIONS RESULTING FROM CHEMICAL DEPLETION OF THE IONOSPHERE

In the previous chapter, it was demonstrated that the release of
reactive chemicals into the F-region ionosphere produces 1) supra-normal
electron temperatures, and 2) increased concentrations of foreign poly-
atomic ions. These two disturbed conditions of the atmosphere can cause
observable increases in airglow emissions. At the time of this writing,
no measurements of enhanced airglow coincident with the release of deplet-
ing gases have been made but the theory behind airglow processes is well
understood so that the results of this chapter can probably be confirmed
by experimental measurements.

A. Airglow in the unperturbed ionosphere

Naturally occurring airglow is defined as the emission of radiation
by gases that have been excited by solar electromagnetic radiation. Energy
that is stored and re-radiated after a short delay produces dayglow.
Nightglow results from a long delay in the release of stored energy.

Airglow may be produced by the absorption of radiation into a
molecule or atom producing a transition from its ground state to an
excited state followed by re-emission and transition back to the ground
state. If the re-emission occurs of a wavelength that is the same as
the excitation wavelength, the excitation process is called resonance
scattering. This is contrasted to fluorescence which involves re-
emission at a wavelength that differs from the excitation wavelength.

Excited particles formed by photodissociation of molecules may emit
radiation upon transition to a lower state. Photodissociation of dia-
tomic oxygen by the Schumann-Runge continuum (1350 - 1750 A) produces
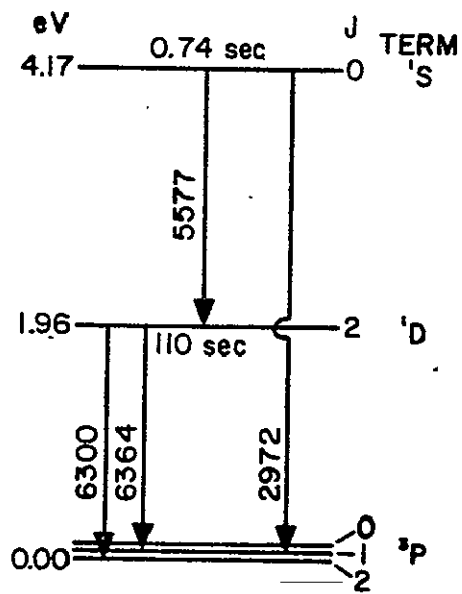
Fig. 1. The energy level diagram of monatomic oxygen for the lowest states.

the first excited state of monatomic oxygen $O(^1D)$ which emits 6300 A radiation upon transition to the ground state $O(^3P)$ [Roble et al., 1975].

Molecules formed by photodissociation may release energy by re-association. The oxygen atoms formed by dissociation of O_2 may undergo 3-body recombination during the night to produce airglow emissions in the 2600 to 3000 A range. [Hunten, 1971].

Chemical energy is stored in a molecule by photoionization. This energy is released by the formation of excited atoms in dissociative recombination reactions. The decay of these excited atoms produces airglow. Consider the following dissociative recombination reactions:

$$O_2^+ + e^- \rightarrow O(^3P) + O(^3P) + 6.85 \quad eV$$
$$or \rightarrow O(^3P) + (^1O) + 4.9 \quad eV$$
$$or \rightarrow O(^3P) + O(^1S) + 2.76 \quad eV$$
$$or \rightarrow O(^1D) + O(^1D) + 3.01 \quad eV$$
$$or \rightarrow (O^1D) + O(^1S) + .79 \quad eV$$
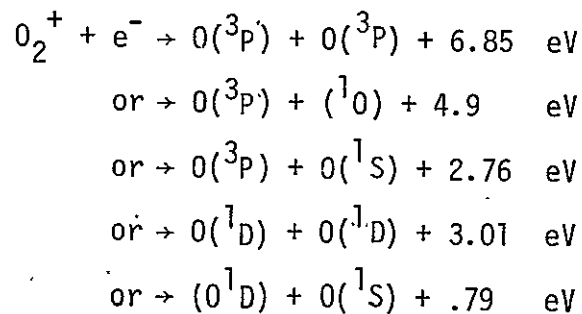
Laboratory measurements indicate that the branching ratios for the production of ^3P, ^1D and ^1S oxygen atoms are 1 : .9 : .1 respectively [Zipf, 1970]. Thus, for every O_2^+ ion annihilated, one ground state $O(^3P)$ atom is formed, .9 excited $O(^1D)$ atom is formed, and .1 excited $O(^1S)$ atom is formed. States $O(^1D)$ and $O(^1S)$ emit radiation at 6300 A and 5577 A respectively (Figure 1).

The production of an excited state may be forbidden by the law of spin conservation. The dissociative recombination reaction

$$NO^+(^1\Sigma^+) + e^- \rightarrow N(^4S) + O(^1D) + .79 \quad eV$$
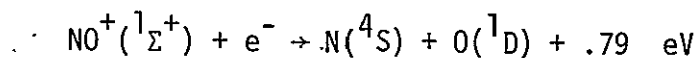
does not conserve spin and therefore is not a mechanism for the production of $O(^1D)$. However the reaction

145

$$NO^+(^1\Sigma^+) + e^- \rightarrow N(^2D) + O(^3P) + .38 \text{ eV}$$
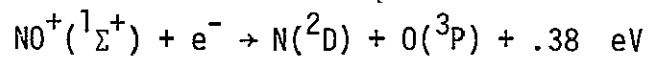
satisfies the spin conservation law. Therefore, dissociative recombination of $NO^+(^1\Sigma^+)$ is a source of $N(^2D)$ which emits 5300 A radiation upon transition to the ground state.

The kinetic energy stored in particles may be transferred to other particles by collisions. The photoelectrons produced in photoionization reactions may excite atoms and molecules through inelastic collisions. Similarly, in regions of high temperatures, the tail of the Maxwellian thermal velocity distribution may contain sufficient electrons to produce significant excitation of neutrals.

Once a particle is in an excited state, it may either radiate by spontaneous emission or be deactivated by transferring its energy to another particle. Thus, deactivation, or "quenching," of excited particles limits the amount of airglow produced. For example, $O(^1D)$ atoms can be quenched by nitrogen molecules and by electrons.

$$O(^1D) + N_2 \rightarrow O(^3P) + N_2 \quad \text{rate:} \quad k_2 = 7 \times 10^{-11} \text{ cm}^3\text{sec}^{-1} \quad [\text{Noxon, 1970}]$$
$$O(^1D) + e^- \rightarrow O(^3P) + e^- \quad \text{rate:} \quad k_3 = 2 \times 10^{-9} \text{ cm}^3\text{sec}^{-1} \quad [\text{Seaton, 195 }]$$
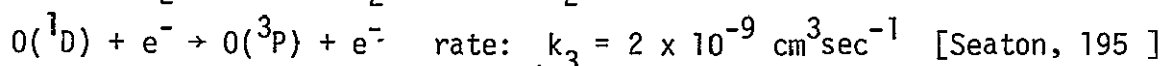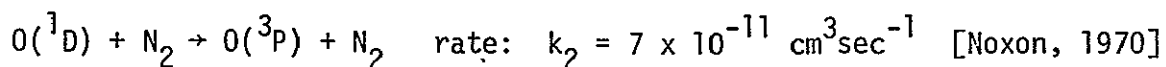
(2)

Many spectral lines are found in the F region airglow. In the rest of this section, only the 6300 A line attributed to $O(^1D)$ will be considered. This line is produced by photodissociation of O_2, photoelectron impact with O, dissociative recombination, and thermal electron impact with O. The four components of the daytime 6300 A airglow are compared in Figure 2. The two components produced by Schuman-Runge photodissociation of O_2 and by photoelectron impact are from Roble [private communication, 1975]. The last two components in Figure 2 are results
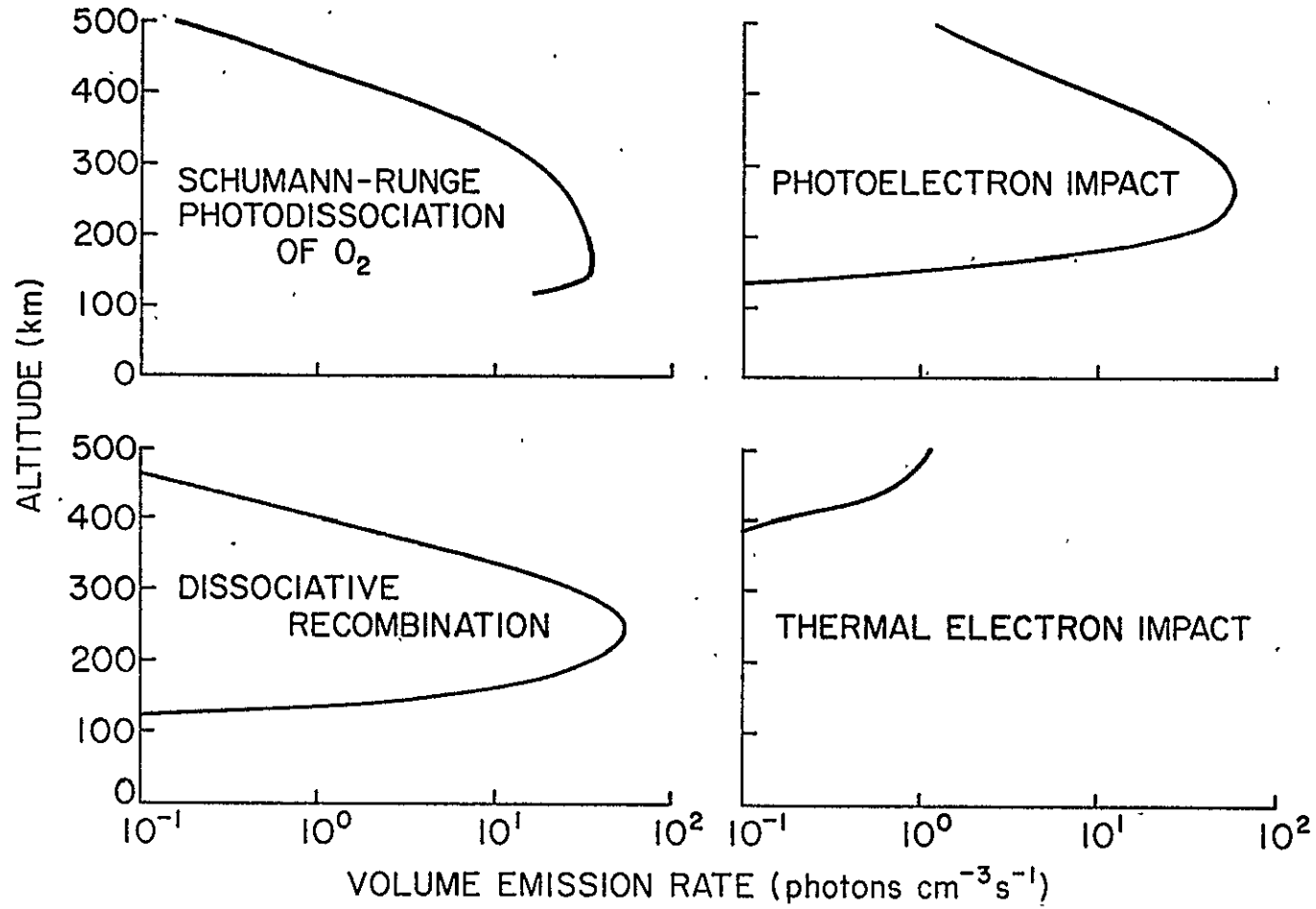
Fig. 2. Daytime 6300 airglow components in the unperturbed F-region.

of a simulation of the unperturbed daytime ionosphere using the model of the concentrations and temperatures described in Chapter VI. During the night, only the dissociative recombination airglow component is significant. Calculations of other airglow lines, such as $O(^1S)$ 5577 A, $N(^2D)$ 5200 A, and $O_2(^1\Sigma)$ 7619 A, are similar to the $O(^1D)$ 6300 A line calculations described below.

The dissociative recombination component of the $O(^1D)$ 6300 A airglow is found by considering 1) the rate of polyatomic ion production by reaction of O^+ and neutrals, 2) the rate of dissociative recombination of these ions to produce $O(^1D)$, 3) the quenching rate (Equation 5.2), and 4) the spontaneous emission rate given by

$$O(^1D) \rightarrow O(^3P) + h\nu \qquad \text{rate} = A_{21} = .01 \text{ sec}^{-1}$$
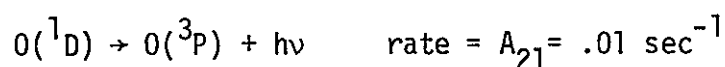
The continuity equation describing the 6300 A emission resulting from the production of $O(^1D)$ according to the O_2^+ dissociative recombination reactions given in Equation 5.1 is

$$\frac{d[O(^1D)]}{dt} = \mu\beta_1[O^+] - k_2[O(^1D)][N_2] - k_3[O(^1D)]n_e - A_{21}[O(^1D)]$$

$$\frac{dh\nu}{\partial t} = A_{21}[O(^1D)] \equiv \epsilon_{DR} \tag{3}$$

where μ is the number of $O(^1D)$ atoms produced by the dissociative recombination of one O_2^+ ($\mu \simeq 1$), $\beta_1 = k_1[O_2]$ is the recombination coefficient due to O_2, $k_1 = 1.5 \times 10^{-11}$ cm^3/sec, k_2 and k_3 are specified in Equation (5.2) and ϵ_{DR} is the photon volume emission rate (photons cm^{-3} sec^{-1}) resulting from dissociative recombination. Under steady state conditions, the volume emission rate becomes

$$\epsilon_{DR} = \beta_1[O^+]/\{1 + (k_2[N_2] + k_4 n_e)/A_{21}\} \qquad \text{photons/cm}^{-3}\text{sec}^{-1} \tag{4}$$

148

The volume emission rate for $O(^1D)$ activated by thermal electron collisions is calculated in a similar manner. The excitation process is represented by

$$O(^3P) + e^* \rightarrow O(^1D) + e \qquad \text{rate} = s_{21} \qquad (5)$$
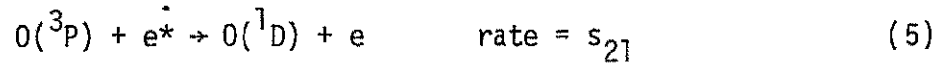
where e^* is a high energy electron.

Collisional excitation of $O(^1D)$ is strongly dependent on temperature because of the exponential nature of the Maxwell thermal velocity distribution. Electrons must have energies above 2 eV to induce transitions from the ground state, $O(^3P)$, to the next highest level, $O(^1D)$ (Fig. 1). The excitation coefficient is calculated from

$$s_{12} = \int_{v_{12}}^{\infty} Q_{12}(v)\, v\, f(v)\, dv \qquad (6)$$

where Q_{12} is the velocity dependent collisional cross section for 0

          v is the velocity

          $f(v)$ is the velocity distribution

          v_{12} is the minimum velocity needed to excite the atom.

For a Maxwellian distribution this equation becomes [Seaton, 1955]

$$s_{12} = 2 \times 10^{-9}\, e^{-(E_2 - E_1)/kT_e} \quad cm^3/sec \qquad (7)$$

where $E_2 - E_1$ = minimum excitation energy = 2 eV

          T_e = electron temperature

          k = Boltzmann constant

The volume emission rate is calculated considering excitation, quenching, and spontaneous emission.

$$\varepsilon_{TE} = s_{12}n_e[0]/[1. + (k_2[N_2] + k_3n_e)/A_{21}] \qquad (8)$$

Profiles of the daytime 6300 A volume emission rate due to dissociation recombination, ε_{DR}, and due to thermal electron collision, ε_{TE}, are shown in Fig. 2. Under typical conditions, ε_{DR} is greater than ε_{TE}, but when T_e becomes greater than 3000 K, ε_{TE} may be significant.

Integration of the emission rate along the line of sight gives the observed brightness. The brightness is measured in terms of a columnar emission rate as given by

$$I = \int_0^\infty \varepsilon(z)dz \cdot 10^{-6} \qquad (9)$$

where   I is intensity in Releighs.

$\varepsilon(z)$ is volume emission rate in photons per m^3 per sec.

z = distance along line of sight in meters.

B. Airglow in the perturbed ionosphere

Chemical energy stored in an injected gas may be released in the form of heat and light. Observations of airglow are a measure of the changes in chemical energy resulting from aeronomic reactions with the perturbing gas.

Any of the reactive gases mentioned in Chapter II will produce polyatomic ions which, upon dissociative recombination, will produce enhanced airglow. In this section only OH^+, the charge exchange product of O^+ and molecular hydrogen, is considered. Energy is released in the dissociative recombination process

$$H_2 + O^+ \rightarrow OH^+(^3\Sigma^-) + H \qquad\qquad \text{RATE: } 2.0 \times 10^{-9} \text{ cm}^3 \text{ s}^{-1}$$

$$\left.\begin{array}{l} OH^+(^3\Sigma^-) + e^- \rightarrow H + O(^3P) + 8.77 \text{ eV} \\[6pt] \qquad\qquad\quad \rightarrow H + O(^1D) + 6.81 \text{ eV} \\[6pt] \qquad\qquad\quad \rightarrow H + O(^1S) + 4.6 \text{ eV} \end{array}\right\} \quad \text{RATE: } k_5 \simeq 1 \times 10^{-7} \text{ cm}^3 \text{ s}^{-1}$$
$$(10)$$
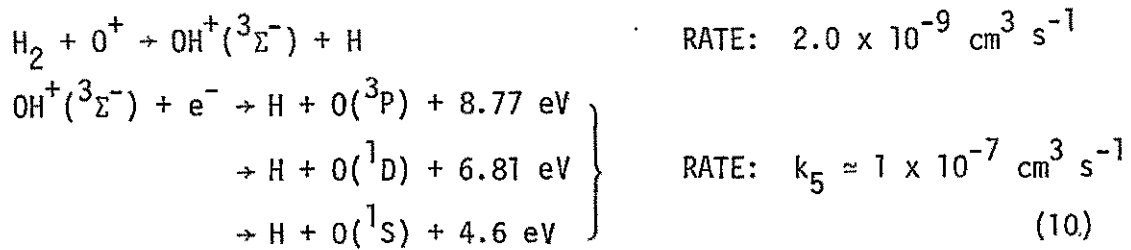
Spin is conserved in all of these reactions. The branching ratios for the production of the three lowest states of oxygen from $OH(^3\Sigma^-)$ are unknown at the present time and are taken to be $\frac{2}{3} : \frac{1}{6} : \frac{1}{6}$ for $O(^3P)$, $O(^1D)$ and (O^1S) respectively.

An interesting form of deactivation results from the chemical reaction between O and H_2. The reaction with the oxygen in its ground state, $O(^3P)$, does not proceed rapidly because the reaction is slightly endothermic

$$O(^3P) + H_2 \quad OH + H - .08 \text{ eV} \qquad \text{rate: } k_6' = 1.7 \times 10^{-13} \text{ cm}^3/\text{sec}$$
$$(11)$$
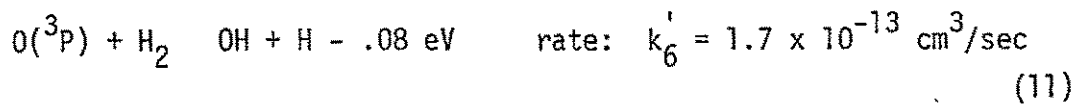
The energy possessed by the $O(^1D)$ state is enough to make the reaction exothermic [Schofield, 1967]

$$O(^1D) + H_2 \rightarrow OH + H + 1.88 \text{ eV} \qquad \text{rate: } k_6 = 2 \times 10^{-11} \text{ cm}^3/\text{sec}.$$
$$(12)$$
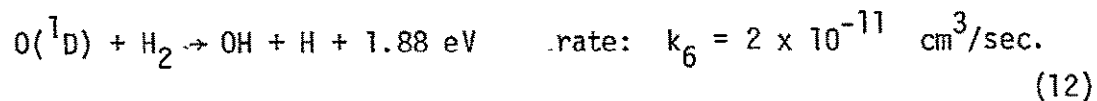
While this is not quenching in the strict sense, it does remove excited oxygen atoms. Thus, the addition of molecular hydrogen to the ionosphere layer produces a modified volume emission rate (compare with (4)).

$$\varepsilon_{DR} = \frac{[\beta_1[O^+] + k_5[OH^+]n_e/3]}{[1 + (k_2[N_2] + k_3 n_e + k_6[H_2])/A_{21}]} \qquad (13)$$

Simulated nighttime profiles of ε_{DR} along the field line through the point of H_2 injection are shown in Figure 3 for various times relative to the time of injection. After one minute, the peak nighttime volume emission rate has increased by a factor of 10. At this time, a

Fig. 3. Nighttime λ6300 airglow produced by dissociative recombination.

large bite-out in the emission profile results from the severe depletion of O^+ around the point of release. As the O^+ and H_2 concentrations diminish, the peak airglow emission level drops below the unperturbed emission level. After one half hour, the nighttime 6300 A emission rate at the point of injection is one third the emission rate just prior to injection.

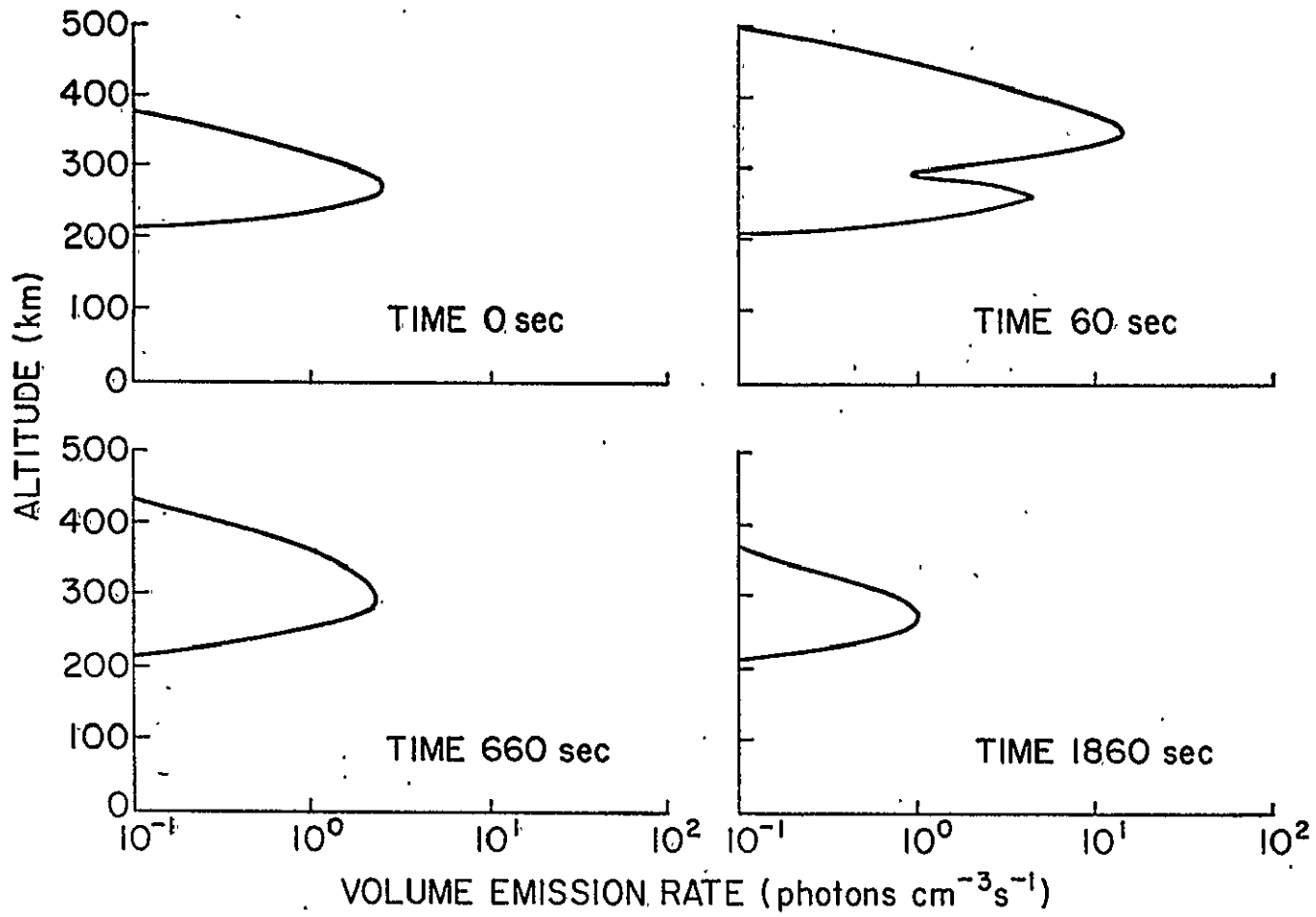The volume emission rate is enhanced in regions where H_2 and O^+ exist simultaneously. This is illustrated in the sequence of meridional plane emission maps shown in Figures 4 through 7. Figure 4 shows the 6300 A airglow layer just before gas injection. One minute after injection, a bright torus around the field line through the point of injection is formed (Figure 5). The intensity inside the ring is low because of the chemical depletion of the O^+ along the central magnetic field tube. The torus expands with the H_2 gas cloud producing a "smoke ring" effect (Figure 6). The emission on the left (southern) side of the ring is stronger than the emission on the right (northern) side of the ring because, at night, an equatorward neutral wind is blowing the left side of the H_2 cloud into regions of undepleted O^+.

The nighttime variation in the 6300 A intensity found by integration along the field line through the point of H_2 injection is shown in Figure 8. The unperturbed nighttime intensity level is 18 Rayleighs in this example. 60 seconds after the H_2 release the intensity rises to a maximum of 120 Rayleighs. Because of the O^+ depletion, the intensity level drops below the unperturbed intensity level reaching a minimum value of 11 Rayleighs after 1800 minutes. Finally, as the ionosphere recovers, the intensity level approaches the unperturbed level.

The large regions of increased electron temperatures resulting from the release of H_2 during the day produce increased airglow. Using

NIGHT-TIME λ6300 VOLUME EMISSION RATE
LOG₁₀(ε₆₃₀₀, photons cm⁻³ sec⁻¹)
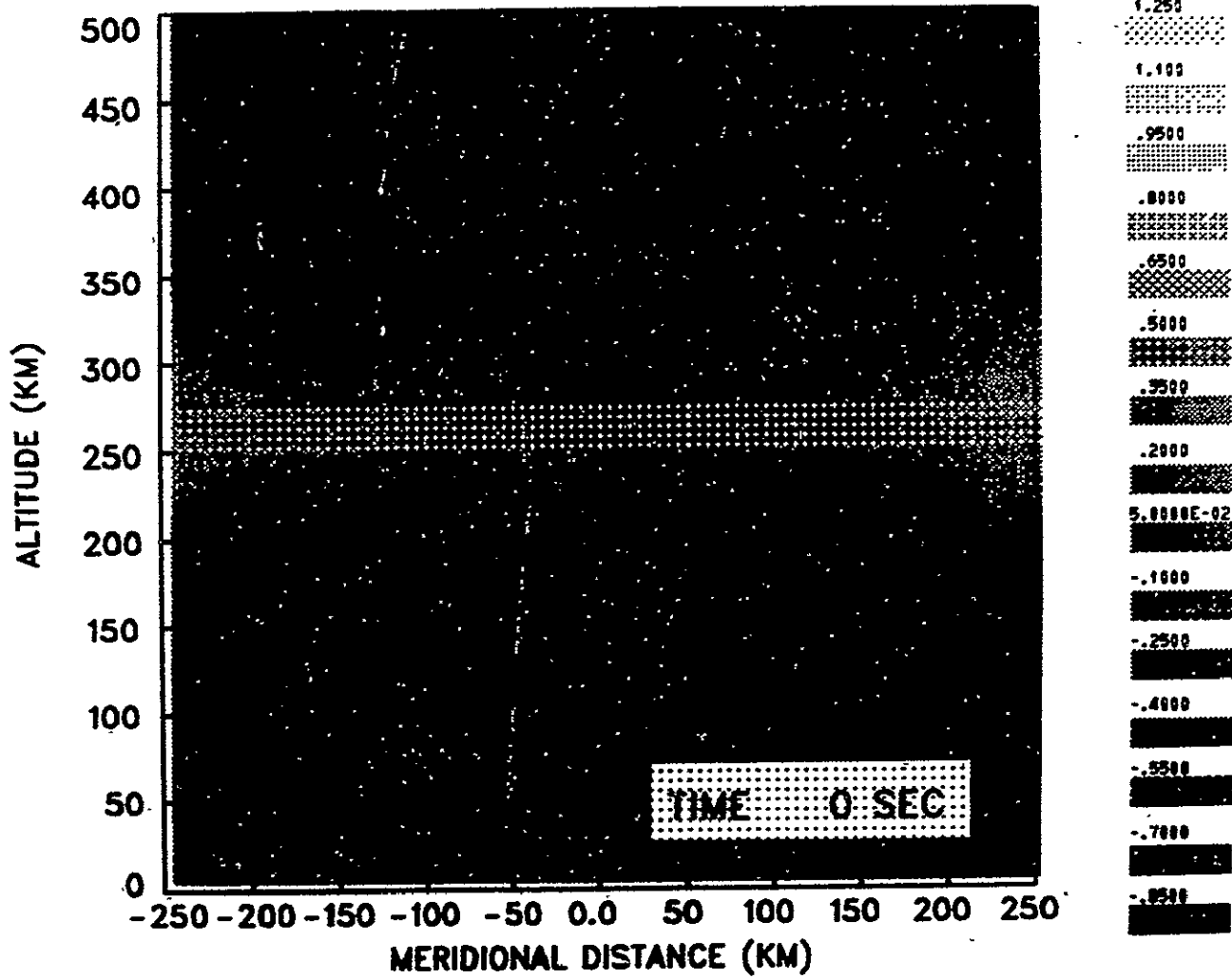
Fig. 4.   Unperturbed nighttime airglow layer.
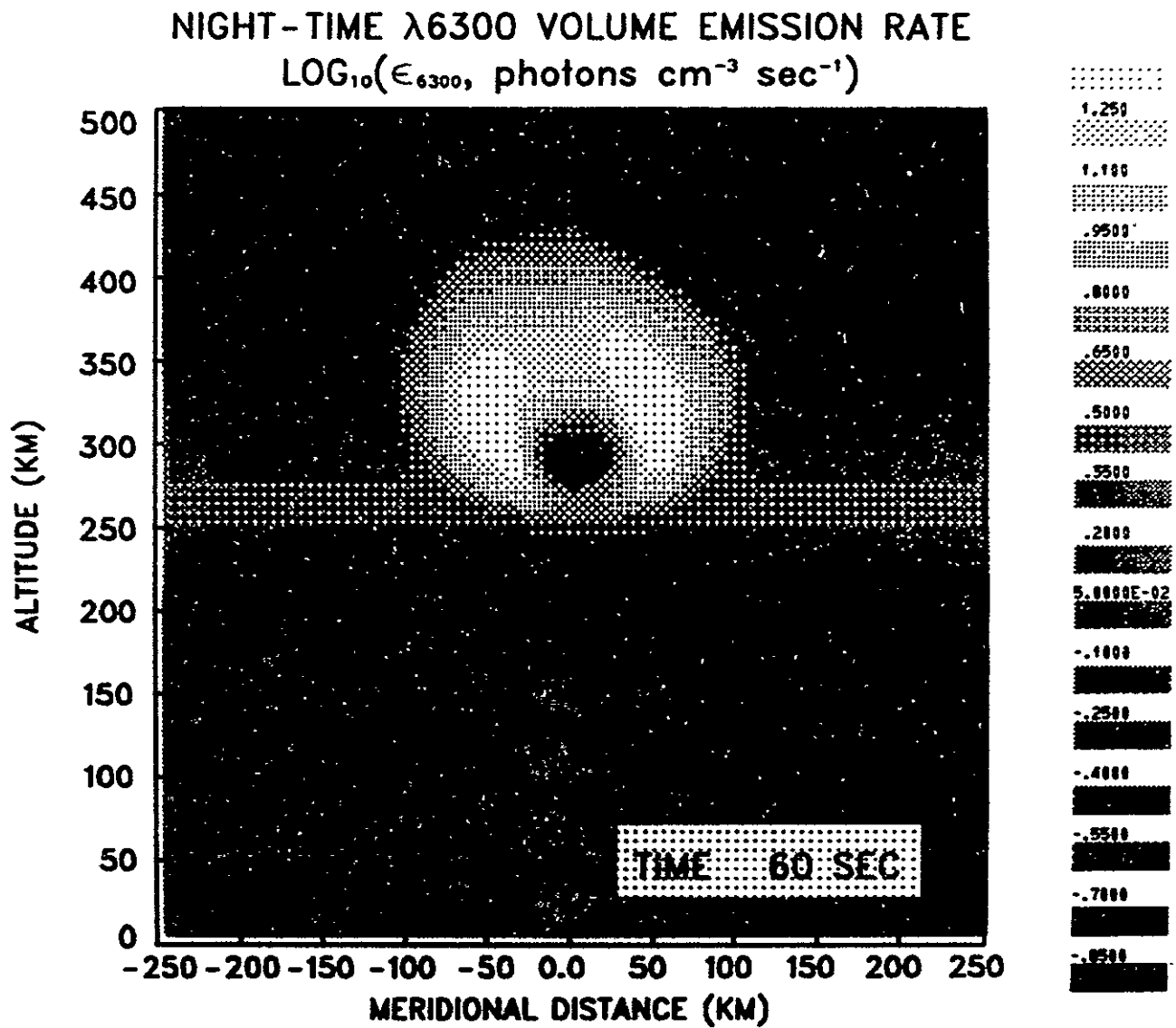
Fig. 5. Bright ring formed one minute after H_2 injection.

155

Fig. 6. Expanding λ6300 airglow ring.

NIGHT-TIME λ6300 VOLUME EMISSION RATE
LOG₁₀(ϵ_{6300}, photons cm⁻³ sec⁻¹)
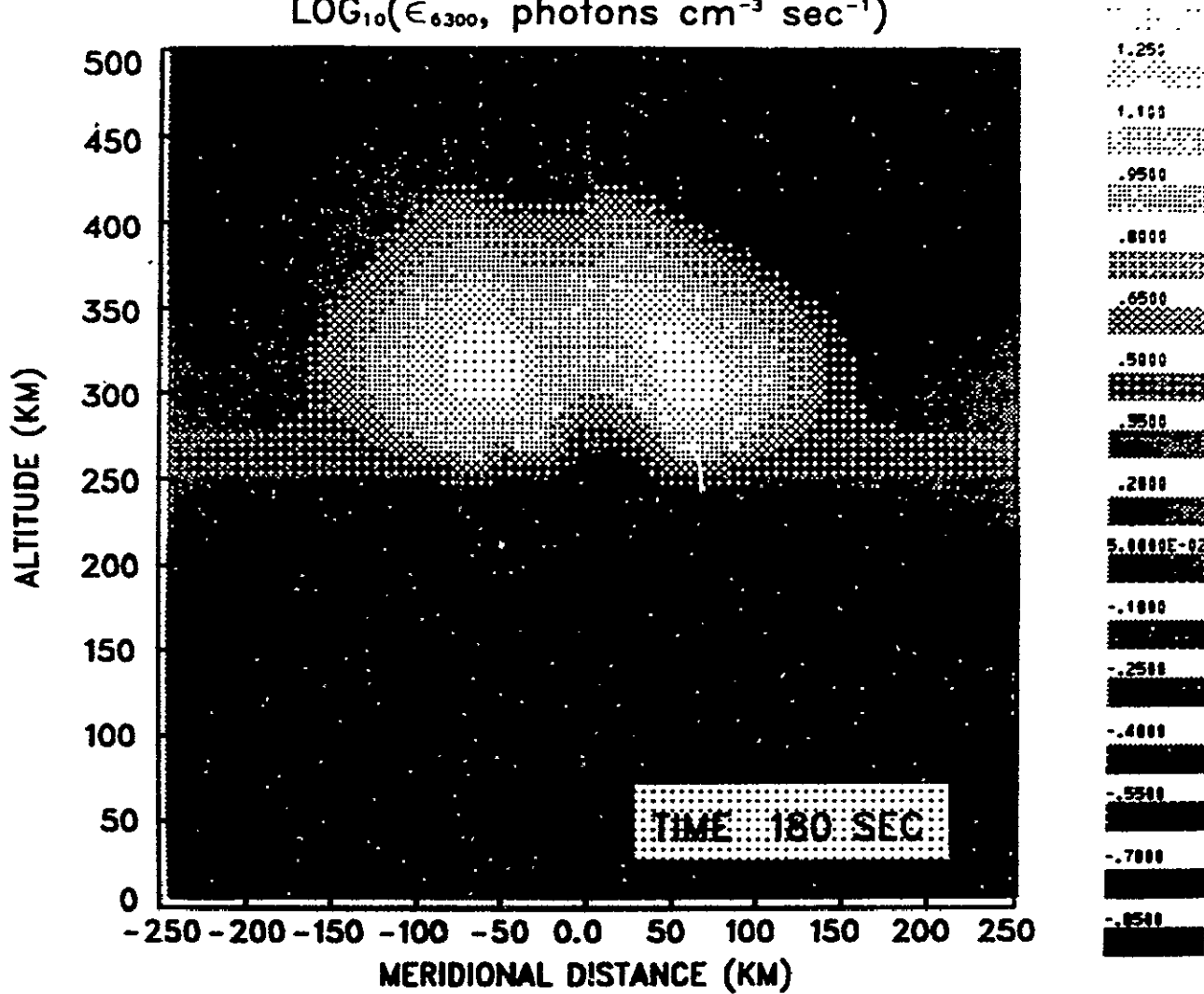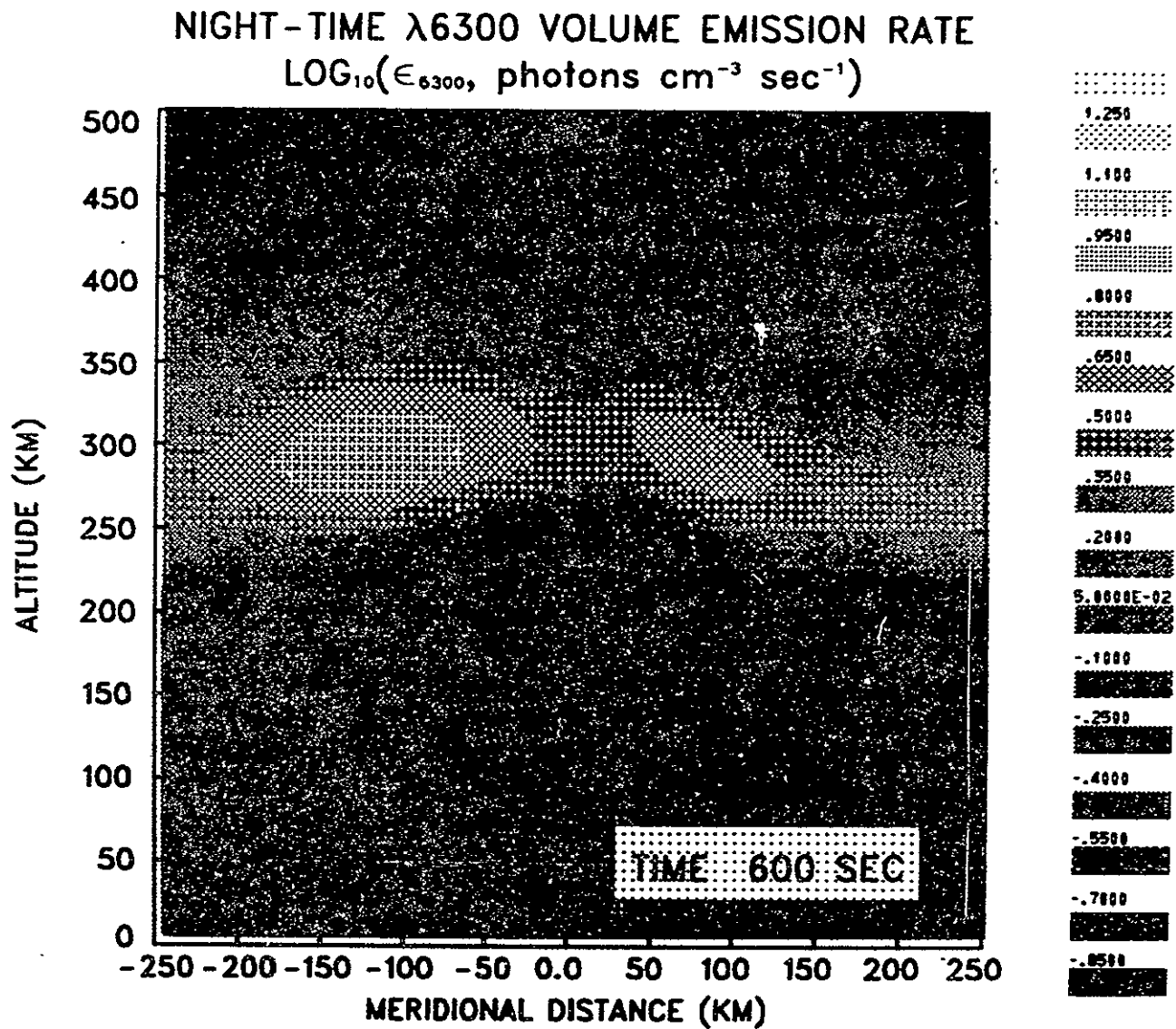
Fig. 7. Asymmetry in nighttime airglow ring due to equatorward neutral wind.
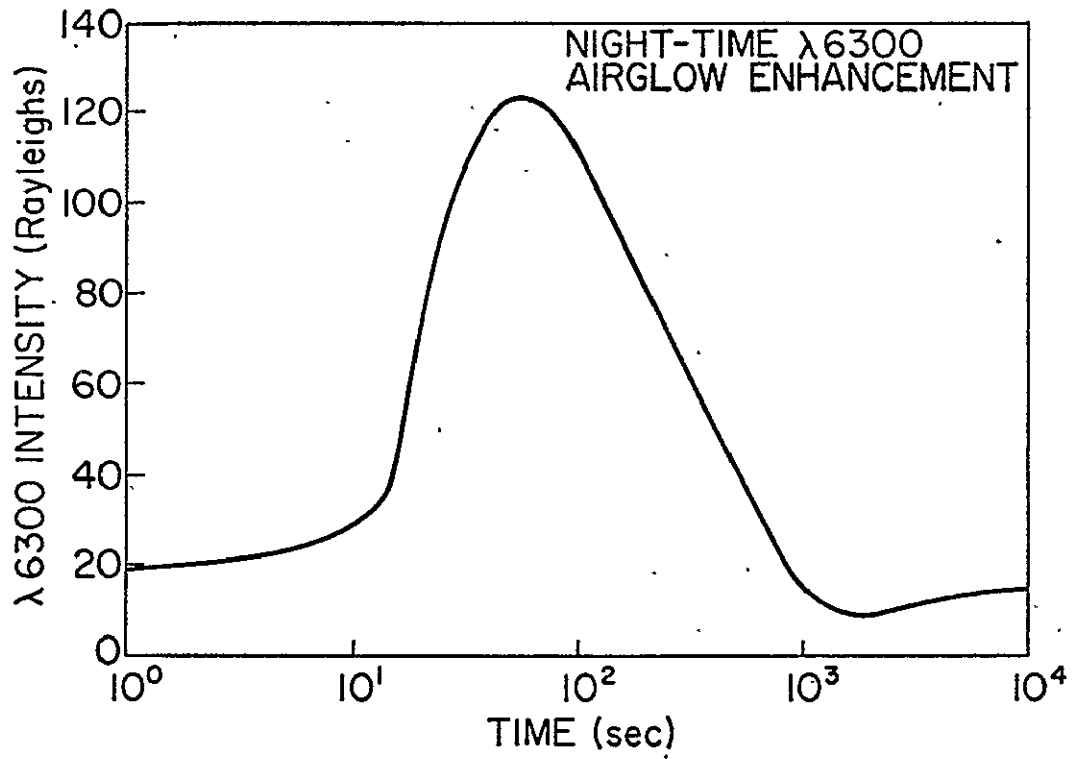
Fig. 8. Temporal variations in intensity through the center of the expanding ring.

Equations 5.7 and 5.8 (modified to include H_2 deactivation), the thermal electron impact volume emission rate profiles are calculated. These profiles are compared with the daytime dissociative recombination airglow profiles in Figure 9. One minute after H_2 release, the dissociative recombination 6300 A airglow component dominates the thermal electron component. However, ten minutes later, after the H_2 and 0^+ have been exhausted and remaining electrons have been heated, ε_{TE} becomes larger than ε_{DR}.

The expanding "smoke ring" effect is seen in the daytime emission maps in Figures 10-13. The daytime ring is more symmetric than the nighttime ring because no neutral wind was used in the daytime model. High altitude, field aligned increases in the emission rate are produced by high temperature electrons 6 minutes after gas release (Figure 14).

As at night, the daytime airglow intensity increases rapidly after chemical release (Figure 15). The peak intensity after 60 seconds is due to dissociative recombination of OH^+. After this time, the dayglow decays at a slower rate than the nightglow because of the contribution from collisional excitation by the electron gas. Without thermal electron impact, the dayglow intensity level would decay below the unperturbed level (Figure 15, dashed curve).

C. Summary - Use of Airglow Enhancement Measurements

The effects of ionospheric depletion are measurable from airglow fluctuations. The temporal and spatial variations in airglow emission are directly related to the physical processes producing and resulting from F-region plasma reduction. The 6300 A line intensity arising from the first excited state of monatomic oxygen is sensitive to variations in the F-region temperature and polyatomic ion concentration.
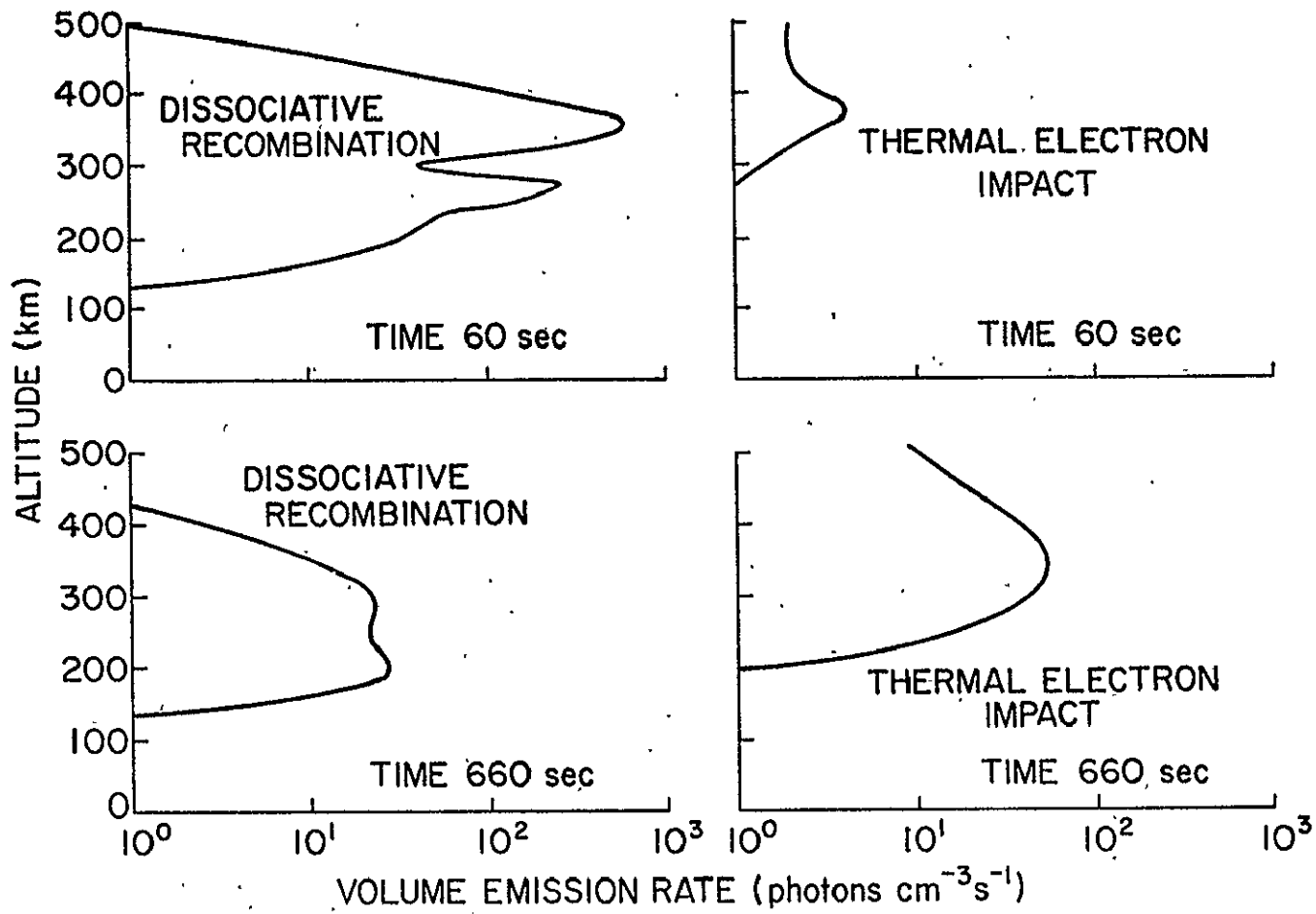
Fig. 9. Perturbed daytime λ6300 airglow components.
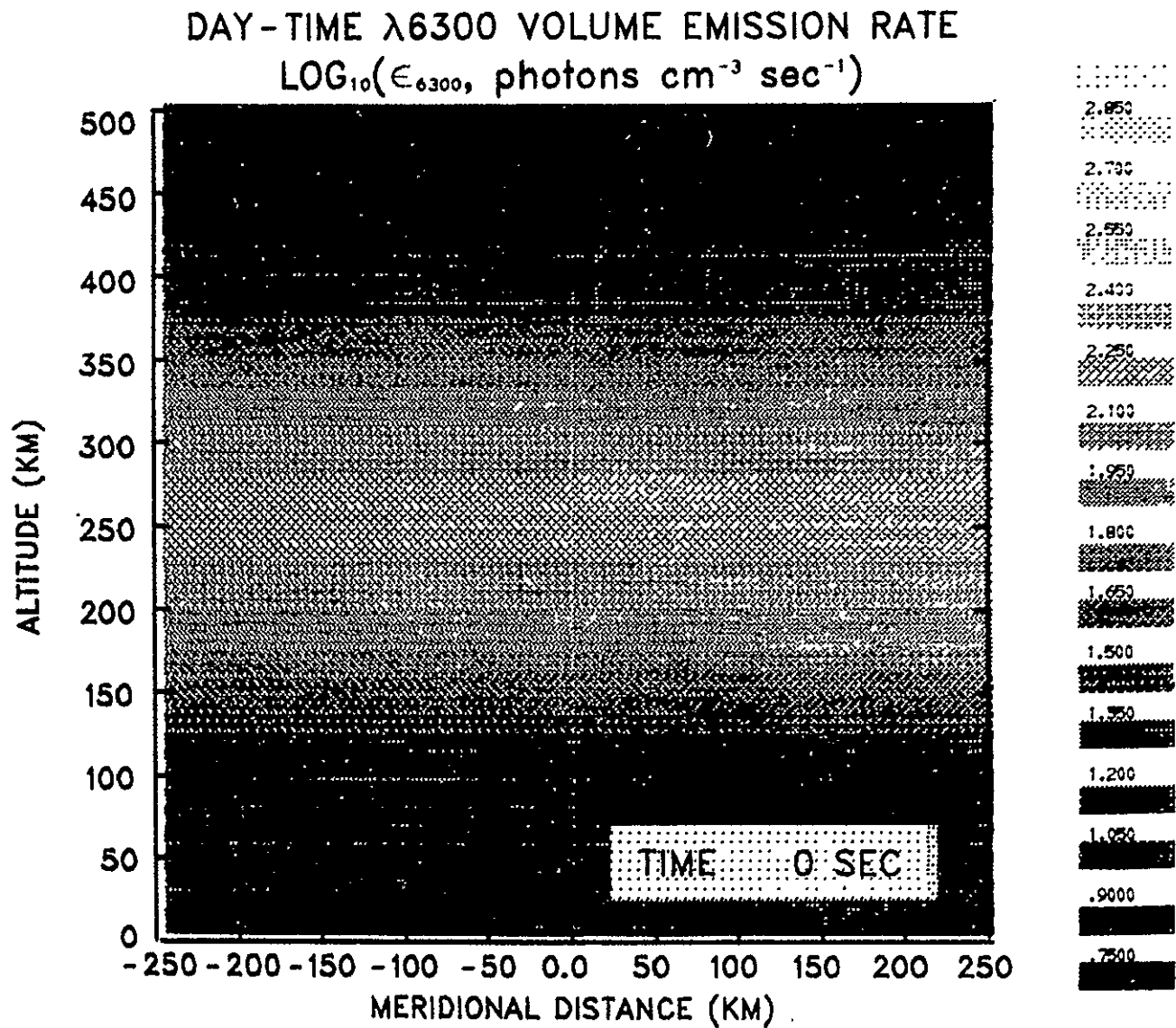
Fig. 10. Unperturbed daytime airglow layer.
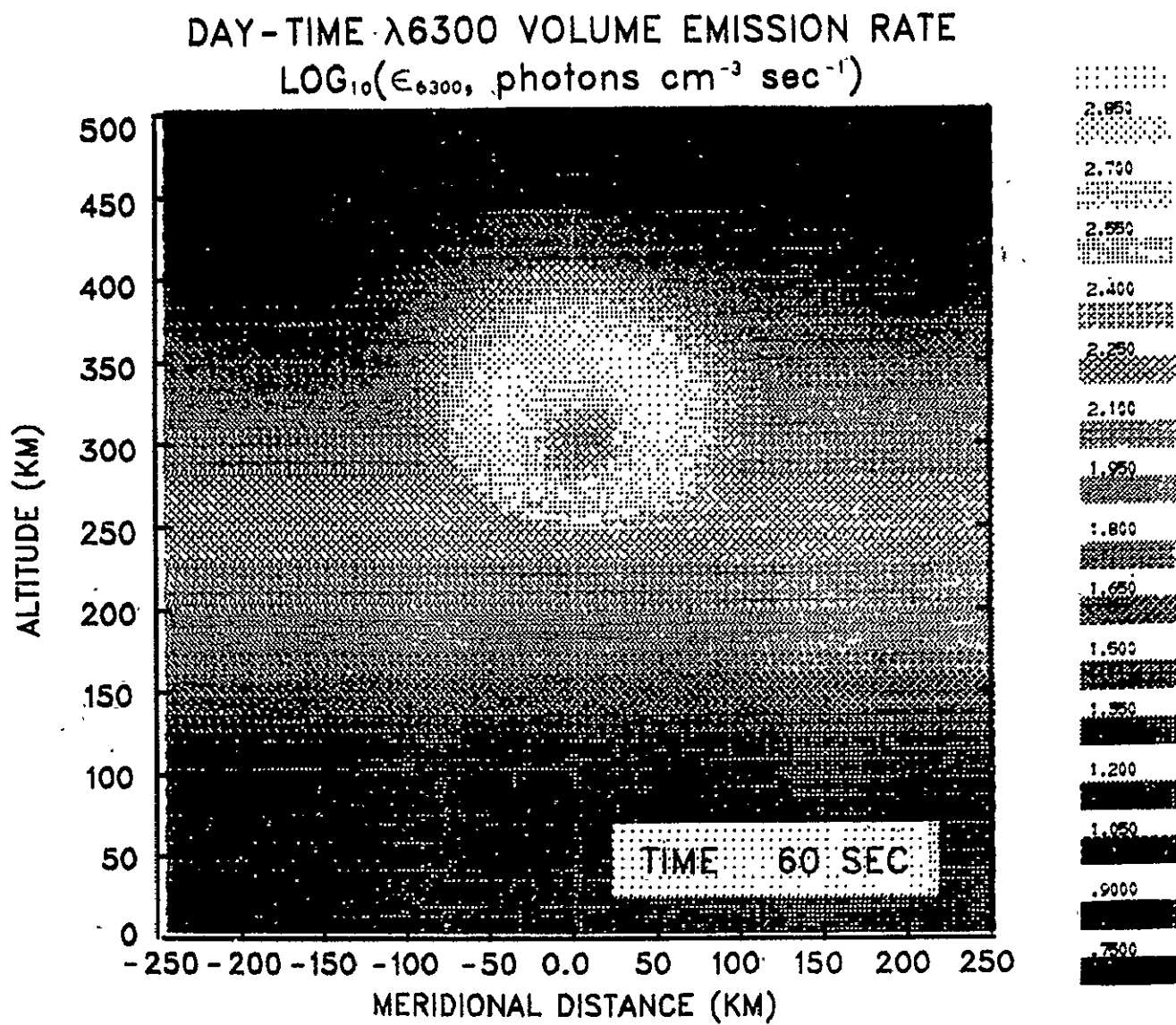
161

DAY-TIME λ6300 VOLUME EMISSION RATE
$LOG_{10}(\epsilon_{6300},$ photons cm^{-3} $sec^{-1})$

Fig. 11. Bright ring formed one minute after H_2 injection.
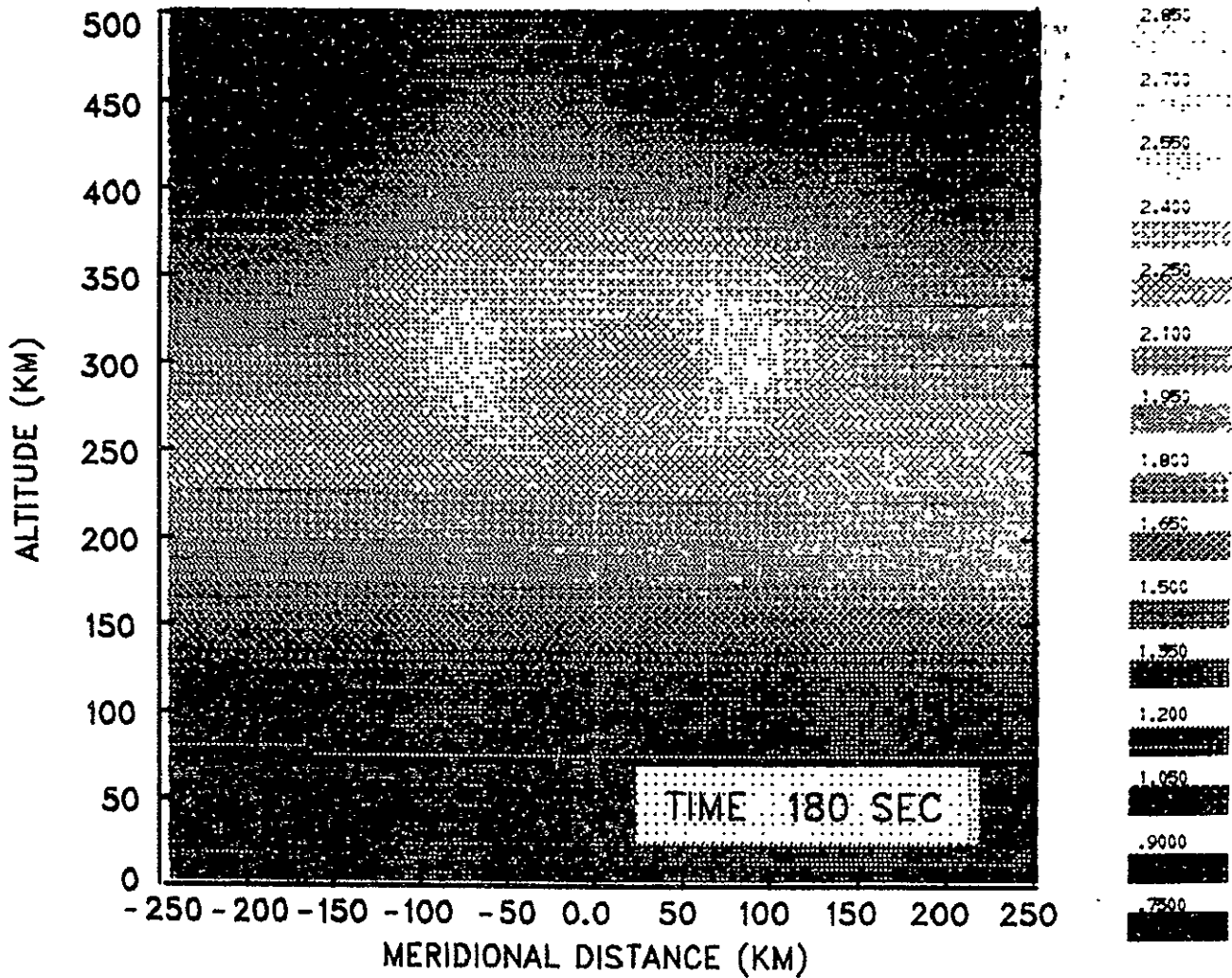
Fig. 12.   Expanding λ6300 airglow ring.
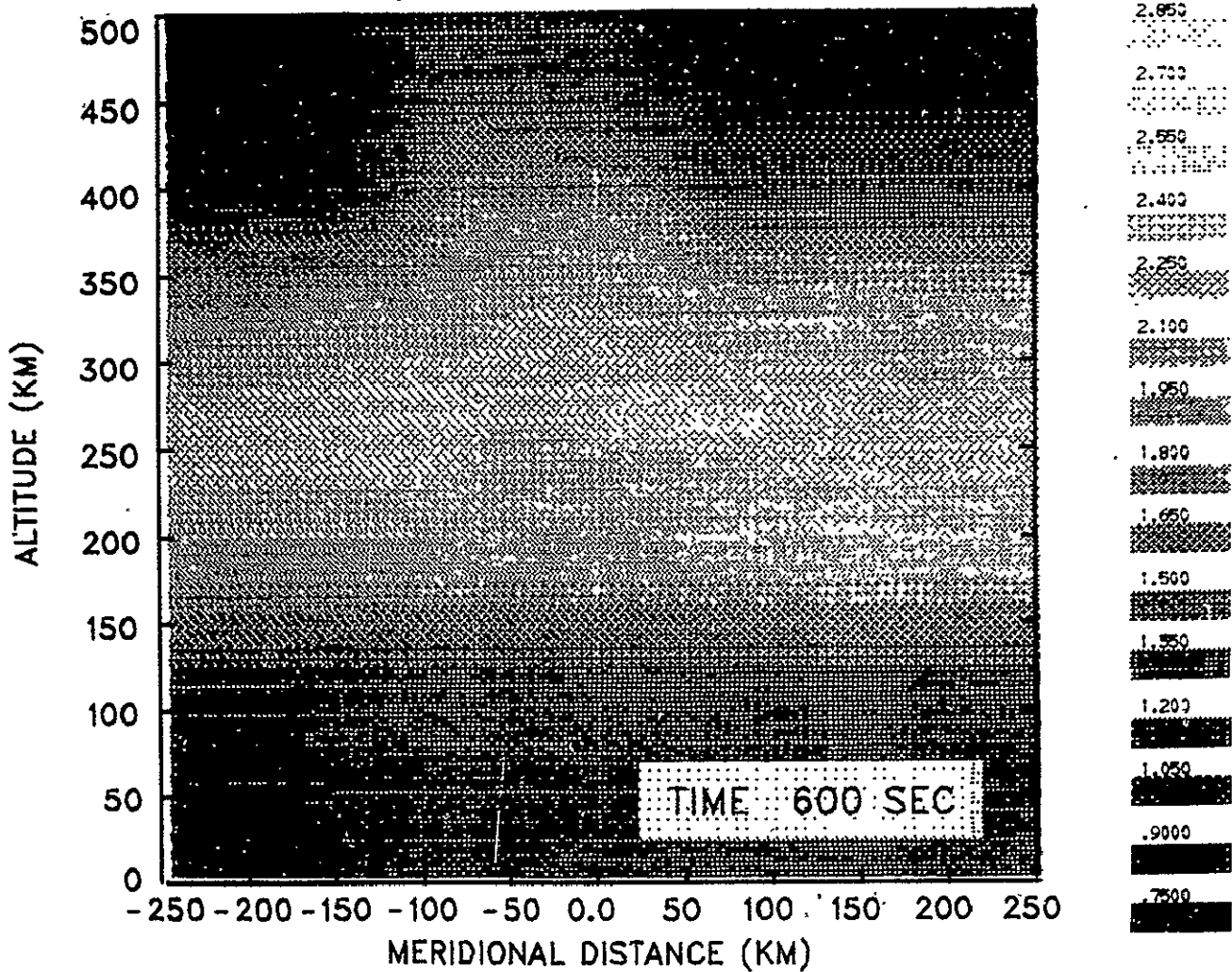
Fig. 13. Perturbed daytime airglow layer containing the effects of dissociative recombination and thermal electron impact.

DAY-TIME λ6300 VOLUME EMISSION RATE

$LOG_{10}(\epsilon_{6300}$, photons cm^{-3} $sec^{-1})$
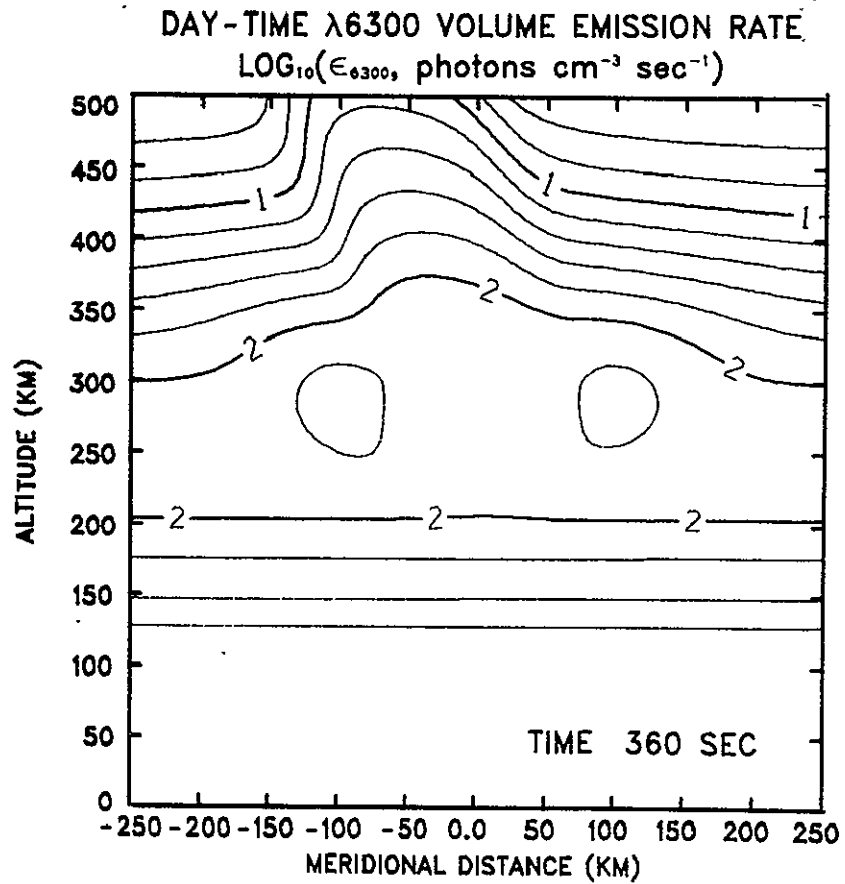
Fig. 14. Daytime airglow modification containing
high altitude perturbation by thermal
electron impact and remnants of the
expanding ring at the F-layer peak.
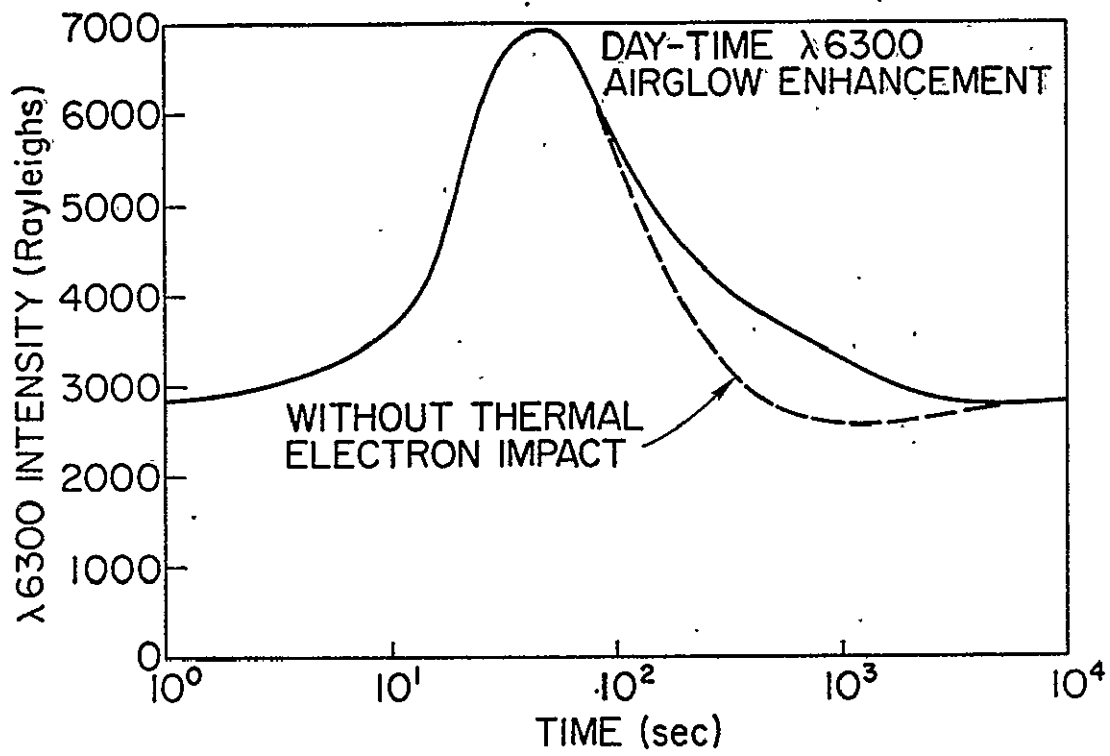
Fig. 15. Temporal variations in intensity containing dissociative recombination and thermal electron impact effects.

NEUTRAL
WIND

$$\bar{E} \times \bar{B}$$
TUBE DRIFT
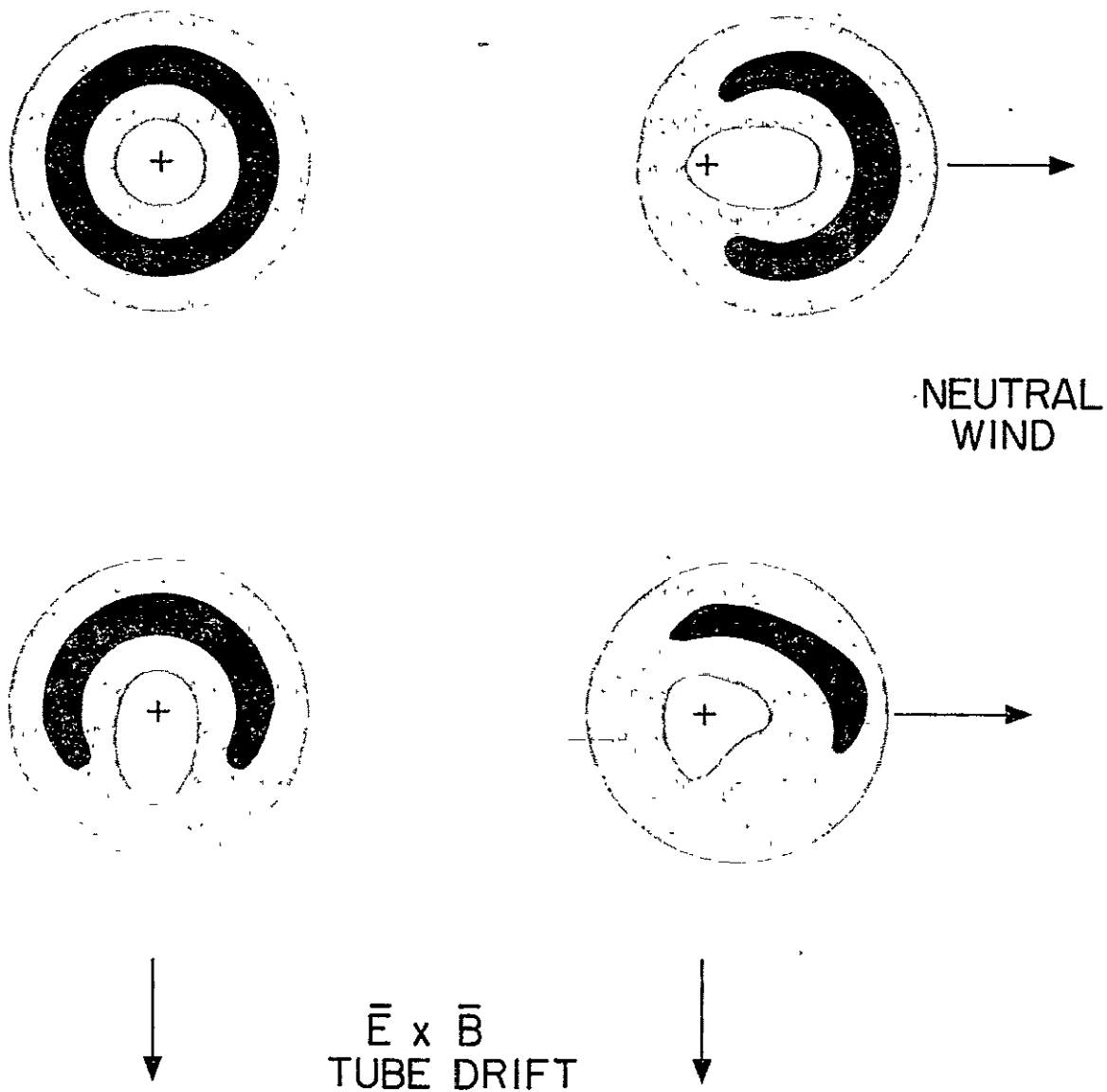
Fig. 16. Structure of the expanding airglow ring in the presence
of external neutral winds or electric fields.

Other lines in the airglow spectrum such as the 5577 A line O(^{1}S), the 5200A line of N(^{2}D), and the 7619A line of O$_2$($^1\Sigma$), have different sensitivities to fluctuations in the state of the F-region. Simultaneous observations of variations in several spectral lines may permit isolation of the thermal and chemical airglow excitation mechanisms.

The morphology of the expanding airglow ring is an indication of the electric fields and neutral winds in space surrounding the point of gas release. The changes in the ring as observed from the ground are shown schematically in Figure 16. Without any externally imposed E-winds or fields the ring will be circularly symmetric around the gas release point. A neutral wind will move the injected gas cloud toward one side of the depleted flux tube resulting in an elongated airglow ring with maximum brightness in the direction of the neutral wind. An electric field will move the partially depleted plasma tube toward the edge of the injected gas cloud. Thus, a neutral wind will move the optical portion of the ring away from the gas release point in the direction of the wind and in contrast, an electric field will move the hole in the ring away from the gas release point in the direction of the $\vec{E}x\vec{B}$ tube drift. By measuring the variations in the structure of the airglow ring with respect to the point of gas injection, the magnitude and direction of neutral winds and electric fields deforming the airglow ring may be estimated.

Chapter VIII

INFLUENCE OF THE CHEMICALLY DEPLETED IONOSPHERE ON THE PROPAGATION OF ELECTROMAGNETIC RADIATION

The artificially depleted ionosphere and magnetosphere will produce variations in refractive index which affect the propagation of E-M radiation. Changes in radio waves propagating through the modified plasmasphere are indicative of physical changes occurring in this region.

A wide spectrum of radiowave signals is affected by the region of depressed plasma density. Section A describes the reflection of HF radio waves from the bottomside ionosphere in the presence of a trough. Section B describes the trapping of HF and VLF waves in a depleted plasma tube formed by the draining of the protonosphere into the hole created in the ionosphere. Trapped waves may interact with the plasma producing amplification and/or particle precipitation. The transit time of a signal between two points in a depletion duct is related to the plasma density along the duct. VHF and HF wave propagation through the F-region trough is examined in Section C. These waves suffer changes in amplitude, phase and polarization. Measurements of these changes may be used to estimate the time evolution of the depletion region. The ionospheric hole may be used as a lens for focusing extragalactic radio signals.

A. Ground-based investigation of the depleted ionosphere by electromagnetic waves.

HF ray trajectories may be significantly affected in the vicinity of a trough. Generally, rays reflected from the sides of the trough

are defocused. Focusing occurs for rays propagating through the depleted region (see section C). Radio waves with frequencies greater than the critical frequency at the trough center may escape through the ionospheric hole. Doppler frequency shifts in the returned HF waves indicate trough movement. Therefore, if an ionosonde is used to measure the structure of the chemically depleted ionosphere, angle-of-arrival and Doppler information may be necessary for proper interpretation of the ionograms. A theoretical study of reflection of high frequency ionospheric radio waves in the vicinity of a trough has been presented by Helms and Thompson [1973].

Incoherent scatter radars are valuable tools for studying electron densities, electron and ion temperatures, and plasma drifts in the 200 to 800 km region. The power of radar signals scattered from the ionosphere is proportional to the electron density at the scattering point. The width of the received power spectrum is directly related to the electron-to-ion temperature ratio. The Doppler shift of the power spectrum is a measure of the plasma motion along the radar line-of-sight [Evans, 1969; Carpenter and Bowhill, 1971]. Thus, Thomson (incoherent) scatter radars may be used to determine density and temperature perturbations resulting from the injection of reactive gases.

B. HF and VLF Radiowave Trapping in Depletion Ducts

This section provides a simple theory of ionospheric and magneto-spheric guided propagation involving depletion ducts. This mode of propagation differs from HF propagation in earth-detached radio ducts [Carrara et al., 1970]. Raypaths following field aligned troughs (as opposed to raypaths guided by the ionospheric layer parallel to the earth's surface) are considered. The self-focusing property of ducted

170

waves has been examined [Sodha et al., 1972]. Only the existence of trapping based on comparison of the ray curvature and the duct curvature is considered here.

A rarified plasma tube extending through the magnetosphere becomes a duct when it guides electromagnetic waves. In the guiding process, the raypaths are bent by the gradients of refractive index resulting from the variations of plasma density in the tube. A ray is said to be trapped if it tends to be bent toward the center of the tube when it is propagating parallel to the tube.

The trapping criteria are found by equating the radius of curvature of the magnetic tube with the radius of curvature of the ray at each point along the tube. If the ray radius of curvature is smaller than the radius of curvature at the upper side of the tube, the ray is bent toward the center of the tube and is trapped. If the ray radius of curvature exceeds the upper side radius of curvature, the ray is not bent sharply enough to remain in the duct (Figure 1). Similar arguments are appropriate for bending of rays at the lower side of the tube. The transition between trapped and untrapped rays occurs for the marginally trapped ray which has a curvature equivalent to the duct curvature.
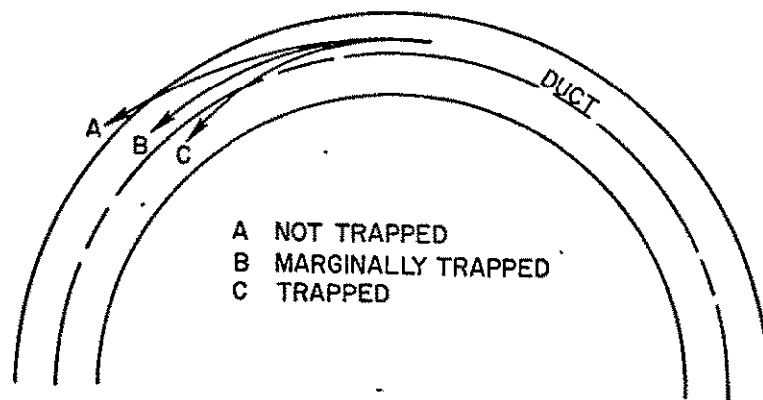
Fig. 1. Trapping in a curved duct.

171

Since the trough is aligned with the geomagnetic field, the radius of curvature changes along the raypath. For a centered dipole approximation of the magnetic field, the duct radius of curvature is given by

$$\rho_0 = \frac{R_0}{3} \frac{(4-3\ R/R_0)^{3/2}}{(2-R/R_0)} = \frac{R_0}{3} \frac{(1+3\ \sin^2\lambda)^{3/2}}{(1+\sin^2\lambda)} \tag{1}$$

where ρ_0 is the duct radius of curvature, R the geocentric distance to a point on the field line, R_0 the geocentric distance to the equatorial point on the field line, and λ the invariant latitude (Figure 2). The radius of curvature is maximum at the equator ($\lambda=0$) with a value of $R_0/3$
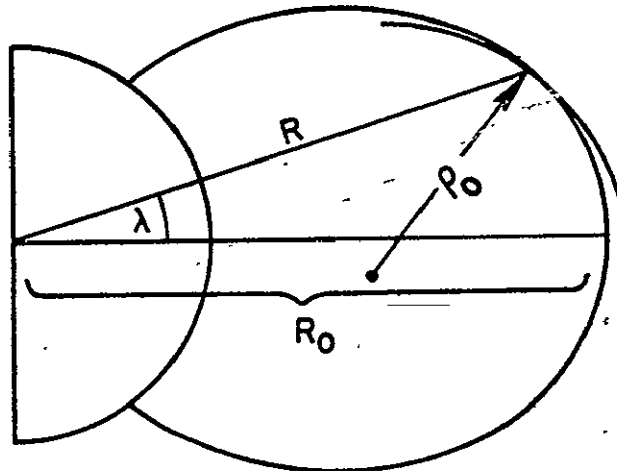
Fig. 2. Centered dipole magnetic field geometry.

The ray radius of curvature is determined from the wave normal radius of curvature and from the relationship between the ray angle and the wave normal angle. The wave normal radius of curvature, determined from the differential phase velocity across the propagation path, is found to be

172

$$\rho_{wn} = \frac{dx}{d\theta} = \frac{v_p}{dv_p/dr} = \frac{-\mu}{d\mu/dr} \tag{2}$$

where ρ_{wn} is the wave normal radius of curvature, dx the incremental distance along the path, $d\theta$ the change in wave normal angle along the path, v_p the phase velocity, dv_p/dr the change in phase velocity across the propagation path and μ the refractive index (Figure 3).
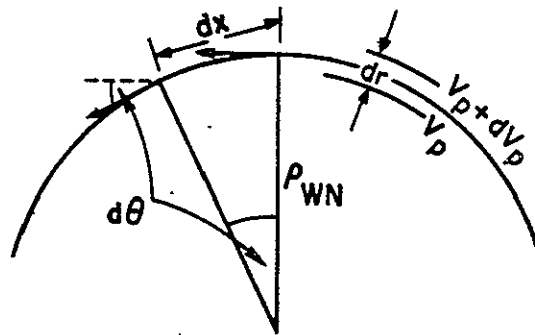
Fig. 3. Wave-normal bending.

The ray radius of curvature is defined as

$$\rho_{ray} = \frac{dx}{d\beta} \tag{3}$$

where $d\beta$ is the change in ray angle. This expression is written in terms of the wave normal radius of curvature.

$$\rho_{ray} = \frac{dx}{d\theta} \frac{d\theta}{d\beta} = \rho_{wn} \frac{d\theta}{d\beta} \tag{4}$$

The term $d\theta/d\beta$ is the differential change of wave normal angle with ray direction and has the value of unity in isotropic media.

HF radio waves propagating nearly parallel to the magnetic field direction (i.e., quasi-longitudinal or "QL" propagation) have identical ray and wave normal directions [Budden, 1966]. It is clear that this condition of quasi-longitudinal (QL) propagation applies to trapped HF radiation in field aligned troughs. For this condition, $d\theta/d\beta = 1$ and the ray radius of curvature is given by

$$\rho_{ray} = \frac{-\mu}{d\mu/dr} \qquad (5)$$

The QL approximation to the refractive index is

$$\mu^2 = 1 - \frac{X}{1 \pm |Y_L|} \qquad (6)$$

where $X = f_n^2/f^2$; f is the wave frequency; $f_n = \frac{1}{2}\sqrt{n_e e^2/(\varepsilon_0 m)}$, the electron plasma frequency; n_e is the local electron density; e the electron charge; ε_0 the dielectric constant of free space; m the electron mass; $Y_L = f_L/f$; $f_L = \frac{eB}{m2\pi} \cos \theta_m$, the longitudinal component of the electron gyrofrequency; B is the imposed magnetic flux density; and θ_m the angle between the magnetic field and the wave normal. The plus and minus signs denote the extraordinary and ordinary modes of propagation, respectively. Practical expressions for X and Y_L are

$$X = 80.6 \ n_e/f^2$$

$$\qquad (7)$$

$$Y_L = 2.8 \times 10^{10} B \cos \theta_m/f$$

where the units for n_e and B are electrons per meter^3 and Webers per meter^2, respectively.

The refractive index is further simplified by noting that Y_L is much less than unity for HF propagation in the magnetosphere. With this approximation,

$$\mu^2 \simeq 1 - x \tag{8}$$

(The difference between extraordinary and ordinary mode trapping is not considered here.) Using (5) and (8), the HF ray curvature becomes

$$\rho_{ray} \simeq \frac{2(1-X)}{dX/dr} \tag{9}$$

A Gaussian variation in the crossfield electron density is assumed and is given by

$$n_e(r,R) = n_0(1-d\ e^{-r^2/2a^2}) \tag{10}$$

where $n_0(R)$ is the unperturbed electron density, d is the relative density reduction at the center of the duct, $a(R)$ is the half width of the duct, and r is the cross duct distance ($r=0$ at the center of the trough). A 500 kg release of H_2 at $L=3$ into the daytime ionosphere produces an 8% depletion duct with an equatorial half width of 500 km (Chapter VI). The numerical examples in this section are for a 500 km duct with a variable depletion factor. The $n_0(R)$ function is based on a diffusive equilibrium model of the magnetosphere [Angerami and Thomas, 1964; Park, 1972]. Figure 4 shows the $n_0(R)$

175
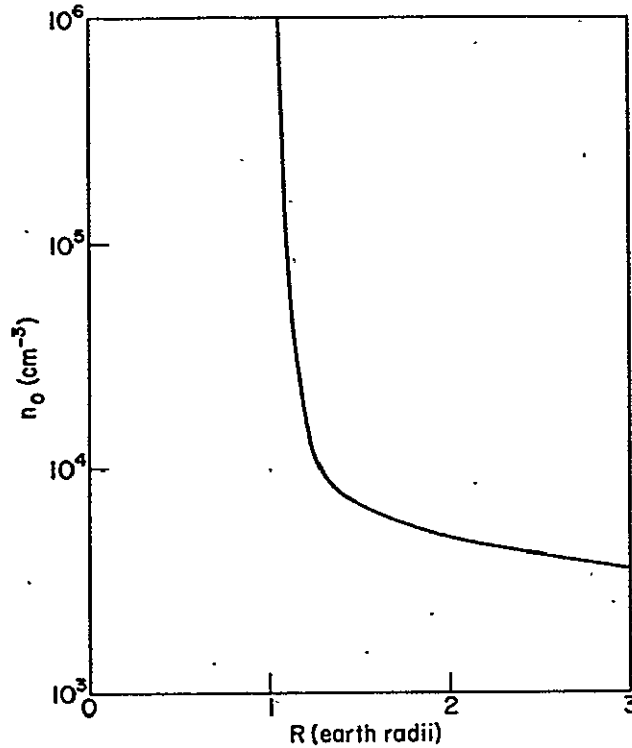
Fig. 4. Electron concentration
variation along field line
at L=3.

variation along the L=3 field line. The half width of the duct,
a(R), varies inversely with the square root of the magnetic flux
density along the tube. The magnetic flux dnesity in the centered
dipole model is

$$B = B_0 \left(\frac{R_0}{R}\right)^3 (4-3\ R/R_0)^{1/2} \qquad (11)$$

where R_0 is the equatorial geocentric distance, R the geocentric
distance to a point on the field line, and B_0 the magnetic flux
density at $R = R_0$. The variation in the trough width is then

$$a(R) = \frac{a_0 (R/R_0)^{3/2}}{(4-3\ R/R_0)^{1/4}} \qquad (12)$$

176

where a_0 is the equatorial half width. This variation is shown in Figure 5 for $a_0 = 500$ km and $R_0 = 3$ earth radii.
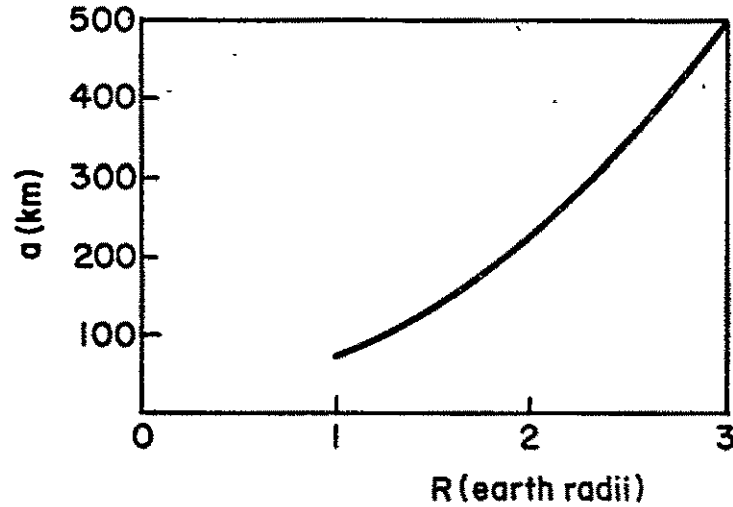
Fig. 5. Variation of duct radius with geo-
centric distance.

Equating the ray curvature and the tube curvature leads to an expression for the marginal trapping frequency as a function of depletion and position inside the duct.

$$f_m = \sqrt{40.3(\rho_0 \frac{\partial n_e}{\partial r} + 2n_e)} \qquad (13)$$

where ρ_0 is given in (1) and (7) and (9) have been used.

The ray curvature is maximized near the point of maximum electron density gradient inside the tube (r=a). Here,

$$n_e = n_0(1-de^{-1/2})$$

$$\frac{\partial n_e}{\partial r} = n_0 \frac{de^{-1/2}}{a} \qquad (14)$$

177

given these substitutions, the marginal trapping frequency becomes

$$f_m = \sqrt{40.3\ n_o[2 + de^{-1/2}(\frac{\rho_o}{a} - 2)]} \qquad (15)$$

the HF trapping conditions as a function of tube depletion are shown in Figure 6 at four points along the duct. The trapping frequency regions are bounded on the high frequency side by the marginal trapping frequency and on the low side frequency by the plasma frequency below which there is no HF propagation. Note that at a constant level of depletion, the range of trapped frequencies increases as the geocentric distance to the duct, R, decreases. Also the minimum trapped frequency, the local plasma frequency, increases with decreasing R.

The utility of the marginal trapping criterion is demonstrated by consideration of two HF rays with frequencies just below and just above the marginal trapping frequency in a 60% depletion duct. The marginal trapping frequency for this duct is found to be 910 kHz from Figure 6. Figure 7 illustrates the path of the ordinary ray at a frequency of 900 kHz. The ray is launched at point A inside the duct. After an initially smooth trajectory, the ray oscillates inside the duct but always remains trapped. After entering the top side ionosphere (point B) the ray reflects and is ducted back to the transmission point. The travel time between points A and B is .14 second. For a ray at frequency 925 kHz, the equatorial portion of the duct is not in a trapping region (Figure 8) and the ray is not guided to the conjugate topside ionosphere. Note that the ray direction angles and the wave normal angles are identical along the path of propagation.
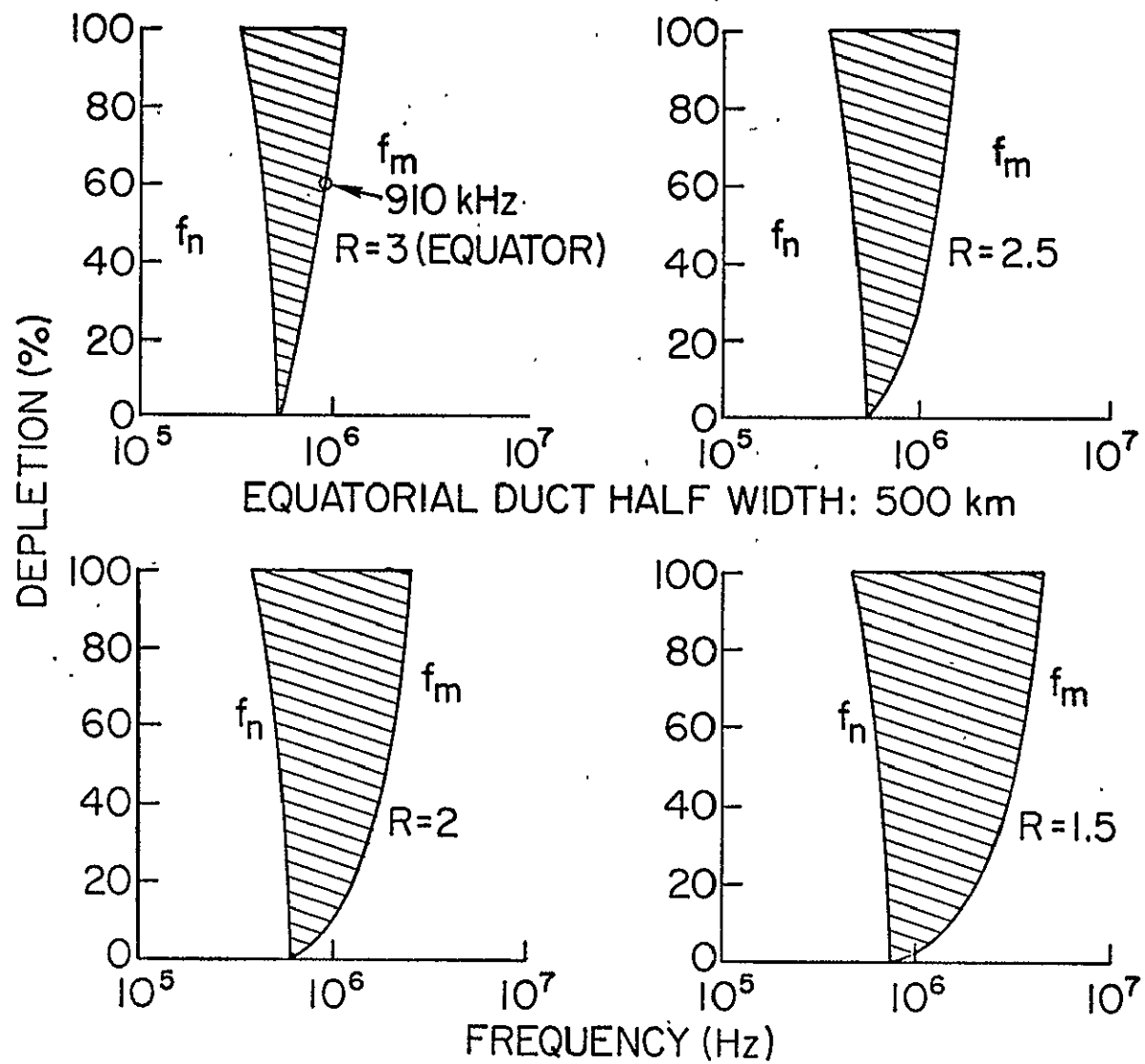
Fig. 6. HF trapping frequencies along an L=3 depletion duct.
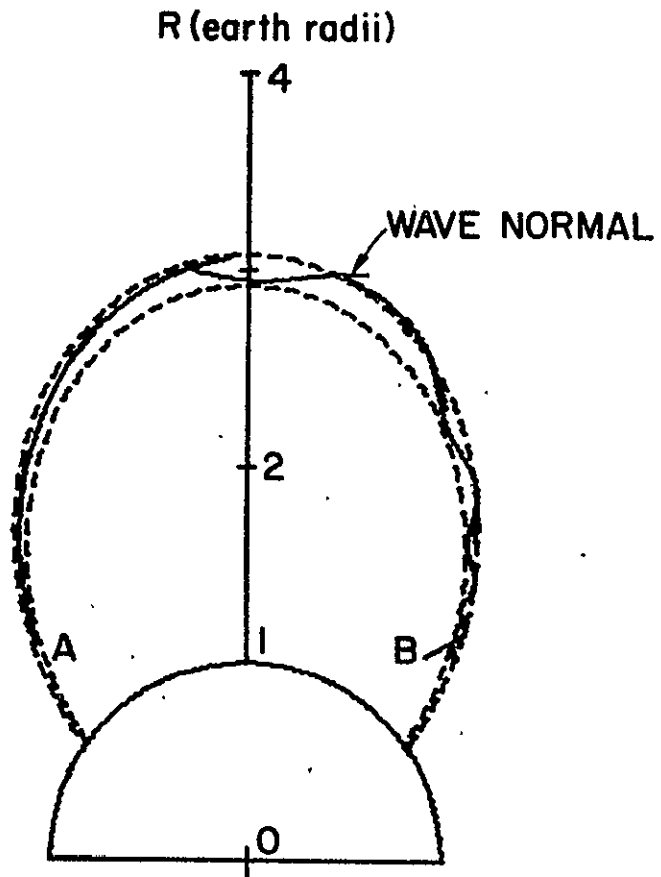
Fig. 7. HF ray trapping: f=900 kHz, depletion = 60%.
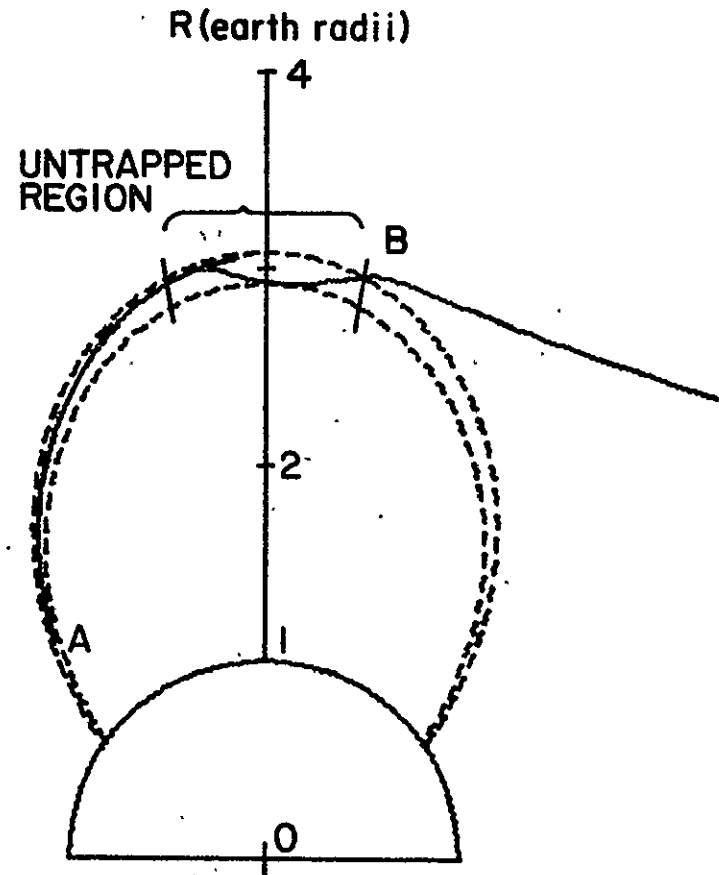
Fig. 8. HF ray escaping duct: f=925 kHz, depletion = 60%.

VLF propagation differs significantly from HF propagation. The propagation of the VLF "whistler" mode occurs for frequencies less than the electron gyrofrequency given by $f_H = \frac{eB}{2\pi m}$ where e is the electron charge, B is the magnetic field flux density, and m is the electron mass. Only the ordinary mode propagates below the gyrofrequency. The VLF approximation to the ordinary mode refractive index may be derived from (6) with the result

$$\mu^2 = \frac{A^2}{\Lambda(\cos \theta_m - \Lambda)} \tag{16}$$

where A is the ratio of plasma frequency to gyrofrequency, θ_m is the angle between the magnetic field and the wavenormal, and $\Lambda = f/f_H$. The refractive index is strongly dependent on the direction of propagation. The anisotropy greatly complicates the analysis of ducting of VLF signals.

The relationship between the wavenormal angle and the ray direction angle for VLF propagation is most easily described by referencing these angles to the magnetic field lines.

$$\tan \beta_m = \frac{\sin \theta_m (\cos \theta_m - 2\Lambda)}{1 + \cos \theta_m (\cos \theta_m - 2\Lambda)} \quad \text{[Helliwell, 1965]} \tag{17}$$

where β_m and θ_m are the ray and wavenormal angles with respect to the local magnetic field direction.

For longitudinal propagation along a field aligned duct, $\beta_m = 0$. This occurs for two wavenormal angle conditions from (17).

$$\begin{aligned} &1) \quad \cos \theta_m - 2\Lambda \\ &2) \quad \sin \theta_m = 0 \end{aligned} \tag{18}$$

181

Trapping of waves at $\theta_m = \cos^{-1} 2\Lambda$ is called Type 1 trapping and at $\theta_m = 0$ is called Type 2 trapping.

Smith, et al. [1960] and Helliwell [1965] have analyzed the ducting of whistlers with the use of refractive index surfaces. The refractive index surface is the curve traced out by a vector drawn from the origin whose length is μ and whose angle with the ordinate axis is θ_m. The angle between a normal to the surface and a vertical line is the ray direction angle β_m.

Figure 9 illustrates the shape of the wave normal surface below and above half the gyrofrequency. If $\Lambda < 1/2$, two minimums exist in the surface for $\theta_m = \pm\cos^{-1} 2\Lambda$. $d\theta_m/d\beta_m$ is less than zero at these points. By examining the changes in the refractive index surface as a ray propagates to regions of differing plasma density, it can be shown that Type 1 trough trapping occurs for waves propagating with wavenormal angles near $\pm\cos^{-1} 2\Lambda$.

A maximum in the refractive index surface (for $\Lambda < 1/2$) occurs at $\theta_m = 0$. Here, $d\theta_m/d\beta_m$ is greater than zero. Examination of the effects of plasma variations on the refractive index surface suggests that Type 2 trapping of VLF waves in enhancements occurs for frequencies less than half the gyrofrequency and at wavenormals aligned with the magnetic field.

There is only one minimum at $\theta_m = 0$ in the surface for frequencies above half the gyrofrequency. $d\theta_m/d\beta_m$ is less than zero at this point. Type 2 trapping in troughs occurs because of this minimum.

In order to analyze the trapping of VLF waves in ducts aligned with the earth's magnetic field, the ray curvature versus the duct curvature approach is used. The VLF ray curvature is a function of the

182
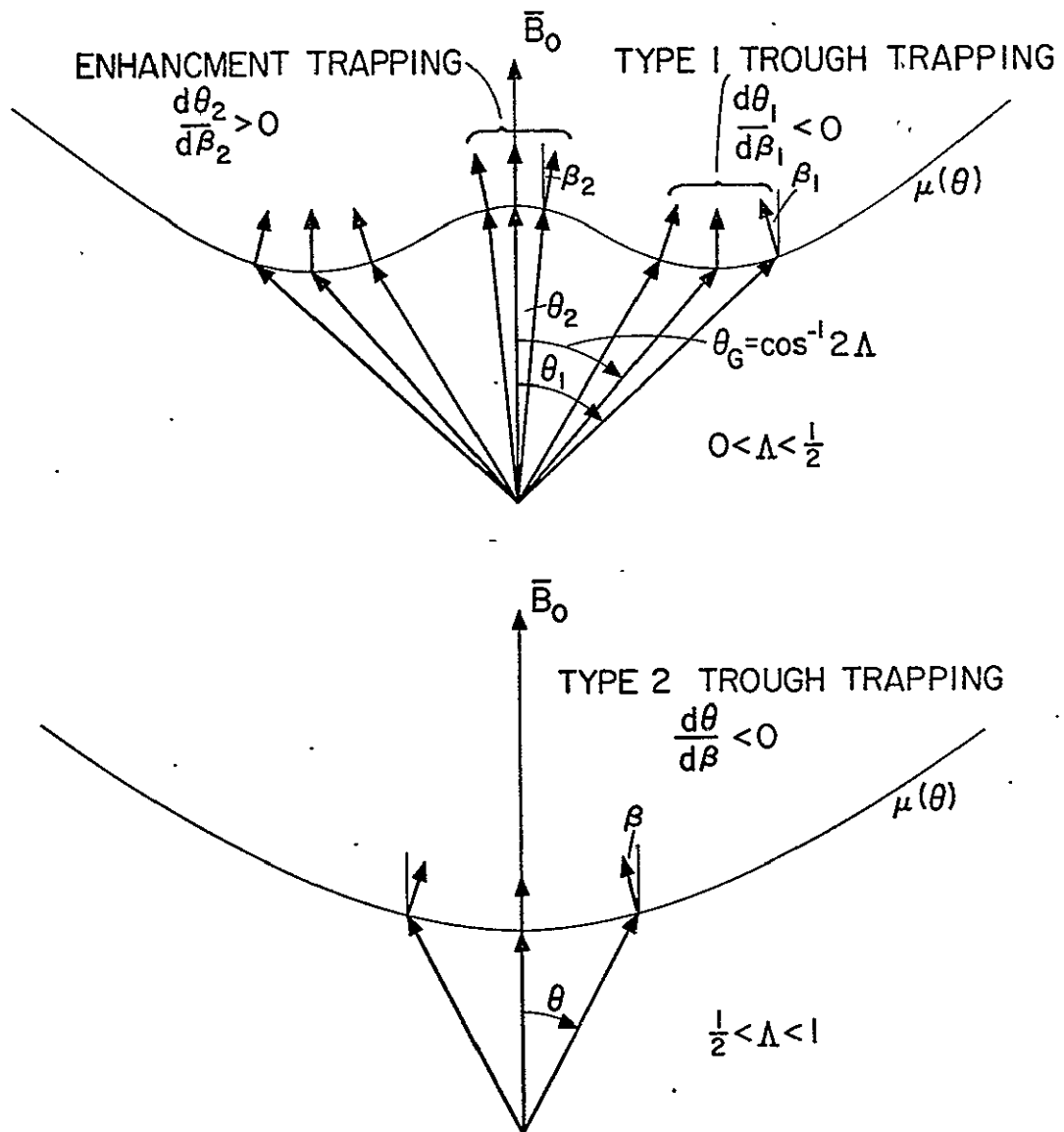
Fig. 9. VLF refractive index surfaces. Below the half gyro frequency, trough trapping occurs at large wavenormal angles around $\theta = \theta_G$. Above the half gyro frequency, trough trapping occurs around $\theta = 0$.

183

plasma gradients, the magnetic flux gradients, the magnetic field line curvature, the wave frequency and the direction of propagation. Thus, the solution to the VLF trapping problem is more involved than the solution to the HF trapping problem.

It is necessary to express the ray and wavenormal angles with respect to the magnetic field in terms of the same angles with respect to the horizontal coordinate axis. The differential relationship between these angles for propagation a distance dx along a field line is

$$d\theta = d\theta_m - \frac{dx}{\rho_0} \tag{19}$$

$$d\beta = d\beta_m - \frac{dx}{\rho_0} \tag{20}$$

where θ and β are the wavenormal and ray angles referred to the horizontal axis, and ρ_0 is the local radius of curvature of the field line.

The ray radius of curvature is found from (4)

$$\rho_{ray} = \rho_{wn} \frac{d\theta}{d\beta} = \rho_{wn}\left(\frac{d\theta_m}{d\beta} - \frac{dx/d\beta}{\rho_0}\right) \tag{21}$$

From (3), $\frac{dx}{d\beta} \equiv \rho_{ray}$ giving

$$\rho_{ray} = \rho_{wn}\left(\frac{d\theta_m}{d\beta} - \frac{\rho_{ray}}{\rho_0}\right) \tag{22}$$

Using (3) and (20)

$$d\beta = \frac{d\beta_m}{1 - \dfrac{\rho_{ray}}{\rho_0}} \tag{23}$$

Substitution into (22) yields

$$\rho_{ray} = \rho_{wn} \left[\frac{d\theta_m}{d\beta_m} \left(1 - \frac{\rho_{ray}}{\rho_0} \right) - \frac{\rho_{ray}}{\rho_0} \right] \tag{24}$$

Solving for the ray radius of curvature one obtains

$$\rho_{ray} = \frac{\rho_0}{1 + \dfrac{(\rho_{wn} + \rho_0)}{\rho_{wn} \dfrac{\partial\theta_m}{\partial\beta_m}}} \tag{25}$$

For trapping, $|\rho_{ray}| \le |\rho_0|$ at the upper edge of the duct and $|\rho_{ray}| \le |\rho_0|$ at the lower edge of the duct.

The relationship between $d\theta_m$ and $d\beta_m$ is found by taking the derivative of (17)

$$\frac{d\theta_m}{d\beta_m} = \frac{1 + 2\cos\theta_m(\cos\theta_m - 2\Lambda) + (\cos\theta_m - 2\Lambda)^2}{-\sin^2\theta_m + (\cos^3\theta_m + \sin^3\theta_m)(\cos\theta_m - 2\Lambda) + (\cos\theta_m - 2\Lambda)^2} \tag{26}$$

The two conditions for longitudinal propagation $(\beta_m = 0)$ require

for Type 1 trapping $\cos\theta_m = 2\Lambda$ then $\left.\dfrac{d\theta_m}{d\beta_m}\right|_1 = \dfrac{-1}{\sin^2\theta_m} = \dfrac{-1}{1 - 4\Lambda^2}$

$$0 \le \Lambda \le 1/2 \tag{27}$$

185

for Type 2 trapping $\cos \theta_m = 1$ then $\dfrac{d\theta_m}{d\beta_m}\Big|_2 = \dfrac{2 - 2\Lambda}{1 - 2\Lambda}$

$$0 \leq \Lambda \leq 1 \tag{28}$$

The wavenormal curvature is calculated from the refractive index using (2).

$$\rho_{wn} = \frac{-\mu}{d\mu/dr} = \frac{-2A^2 \Lambda (\cos \theta_m - \Lambda)}{\dfrac{dA^2}{dr} \Lambda (\cos \theta_m - \Lambda) - A^2 \dfrac{d\Lambda}{dr} (\cos \theta_m - 2\Lambda)} \tag{29}$$

where $\dfrac{d}{dr}$ is the derivative perpendicular to the field aligned direction of propagation. Using the expression for A (the ratio of plasma to gyrofrequency) in terms of magnetic flux density and plasma density and the Type 1 and 2 propagation conditions, (29) simplifies to

$$\text{Type 1:} \quad \rho_{wn1} = \frac{1}{\dfrac{dB}{Bdr} - \dfrac{1}{2}\dfrac{dn_e}{n_e dr}} \tag{30}$$

.and

$$\text{Type 2:} \quad \rho_{wn2} = \frac{1}{\dfrac{dB}{Bdr}\dfrac{1}{2(1-N)} - \dfrac{1}{2}\dfrac{dn_e}{n_e dr}} \tag{31}$$

The crossfield gradient of magnetic flux density is related to the field line radius of curvature. A magnetic flux vector can be decomposed into a scaler magnitude and a unit vector.

$$\vec{B} = B \, \vec{T} \tag{32}$$

where $B = |\vec{B}|$ and $\vec{T}$ is a unit vector tangent to the magnetic field. The radius of curvature of a field line is defined by the equation

$$(\nabla \times \vec{T}) \times \vec{T} = \frac{-1}{\rho_0} \vec{N} \tag{33}$$

where $\vec{N}$ is unit normal to the field line (i.e., $\vec{N} \cdot \vec{T} = 0$). In a static, current-free region of space, Maxwell's second equation reduces to

$$\nabla \times \vec{B} = 0$$

Equation (32) is substituted in (34) to give

$$\nabla \times \vec{T} = \frac{-\nabla B \times \vec{T}}{B} \tag{35}$$

This expression for the curl of $\vec{T}$ is used in (33). The resulting triple vector product is expanded yielding

$$\frac{\nabla B - (\nabla B \cdot \vec{T}) \vec{T}}{B} = \frac{-1}{\rho_0} \vec{N} \tag{36}$$

The dot product of $\vec{N}$ with both sides of (36) yields

$$\frac{\nabla B \cdot \vec{N}}{B} = \frac{-1}{\rho_0} \tag{37}$$

The directional derivative $\nabla B \cdot \vec{N}$ is simply the cross field gradient of magnetic flux density dB/dr. Therefore,

$$\rho_0 = \frac{-B}{dB/dr} \tag{38}$$

This expression is used to remove the magnetic field dependence from the expressions for wavenormal radii of curvature.

187

Type 1 $\rho_{wn1} = \dfrac{-1}{\dfrac{1}{\rho_0} + \dfrac{1}{2}\dfrac{dn_e}{n_e dr}}$ (39)

Type 2 $\rho_{wn2} = \dfrac{-1}{\dfrac{1}{2\rho_0(1-\Lambda)} + \dfrac{1}{2}\dfrac{dn_e}{n_e dr}}$ (40)

Note that for Type 1, longitudinal propagation ρ_{wn1} is independent of frequency.

The expressions for $d\theta_m/d\beta_m$, (27) and (28) and for ρ_{wn}, (39) and (40), are substituted into (25) to give

Type 1 $\rho_{ray} = \rho_0 \left[\dfrac{1}{1 + \dfrac{\rho_0}{2}\dfrac{dn_e}{n_e dr}(1-4\Lambda^2)} \right]$ (41)

$0 \le \Lambda \le 1/2$

Type 2 $\rho_{ray} = \rho_0 \left[\dfrac{1}{1 + \dfrac{1-2\Lambda}{2(1-\Lambda)}\left(\dfrac{1-2\Lambda}{2(1-\Lambda)} - \dfrac{\rho_0}{2}\dfrac{dn_e}{n_e dr}\right)} \right]$ (42)

$0 \le \Lambda \le 1$

The conditions for VLF trapping can now be determined. First, consider marginal Type 1 trapping. Marginal trapping occurs when the ray just follows the field line. In (41) $\rho_{ray} = \rho_0$ if and only if

$$\frac{dn_e}{n_e dr} = 0 \text{ or } (1-4\Lambda^2) = 0$$ (43)

Therefore, marginal Type 1 trapping occurs if no plasma density gradient exists or if $\Lambda = 1/2$.

This is a very significant result. Type 1 trough trapping occurs for any trough $\frac{dn_e}{n_e dr} > 0$. In the absence of a trough the ray naturally follows the field line when propagating with a wavenormal angle $\theta_m = \cos^{-1} 2\Lambda$. The bending of the ray by magnetic field gradients just compensates for the curvature of the field line (see (37)). A trough, no matter how weak, reinforces the gradients by bending the Type 1 ray toward the center of the depletion duct.

Type 2 trapping is considered. If the density gradients are zero, (42) becomes

$$\rho_{ray} = \frac{\rho_0}{1 + \frac{1-2}{(1-\Lambda)}^2} \quad . \tag{44}$$

Thus, with constant plasma concentration, the ray radius of curvature is less than the field line radius of curvature. Consequently, deflection from the upper edge of the duct is automatic. The problem in Type 2 trapping is deflection of the ray on the lower edge of the duct.

The conditions for bending of a Type 2 ray at the lower edge of a duct are frequency dependent. By examination of (42),

if $\Lambda < 1/2$ then $\frac{-dn_e}{n_e dr}$ $\frac{1-2\Lambda}{2(1-\Lambda)\rho_0}$ (i.e., enhancement trapping)

or if $\Lambda > 1/2$ then $\frac{-dn_e}{n_e dr}$ $\frac{1-2\Lambda}{2(1-n)\rho_0}$ (i.e., trough trapping)

Note that if $\rho_0 \to 0$ or $\Lambda \to 1$, infinite plasma gradients are required for trapping. The effects of density gradients on Type 2 trapping are exactly as predicted by the use of refractive index surfaces.

The conditions for trapping of VLF waves in ducts are summarized in Table 1.

Table 1

Criteria for VLF trapping in field aligned ducts

FREQUENCY

Propagation Mode		$0 \leq \Lambda \leq 1/2$	$1/2 \leq \Lambda \leq 1$
Type 1 $\cos \theta_m = 2\Lambda$		$\dfrac{dn_e}{n_e dr} \geq 0$ trough	————
Type 2 $\theta_m = 0$		$\dfrac{dn_e}{n_e dr} \leq \dfrac{2\Lambda-1}{\rho_0(1-\Lambda)}$ enhancement	$\dfrac{dn_e}{n_e dr} \geq \dfrac{2\Lambda-1}{\rho_0(1-\Lambda)}$ trough

In both Type 1 and Type 2 trappings, field aligned propagation occurs for $\Lambda = 1/2$ independent of plasma concentration. This is because the refractive index surface is maximally flat at half the gyrofrequency (picture the transition between the upper and lower diagrams in Figure 9).

Using the Gaussian duct model evaluated at the point of maximum density gradient ((14)), the depletion required for trough trapping is found to be

$$d \geq 0 \quad \text{for} \quad 0 \leq \Lambda \leq 1/2; \text{ Type 1}$$

$$d \geq \frac{(2\Lambda-1) \, ae^{1/2}}{\rho_0(1-\Lambda) + (2\Lambda-1)a} \quad \text{for} \quad 1/2 \leq \Lambda \leq 1; \text{ Type 2}$$

Above half the gyrofrequency, a lower duct radius of curvature requires a higher depletion level for trapping.
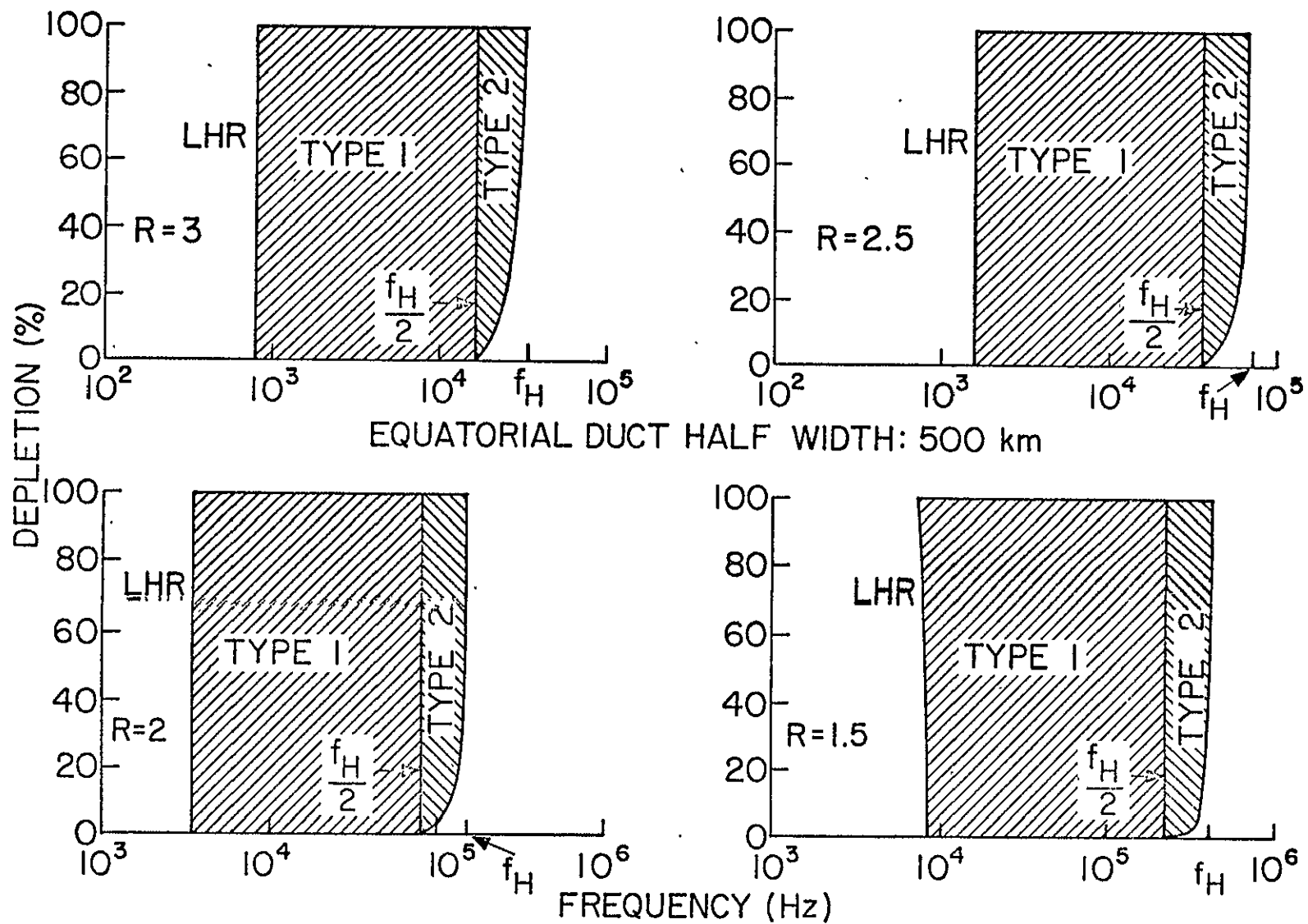
Fig. 10.   VLF Trapping Frequencies.
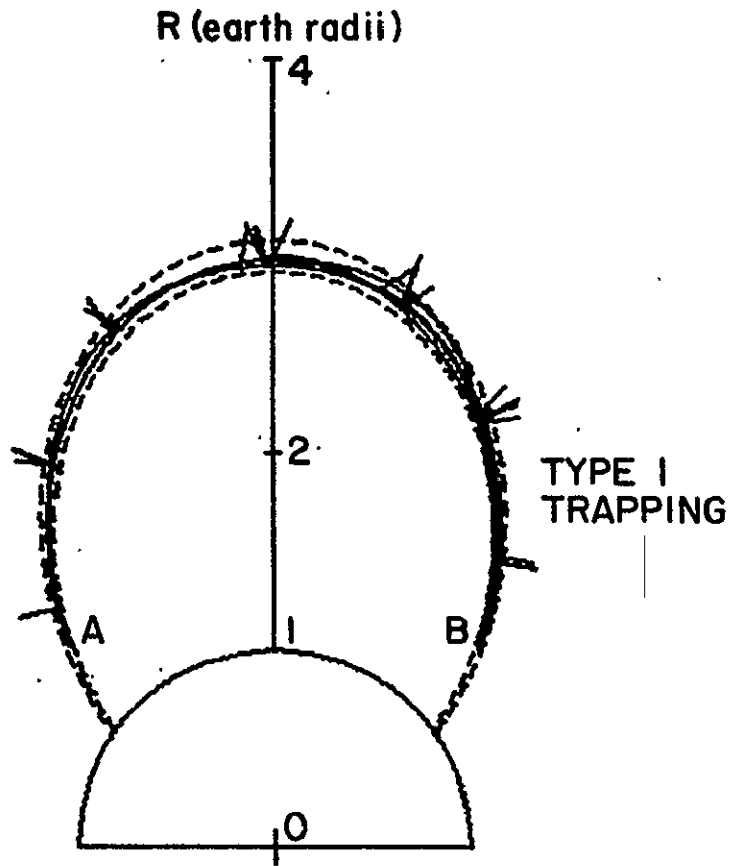
Fig. 11. Magnetospherically reflected whistler
in a depletion duct: f = 7 kHz,
depletion = 40%.
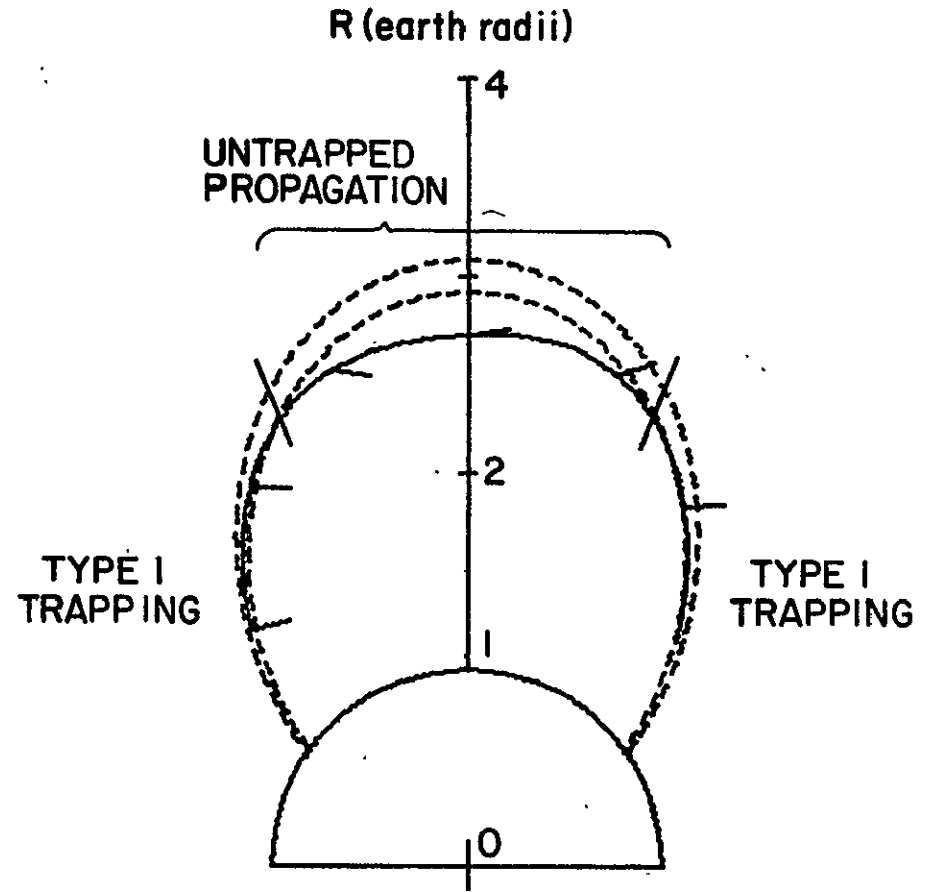
Fig. 12. Retrapping of a VLF ray in a depletion
duct: f = 7 kHz, depletion = 20%.
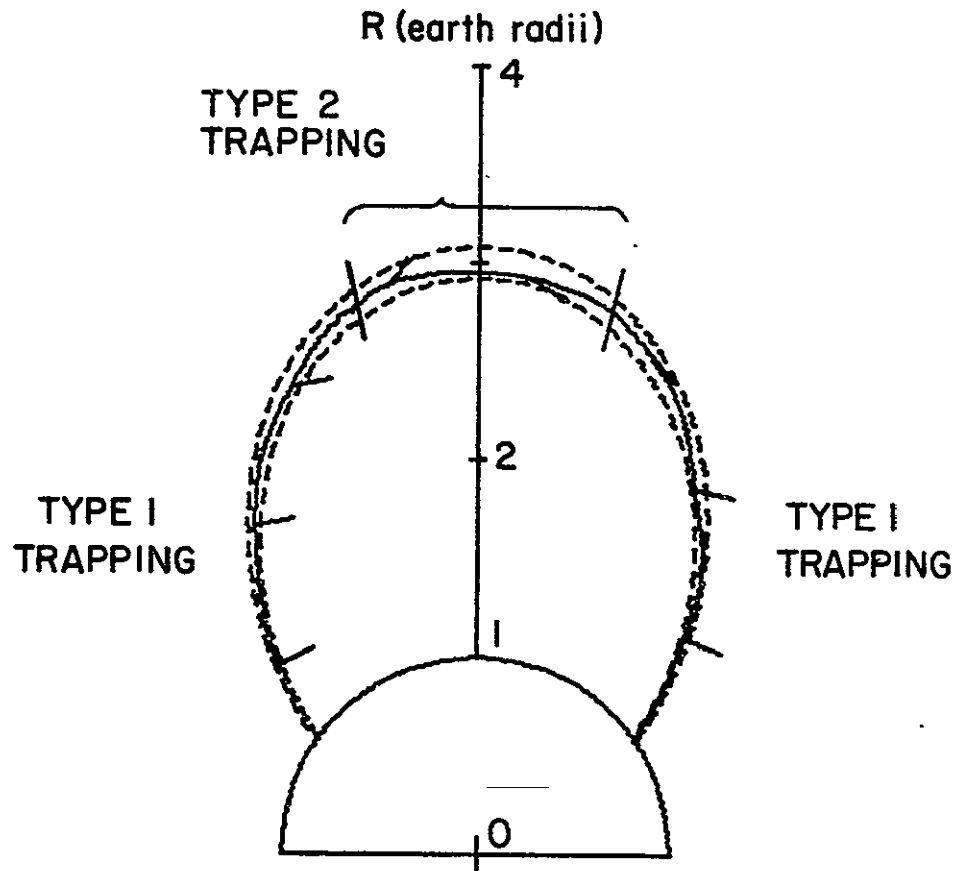
Fig. 13. VLF trapping for frequencies greater than half the equatorial gyro frequency: f = 20 kHz, depletion = 50%.
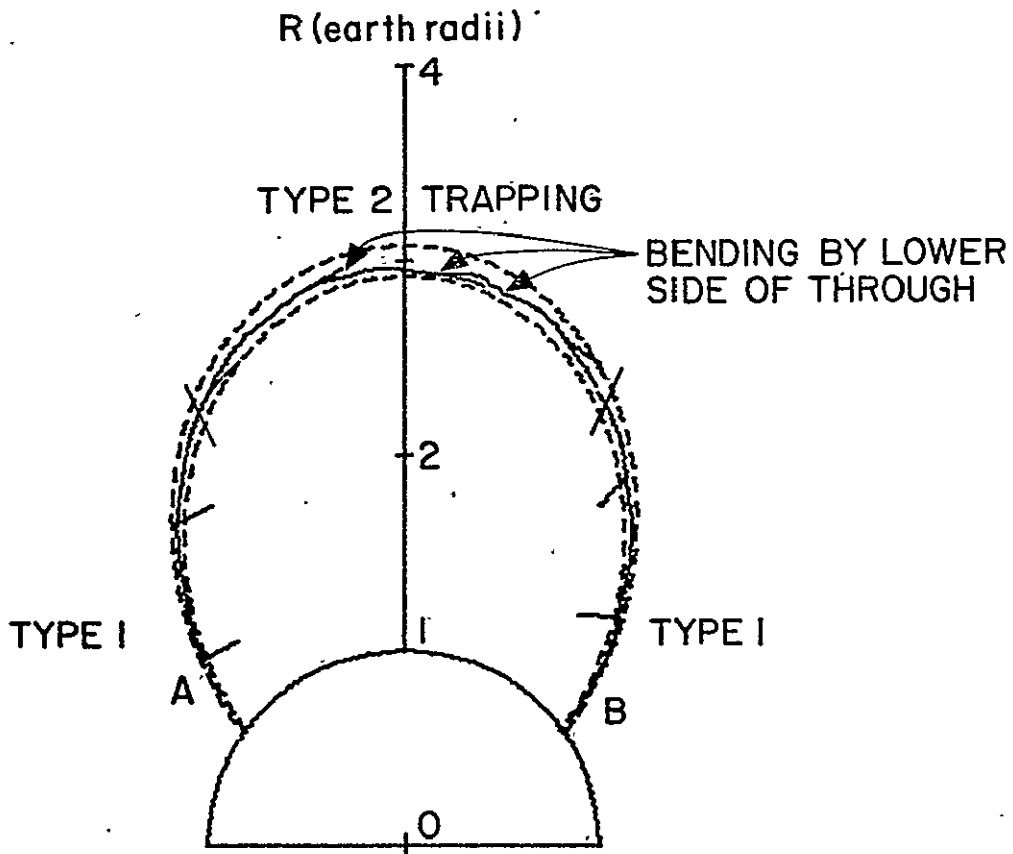
Fig. 14. Strong depletion required for trapping near the equatorial gyro frequency: f_H = 34 kHz, f = 30 kHz, depletion = 70%.

The lower and upper limits to the VLF propagation frequency are the lower hybrid resonance (LHR) frequency and the electron gyro-frequency, respectively. The LHR is given by

$$\frac{1}{f_{LHR}^2} = \frac{1}{f_{Hi}^2 + f_{ni}^2} + \frac{1}{f_{Hi} \cdot f_{He}} \qquad [Stix, 1962] \qquad (45)$$

where f_{Hi} is the ion gyrofrequency, f_{He} is the electron gyro-frequency and f_{ni} is the ion plasma frequency. A practical expression for the LHR frequency is

$$f_{LHR} = 6.53 \times 10^8 \, B \left[\frac{5.26 \times 10^{15} \, B^2 + n_e}{9.68 \times 10^{18} \, B^2 + n_e} \right]^{1/2} \qquad (46)$$

where B and n_e are in MKS units. A more general expression for f_{LHR} including the effects of heavy ions is given by Smith and Brice [1964].

The VLF trapping frequencies as a function of tube depletion are shown in Figure 10. Between the LHR and half the gyrofrequency, trapping is always possible. As frequencies increase above $f_H/2$, larger depletion is required for trapping. A trapped signal propagating below the local half gyrofrequency at low altitude will have the greatest probability of becoming untrapped in the high altitude equatorial regions of the trough where its frequency may be greater for $f_H/2$.

Examples of Type 1 ducted propagation in a trough are shown in Figures 11 and 12. Figure 11 illustrates a magnetospherically reflected whistler undergoing LHR reflection at points A and B.

The travel time from point A to point B is 1.35 seconds. Note that for Type 1 propagation the wavenormal makes a large angle with respect to the ray direction.

The natural guiding properties of the geomagnetic field are illustrated in Figure 12. The ray leaves the Type 1 trapping region and then returns to the duct to be retrapped. Figure 12 illustrates the fact that the curves of trapping frequency versus depletion level are only useful as approximate criteria. The trapping of a specific ray at a given frequency and initial ray angle is most reliably determined by raytracing techniques.

Type 2 propagation near the equator is illustrated in Figures 13 and 14. The wave is initiated below $f_H/2$ at low altitudes, enters a Type 2 region $(f > f_H/2)$ and is guided along the lower side of the tr ugh into a Type 1 region. As predicted by the marginal trapping theory, higher levels of depletion are required for Type 2 equatorial trapping than for Type 1 equatorial trapping.

As the wave frequency approaches the gyrofrequency, larger duct depletion is required for trapping. In Figure 14, the wave frequency is 90% of the gyrofrequency. A 70% depletion is required for trapping. The arrows in Figure 14 point to the lower side reflections in the trough. For cases of Type 2 trough trapping, the ray stays between the center and the lower edge of the trough.

The guiding of HF radio waves in naturally occurring depletion ducts has been discussed by Muldrew [1963, 1967a,b], Muldrew and Hagg [1969], Nishizaki and Matura [1972], Sharma and Muldrew [1973, 1975] and Cerisier [1974]. Conjugate echo studies involving satellites Alouette 1 and 2, ISIS 1 and 2, and FR-1 suggest that these ducts are

small in comparison with the artificially created ducts previously described in this report. The natural troughs have diameters less than one kilometer and are on the order of several thousand km in length. The natural depletion level is about 1%. Below L = 1.7, propagation in natural ducts has not been detected [Cerisier, 1974]. The formation of natural ducts is attributed to electrostatic fields produced in the E-region and extending up into the magnetosphere [Sharma and Muldrew, 1975] or to thunder cloud electricity [Park and Helliwell, 1971].

Artificial ducts produced by chemical gas release have the advantage of precise control of size, location and depletion level. Artificial troughs with better wave trapping properties than found in naturally occurring ducts may be easily produced.

As mentioned previously, signals propagating in depletion ducts do not usually reach the ground. VLF signals have large wavenormal angles at low altitudes that do not penetrate the bottomside ionosphere. HF trapped signals are usually reflected because the low trapping frequency does not penetrate the topside F-layer. However, in artificially created troughs with steep density gradients, radiowave frequencies above the ionospheric critical frequency may be able to penetrate the F-layer and be trapped in the duct to be guided to a conjugate ground receiver. Thus, there exists the possibility of inter-hemispheric HF propagation by ducting through the magnetosphere.

Valuable information may be obtained from HF and VLF ducting of signals that do not penetrate the F-layer. HF topside ionograms of ducted signals can be used to estimate the electron concentration in

the trough. Similarly, variable frequency whistler propagation in depletion ducts may be used to determine the electron concentration along the raypath as has been done for whistler propagation in enhancement ducts (see, for example, Park [1972]).

The ability to produce waveguides in the magnetosphere makes possible a number of experiments involving wave-particle interactions. For certain relationships between a charged particle velocity and an electromagnetic wave frequency and phase velocity, strong interactions occur [Stix, 1962]. These interactions represent coupling between wave and particle energies. The energy exchange between streaming particles and waves has been suggested for the amplification and absorption of whistler signals (see, for example, Bernard [1973]). The collision-free magnetospheric plasma is not in a state of thermal equilibrium and, consequently, contains high energy trapped particles with a wide spectrum of pitch angles. Interaction between electromagnetic radiation and trapped particles may produce pitch angle scattering. Some of the scattered particles are no longer trapped and will precipitate along magnetic field lines to low altitudes where they will interact with the relatively dense D, E, and F-region atmosphere and may produce observable ionospheric phenomena such as enhanced airglow, heating or ionization. Observations at the base of the trough may indicate precipitation effects triggered by natural or manmade VLF propagation [Rosenberg et al., 1971].

Ground-based wave-particle interaction studies involving VLF transmission through the F-region into the magnetosphere have required signals with small wavenormal angles with respect to the magnetic field direction for penetration of the ionosphere and for guiding along
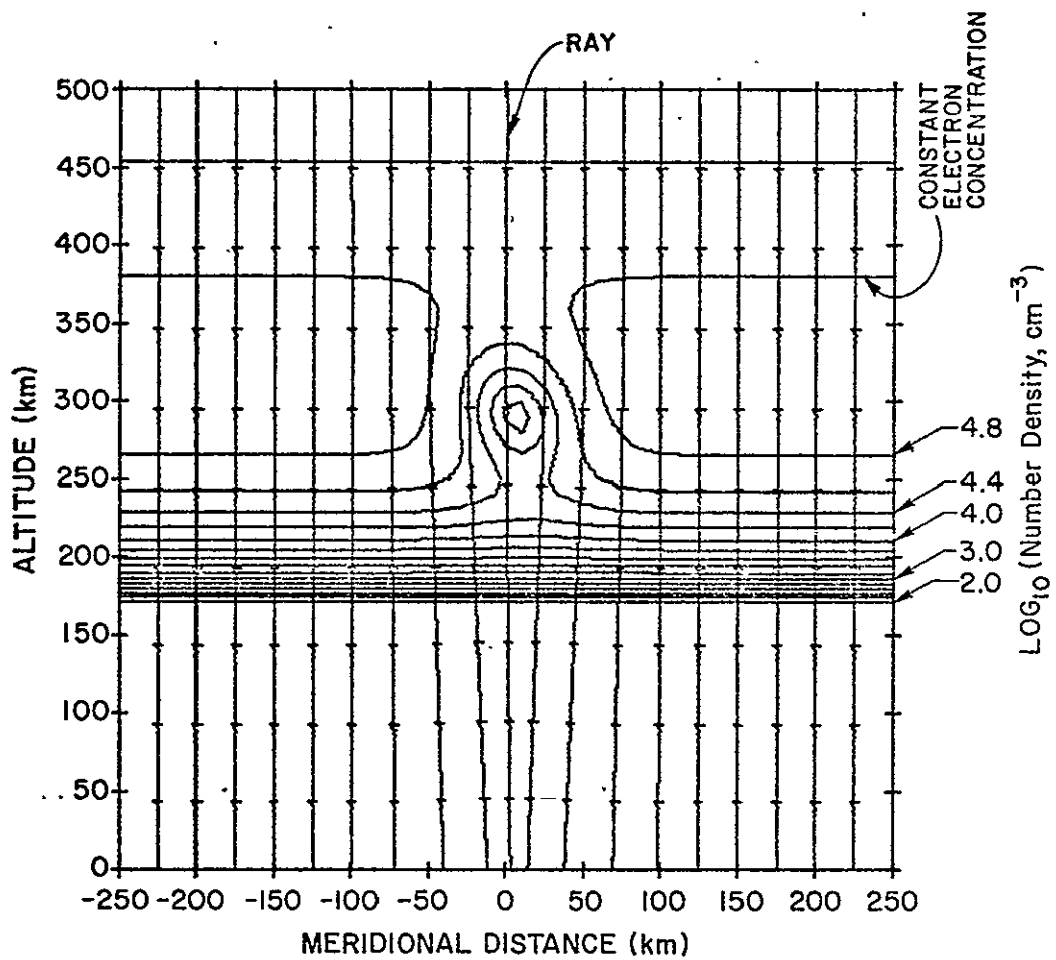
Fig. 15. Focusing of a vertically incident plane wave by the nighttime ionospheric depletion one minute after the release of 100 kg H_2. The downward propagating wave has a frequency of 10 MHz.

199
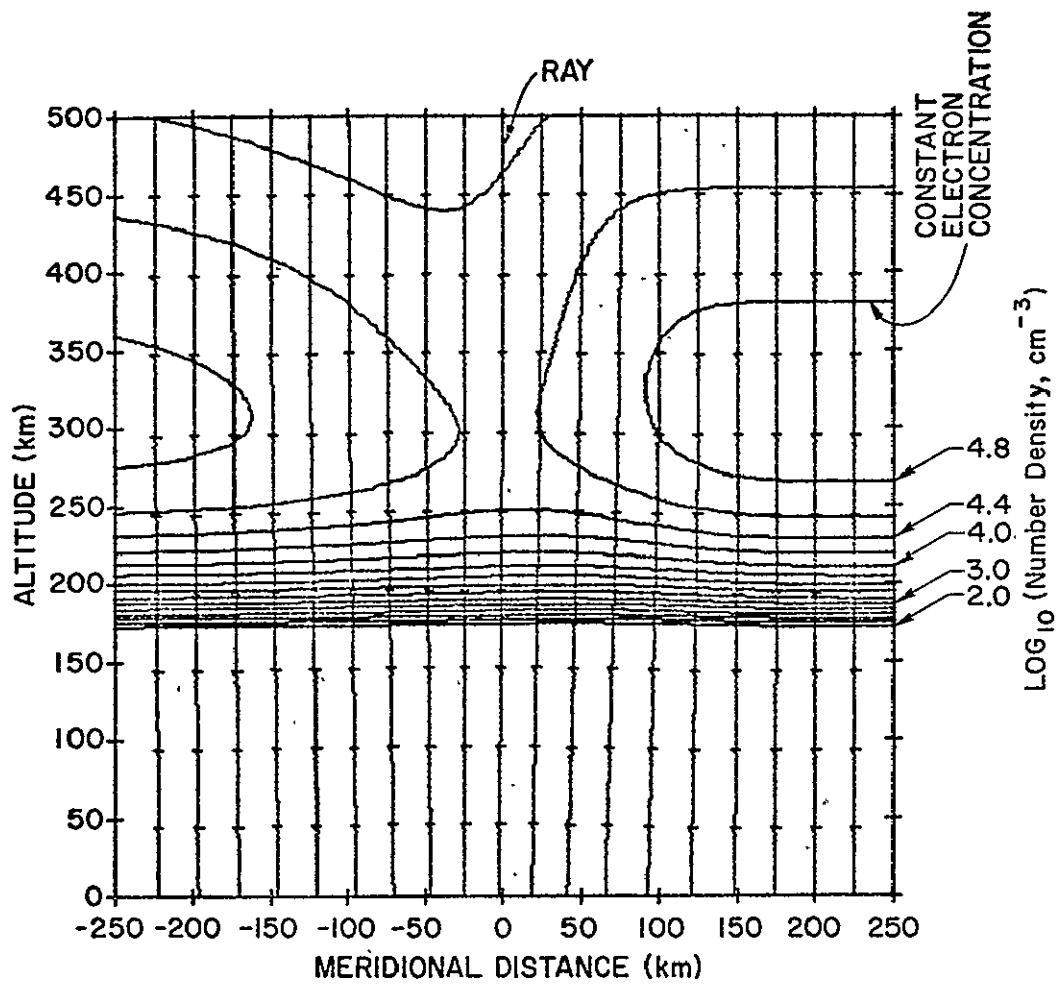
Fig. 16. Same as Figure 15 but one half-hour after the H_2 release.

natural, randomly placed enhancement ducts [Helliwell and Katsufrakis, 1974]. The excitation of VLF emissions by transmissions from spacecraft into the depletion ducts at known locations permits the study of wave-particle interactions with signals at all wave normal angles under controlled conditions.

C. ·Propagation Through the Depletion Region - The Ionospheric Lens

The variation in phase velocity in the ionospheric depletion region produces bending and phase perturbations in the rays passing this region. The ionospheric hole may be modeled as a lens of unknown diameter and thickness. The size.of the lens may be determined from the variations in phase and amplitude of signals propagating through the lens.

The focusing property of the chemically modified ionosphere is illustrated in Figures 15 and 16. A plane wave generated above the ionosphere becomes distorted by propagating through the ionospheric lens. The refractive index increase in the depleted ionosphere produces a decrease in phase velocity. Rays immediately below the ionospheric hole are bent toward the central axis of the lens resulting in an increase in signal amplitude. Surfaces of constant phase are indicated by tick marks along the rays in Figure 15. A ring of infranormal amplitude surrounds the focal point of the lens as is indicated by the reduction in ray density on either side of the central axis of the lens. Rays passing through the ionosphere far from the depletion region are unaffected. As the diameter of the hole increases, the rays are not as sharply bent, and the focusing is not as pronounced (Figure 16).

The horizontal extent of the hole and the magnitude of the vertical depletion through the hole may be determined from the variations in phase and amplitude of a plane wave propagating through the depletion region. A Fresnel diffraction approach is used to relate the size of the depletion region to the variations in phase and amplitude. The plane wave is assumed to propagate through the ionospheric lens with only a delay in the phase front. (This is a reasonable assumption for VHF propagation.) Just past the ionospheric lens, the phase perturbed signal is decomposed into an angular spectrum of plane waves. Each of these plane waves propagates to the point of reception where they are recombined into the received signal. This is schematically illustrated in Figure 17.

A Gaussian phase delay will be used to simulate the effects of the ionospheric lens. A unit amplitude plane wave is represented as

$$U(x,y,z,t) = \exp[j(2\pi z/\lambda - \omega t)] \qquad (47)$$

where λ is the wavelength and ω is the frequency in radians/sec. (The complex time factor $e^{-j\omega t}$, will be suppressed in future equations.) After propagation through a Gaussian phase lens, the complex amplitude becomes

$$U(x,y,z) = \exp[j(2\pi z/\lambda + \varepsilon e^{-(x^2+y^2)/2a^2})] \qquad (48)$$

where a is the horizontal radius of the lens and ε is the phase perturbation (in radians) produced at the center of the lens. The origin of the (x,y) coordinate system is centered on the lens. Taking $z = 0$ just past the lens,

202

PLANE
WAVE
SIGNAL

IONOSPHERIC
LENS

PHASE DELAYED
PLANE WAVE

DECOMPOSITION
INTO ANGULAR
SPECTRUM OF
PLANE WAVES

RECONSTRUCTION
OF PLANE WAVES

RECEIVED
SIGNAL
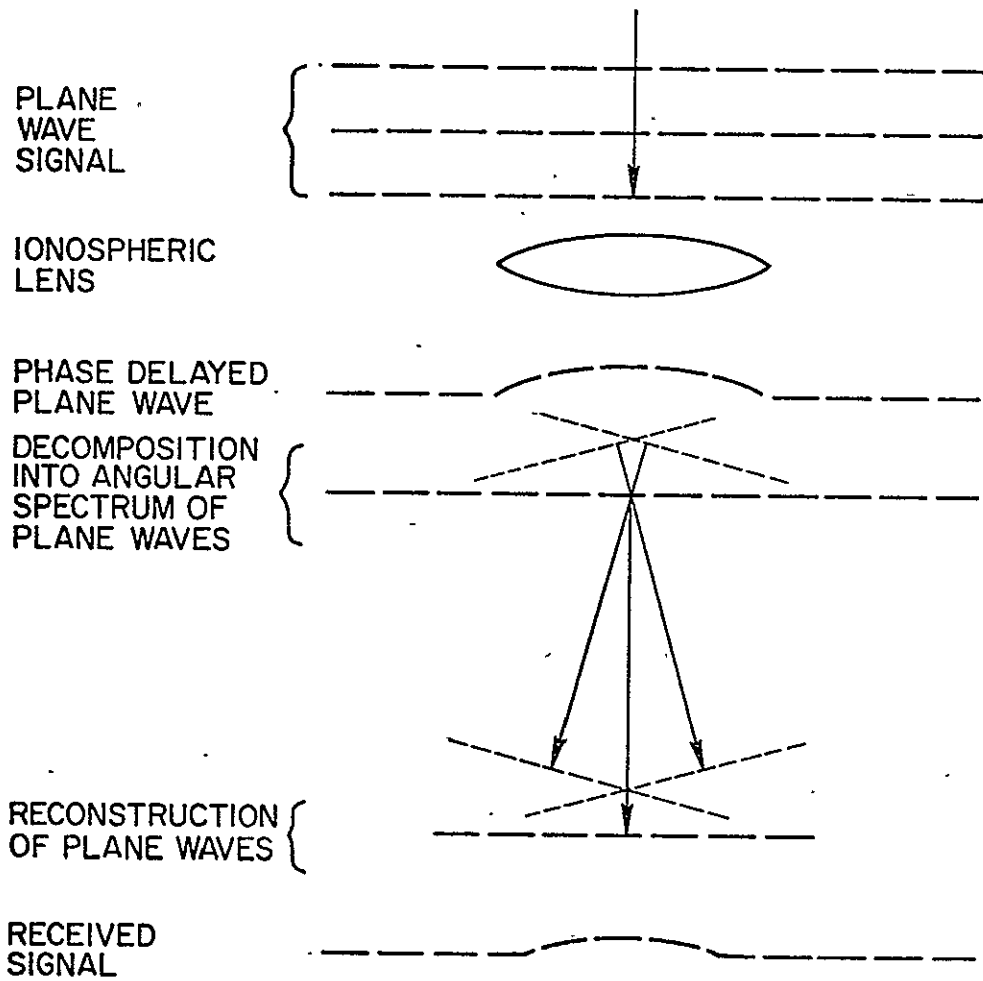
Fig. 17. Propagation past the ionospheric lens

203

$$U(x,y,0) = \exp[j\varepsilon e^{-r^2/2a^2}] \qquad (49)$$

where $r^2 = x^2 + y^2$. The Gaussian phase model is both a reasonable approximation to the ionospheric hole and an easily manipulated mathematical expression.

For wave frequencies well above the ionospheric electron plasma frequencies, ε is related to the change in electron content produced by the injected gas according to

$$\varepsilon = k \int \frac{\Delta X}{2} dz = \frac{40.3}{f^2} \Delta I k = \frac{8.44 \times 10^{-7} \Delta I}{f} \qquad (50)$$

where ΔX is the change in f_n^2/f^2 produced by the chemical depletion, f_n the local plasma frequency, f the wave frequency, k the wave number given by $2\pi/\lambda$, and ΔI the reduction in total electron content along the wavepath.

The decomposition of a signal into its angular spectrum of plane waves is given by

$$A_0\left(\frac{\alpha}{\lambda}, \frac{\beta}{\lambda}\right) = \int\int_{-\infty}^{\infty} U(x,y,0)\exp[-j2\pi(\frac{\alpha}{\lambda}x + \frac{\beta}{\lambda}y)]\ dx\ dy \qquad (51)$$

where α and β are the direction cosines of each component plane wave. Each plane wave is represented as

$$B(x,y,z) = \exp[j\frac{2\pi}{\lambda}(\alpha x + \beta y + \gamma z)] \qquad (52)$$

where $\gamma = \sqrt{1-\alpha^2-\beta^2}$. The received signal at a distance z is found by summing the angular spectrum components taking into account the different distances each plane wave travels. This is given as

204

$$U(x,y,z) = \int\limits_{-\infty}^{\infty} A_o(\tfrac{\alpha}{\lambda}, \tfrac{\beta}{\lambda}) \exp[\tfrac{j2\pi z}{\lambda}\sqrt{1-\alpha^2-\beta^2}] \exp[j2\pi(\tfrac{\alpha}{\lambda}x + \tfrac{\beta}{\lambda} y)] \tfrac{d\alpha}{\lambda} \tfrac{d\beta}{\lambda}$$

<p align="right">[Goodman, 1968]   (53)</p>

If the angular spectrum of plane waves has a negligible contribution at high wavenormal angles, considerable simplification is possible. will be assumed that $A_o(\tfrac{\alpha}{\lambda}, \tfrac{\beta}{\lambda})$ is nonzero only if $|\tfrac{\alpha}{\lambda}|$, $|\tfrac{\beta}{\lambda}| \ll 1$. This means that most of the energy in the signal is concentrated with wavenormal directions close to the z axis direction. Under these conditions, the square root in (53) is approximately given by

$$\sqrt{1-\alpha^2-\beta^2} \simeq 1 - \frac{\alpha^2}{2} - \frac{\beta^2}{2} \tag{54}$$

This is referred to as the Fresnel approximation and is discussed in further detail by Goodman [1968]. With this approximation, (51) is substituted into (53) and the integration over $(\tfrac{\alpha}{\lambda}, \tfrac{\beta}{\lambda})$ is carried out to give

$$U(x,y,z) = \iint\limits_{-\infty}^{\infty} U(x,y,0) \exp[j\pi((x_1-x)^2 + (y_1-y)^2)/\lambda z] \, dx_1 \, dy_1$$

$$\exp[j2\pi z/\lambda]/(j\lambda z) \tag{55}$$

This is the Fresnel diffraction formula.

For a Gaussian phase signal given by (49), the half width of the angular spectrum is approximately, $\alpha = \frac{\lambda \varepsilon}{2\pi a}$, and must be much less than unity for the Fresnel diffraction formula to be valid.

Substitution of the Gaussian phase signal into the Fresnel dif-
fraction formula and evaluation at $x,y = 0$ produces the following
infinite series [see Appendix D]

$$U(0,0,z) = \exp[j(2\pi z/\lambda + \varepsilon)] \sum_{s=0}^{\infty} \left(\frac{\lambda z \varepsilon}{2\pi a^2}\right)^s P_s \frac{1}{j\varepsilon}$$

$$(56)$$

where $P_s(x) = \sum_{m=1}^{s} \mathcal{S}_s^{(m)} x^{s-m}$ and $\mathcal{S}_s^{(m)}$, are Stirling numbers of the
second kind as given by

$$\mathcal{S}_s^{(m)} = \sum_{k=0}^{m} \frac{(-1)^{m-k} k^s}{k!(m-k)!}$$

$$(57)$$

The first few polynomials are

$$P_0(x) = 1 \qquad P_3(x) = 1 + 3x + x^2$$

$$P_1(x) = 1 \qquad P_4(x) = 1 + 6x + 7x^2 + x^3$$

$$P_2(x) = 1 + x \qquad P_5(x) = 1 + 10x + 25x^2 + 15x^3 + x^4$$

The series converges if $(\lambda z \varepsilon / 2\pi a^2)$ is less than unity. Assuming that
the distance to the lens (z) is greater than the lens radius (a), this
convergence criterion is compatible with the validity criterion for use
of the Fresnel diffraction formula.

The variation in the received signal on the lens axis is represented
by

$$U(0,0,z) = Ae^{[j(2\pi z/\lambda + \Delta\phi)]}$$

$$(58)$$

Without the ionospheric hole, $A = 1$ and $\Delta\phi = 0$. Equating this with
(56) gives

206
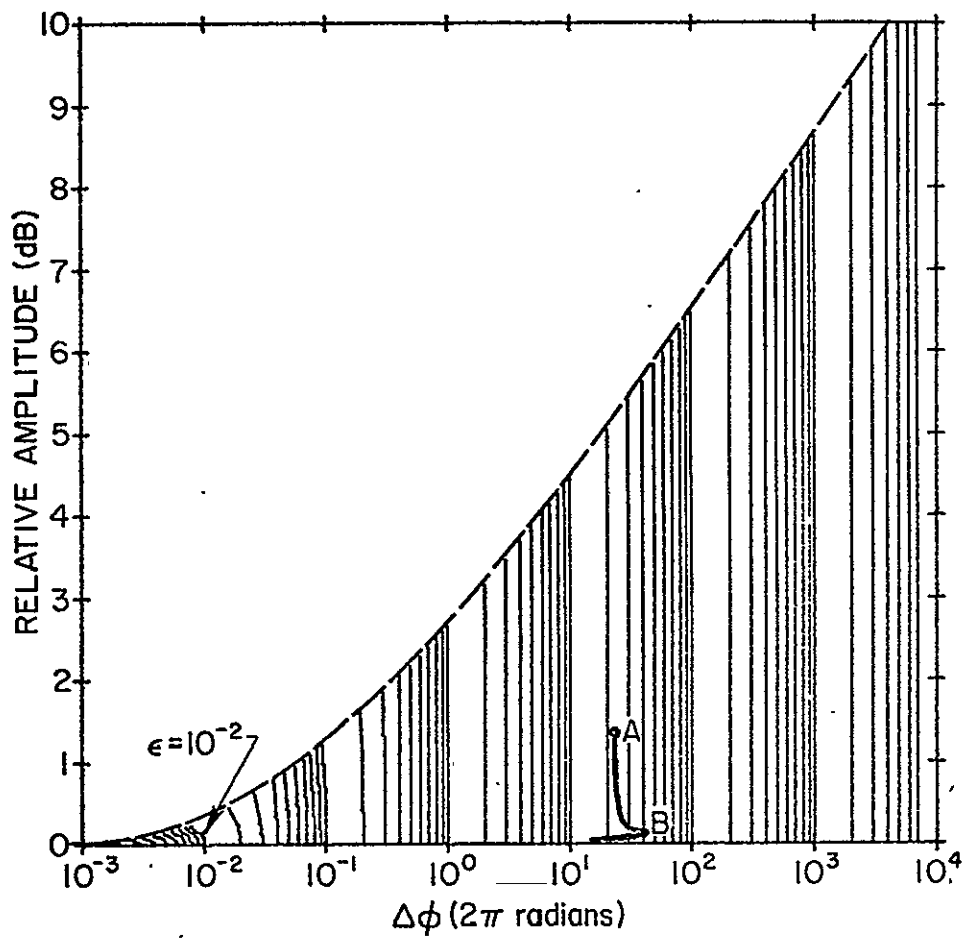
Fig. 18. Phase thickness [ε(2π radians)] of the iono-
spheric lens as a function of measured relative
amplitude and phase. (ε = Δφ for 20 log₁₀(A)=0.)
Darkened curve represents phase and amplitude
variations produced in a 30 MHz wave propagating
through the disturbed nighttime ionosphere.
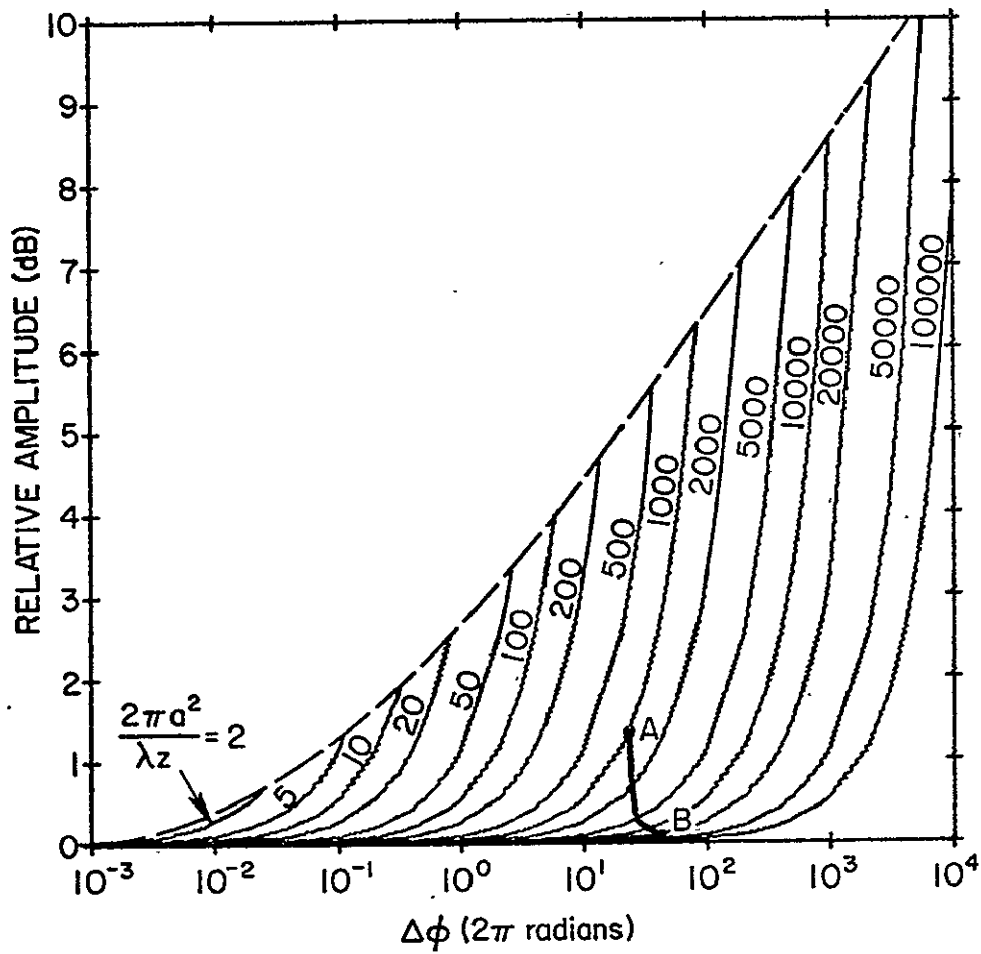
Fig. 19. Horizontal size of the ionospheric lens as a
function of measured relative amplitude and
phase.

$$Ae^{j\Delta\phi} = e^{j\epsilon} \sum_{s=0}^{\infty} \left(\frac{\lambda z \epsilon}{2\pi a^2}\right)^s P_s(\frac{1}{j\epsilon}) \qquad (59)$$

Because this equation is complex, it represents two equations with two unknowns. The unknowns are ϵ, the central phase perturbation produced by the hole, and $\frac{2\pi a^2}{\lambda z}$ the ratio of the lens circular area to the square of the classical Fresnel zone radius.

Contours of constant ϵ and $\frac{2\pi a^2}{\epsilon z}$ are plotted on a $\Delta\phi$ versus A graph in Figures 18 and 19. The units of observed phase change are 2π radians and of observed amplitude change are decibels. Except for low values of phase, ϵ and $\Delta\phi$ are nearly identical. The deduced horizontal width of the ionospheric lens is strongly dependent on the measured signal amplitude.

Also indicated in Figures 18 and 19 is the calculated variation in A and $\Delta\phi$ of a 30 MHz signal propagating vertically downward through the nighttime depletion region produced by the release of 100 kg H_2 gas. These variations are also plotted versus time in Figure 20. Ten seconds after the H_2 has been released, the signal amplitude has increased by 1.5 dB and the phase has increased by 48 radians point A). As the ionospheric hole evolves, the amplitude decreases and the phase increases. A peak of 80π radians in the phase is reached at 900 seconds after gas release (point B). After this time, the ionosphere recovers producing a drop in both phase and amplitude.

Using Figures 18 and 19, or an equivalent numerical procedure, the variations in $\Delta\phi$ and A may be converted into variations in ϵ and $\frac{2\pi a^2}{\lambda z}$ which then may be used to produce estimates of electron content reduction and ionospheric hole size (Figure 21). The usefulness of this method is limited by the accuracy of phase and amplitude
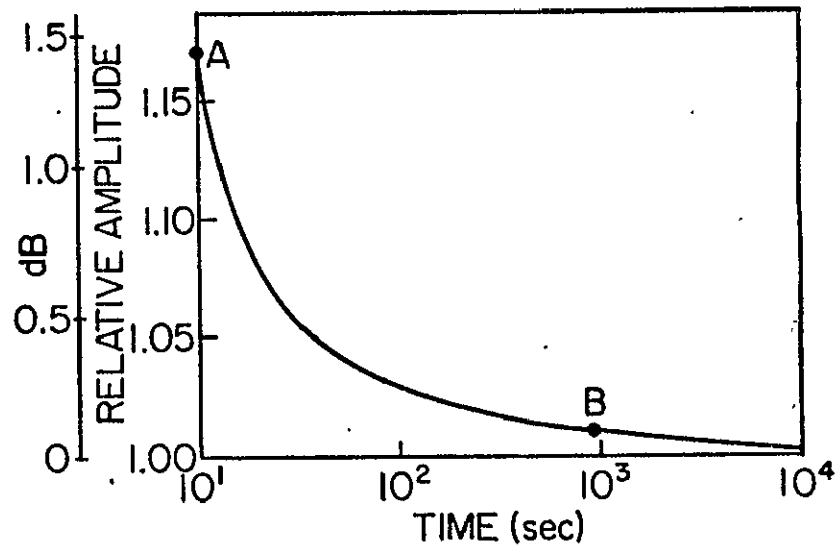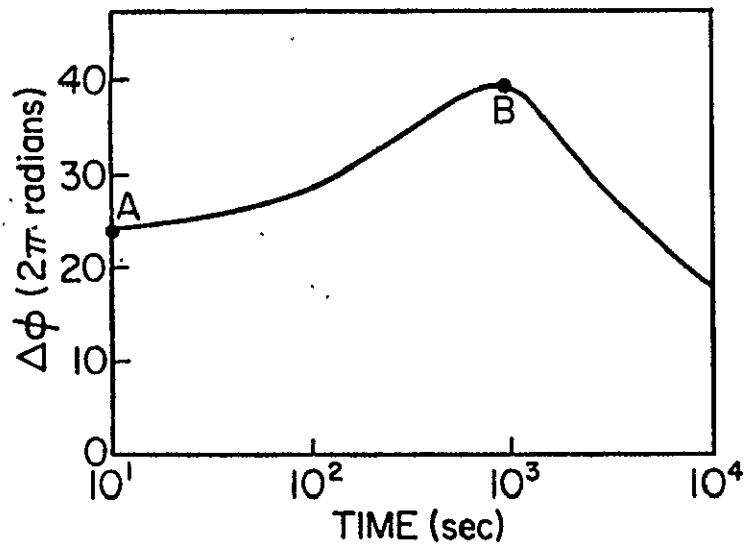
Fig. 20. Phase and amplitude variations in a 30 MHz signal propagating through the ionospheric lens. The point of reception is on the surface of the earth at the geometric projection of the center of the lens.
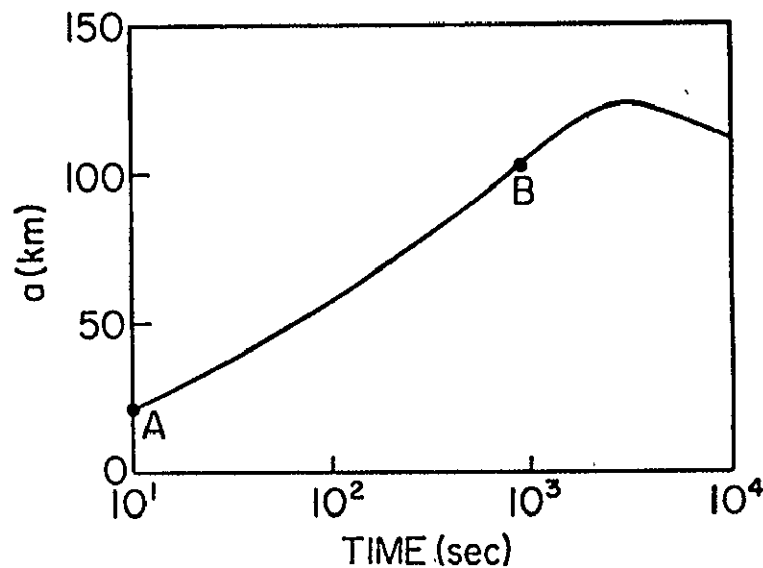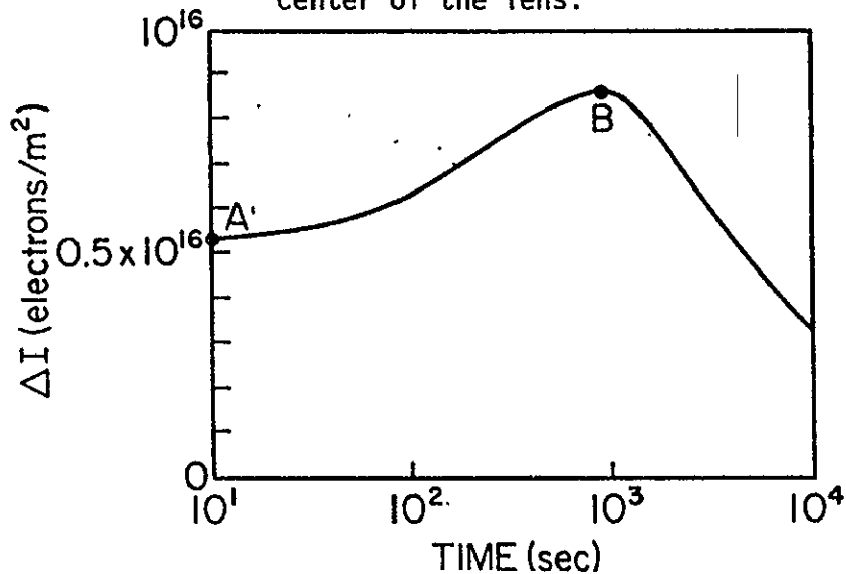
Fig. 21. Electron content reduction and ionospheric hole size deduced from the variations in Figure 20.
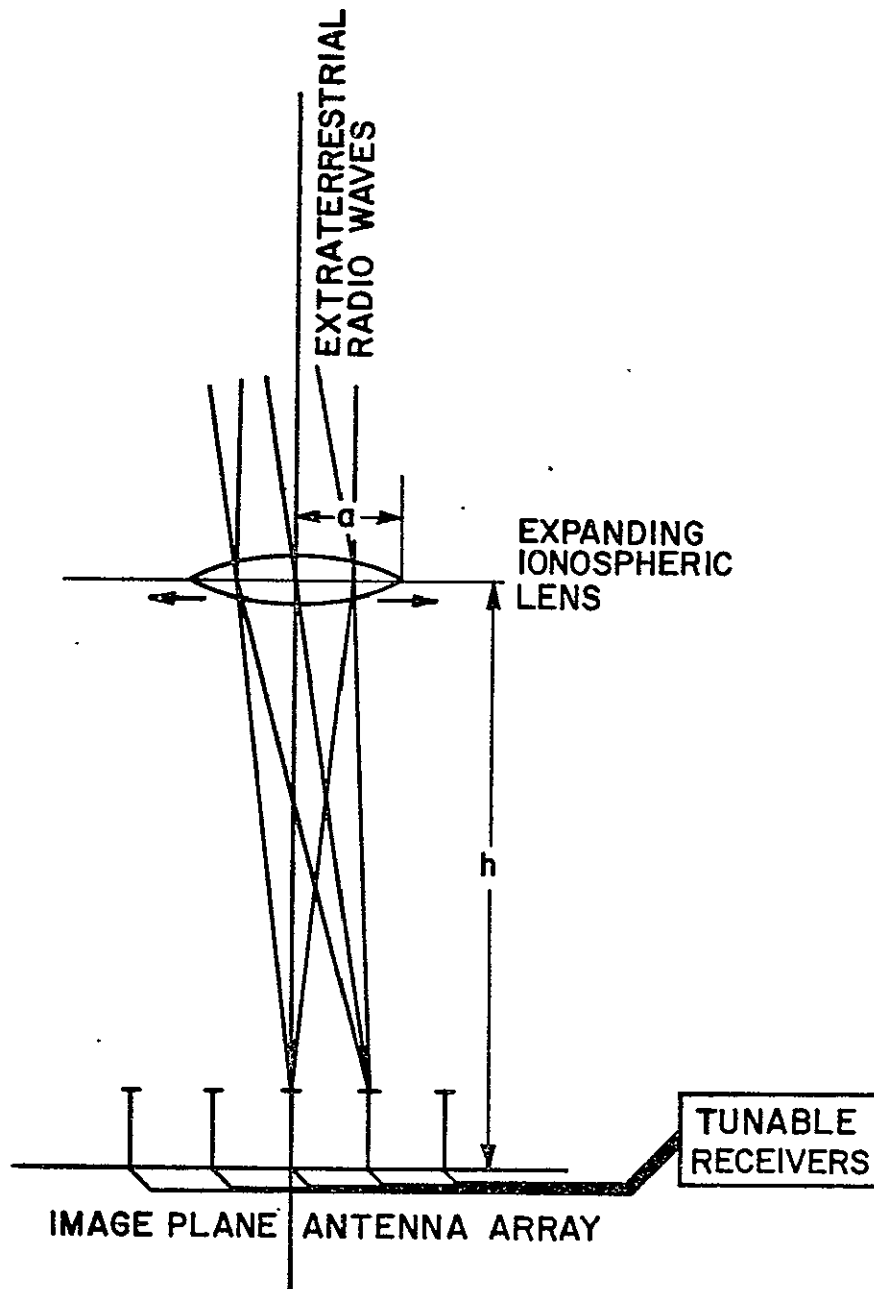
Fig. 22. The Refracting Radiotelescope.

measurements. Since the relative amplitude is larger during the initial stages of ionospheric modification, more accurate estimates of the horizontal extent of the depletion region are made at this time.

In practice, the measurement of absolute phase is accomplished by comparing the received signal phase with a fixed phase reference. The reference signal phase may be supplied by the transmission point in the form of a microwave signal that is not significantly affected by the ionospheric variations. Alternately, two VHF signals with different frequencies, and consequently different phase and amplitude sensitivities to ionospheric plasma variations, may be used. Since the extraordinary and ordinary modes of propagation in a magneto-ionic medium travel with different phase velocities, the change in relative phase between the two modes, and equivalently the change in polarization, has an information content equivalent to the absolute phase change of one mode. The theory outlined in this section may be easily extended to convert differential phase or polarization measurements, along with amplitude measurements, into estimates of the size of the ionospheric hole.

Low frequency radio astronomy is limited by the reflection of cosmic radio waves from the topside ionosphere. Controlled ionospheric depletion will permit the penetration of low frequency extraterrestrial radio waves for reception in a radiotelescope.

Low frequency radio astronomy is also limited by the radiotelescope aperture size. The half power beam width of a radio telescope is on the order of λ/a where λ is the radio wavelength and a is the radius of the reception aperture. The construction of extremely large
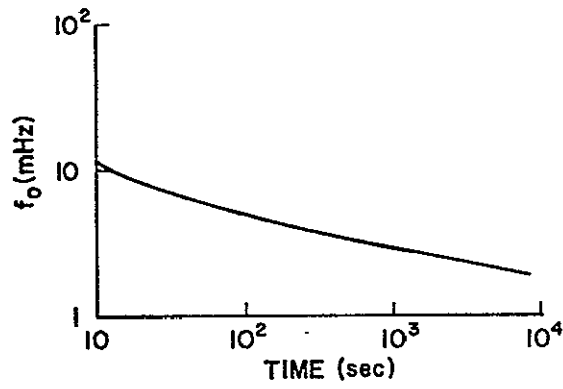
Fig. 23. Frequency of the wave
focused in the ground-
based image plane.
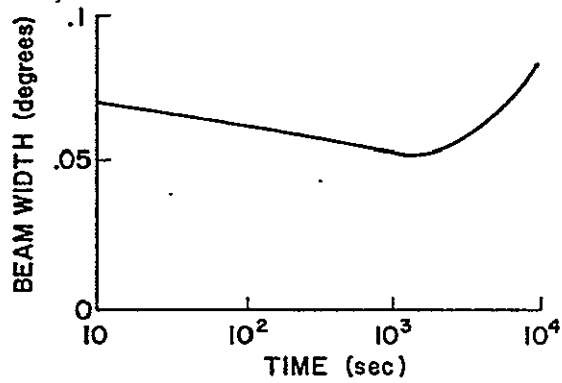
Fig. 24. Approximate beamwidth of
the lens (λ/a).

213

EXTRATERRESTRIAL RADIO WAVES

EXPANDING IONOSPHERIC LENS

TUNABLE RECEIVER

DISH REFLECTOR
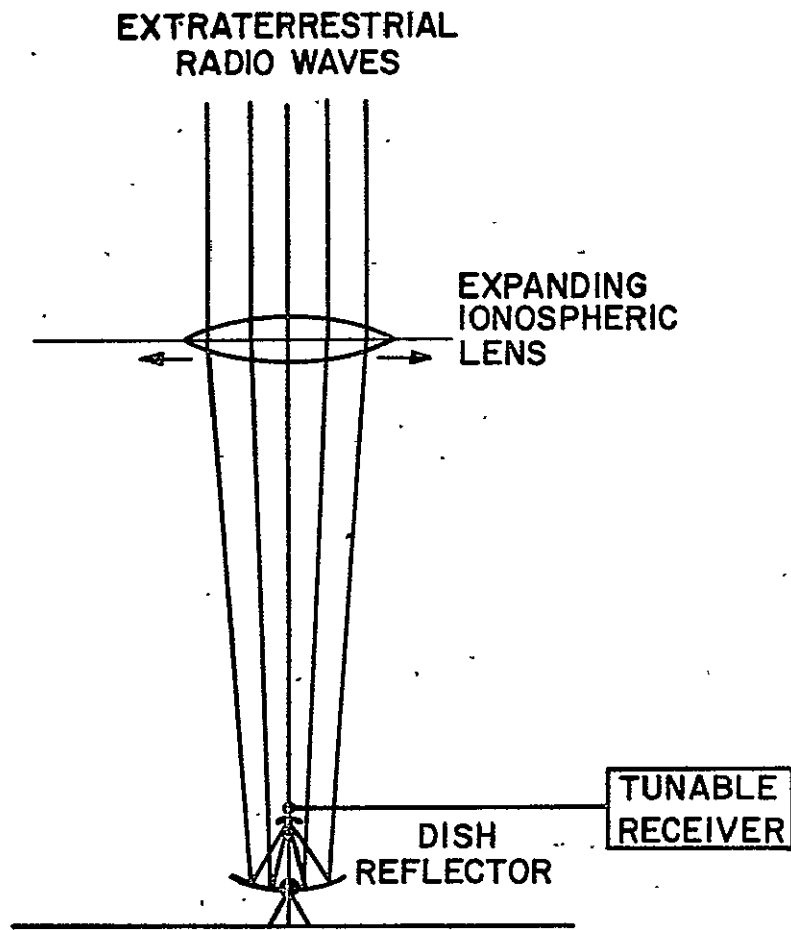
Fig. 25. Refracting-reflecting radiotelescope.

dishes comprising reflecting radiotelescopes for reception of low frequency (long wavelength) radio signals is impractical.

A refracting telescope using the ionospheric lens is proposed. An array of antennas is located in the image plane below the hole in the ionosphere (Figure 22). The output of each antenna is connected to a separate tunable receiver. The frequency of each receiver is varied keeping the image plane at the focus of the lens.

Consider the ionospheric lens with the time varying parameters given in Figure 21. The focal length of the lens is found from

$$h = 2\pi a^2/\varepsilon\lambda = a^2 f^2/(40.3 \ \Delta I)$$

where h is the focal length, a the lens radius, f the radiowave frequency in Hz, and ΔI the reduction in ionospheric content through the center of the lens. Letting $h = 300$ km, the frequency of the extra-terrestrial plane wave focused in the ground-based image plane is given by

$$f_o = \frac{3480(\Delta I)^{1/2}}{a}$$

The temporal variations in this frequency are shown in Figure 23. The beamwidth of the telescope is less than .2 of a degree (Figure 24).

A greater degree of flexibility is achieved with the refracting-reflecting radio-telescope illustrated in Figure 25. The radio ray trajectories are initially bent by the ionospheric lens and then focused by a parabolic reflector. This telescope permits a wider range of focused reception frequencies than the simple refracting radiotelescope.

Some degree of directional variability is achieved by movement of the dish. The dish may also serve to cut down interference by blocking manmade radio signals. Existing radiotelescope dishes may be used in this imaging system. .

The resolving power of the refracting radio telescope is limited by aberrations in the ionospheric lens. Detailed studies of the lens imaging properties will hopefully indicate that the distortion produced by the lens is not serious.

Chapter IX

CONCLUSIONS - RECOMMENDATIONS FOR AN IONOSPHERIC PERTURBATION EXPERIMENT

With the advent of the Space Shuttle System, routine launches into the lower thermosphere will be possible. The Shuttle Spacelab can be used to release chemically reactive gases directly into the F-region. The large payload capability (30,000 kg in 380 cubic meters) of the Shuttle makes it an ideal vehicle for experiments involving controlled chemical modificat on of the ionosphere. Not only can the Shuttle initiate the chemical depletion of the plasmasphere but, it can be used to observe the effects of the depletion. Chemical releases may also be performed by rockets or satellites, but the Space Shuttle is the preferred vehicle for multiple releases of large quantities of injected gas.

This research has presented an analysis of the fundamental aspects of the chemical modification experiment. It has demonstrated that substantial knowledge will be gained from observations of the effects of the reactive gas release. This research has also suggested conditions for the optimal experiment.

Of all the reactive gases investigated, hydrogen is the most promising. H_2 has the highest depletion efficiency per unit mass and the highest resistance to photodissociation. Loss of H_2 by condensation is highly unlikely. Chemical dissociation of H_2 is simpler to describe than the multi-stage dissociation of triatomic injectants such as H_2O.

Two disadvantages in using hydrogen instead of heavier gases are 1) the large volume of the gas in storage, and 2) the rapid expansion of the gas upon release. For a pressure of 1 atm and a temperature of

15°C, 100 kg of H_2 occupies about 10^3 m^3. This volume reduces to 11 m^3 at 100 atm pressure and to 1.4 m^3 for liquid hydrogen. In comparison, the volume of 100 kg of H_2O vapor at one atm and 100°C is 170 m^3 and in liquid form, 100 kg of H_2O occupies 0.1 m^3. The relatively low mass of the H_2 molecule results in rapid diffusive expansion and less localized depletion than would be produced by the heavier H_2O gas.

Initial modification experiments should be conducted with hydrogen because of the simplicity in describing depletion by diatomic molecules and because of the efficiency of H_2 when considering weight and condensation limitations. Sophisticated controlled depletion experiments can later be conducted by H_2O injection.

The optimum altitude of gas injection is dependent on the experimental goals. Maximum depletion of the protonosphere is attained by release approximately 50 km above the F-layer peak. The maximum reduction in the daytime F-layer peak density occurs for releases 50 km below the unperturbed peak. Other effects such as electron temperature rise and airglow enhancement are maximized for chemical releases in the vicinity of the F-layer peak.

The release altitude may be chosen from orbital considerations. The ground track for a space vehicle at 276.6 km altitude with an orbit inclination of 50° is shown in Figure 1. Orbits at this altitude overlap themselves every 24 hours (17 rotations for a vehicle traveling from west to east) and are therefore ideal for multiple gas releases over a given geographic location spaced by intervals of time of one day or greater. Orbits with large inclination with respect to the ecliptic cover a wide geographic latitude band.
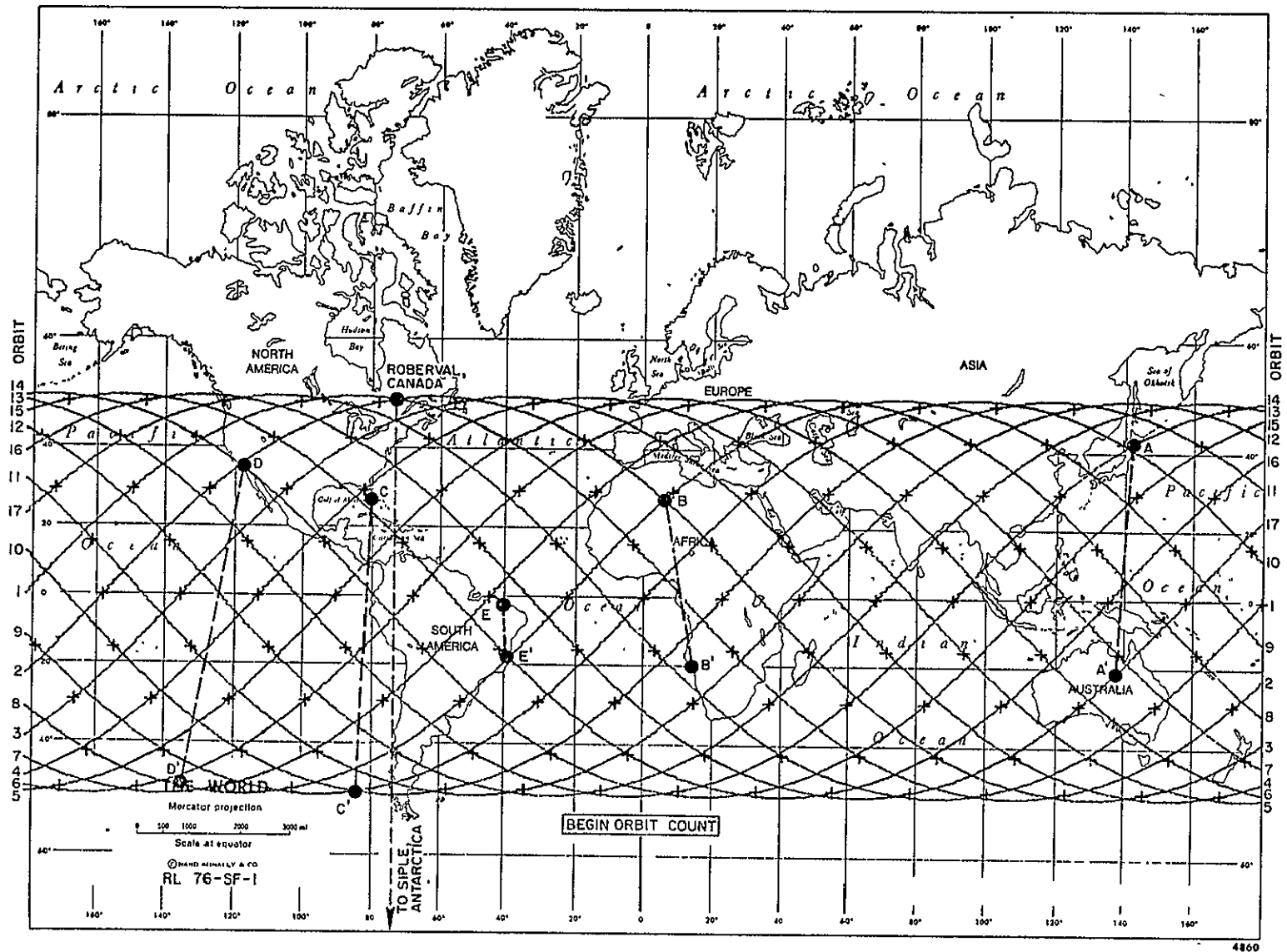
Fig. 1. Overlapping ground track for an inclined orbit at F-region altitudes. The spacecraft is moving eastward with a velocity of 7.743 km/sec at an altitude of 276.6 km making 17 orbits about the earth per day. Selected conjugate points are connected by dashed lines.

The minimum time between orbit crossings decreases with increasing latitude. Table I lists the latitude of and the time between the orbit

TABLE I

Crossing latitude	Time between crossing	
± 6°	11 hours	19 minutes
± 17.6°	9	59
± 27.4°	8	33
± 35.1°	7	00
± 41.1°	5	45
± 45.1°	4	15
± 47.9°	2	8
± 49.7°	1	29

crossings shown in Figure 1. The short time between the higher latitude crossings permits subsequent observation and/or remodification of the depletion region by releases from the orbiting space vehicle.

The gas should be released either over a ground station capable of measuring the effects of the deplet on or over the geomagnetic conjugate of the station. Local effects produced by the gas release are F-region plasma depletion, temperature change and airglow excitation. Conjugate effects include protonospheric and conjugate F-layer depletion.

Several conjugate locations are indicated in Figure 1. It is difficult to find stations that exist over land and intersect the orbital ground track as at points A and A'. Releases at an orbit crossing, points B or point C', may produce noticeable changes in ground-based observations of the conjugate ionosphere (points B' or point C). If the conjugate point is over the sea (point D') only

local effects may be easily measured (point D). Equatorial releases may be investigated at low latitude conjugate observatories such as at points E and E'.

Modification of regions with high-geomagnetic-latitudes may be conducted from orbits covering the mid-geographic-latitudes. Consider the geomagnetic conjugate stations Roberval, Canada and Siple Station, Antarctica (Figure 1). Because of the tilt of the geomagnetic poles, an orbit with an inclination of 50° crosses only Roberval. The release of reactive gases over Roberval may permit modification of the plasma-pause and creation of high-geomagnetic-latitude whistler ducts. Observation of the effects of gas releases may be conducted at Siple Station, Antarctica, far from the regions covered by the orbital ground track.

The ducted wave portion of the modification experiment must be conducted from space-born vehicles because VLF or HF signals trapped in depletion ducts probably don't reach the ground. An orbiting vehicle could release the gas at an orbit crossing such as point D in Figure 1 and on returning to the release point emit HF or VLF waves. The rapid round trip travel time ($\simeq$ .3 seconds) of the HF signal may permit reception of the ducted echo by the spacecraft. The long round trip time ($\simeq$ 3 seconds) of the VLF signal makes it likely that the spacecraft will move out of the duct before an echo is received. The effects of VLF trapped signals may be detected from high altitude satellites or from ground-based observations of precipitation produced by the scattering of trapped electrons.

The nature of the modification experiment is dependent on the time of day. Investigation of the recovery of the nighttime F-layer from

chemical depletion will provide information on mechanisms such as plasma flow from the protonosphere or corpuscular ionization. The nighttime enhancement of 6300A and other airglow lines is associated with the dissociative recombination chemistry involved in the modification process.

The analysis of the daytime experiment is complicated by photo- electron and ion production by solar rays. The recovery of the daytime F-layer is governed by the mechanisms that govern the nighttime layer plus the photo processes that are present during the day. The daytime airglow lines are not only produced by the dissociative recombination process but by particle impact and photodissociation excitation processes.

Interesting effects may be observed by conducting the ionospheric experiment at dawn during equinox. Consider the conjugate points B and B' in Figure 1. At dawn, point B' will be illuminated by the sun before point B. Photoionization at B' may produce a plasma flow along the magnetic field lines to point B. The importance of the dawn production at B' on the ionosphere at point B may be determined by chemically depleting the ionosphere at B' just as it is illuminated by the sun. The seasonal dependence on plasma inter- change between conjugate ionospheres at dawn may be similarly determined.

The ionospheric hole created during the modification experiment may be used as a lens in a refracting radio telescope. This telescope may be used to investigate previously unmeasured galactic radio sources in the 1 - 10 MHz frequency range. The nighttime release of 100 kg H_2 at the peak of the F-layer produces a lens with an aperture radius ranging from 20 to 120 km capable of focusing radio waves with

decameter wavelengths. The angular resolution of a radio telescope using this lens is better than 0.2 degrees.

Sources observable by the refracting radio telescope are the "brightest" in the galaxy. The galactic brightness temperature reaches a maximum for sources with frequencies around 10 MHz. The nonthermal (synchrotron) component of decameter radiation from the galaxy reaches brightness temperature of 250,000 K. (For meter wavelengths, the brightness temperature on the nonthermal radiation are of the order of 10,000 K.) .

The "aiming" of the refracting radio telescope in initial experiments need not be precise. The galactic disk has an angular thickness of about 5°. The position of the gas release should be between the galactic disk and the receiving antenna. The extraterrestrial signals can be recorded using a receiver sweeping the range of focused frequencies. The precise location of the lens may be determined a posteriori by optical measurements of the airglow ring surrounding the ionospheric hole. Further information on the location and the structure of the lens may be obtained from ionsonde or incoherent scatter radar measurements or from perturbations in satellite radiowave transmissions propagating through the lens.

Narrow-beam observation of the sun at decameter radio wavelengths has been previously impossible using reflecting radio telescopes. With accurate positioning of a gas release between the sun (angular diameter $\simeq$ .5°) and a receiving aperture, high resolution pictures of the radio sun may be obtained.

The expenditure of time and money involved in performing the ionospheric modification experiment can be justified by the enormous amount

of information derived from the experiment. By observing the perturbations in the F-region, one can use the ionosphere as a laboratory for measuring selected physical and chemical properties. Diffusion parameters may be determined from the evolution of the released gas cloud, the ionospheric trough, and the airglow ring outlining the depletion region. Chemical reaction rates may be determined from the magnitude of the ionospheric depletion and the intensity of the enhanced airglow. Knowledge of thermospheric heating and cooling rates may be obtained from measurements of the ion and electron temperature fluctuations.

Imposed winds and electric fields may be determined from observations of the effects of chemical releases. Transport of the injected gas cloud by neutral atmospheric drifts produces motion of the airglow ring. Movement of the depleted plasma tube results in motion of the hole inside the airglow ring. Therefore, neutral winds and electric fields may be determined from observations of the airglow emissions. Measurements of these optical emissions may be taken at any time of day. Electric field estimation by tracking the motion of the depleted plasma tube may also be obtained by radiowave measurements.

The depleted ionospheric and magnetospheric regions can be used in determining physical quantities not directly connected with the formation of these regions. The magnetospheric trough may guide radio signals for use in wave-particle interaction experiments. Some phenomena that can be studied using depletion ducts are amplification of VLF radio waves and scattering of trapped particles by these waves. By using the perturbed ionosphere as a lens, observations of extraterrestrial radio sources may be made.

Several areas of investigation are indicated as an extension of this work. Further study of the early effects of the injected gas sweeping out the background atmosphere is needed. The effects of depletion of the dusk and dawn ionosphere should be examined. The study of releases at low latitudes (with nearly horizontal field lines) or high latitudes (with field lines opening into the magnetotail) are of interest. Extending the mid-latitude ionospheric model to the conjugate ionosphere would be useful in investigating nonlocal effects of the depletion. An extension of this work is to investigate the injection of gases other than H_2 and to investiate airglow emissions besides the $O(^1D)$ 6300A emission. Further investigation of the depleted magnetosphere should include a stability analysis of the depleted plasma tube and the interaction between the plasma and waves trapped in the tube. Finally, the imaging properties of the ionospheric lens for use in a refracting radio telescope should be examined in greater detail.

Appendix A

CALCULATION OF CHEMICAL PROPERTIES

Most of the data in Table 1 were obtained from experimental measurements of chemical properties. In a few cases the reaction rate of a chemical process was inferred from rates of similar processes.

The reaction rates in all the ion-molecule reactions in Table 1 are based on measurements [Ferguson, 1973], but the heat released in these reactions is not. The heat of reaction is calculated from the ionization potential and heat of formation of each substance in the reaction.

As an example, consider the reaction $O^+ + H_2 \rightarrow OH^+ + H$. This reaction is subdivided into a series of steps each requiring the addition or subtraction of a known amount of energy.

The ionization potential of O is 13.618 eV

$$O^+ + H_2 + e \rightarrow O + H_2 + 13.618 \text{ eV}$$
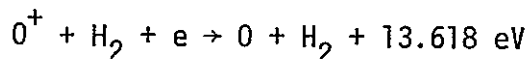
The heat of formation of H is -52.096 kcal/mole or -2.261 eV. Since H_2 is the normal state of hydrogen at 300 K this means

$$1/2 \ H_2 \rightarrow H - 2.261 \text{ eV}.$$

Therefore,

$$O^+ + H_2 + e \rightarrow O + H + H + 13.618 - 2(2.261) \text{ eV}$$

$$= O + H + H + 9.096 \text{ eV}.$$
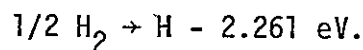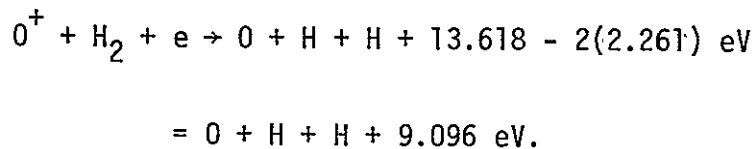
The heat of formation of OH is -9.31 kcal/mole = -.404 eV. The

heat of formation of O is -59.553 kcal/mole = -2.585 eV.

The formation of OH from O_2 and H_2 is characterized as

$$1/2 \ O_2 + 1/2 \ H_2 \rightarrow O + H - 2.585 - 2.261$$

$$\rightarrow OH - .404$$

or $O + H \rightarrow OH + 4.442$ eV.
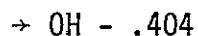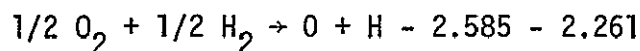
Therefore, the exchange reaction between e^-, O^+ and H_2 is

$$O^+ + H_2 + e^- \rightarrow OH + H + 9.096 + 4.442$$

$$= OH + H + 13.538$$
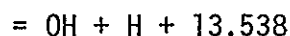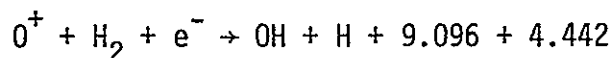
The ionization potential of OH^+ is 13.17 eV. The overall energy

released is 13.538 - 13.17 = .368 eV giving

$$O^+ + H_2 \rightarrow OH^+ + H + 3.68 \text{ eV}.$$
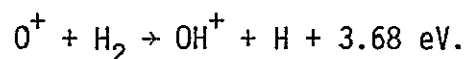
This somewhat lengthy procedure has been used to calculate the heat

released for all the reactions in Table 1. All heat of formation and

ionization potential data are taken from Franklin and Dillard [1969].

The dissociative recombination reaction rates for NO_2^+, OH^+,

H_2O^+, N_2O^+ and NH^+ are based on rate coefficients for similar ions.

Biondi [1973] has shown that electron-ion rates are dependent on ion

complexity: the rates decrease monotonically for ions of increasing

atomic number and for ions with a higher number of atoms. For

example, the diatomic ion, OH^+, is assumed to have a rate of 1×10^{-7} because its atomic number lies between two diatomic ions with known reaction times

$$H_{e_2}^+ \text{ (rate} = 1 \times 10^{-8}) \text{ and } N_2^+ \text{ (rate} = 2.2 \times 10^{-7}).$$
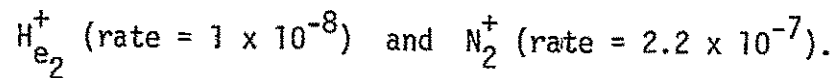
Photodissociation rates are calculated by integration of the product of absorption cross section times radiation density over the solar input spectrum [Banks and Kockarts, 1973 and Bates and Hayes, 1967]. The photodissociation coefficients in Table 1 are for an overhead sun. Data at other times of the day must be scaled according to solar declination.

Appendix B

H_2O AND H_2 PHYSICAL DATA

Parameter	Symbol	Units	H_2O	H_2
Molecular radius	r_m	Angstroms	2	1.25
Molecular mass	m	kg	3.0×10^{-26}	3.34×10^{-27}
Molecular volume in liquid	v_B	m^3	3.0×10^{-29}	1.11×10^{-28}
Specific heat ratio	γ	--	1.41	1.3
Latent heat of vaporization	U	J/kg	2.47×10^{-10}	6.8×10^5
Saturated vapor constant	B	$m^3/(K\text{-}kg)$	1.31×10^{-10}	1.48×10^{-5}
Gas constant	R	J/(K-kg)	462	4155
Specific heat: vapor	c_1	J/(K-kg)	1607	10200
solid	c_2	J/(K-kg)	4186	6120
Surface tension	σ	Nt/m	.09	.00231
Critical point temperance	T_c	K	374.2	33.18
Triple point temperature	T_t	K	273.16	13.947

H_2O data from American Institute of Physics Handbook [1963]

H_2 data from Scott [1964]

Appendix C

EQUILIBRIUM CONDENSATION DURING EXPANSION

The time varying degree of condensation is calculated for an expanding gas cloud in thermodynamic equilibrium. The specific gas volume v is a function of temperature T and degree of condensation x as given by

$$v = (1-x) \; BT \; \exp(U/RT) \qquad (1)$$

where B is the gas dependent saturated vapor constant, and U the latent heat of vaporization, and R the universal gas constant. The first law of thermodynamics for a perfect gas is

$$dQ = dE + PdV \qquad (2)$$

For an isentropic expansion, $dQ = 0$. The internal energy differential dE is written in terms of partial derivatives with respect to T, v, x.

$$dU = \left(\frac{\partial E}{\partial T}\right)dT + \left(\frac{\partial E}{\partial v}\right)dv + \left(\frac{\partial E}{\partial x}\right)dx \qquad (3)$$

The change in internal energy with temperature at constant volume and degree of condensation is a weighted sum of the gaseous and solid specific heats.

$$\left(\frac{\partial E}{\partial T}\right)_{v,x} = \left(\frac{\partial E}{\partial T}\right)_{v,x,solid} + \left(\frac{\partial E}{\partial T}\right)_{v,x,vapor} = x \, c_2 + (1-x)c_1 \qquad (4)$$

233

where c_1 is the specific heat of the vapor at constant volume and c_2 the specific heat of the condensate. $(\partial E/\partial v)_{T,x} = 0$ for a perfect gas. The energy change with condensation is heat gained by the change in the amount of each phase less the heat lost by condensation.

$$\left(\frac{\partial E}{\partial x}\right)_{v,T} = (c_2 - c_1)T - U \tag{5}$$

Finally, the perfect gas law gives

$$P = RT/v_g = RT(1-x)/v \tag{6}$$

where the gas volume v_g is related to the fluid volume v by the expression $v = (1-x)v_g$.

Making these substitutions, the adiabatic heat equation becomes

$$[c_1(1-x) + c_2 x]dT + RT(1-x)dv/v - [U - (c_2-c_1)T]dx = 0 \tag{7}$$

Differentiate (1) to get

$$dv = [(1-x)BT \exp(-U/(RT^2))] + (1-x)B \exp(U/RT)]dt + [-BT \exp(U/RT)]dx \tag{8}$$

Divide by v to obtain

$$dv/v = [-U/(RT) + 1/T]dT - dx/(1-x) \tag{9}$$

234

Substitute for dv/v in (7) to get

$$[c_1(1-x) + c_2 x + (1-x)(RT-U)/T] - [RT + U - (c_2-c_1) T] dx = 0$$

$$(10)$$

Solve for dx/dT to obtain

$$\frac{dx}{dT} = \frac{(a_1 T-1)}{(1-b_1 T)T} + \frac{x(1+b_1 T)}{(1-b_1 T)T}$$

$$(11)$$

where $a_1 = (R + c_1)/U$ and $b_1 = (c_2-c_1 + R)/U$

The solution for x subject to $x = x_0$ when $T = T_0$ is

$$x = e^{-F}\left(x_0 + \int_{T_0}^{T} \frac{(1-a_1 T_1)}{T_1(b_1 T_1-1)} e^{F(T_1)} dT_1\right)$$

$$(12)$$

where $F(T) = \int_{T_0}^{T} \frac{b_1 T_1+1}{(B_1 T_1-1)T_1} dT_1 = \overline{\log_e[(b_1 T-1)^2 T_0/(b_1 T_0-1)^2 T]}$

Integrate to get

$$x(T) = \frac{T}{(b_1 T-1)^2}\left[\frac{(b_k T_0-1)^2 x_0}{T_0} + (T_0-T) [a_1 b_1 +1/(TT_0)]\right.$$

$$\left. + (a_1+b_1) \cdot \log_e(T/T_0)\right]$$

$$(13)$$

If x_0 is zero and T_0 the temperature when condensation begins, (13) becomes

235

$$x(T) = \frac{T}{(b_1 T - 1)^2} \left[(T_0 - T)[a_1 b_1 + 1/(TT_0)] + (a_1 + b_1) \log_e (T/T_0)] \right]$$

(14)

Equations (1) and (14) specify the temperature and condensation degree for each value of specific gas volume.

Appendix D

DERIVATION OF THE DIFFRACTION SERIES FROM THE FRESNEL DIFFRACTION EQUATION - SPECIFIC APPLICATION TO THE GAUSSIAN PHASE SIGNAL

The Fresnel diffraction of a wave is given by

$$U(x,y,z) = \int_{-\infty}^{\infty}\int_{-\infty}^{\infty} U(x_1,y_1,0) \exp[j\pi((x_1-x)^2 + (y_1-y)^2)/\lambda z] \, dx_1 \, dy_1$$

$$\cdot \exp[j2\pi z/\lambda]/(j\lambda z) \qquad (1)$$

where λ is the wavelength, (x,y) the coordinate system parallel to the plane of reception, $U(x,y,0)$ the complex amplitude of the signal at $z = 0, x$ and $U(x,y,z)$ the received complex amplitude. Because the complex exponential in the integral varies rapidly with x_1 and y_1 for small values of z, this integral is difficult to evaluate numerically. This function is written in terms of the convolution of the initial signal with the Fresnel kernal

$$U(x,y,z) = \exp[j2\pi z/\lambda]\left[\frac{\exp[-\pi(x^2 + y^2)/(j\lambda z)]}{j\lambda z} * U(x,y,0)\right] \qquad (2)$$

Use the convolution theorem of Fourier transform theory to obtain

$$U(x,y,z) = \exp[j2\pi z/\lambda]\mathcal{F}^{-1}[\exp[-j\lambda z\pi(f_x^2 + f_y^2)]\mathcal{F}U(x,y,0)] \qquad (3)$$

where $\mathcal{F}^{-1}$ and $\mathcal{F}$ are the inverse and forward Fourier transforms respectively. Expand the exponential inside the inverse transform to give

$$U(x,y,z) = \exp[j2\pi z/\lambda]\mathcal{F}^{-1}\left[\sum_{s=0}^{\infty}(-j\lambda z\pi)^s(f_x^2 + f_y^2)^s/s! \; \mathcal{F}U(x,y,0)\right] \qquad (4)$$

237

The differentiation theorem of Fourier Transform theory is

$$\nabla^{2s}_{x,y} U(x,y) = \mathcal{F}^{-1}[(-4\pi)^s (f_x^2 + f_y^2)^s \mathcal{F}U(x,y)] \qquad (5)$$

where $\nabla^2_{x,y} = \dfrac{\partial^2}{\partial x^2} + \dfrac{\partial^2}{\partial y^2}$. The application of this theorem results in

$$U(x,y,z) = \exp[j2\pi z/\lambda] \sum_{s=0}^{\infty} (j\lambda z/4\pi)^s [\nabla^{2s}_{x,y} U(x,y,0)]/s! \qquad (6)$$

If U is radially symmetric (i.e., $U(z=0)$ is a function of $x^2 + y^2 = r^2$ only) then

$$U(r,z) = \exp[j2\pi z/\lambda] \sum_{s=0}^{\infty} (j\lambda z/\pi)^s \left[\frac{d^s}{(dr^2)^s} \left(r^{2s} \frac{d^s}{dr^{2s}} \right) U(r,0) \right] /s \qquad (7)$$

The received complex amplitude signal is an infinite sum of spatial derivatives of the signal at z=0. Only the first few terms of this series are significant for small values of z.

If the initial complex amplitude signal is continuously differentiable, the multiple derivatives in (7) simplify at r=0 giving

$$U(0,z) = \exp[j2\pi z/\lambda] \sum_{s=0}^{\infty} (j\lambda z/\pi)^2 \left[\frac{d^2}{(dr^2)^s} U(r,0) \right] \qquad (8)$$

A radially symmetric Gaussian phase perturbation is considered.

$$U(r,0) = \exp[j\phi(r)] \quad \text{where} \quad \phi(r) = \varepsilon \exp[-4^2/2a^2] \qquad (9)$$

It can be shown that

$$\frac{d^s}{(dr^2)^s} [\exp(j\varepsilon e^{-r^2/2a^2})] = e^{j\varepsilon e^{-r^2/2a^2}} \left(\frac{-j\varepsilon}{2a^2} e^{-r^2/2a^2} \right)^s P_s\left(\frac{1}{j\varepsilon e^{-r^2/2a^2}} \right)$$

$$(10)$$

where $P_s(x) = \sum_{m=1}^{s} \mathcal{S}_s^{(m)} x^{s-m} x^{s-m}$ and $\mathcal{S}_s^{(m)}$ are the Sterling numbers of the second kind [Abramowitz and Stegun, 1965]. $\mathcal{S}_m^{(m)}$ satisfies the following recursive equation

$$\mathcal{S}_{n+1}^{(m)} = m\mathcal{S}_n^{(m)} + \mathcal{S}_n^{(m-1)}$$

In closed form

$$\mathcal{S}_n^{(m)} = \sum_{k=0}^{m} \frac{(-1)^{m-k} k^n}{k!(m-k)!} \tag{11}$$

The observed complex amplitude at $r=0$ found from (8) and (10) is

$$u(0,z) = \exp[j(2\pi z/\lambda + \varepsilon)] \sum_{s=0}^{\infty} \left(\frac{\lambda z \varepsilon}{2\pi a^2}\right)^s P_s\left(\frac{1}{j\varepsilon}\right) \tag{12}$$

BIBLIOGRAPHY

Abraham, F. F., *Homogeneous Nucleation Theory*, Academic Press, New York, 1974.

American Institute of Physics Handbook (D. E. Gray, Ed.), McGraw-Hill Book Co., New York, 1963.

Angeromi, J. J., and J. O. Thomas, "Studies of Planetary Atmospheres, 1. The Distribution of Electrons and Ions in the Earth's Exosphere," *J. Geophys. Res.*, 69, 1964.

Antoniadis, D. A., "Thermospheric Winds and Exospheric Temperatures from Incoherent Scatter Radar Measurements in Four Seasons," *J. Atm. Terr. Phys.*, 38, 187, 1976.

Banks, P. M., and G. Kockarts, *Aeronomy*, *Vol A and B*, Academic Press, New York, 1973.

Barnes, Cecil Jr.,"Comment on paper by Henry G. Booker, 'A Local Reduction of F-Region Ionization Due to Missile Transit,'" *J. Geophys. Res.*, 66, 2589, 1967.

Baum, H. R., "The Interaction of a Transient Exhaust Plume with a Rarified Atmosphere," *J. Fluid Mech.*, 58, 795, 1973.

Baum, H. R., "The Interaction of an Exhaust Plume with a Rarefied Atmosphere," *Ninth International Symposium on Rarified Gas Dynamics*, Göttingen, July 15-20, 1974.

Baxter, D. C., and L. M. Linson, "Dynamics of Gas Clouds Released from Spacelab," *Amer. Geophys. Union Spring Annual Meeting*, SA-13, 1976.

Bernard, L. C., "Amplitude Variations of Whistler-mode Signals Caused by their Interaction with Energetic Electrons of the Magnetosphere," *Technical Report No. 3465-2*, Radioscience Laboratory, Stanford Electronics Laboratories, Stanford University, Stanford, CA, Dec 1973.

Bernhardt, P. A., C. G. Park, and P. M. Banks, "Depletion of the F2-Region Ionosphere and the Protonosphere by the Release of Molecular Hydrogen," *Geophys. Res. Lett.*, 2, 341, 1975.

Bienkowski, G., "Collisionless Expansion of Gas Clouds in the Presence of an Ambient Gas," *Phys. of Fluids*, 7, 382, 1964.

Biondi, M. A., "The Effects of Ion Complexity on Electron-ion Recombination," *Comments on Mod. Phys.*, D4, 85-91, 1973.

Booker, Henry G., "A Local Reduction of F-Region Ionization due to Missile Transit," *J. Geophys. Res.*, 66, 1079, 1961.

Brode, H. L., and J. E. Enstrom, "Analysis of Gas Expansion in a Rarified Atmosphere," Phys. of Fluids, 15, 1913, 1972.

Brook, J. W., and B. B. Hamel, "Spherical Source Flow with a Finite Back Pressure," Phys. of Fluids, 15, 1898, 1972.

Budden, K. G., Radio Waves in the Ionosphere, Cambridge University Press, 1966.

Carpenter, L. A., and S. A. Bowhill, "Investigation of the Physics of Dynamical Processes in the Topside F-region," Aeronomy Report No. 44, University of Illinois, 1971.

Cerisier, J. C., "Ducted and Partly Ducted VLF Waves through the Magnetosphere," J. Atm. Terr. Phys., 36, 1443-1467, 1974.

Crank, J., and P. Nicolson, "A Practical Method for Numerical Evaluation of Solutions of Partial Differential Equations of the Heat-Conduction Type," Proc. Camb. Phil. Soc., 43, 50, 1947.

Chapman, S., and T. G. Cowling, The Mathematical Theory of Nonuniform Gases, Cambridge University Press, 1970.

Carrara, N., M. T. DeGiorgio, and P. F. Pelligrini, "Guided Propagation of HF Radio Waves in the Ionosphere," Space Sci. Rev., 11, 555-592, 1970.

Cheng, H. K., and J. W. Kirsch, "On the Gas Dynamics of an Intense Explosion with an Expanding Contact Surface," J. Fluid Mech., 39 289, 1969.

da Rosa, A. V., "The Theoretical Time-Dependent Behavior of the Ionospheric Electron Gas," J. Geophys. Res., 71, 4107, 1966.

Edwards, R. H., and H. K. Cheng, "Steady Expansion of a Gas into a Vacuum," AIAA Journal, 4, 558-560, 1966.

Edwards, R. H., and H. K. Cheng, "Distribution Function and Temperature In a Monatomic Gas under Steady Expansion into a Vacuum," Advances in Applied Mechanics: Proceedings of the 5th Symposium of Rarified Gas Dynamics, Suppl. 4., Vol 1, Academic Press, New York, 819, 1967.

Evans, J. V., "On the Behavior of f_oF2 during Solar Eclipses," J. Geophys. Res., 70, 733, 1965.

Evans, J. V., "Theory and Practice of Ionospheric Study of Thomson Scatter Radar," Proc. IEEE, 57, 496, 1969.

Feder, J., D. C. Russell, J. Lothe, and G. M. Pound, "Homogeneous Nucleation and Growth of Droplets in Vapours," Adv. Phys., 15, 111, 1966.

Ferguson, E. E., "Rate Constants of Thermal Energy Binary Ion-Molecule Reactions of Aeronomic Interest," Atomic Data and Nuclear Data Tables, 2, No. 2, 159, 1973.

Franklin, J. L., and J. G. Dillard, Ionization Potentials, Appearance Potentials, and Heats of Formation of Gaseous Positive Ions, NSRDS-NBS 26, U. S. Department of Commerce, National Bureau of Standards, U. S. Government Printing Office, Washington, D. C., 1969.

Freeman, N. C., "Solutions of Boltzamn Equation for Expanding Flows," AIAA Journal, 5, 1696, 1967.

Freeman, N. C., and D. R. Thomas, "On Spherical Expansions into a Vacuum," Advances in Applied Mechanics: Rarified Gas Dynamics, Suppl. 5, Vol. 1, Academic Press, New York, 1969.

Frenkel, J., Kinetic Theory of Liquids, Oxford University Press, New York, 1946.

Garriott, O. K., A. V. da Rosa, M. J. Davis, and O. G. Villard Jr., "Solar Flare Effects in the Ionosphere," J. Geophys. Res., 72, 6099-6103, 1967.

Goodman, J. W., Introduction of Fourier Optics, McGraw-Hill Book Co., 1968.

Greifinger, C., and J. D. Cole, "Expansion of a Finite Mass of Gas into a Vacuum," AIAA Journal, 3, 1200, 1965.

Grundy, R. E., "Unsteady Expansions into Vacuum with Spherical Symmetry," J. Fluid Mech., 39, 529, 1969.

Grundy, R. E., and D. R. Thomas, "Unsteady Spherically Symmetric Expansion of a Fixed Mass of Gas into a Vacuum," AIAA Journal, 7, 967, 1969.

Haser, L., "Use of Artificial Barium Clouds to Study Magnetic and Electric Fields in the Atmosphere," Aurora and Airglow (B. M. McCormac, Ed.) Reinhold Pub. Corp., New York, 391-403, 1967.

Helliwell, R. A., Whistlers and Related Ionospheric Phenomena, Stanford University Press, 1965.

Helliwell, R. A., and J. P. Katsufrakis, "VLF Wave Injection into the Magnetosphere from Siple Station, Antarctica," J. Geophys. Res., 79, 2511, 1974.

Helms, W. J., and A. D. Thompson, "Ray-Tracing Simulation of Ionization Trough Effects upon Radio Waves," Radio Science, 8, 1125, 1973.

Herman, J. R., and S. Chandra, "The Influence of Varying Solar Flux on Ionospheric Temperatures and Densities: a Theoretical Study," Planet Space Sci., 17, 815, 1969.

Hirth, J. P., and G. M. Pound, Progress in Materials Science, Vol XI, Pergamon Press, London, 1963.

Hoerner, S. F., Fluid-Dynamic Drag, Published by author, 1965.

Hubbard, E. W., "Expansion of Uniform Gas Clouds into a Vacuum," AIAA Journal, 5, 378, 1967.

Hunten, D. M., "Airglow - Introduction and Review," The Radiating Atmosphere (B. M. McCormac, Ed.), Springer-Verlag, New York, 1971.

Irvine, W. M., and J. B. Pollack, "Infrared Optical Properties of Water and Ice Spheres," ICARUS, 8, 324, 1968.

Jackson, J. E., H. A. Whale, and S. J. Bauer, "Local Ionospheric Disturbance Created by a Burning Rocket," J. Geophys. Res., 67, 2059-2061, 1962.

Kamke, E., Differentialgleichungen Lösungsmethoden und Lösungen, Chelsea Publishing Co., New York, 1959.

Madonna, L. A., C. M. Scuilli, L. N. Canjar, and G. M. Pound, "Low Temperature Cloud Chamber Studies on Water Vapour," Proc. Roy. Soc., Vol LXXVIII, 1218, 1961.

Mason, E. A., and R. T. Marrero, "The Diffusion of Atoms and Molecules," Advances in Atomic and Molecular Physics (D. R. Bates, Ed.), Vol. 6, Academic Press, New York, 155, 1970.

McDonald, J. E., "Homogeneous Nucleation of Vapor Condensation, 1. Thermodynamic Aspects," Amer. J. of Phys. 30, 870, 1962.

McDonald, J. D., "Homogeneous Nucleation of Vapor Condensation, 2. Kinetic Aspects," Amer. J. of Phys., 31, 31, 1963.

Mendillo, M., G. S. Hawkins, and J. A. Klobuchar, "A Large-Scale Hole in the Ionosphere Caused by the Launch of Skylab," Science, 187, 343, 1975a.

Mendillo, M., G. S. Hawkins, and J. A. Klobuchar, "A Sudden Vanishing of the Ionosphere due to the Launch of Skylab," J. Geophys. Res., 80, 2217, 1975b.

Mirels, H., and J. F. Mullen, "Expansion of Gas Clouds and Hypersonic Jets Bounded by a Vacuum," AIAA Journal, 1, 596, 1963.

Morse, P. M., Thermal Physics, W. A. Benjamin, Inc., New York, 1969.

Muldrew, D. B., "Radio Propagation along Magnetic Field-Aligned Sheets of Ionization Observed by the Alouette Topside Sounder," J. Geophys. Res., 68, 5355, 1963.

Muldrew, D. B., "Whistler-Mode Transmissions by the Alouette II Topside Sounder," URSI Abstracts (Ottawa), 171, May 1976a.

Muldrew, D. B., "Delayed Generation of an Electromagnetic Pulse in the Topside Ionosphere," J. Geophys. Res., 72, 1967b.

Muldrew, D. B., and E. L. Hagg, "Properties of High-Latitude Ionospheric Ducts Deduced from Alouette II Two-Hop Echoes," Proc. IEEE, 57, 1128, 1969.

Narasimha, J., "Collisionless Expansion of Gases into Vacuum," J. Fluid Mech., 12, 294, 1962.

Ness, N., and J. P. Ambrosiani, "A Spherical Piston Problem Including the Effects of Equilibrium Chemistry," AIAA Journal, 6, 1200, 1968.

Nishizoki, R., and N. Matura, "Conjugate Ducted Echoes Observed on Topside-Sounder Data," J. Radio Res. Lab., 19, 53, 1972.

Noxon, J. F., "Optical Emission from $O(^1D)$ and $O_2(b^1\Sigma g)$ in ultraviolet photolysis of O_2 and CO_2," J. Chem. Phys., 52, 1852, 1970.

Park, C. G., "Methods of Determining Electron Concentrations in the Magnetosphere from Nose Whistlers," Technical Report No. 3454-1, Radioscience Laboratory, Stanford Electronics Laboratories, Stanford University, Stanford, CA, 1972.

Park, C. G., and P. M. Banks, "Influence of the Thermal Plasma Flow on the Mid-Latitutde F2-Layer: Effects of Electric Fields and Neutral Winds in the Plasmasphere," J. Geophys. Res., 79, 4661, 1974.

Park, C. G., and P. M. Banks, "Influence of Thermal Plasma Flow on the Daytime F2-Layer," J. Geophys. Res., 80, 2819, 1975.

Park, C. G., and H. A. Helliwell, "The Formation by Electric Fields of Field-Aligned Irregularities in the Magnetosphere," Radio Science, 6, 299, 1971.

Roble, R. G., J. F. Noxon, and J. V. Evans, "The Intensity Variation of the Atomic Oxygen Red Line during Morning and Evening Twilight on April 9-10, 1969," Planet. Space Sci., in press, 1976.

Rosenberg, N. W., "Project Firefly 1962-1963," Environmental Research Papers, No. 15, FACRL-64-364, May 1964.

Rosenberg, T. J., R. A. Helliwell, and J. Katsufrakis, "Electron Precipitation Associated with Discrete Very Low Frequency Emissions," J. Geophys. Res., 76, 8445, 1971.

Schunk, R. W., and J. C. G. Walker, "Minor Ion Diffusion in the F2-Region of the Ionosphere," Planet. Space Sci., 18, 1319, 1970.

Schofield, K., "An Evaluation of Kinetic Data for Reactions of Neutrals of Atmospheric Interest," Planet. Space Sci., 15, 643, 1967.

Scott, R. B., Technology and Uses of Liquid Hydrogen, Pergamon Press, New York, 1964.

Seaton, M. J., "The Calculation of Cross-sections for Excitation of Forbidden Transition Lines by Electron Impact," J. Atmos. Terr. Phys., 5, spec. suppl., 289, 1955.

Sharma, R. P., and D. B. Muldrew, "Seasonal and Longitudinal Variations in the Occurance Frequency of Magnetospheric Ionization Ducts," J. Geophys. Res., 80, 977, 1975.

Smith, R. L., and N. Brice, "Propagation in Multicomponent Plasmas," J. Geophys. Res., 69, 5029, 1964.

Smith, R. L., R. A. Helliwell, and I. Yabroff, "A Theory of Trapping of Whistlers in Field-Aligned Columns of Enhance Ionization," J. Geophys. Res., 65, No. 3, 815, 1960.

Sodha, M. S., A. K. Ghatok, D. P. Tewari, and P. K. Dubey, "Focusing of Waves in Ducts," Radio Science, Vol 7, 1005-1010, 1972.

Stanyukovich, D. P., Unsteady Motion of Continuous Media, Pergamon Press, New York, 1960.

Stix, T. H., The Theory of Plasma Waves, McGraw-Hill Book Co., New York, 1962.

Swartz, W. E., and J. S. Nisbet, "Revised Calculations of F-Region Ambient Electron Heating by Photoelectrons," J. Geophys. Res.,

Taylor, G. I., "The Air Wave Surrounding an Expanding Sphere," Proc. Royal Soc., A186, 273, 1946.

Todd, J., Survey of Numerical Methods, McGraw-Hill, New York, 1962.

Yu, K., and M. M. Klein, "Diffusion of Small Particles in a Nonuniform Atmosphere," Phys. Flu., 7, 651, 1964.

Vincenti, W. G., and C. H. Kruger, Introduction to Physical Gas Dynamics, Wiley, New York, 1965.

Waldman, H., "The Coupling between the Ionosphere and the Protono-
sphere and its Implications on the Long-Term Variations of the
Ionospheric Electron Content," Technical Report No. 13, Radio-
science Laboratory, Stanford Electronics Laboratories, Stanford
University, Stanford, CA, 1971.

Zel'dovich, Ya. B., and Yu. P. Raizer, Physics of Shock Waves and
High-Temperature Hydronamic Phenomena, Vol I and II, Academic
Press, New York, 1967.

Zettlemoyer, A. C., Nucleation, Marcel Dekker, New York, 1969.